Spins in Rings: New Chemistry and Physics with Molecular Wheels

A thesis submitted to the University of Manchester for the degree of

Doctor of Philosophy

in the Faculty of Science and Engineering

2016

Robert Jack Woolfson

School of Chemistry

Contents

Table of Contents

Contents **3**
Table of Contents 3
List of Figures 5
List of Schemes 9
List of Equations 11
List of Abbreviations 13
List of Constants and Symbols 15
Abstract **17**
Declaration **19**
Copyright Statement **21**
Acknowledgements **23**
Chapter 1 Introduction **27**
1.1 Rational for Submission by Alternative Format 27
1.2 Project Aims 27
1.3 Thesis Structure 27
1.4 Author Contributions 28
Chapter 2 Quantum Computing **29**
2.1 The Qubit 30
2.1.1 Potential Applications 31
2.1.2 The DiVincenzo Criteria 32
2.2 Potential Qubits 33
2.2.1 Nuclear Spin Qubits 33
2.2.2 Molecular Electron Spins as Qubits 34
2.2.3 A Single Molecule Spin Qubit 35
2.2.4 Triangles as Qubits 36
2.2.5 Molecular Wheels 38
2.2.6 Molecular Wheels as Qubits 41
2.2.7 Linking {Cr_7Ni} wheels via Ligand Substitution 42
2.2.8 Functionalising {Cr_7Ni} wheels via Threads 46
Chapter 3 Methodology **49**
3.1 Methods Used 49
3.1.1 Orbitrap Mass Spectrometry 49

3.1.2 Elemental Analysis 50
3.1.3 X-ray Crystallography 50
3.1.4 Physical Characterisation 52
3.1.5 SQUID Magnetometry 52
3.1.6 Computational Modelling 53
Chapter 4 Paper 1 55
"$[CrF(O_2C^tBu)_2]_9$: Synthesis and Characterization of a Regular Homometallic Ring with an Odd Number of Metal Centres and Electrons" 55
Chapter 5 Paper 2 77
"The Synthesis, Characterisation and Coordination Chemistry of a Highly Sterically Hindered Phosphine Ligand" 77
Chapter 6 Paper 3 107
"Application of Paramagnetic NMR to the Characterisation of Magnetic Anisotropy in Supramolecular Systems" 107
Chapter 7 Paper 4 129
"Heterometallic Wheels Linked by Lanthanide tris- β-diketonates as ABA Qubit Systems" 129
Chapter 8 Conclusions and Future Work 155
References 159

WORD COUNT: 44,172

List of Figures

Figure 1: a. Structure of a nitrogen vacancy centre with nitrogen (green) and vacancy (blue). b. Energy level diagram of the NV centre showing photon emission at 637 nm. c. Hahn Echo decay curve (at r.t.) of a single NV centre with measured T_2 (from modelled curve, orange) of 0.35 ms. d. Pulse sequence for optical detection of spin echo. Adapted with permission from Nature Publishing Group.[43] 34

Figure 2: a. Rendering of the structure of the nuclear spin qubit transistor. The nuclear levels of the Tb (coloured circles) within the Tb (pink) are coupled to the Pc ligand (white) which is then coupled to the source, drain and gate (not shown). b. The internally coupled systems of the transistor. The four Tb nuclear spin states are hyperfine coupled to the electronic spin of the Tb which are antiferromagnetically exchange coupled to the ligand electrons. Adapted with permission from the AAAS.[67]36

Figure 3: a. Original schematic of the proposed structure of $[Fe_3(O_2CMe)(OH_2)]NO_3$. Reproduced from Welo (1928).[84] b. The first X-ray crystal structure of $[Cr_3O(O_2CMe)_6]^+$. Reproduced with permission from the Nature Publishing Group.[84].37

Figure 4: Diagram of magnetic field induced (*B*-field) transitions between spin states of opposite spin (S_Z) and electric field induced (*E*-field) transitions between spin states of opposite chirality (C_Z). Reproduced with permission of the American Physical Society.[87] 38

Figure 5: a. X-ray crystal structure of $\{Fe_{10}\}$. Fe (brown), Cl (pale green), O (red), C (grey). Protons omitted for clarity. b. X-ray crystal structure of $\{Cr_8\}$. Cr (green), F (yellow), O (red), C (grey). Protons, tert-butyl methyl groups and solvent omitted for clarity.....39

Figure 6: a. X-ray crystal structure of $\{Fe_8\}$ reported by Ahmed *et al*.[99] Fe (brown), N (blue), O (red), C (grey). Protons and disorder omitted for clarity. b. X-ray crystal structure of $\{Mn_6U_{12}\}$ reported by Mazzanti and co-workers. Mn (purple), U (pale blue), N (blue), O (red), C (grey). Protons and solvent molecules omitted for clarity. ..40

Figure 7: X-ray crystal structure of $[NH_2{}^nPr_2][Cr_7NiF_8(O_2C{}^tBu)_{16}]$ $\{Cr_7Ni\}$. Cr (green), Ni (pale green), F (yellow), O (red), C (grey). Protons, methyl carbons and template omitted for clarity.....42

Figure 8: a. X-ray crystal structure of $[NH_2{}^nPr_2][Cr_7NiF_8(O_2CC_4H_3S)_{16}]$. Cr (green), S (yellow), F (blue), O (red), C (grey). Protons and template omitted for clarity. b. 3D view of a single cluster. c. STM image (50 x 25 nm^2) of the $\{Cr_7Ni\}$ wheels on the Au(111) surface. Modified with permission from the American Physical Society.[123] ...44

Figure 9: a. Two {Cr_7Ni} wheels linked through a single Cu^{II} centre with communication throughout system (shown schematically on top). b. Two {Cr_7Ni} wheels linked through a diamagnetic Cu^{II} dimer with no coupling (shown schematically on top). Cr (green), Ni (dark green), Cu (orange) F (yellow), O (red), C (black). Methyl groups, protons and templating ammonium cation omitted for clarity. Reprinted with permission from Nature Publishing Group.[109] 45

Figure 10: a. X-ray crystal structure of substituted {Cr_7Ni} wheels linked together by $Co(SCN)_2$. b. Schematic representation of the CNOT gate. c. X-ray crystal structure of iso-nicotinic substituted {Cr_7Ni} wheels linked together by a {Ru_2Co} triangle. d. X-ray crystal structure of substituted {Cr_7Ni} wheels linked together by $Co(ClO_4)$. e. X-ray crystal structure of substituted {Cr_7Ni} wheels linked together by $Co(ClO_4)$. f. Schematic representation of an iSWAP gate. Cr(green), Co (dark red), Ni (purple), Ru (brown), N (cyan), O (red), S (yellow), C (grey), F (pale green). Tert-butyl groups, protons, templating ammonium cation and perchlorate anions omitted for clarity. Reproduced under the Creative Commons Licence.[131] 46

Figure 11: X-ray crystal structure of {Cr_7Ni} with a [$PyCH_2NH_2C_2H_5Ph$] thread linked to $Cu(hfac)_2$ view a. side on and b. perpendicular to the {Cr_7Ni} metal plane. C. Representation of the g_z-components of the Cu^{II} and {Cr_7Ni} spin vectors. Cr (green), Ni (purple), Cu (dark blue), F (yellow), O (red), C (grey). Tert-butyl groups, protons and disorder omitted for clarity. Adapted with permission from John Wiley and Sons.[65] 47

Figure 12: Cutaway diagram of an Orbitrap mass analyser. Ion pathway indicated by the red arrow. Injection occurs with velocity perpendicular to the axial direction (z-axis) of the Orbitrap, followed by rotation both around and along the inner electrode. Reproduced with permission from John Wiley and Sons.[141] 50

Figure 13: Graphical representation of the sphere used for calculation of $\%V_{bur}$ values with *d* and *r* shown. Reproduced with permission from John Wiley and Sons.[154] 53

Figure 14: a. X-ray crystal structure of {Cr_9F_{10}} with terminal fluoride emphasised. b. X-ray crystal structure of {Cr_9F_{11}} with terminal fluorides emphasised. Cr (green), F (yellow), O (red), C (grey). Tert-butyl methyl groups, protons and templating ammonium cation omitted for clarity..... 55

Figure 15: a. X-ray crystal structure of $Ni(hfac)_2$ linked structure ([$NH_2{}^nPr_2$] [$Cr_7NiF_8(O_2C{}^tBu)_{15}(O_2CC_5H_5N)$])$_2$ $Ni(hfac)_2$ with wheels in *trans*- geometry around metal. b. X-ray crystal structure of $Ni(hfac)_2$ linked structure ([$NH_2{}^nPr_2$] [$Cr_7NiF_8(O_2C{}^tBu)_{15}(O_2CC_4H_4N_2)$]) with wheels in *cis*- geometry around metal. Cr

(green), Ni (turquoise), F (yellow), O (red), C (black), N (blue). Tert butyl methyl groups, protons and ammonium cation omitted for clarity. 78

Figure 16: Diagram showing principle axes of the *g*-tensors for two Co^{II} dimers. The magnitude of the vectors is proportional to the magnitude of *g*. a. X-ray crystal structure of $[Co_2(H_2O)(O_2C^tBu)_4(HO_2C^tBu)_4]$ b. X-ray crystal structure of $[Co_2(H_2O)(O_2C^tBu)_4(HO_2C^tBu)_2(py)_2]$. Co (blue), O (red), N (dark blue), C (grey). Protons omitted for clarity. Reproduced with permission from John Wiley and Sons.[164] 107

Figure 17: a. Structure of the bridging ligand in the equatorial plane of the $\{Mn_4\}$ clusters. b. X-ray crystal structure of $\{Mn_4\}$ with thermal ellipsoids set at 50 % probability. Solvent and protons omitted for clarity. c. Schematic representation of the distorted cubane-like core consisting of four manganese ions, four oxygens, two bridging carboxylates and two chelating carboxylates. 108

Figure 18: Energy level diagram qualitatively showing the splitting of the Co^{II} ^4F free ion term under various crystal fields. [169] 109

Figure 19: a. Chemical structure of the monomer for the triple helicate (Sim) structure. b. Space fill model of the triple helicate with strands shown in red, blue and yellow, Mn green. Non-equivalent g-tensors for each Mn^{II} ion shown schematically. Adapted with permission from the American Chemical Society.[63] 130

Figure 20: a. X-ray crystal structure of [CeEr] dimer with spin direction and magnitude. b. Scheme of ground state energy level separation. Reproduced under the ACS AuthorsChoice license.[70] 130

List of Schemes

Scheme 1: Structures of chemicals used to introduce donor functionality to {Cr_7Ni}…45

List of Equations

Eq. 1 30
Eq. 2 30
Eq. 3 51
Eq. 4 51
Eq. 5 51
Eq. 6 51
Eq. 7 53
Eq. 8 56
Eq. 9 56

List of Abbreviations

ATIR – Attenuated Total Reflectance Infra-Red

CCDC – Cambridge Crystallographic Database Centre

COSY – Correlation Spectroscopy NMR

{Cr_7M} – $[NH_2{}^nPr_2][Cr_7MF_8(O_2C{}^tBu)_{16}]$

{Cr_8} – $[Cr_8F_8(O_2C{}^tBu)_{16}]$

{Cr_9F_9} – $[Cr_9F_9(O_2C{}^tBu)_{18}]$

{Cr_9F_{10}} – $[NH_2{}^iPr_2][Cr_9F_{10}(O_2C{}^tBu)_{18}]$

{Cr_9F_{11}} – $[NH_2{}^iPr_2][Cr_9F_{11}(O_2C{}^tBu)_{17}]$

DFT – Density Functional Theory

DOSY – Diffusion Spectroscopy NMR

DPPB – 4-diphenylphosphinobenzoic acid

EPR – Electron Paramagnetic Resonance

{Fe_8} – $[Fe_8O_4(C_{15}H_{15}NO_3)_8]$

{Fe_{10}} – $[Fe_{10}(OMe)_{20}(O_2CCH_2Cl)_{10}]$

ESMS – Electrospray Mass Spectrometry

FTMS – Fourier Transform Mass Spectrometry

Hfac - hexafluoroacetylacetonate

HOPG – Highly Oriented Pyrolytic Graphite

ICP-AES – Inductively Coupled Plasma Atomic Emission Spectroscopy

INS – Inelastic Neutron Scattering

{Mn_{12}} – $[Mn_{12}O_{12}(O_2CCH_3)_{16}(H_2O)_4]$

{Mn_6U_{12}} – $[(Mn(C_5H_5N)_3[UO_2(salen)_2]_2)_6]$

NHC – N-heterocyclic carbene

NMR – Nuclear Magnetic Resonance

NV – Nitrogen Vacancy

Pc – Phthalocyaninato

pcs – pseudocontact shift

^{n}Pr – n-propyl

^{i}Pr – iso-propyl

py – pyridine

QIP – Quantum Information Processing

RF – Radiofrequency

SOI – Spin Orbit Interactions

r.t. – Room Temperature

SMM – Single Molecule Magnet

SQUID – Superconducting Quantum Interference Device

STM – Scanning Tunnelling Microscopy

^{t}Bu – tert-butyl

THF – Tetrahydrofuran

VT – Variable Temperature

ZFS – Zero Field Splitting

Please note that in the discussions below, the notation {M} refers to a central core of metals regardless of the surrounding ligand environment. Where necessary, full chemical formulae will be given in the text otherwise please refer to the abbreviations section.

List of Constants and Symbols

A – Hyperfine Nuclear Coupling Constant

B – Magnetic field

C - Chirality

D – Axial Zero Field Splitting Parameter

δ – Chemical Shift

E – Electric Field

E – Energy

E – Rhombic Zero Field Splitting Parameter (Chapter 7 only)

F – Structure Factor

g-value – Landé g-value

γ_I – Nuclear Magnetogyric Ratio

ħ – Reduced Planks Constant

I – Nuclear Spin

J – Spin-spin coupling constant

k – Wavevector

ppm – parts per million

ρ – Electron Density

Q – Quality Factor

$\vec{Q}$ – Momentum Transfer

S – Electron Spin

σ – Standard Deviation

T – Temperature

T_1 – Spin-lattice relaxation time

T_2 – Spin-spin relaxation time

T_m – Phase memory time

τ – Half-life

τ_s – Electron Correlation Time

μ_0 – Magnetic Permeability of Vacuum

μ_B – Bohr Magneton

$\%V_{bur}$ – Percentage Buried Volume

ψ – Wavefunction

w – Weighting

ω - Momentum

χ – Magnetic Susceptibility

λ – Wavelength

The convention for reporting J coupling used in this thesis is the -2J convention, where the Hamiltonian used is $\hat{H} = -2JS_1S_2$. A positive sign implies a ferromagnetic interaction whilst a negative sign implies an antiferromagnetic interaction.

Abstract

Title: Spins in Rings: New Chemistry and Physics with Molecular Wheels
Author: Robert Jack Woolfson
Institution: The University of Manchester
Faculty: Science and Engineering
Degree: Doctor of Philosophy
Submitted: 01/09/2016

This thesis explores the synthesis and characterisation of a range of molecular wheels containing unpaired electron spins. These molecular spin systems are of considerable interest, both for the insight they provide into the physics of such systems and for their potential as quantum bits ("qubits") in a quantum information processing device. In particular, this thesis explores using these wheels to meet criteria 1 and 5 of the DiVincenzo criteria.

The synthesis of a novel homometallic and nonametallic ring of Cr^{III} ions is introduced, along with extensive physical characterisation. Inelastic Neutron Scattering measurements suggest that the molecule has an almost degenerate $S = 1/2$ ground state with only 0.1 meV separation, making this ring a near perfect example of a Type I frustrated spin system.

Chemical modification of the heterometallic $\{Cr_7M\}$ family of wheels with both hard and soft Lewis base functionality is also explored. Using a triphenylphosphine derivative, the coordination chemistry of a highly sterically hindered mono-substituted triphenylphosphine derivative with gold is explored, yielding new arrangements of the wheels. Changes in the electronic and steric properties of the system are studied by a combination of ^{31}P NMR spectroscopy and DFT modelling, revealing dramatic changes in the phosphorus donor properties.

The effect of this ligand substitution on the anisotropy tensor of Co^{II} contained in a heterometallic $\{Cr_7Co\}$ ring is explored using variable temperature ^{1}H NMR spectroscopy. Using a combination of the experimentally observed ^{1}H NMR dipolar shifts and computational modelling, a significant change in the anisotropy tensor of the cobalt is found.

Finally, as part of a *g*-engineering approach to qubit design the chemistry of the octametallic $\{Cr_7Ni\}$ ring functionalised with triphenylphosphine oxide is introduced. Initial efforts towards developing a hybrid $\{Cr_7Ni\}_2Ln$ (Ln = Gd, Eu) qubit system, along with characterisation by EPR and luminescence spectroscopy, suggest that this may be a route to developing a qubit with the capacity for optical control of the communication.

Declaration

Title: Spins in Rings: New Chemistry and Physics with Molecular Wheels

Author: Robert Jack Woolfson

I declare that no portion of the work referred to in the thesis has been submitted in support of an application for another degree or qualification of this or any other university or other institute of learning.

Signed:

Date: 01/09/2016

Copyright Statement

i. The author of this thesis (including any appendices and/or schedules to this thesis) owns certain copyright or related rights in it (the "Copyright") and he has given The University of Manchester certain rights to use such Copyright, including for administrative purposes.

ii. Copies of this thesis, either in full or in extracts and whether in hard or electronic copy, may be made only in accordance with the Copyright, Designs and Patents Act 1988 (as amended) and regulations issued under it or, where appropriate, in accordance with licensing agreements which the University has from time to time. This page must form part of any such copies made.

iii. The ownership of certain Copyright, patents, designs, trademarks and other intellectual property (the "Intellectual Property") and any reproductions of copyright works in the thesis, for example graphs and tables ("Reproductions"), which may be described in this thesis, may not be owned by the author and may be owned by third parties. Such Intellectual Property and Reproductions cannot and must not be made available for use without the prior written permission of the owner(s) of the relevant Intellectual Property and/or Reproductions.

iv. Further information on the conditions under which disclosure, publication and commercialisation of this thesis, the Copyright and any Intellectual Property University IP Policy (see http://documents.manchester.ac.uk/display.aspx?DocID=24420), in any relevant Thesis restriction declarations deposited in the University Library, The University Library's regulations (see http://www.library.manchester.ac.uk/about/regulations/) and in The University's policy on Presentation of Theses.

Acknowledgements

First and foremost I owe thanks to my supervisors, Professor Ian Kinloch and particularly Professor Richard Winpenny for his unceasing support during both my MChem and my Ph.D.

Secondly, thanks to the EPSRC for funding the NoWNANO Doctoral Training Centre which has supported me financially. Thanks also to The University of Manchester for 8 years of memorable experiences, and to my colleagues in the magnets lab.

Thank you to the School of Chemistry staff and research services – particularly Professor Eric McInnes for his help with EPR, Dr Inigo Vitorica-Yrezabal from X-ray crystallography, Dr Ralph Adams from the NMR service, Dr Floriana Tuna from the EPR facility and Mr Gareth Smith from mass spectrometry.

Much of this work wouldn't have been possible without collaborations across Europe. Thanks to Simon Ansbro for his help with neutrons, and to Alessandro Chiesa for the simulations. Also Tatiana Guidi, Sax Mason, Hannu Mukta, Anne Stunault and Jacques Ollivier.

I gratefully thank the many friends I've had throughout my Ph.D, but particularly Chloë Oakland, Stephen Worrall, Peter Youle, Rebecca Dey, Andreas Kostopoulos, Sam Marshman, Chris Martin, Ross Heard and Kane Heard for friendship freely given.

It wouldn't be a thesis from the Molecular Magnetism group without a huge thank you to Dr Grigore Timco, who didn't quite teach me everything I know about synthetic chemistry but it certainly felt like it most days.

A heartfelt thanks to Professor David Collison, whose door was always open and with whom I had a great many challenging and enjoyable discussions about science and what it means to be a scientist.

And finally, thank you to my ever patient girlfriend Sarah Ward, to my "uncle" Frank Warner and most of all to my loving parents Howard Woolfson and Caroline Bottoms without whom – in a great many ways – none of this would have been possible.

“The pleasure of finding things out”

Richard Feynman

Chapter 1 Introduction

1.1 Project Aims

The general aim of this work has been to explore spins within molecular wheels. This has taken two distinct routes. Firstly, building on a previous project in which the spin frustration of two members of a {Cr_9} family was characterised – leading to spin frustration being redefined – a novel nonametallic wheel has been synthesised and the electronic structure characterised by a range of spectroscopic techniques to understand the nature of the frustrated spin system and whether it shows spin frustration in the strictest sense.

Secondly, the scope of the coordination chemistry accessible using the {Cr_7M} family has been extended by introducing phosphine and phosphine oxide donor functionality for the first time. The coordination chemistry of these new ligand systems has been explored and various effects of the new ligands on the spin system within the rings and on the communication between linked rings has been studied to attempt to meet criteria 1 and criteria 5 of the DiVincenzo criteria.

1.2 Rational for Submission by Alternative Format

This thesis is presented in an alternative format in which each chapter is written in the style required for journal publication. The main benefits of writing a thesis in this way are that: (i) it reduces the conflict of interest between the desire to publish work before the end of the project and the necessity of completing a thesis, since both can be achieved at the same time, (ii) it avoids the redundancy present in the rewriting of traditional chapters as articles for journal publication later on, whilst also eliminating the risks of self-plagiarism that arise from such rewriting, and (iii) it encourages the publication of results during the Ph.D. project (and greatly facilitates publication afterwards).

1.3 Thesis Structure

An introduction to the area of quantum computing and the general context of the research contained in this thesis is presented in Chapter 2. This is followed by a summary of the overall aims of the research and the instrumental methods used. Chapters' 4 – 7 contain the papers that constitute the body of research in this thesis. Chapter 8 outlines a summary of this work and some suggestions on future research directions.

1.4 Author Contributions

Paper 1

R.J.W. performed synthetic procedures and chemical characterisation of the novel complex with assistance from G.A.T., and I.J.V. performed the detailed crystallographic analysis. T.G. collected INS measurements, A.C., P.S. and S.C. performed computational modelling, E.P. kindly performed DFT calculations at short notice and R.E.P.W. advised on all aspects of the work.

Paper 2

R.J.W. performed all synthetic procedures and characterisation in collaboration with G.A.T. D.C. and R.E.P.W. advised on all aspects of the work.

Paper 3

R.J.W. performed all synthetic procedures in collaboration with G.A.T., the variable temperature NMR study with assistance from R.W.A. and the modelling with the assistance of D.C. R.E.P.W advised on all aspects of the work.

Paper 4

R.J.W. performed all synthetic procedures and modelling in collaboration with G.A.T, A.K.K. collected EPR measurements, A.J.F. advised on the transient EPR measurements and R.E.P.W. advised on all aspects of the work.

Chapter 2 Quantum Computing

Computers are ubiquitous. Since 1936 and the eponymous Turing's suggestion of a Universal Turing machine, the development of silicon chips has resulted in a huge growth in the availability and utility of computers.[1] Computing power has increased roughly in line with Moore's Law, *i.e.* a doubling of the number of transistors in a given area approximately every two years since the 1960's.[2] The Apollo Guidance computer that sent Neil Armstrong and colleagues to the moon in 1969 had ≈ 64 kb of memory and a clock speed of 0.043 MHz. For comparison, an Apple iPhone 6 released in 2014 has an inbuilt processor memory of 1.94 Gb and a clock speed of 1.85 GHz – approximately 430 million times the memory and processing power.

However, computers are also limited. The bits in computers operate under classical physics, *i.e.* they are 1 or 0, on or off. The use of classical physics limits the ways a computer can operate as it requires classical inputs and classical equations. As the fundamental components of a computer chip move towards the nanoscale, the physics moves towards the quantum realm in which things can be on, off or somewhere in between. In 1981, the late, great Dr Richard Feynman gave a keynote address at MIT in which he suggested that the challenge of modelling physical systems in a realistic fashion, rather than through the classical approximations used with a classical computer, required a fundamentally different approach.[3] A new type of computer needed to be developed, based on quantum bits, or "qubits", combined with a different set of operations based on quantum mechanics. This idea was refined by David Deutsch in 1985, in which he suggested that Feynman's proposed computer was not a true quantum computer but a quantum simulator.[4] However, both systems come under the general area of Quantum Information Processing (QIP), i.e. harnessing the power of the information inherent in quantum states.

To understand the difference between Feynman's Quantum Simulator and Deutsch's Quantum Computer, it is helpful to first understand the general principles underpinning quantum computing. Simply put, quantum states are entangled such that one part of the system cannot be described without referring to the rest.[5] By initialising a system in a given state, it is possible to set a quantum system up to ask a question. Because there are many possible states that can exist (for n entangled qubits, there are 2^n possible states), and through superposition they all potentially exist until the system is observed, it is possible to manipulate a set of entangled states and then, by observing the system,

collapse the superposition and get an answer to the question.[6] It should be noted that quantum computing, as with all QIP, is probabilistic rather than deterministic and so each experiment must be repeated many times to determine the correct answer.

In a 2005 lecture, Andrew Briggs concisely outlined the differences between Feynman's Quantum Simulator and Deutsch's Quantum Computer.[7] Feynman suggested an ideal system of a lattice of spin systems where each nearest-neighbour interaction can be specified at will. Each time the system is initialised, the required rules for the simulation are programmed in by controlling the nearest neighbour interactions and the system is then ready to perform calculations.[3] To be a true computer, rather than a simulator, David Deutsch suggested that the laws that govern the computer (the quantum basis set, analogous to binary) must be chosen once and then all states are initialised with reference to this basis state. Whilst initially more restrictive than a quantum simulator, classical computing has shown a careful choice of basis set allows complex algorithms to be designed and run without the need to define a new basis set each time.

In the discussion that follows, the term quantum computing is used to refer to the general idea of a computer based on qubits and quantum mechanics – *i.e.* Quantum Information Processing – without consideration of the physical rules of the final system.

2.1 The Qubit

As mentioned above, the fundamental component of a quantum computer is the qubit. Similar to a bit, a qubit must be a well-defined two state system i.e. $|0\rangle$ and $|1\rangle$. However, unlike a bit, a qubit can exist in any arbitrary superposition of these two states as well as the pure state (Eq. 1):

$$\psi = \alpha|0\rangle + \beta|1\rangle \qquad \text{Eq. 1}$$

where α and β are the amplitudes of each state in the wavefunction φ and their values normalised (Eq. 2) such that:

$$|\alpha|^2 + |\beta|^2 = 1 \qquad \text{Eq. 2}$$

If two qubits are placed together in such a way that their wavefunctions (ψ) are correlated, i.e. they form a state in which neither qubit can be described without reference to the other, they are said to be entangled. If a pair of qubits are in an entangled state, manipulating the wavefunction of one qubit will necessarily cause some change with the second qubit.[8] The gate operations in quantum computing, such as the

CNOT and i$\sqrt{\text{SWAP}}$ gates introduced in Section 2.2.8, are the operations used to perform calculations on qubits. By exploiting the new states created by superposition, combined with the ability to exponentially increase the number of accessible states by entanglement, QIP has the potential for a dramatic increase in both the power of the computer and, due to its quantum nature, the scope of the problems that can be addressed.[9]

2.1.1 Potential Applications

There are two algorithms that provide excellent demonstrations of the potential power of QIP. The Grover algorithm[10, 11] for searching databases has the potential to dramatically speed up such searches, a non-trivial task as the database becomes larger. The Shor algorithm[12, 13] for factorising prime numbers has the potential to break many modern methods of encryption and bring about a fundamental change in electronic security. Each of these algorithms is considered in turn below, along with representative examples of their implementation.

In a classical system, searching an unsorted database with N entries requires an average of $N/2$ steps as each entry has to be searched sequentially (or randomly) until the correct entry is found. Using the Grover algorithm, the system is initialised in a superposition of all N states. A series of operations are then applied to amplify the probability amplitude of the desired state, leaving only this state at the end. This allows the database to be searched in $\sqrt{N}$ steps, providing a quadratic speed up of search relative to classical computing. The Grover algorithm has been implemented on a wide range of systems, for example exploiting the differing chemical shifts of ^{13}C labelled chloroform to search a 12-item database,[14] using $I = ½$ $^{111}Cd^{+}$ nuclei pulsed with microwaves and a laser to search a 4-item database,[15] and using a single nitrogen-vacancy centre in diamond to search a 12-item database.[16]

Prime numbers are at the core of modern cryptography, most visibly in the RSA keys used to encrypt online commercial transactions.[17] Two large prime numbers (of at least 512 digits, and normally 1024) are multiplied to give an encryption key with a second (private) key then used to decrypt it after transmission. The security comes from the fact that the factorisation of large prime numbers is not a nondeterministic polynomial time complete (NP complete) problem – or at least is not known to be – so the time taken to solve the problem does not scale in a polynomial relationship to the complexity.[18] The Shor algorithm utilises the power of quantum information to factorise whole numbers

into their prime factors exponentially faster than any known classical algorithm. The technical details of the Shor algorithm are beyond the scope of this introduction[19] but it has been successfully implemented using a wide range of systems, including to factorise 15 using the differing chemical shifts of a perfluorobutadienyl-iron complex in an NMR based system[20] and in a ion-trap system with $^{40}Ca^{+}$ ions.[21] If these calculations can be scaled to larger prime numbers, the Shor algorithm has the potential to render prime number based encryptions redundant and revolutionise cryptography.

2.1.2 The DiVincenzo Criteria

Having looked at both the fundamental principles of quantum computing and the potential applications, let us now consider how to build a working quantum computer. The key physical requirements to implement a working quantum computer were outlined by David DiVincenzo in 2000.[22] These criteria state that there must be:

1. A scalable physical system with well characterised qubits
2. The ability to initialise the qubits to a reference state
3. Long decoherence times
4. A universal set of quantum gates
5. A qubit specific measurement capability

In practice, these criteria suggest that the behaviour of the underlying qubits should be fully understood and that it must be possible to introduce more qubits to the entangled network at will whilst retaining the ability to control the system. It should be possible to turn the system on and set it into an initial state – for example $|0000\rangle$ – and that it must be coherent (the qubits must continue communicating without noise disrupting the quantum states) for a long enough period of time (T_2 – spin-spin relaxation time – or T_M – Phase Memory Time) to allow for both computational and error correcting operations.[13] There should be a standard set of operations, or gates, with which to perform computations and, once the computations are finished, there should be a selective way of reading out the results.

This work has aimed primarily at meeting the first of these criteria, developing a chemical system that is well understood physically and electronically, and that is scalable.

2.2 Potential Qubits

There are a huge number of systems being explored as potential qubits from topological systems and trapped ions in Bose-Einstein condensates to superconducting circuits.[23-27] A selection of references is given below, readers are particularly directed to the reviews by Ladd *et al.* (2010), Devoret and Schoelkpof (2013), and Gao *et al.* (2015).[27-40] For the purpose of brevity and clarity, discussions are limited here to electron and nuclear spin based qubits, and primarily molecular systems with unpaired electrons.

2.2.1 Nuclear Spin Qubits

Nuclear spin qubits have shown significant potential, particularly in isotopically pure ^{28}Si doped with ^{31}P atoms and in isotopically pure ^{12}C diamonds with nitrogen vacancies (NVs) introduced.[41-44] Both ^{28}Si and ^{12}C are nuclear spin free, providing a spin free "nuclear bath" and increasing the coherence times. In silicon, a remarkable T_2 of 39 minutes has been reported for a $^{31}P^+$ atom[45] and of 180 s for a neutral ^{31}P atom at cryogenic temperatures.[46] Entanglement between electron and nuclear spins [47] allowed information transfer and readout (via EPR measurements).[48, 49] Similarly, NV centres in diamonds (

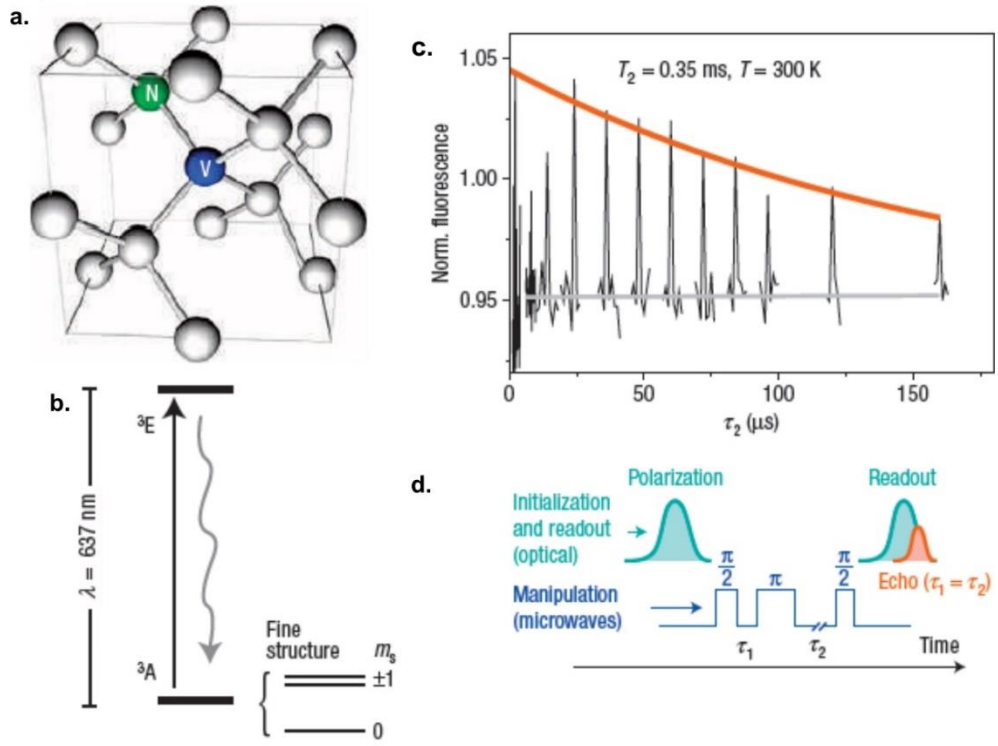

Figure 1)[42] have shown electron-nuclear coupling as well as addressability by EPR[33] and readout via optical methods.[43, 50] Furthermore, it has been shown that NV centres

can be optically coupled via "flying qubits" allowing information transfer between them.[51-53]

However, in both cases precise control of the location of the qubit in the substrate presents a considerable challenge, as does preventing decoherence through unwanted coupling between adjacent qubits. Similarly, scaling such systems up to the size necessary for implementing large scale quantum algorithms is not a trivial task.[43, 54]

Nuclear spins in molecular systems have been successfully used as qubits in prototype quantum computers. As mentioned above, the differing chemical shifts in various compounds have been exploited to implement both the Grover and Shor algorithms.[14, 20] However, there are several inherent flaws in NMR based qubits. Firstly, the systems are challenging to initialise and entangle. Secondly, as the molecule becomes more complex (*i.e.* incorporating more qubits) the difference in the chemical shifts between individual qubits becomes smaller and each qubit becomes harder to address individually – limiting both the scalability and the sensitivity of the system. One recent estimate places the upper limit of qubits in an NMR based readout system at ~ 20 bits of input.[55]

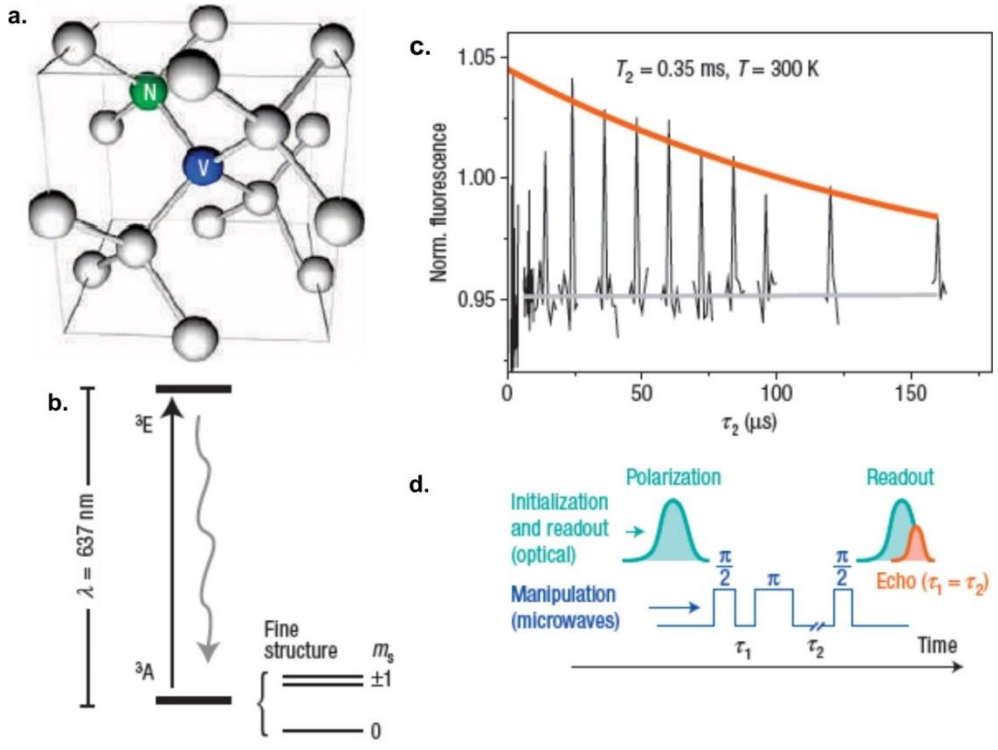

Figure 1: a. Structure of a nitrogen vacancy centre with nitrogen (green) and vacancy (blue). b. Energy level diagram of the NV centre showing photon emission at 637 nm. c.

Hahn Echo decay curve (at r.t.) of a single NV centre with measured T_2 (from modelled curve, orange) of 0.35 ms. d. Pulse sequence for optical detection of spin echo. Adapted with permission from Nature Publishing Group.[43]

2.2.2 Molecular Electron Spins as Qubits

In 2001, Leuenberger and Loss published a seminal paper proposing the use of molecular magnets as qubits to implement the Grover algorithm.[56] A single molecule which shows retention of its magnetisation (spin state) in the absence of a magnetic field is called a single molecule magnet (SMM). The spin states of SMMs such as the $\{Mn_{12}\}$[57-59] or $\{Fe_8\}$[60] clusters were proposed as ideal candidates for a qubit. Both $\{Mn_{12}\}$ and $\{Fe_8\}$ have large spin values (S = 10) and large negative anisotropy (D) values, leading to well defined M_S states with sizeable barriers to spin flipping between $\pm M_S$. Qubit manipulation and readout can both be performed using a combination of EPR and applied magnetic fields, leading to the entire process potentially taking as little as 0.1 ns from start to finish.

SMM behaviour is not required for a molecular system to be a good candidate for a qubit. Due to the multiple low lying spin states in $\{Mn_{12}\}$ and many other cluster based SMMs, they are stronger candidates for molecular memory and molecular spintronic devices than as qubits.[56, 61] The key requirement for a molecular qubit is a well-defined spin ground state, giving the $|0\rangle$ and $|1\rangle$ states. This ground state must be well isolated from excited states to prevent decoherence by induced transitions, ensuring a long enough coherence time to perform both gate operations and error correction (see Section 2.1.2).

A wide variety of molecular systems with varying arrangements of spins are being explored as potential qubits. Notable examples include systems based on Seth Lloyd's proposal of weakly entangled {ABC} spin heteropolymers[62] in which electromagnetic pulses are used to induce superposition and perform gate operations on spins with different g-values. This "g-engineering" approach has been explored using a triple stranded metallo-helicate with Mn^{II} as the qubit,[63] using organic radical spin systems,[64] and using the molecular wheels of Winpenny and co-workers. (see Section 2.2.6 and Chapter 7 for further discussions on g-engineering). [65] Other molecular systems being explored include single ion systems such as $TbPc_2$ (see Section 2.2.3) [66-69], a mixed Cu-Ln (Ln = Y, Gd, Tb) helicate showing SMM behaviour with weak intermolecular interactions,[70] as well as rings of metals known as molecular wheels.[71-73]

In the review below, the starting point is the simplest possible metal based molecular spin system, a single metal encased in an organic framework. Systems of increasing size and complexity will be introduced, culminating in the wheel-like arrangements of metals that are the topic of this thesis.

2.2.3 A Single Molecule Spin Qubit

As previously discussed for silicon and carbon systems, the coupling of electron and nuclear spins provides a powerful route to developing a working qubit - providing the lifetimes of both spin states are sufficiently long. Wernsdorfer and co-workers have shown that the nuclear spin state of $TbPc_2$ (Figure 2a) can be read out using an electric current when the molecule is deposited in a three terminal molecular spin transistor.[66, 67] The Tb^{III} ion has a well isolated $J = 6$ ground state with axial anisotropy that prevents flipping of the spins states. The Tb f-electrons are strongly hyperfine coupled to the nuclear spin ($I = 3/2$), splitting the $J = \pm 6$ ground state into four sub-states. These states are then weakly antiferromagnetically coupled to the unpaired electron in the Pc ligand. Using an applied magnetic field, pairs of these states can be brought into resonance in turn, resulting in a transition between the two states via quantum tunnelling. As the electron spins in the Tb^{III} and the ligand are weakly coupled, a change in the nuclear spin on the Tb results in a measurable change in the current flowing through the device. Later work showed that the $TbPc_2$ spin system could be controlled by means of an electric field instead of a magnetic field. Initialising the system into a given state followed by application of a local electric field resulted in observation of Rabi oscillations (consistent driven cycling between two electronic states), a signature of a coherent state.[67, 74]

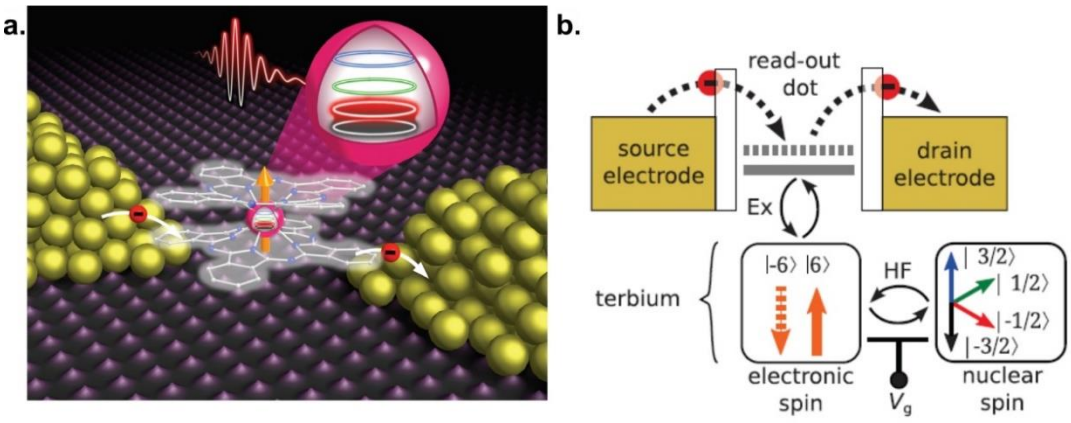

Figure 2: a. Rendering of the structure of the nuclear spin qubit transistor. The nuclear levels of the Tb (coloured circles) within the Tb (pink) are coupled to the Pc ligand

(white) which is then coupled to the source, drain and gate (not shown). b. The internally coupled systems of the transistor. The four Tb nuclear spin states are hyperfine coupled to the electronic spin of the Tb which are antiferromagnetically exchange coupled to the ligand electrons. Adapted with permission from the AAAS.[67]

2.2.4 Triangles as Qubits

The smallest possible metallocycle, a triangular arrangement of metals, was first reported in 1908 independently by Alfred Werner[75] and Rudolf Weinland[76] with the proposed formula $[Cr_3(O_2CMe)_6H_2O]^{3+}$ or $[Cr_3(O_2CMe)_6(OH)_2]^{+}$, but the structure was not assigned. In 1928, Milo Welo performed variable temperature magnetic studies on a range of $\{Cr_3\}$ and $\{Fe_3\}$ complexes and suggested that the only plausible structure that fit the data was a triangular arrangement of metals (Figure 3a). In 1965, the first crystal structure of a metallic triangle was obtained by Brian Figgis and Glen Robertson, confirming the triangular geometry and definitively settling the chemical formula as $[Cr_3O(O_2CMe)_6]Cl{\cdot}5H_2O$ (Figure 3b).

Since then, a wide range of $\{M_3\}$ structures have been reported. All share the same general features, with three metals bridged internally by a small electronegative element such as oxygen or fluorine and surrounded by bridging oxygen donor ligands. $\{M_3\}$ structures have been reported using metals throughout the Periodic Table, in both homo- and heterometallic arrangements.[77] Notable examples include o-vanillin bridged $\{Gd_3O\}$ and $\{Dy_3O\}$ triangles with antiferromagnetic coupling between the metals – and the dysprosium analogue showing SMM like behaviour,[78, 79] a range of electrochemically active $\{Ru_3\}$ and $\{Ru_2M\}$ triangles (see Section 2.2.8),[80, 81] a $\{Fe_2Co\}$ triangle used as a linking unit in rotaxanes (see Section 2.2.8),[82] as well as homometallic examples with the majority of the transition metals. An unusual example of a non-oxygen centred triangle was reported recently by Walsh *et al.* (2015). [83] The $\{Cr_2Ni\}$ triangle was found to have an unusual *g*-value of $g = 2.48$, suggesting potential applications as a qubit in a system exploiting the *g*-engineering approach.

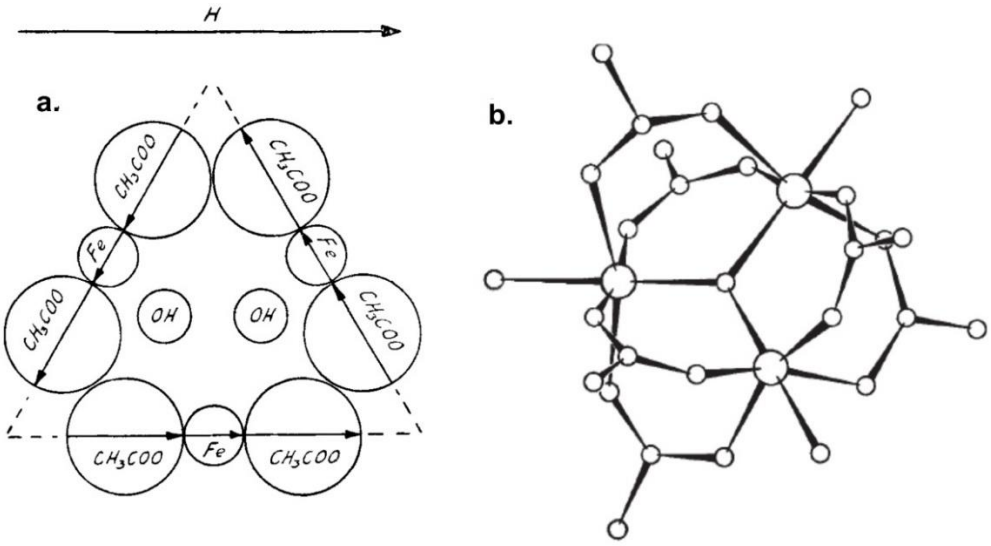

Figure 3: a. Original schematic of the proposed structure of $[Fe_3(O_2CMe)(OH_2)]NO_3$. Reproduced from Welo (1928).[84] b. The first X-ray crystal structure of $[Cr_3O(O_2CMe)_6]^+$. Reproduced with permission from the Nature Publishing Group.[84]

For this work, triangles are of particular interest as an introduction to spin frustration. Under the strict definition proposed by Kahn for molecular systems, a spin frustrated system is one where antiferromagnetic interactions between an odd number of equivalent half-integer spins results in a degenerate $S = 1/2$ ground state.[85] For a full discussion of the signature effects of spin frustration on the magnetism of a molecular system, the perspective by Jürgen Schnack is enlightening.[86] Frustration has two effects relevant for this work, one is the degeneracy of the ground state as this provides a potential two-level system for a qubit. The other involves the use of chiral spin states as a route to electric field switching of molecular spin states.

In 2010, Trif *et al*. published a paper outlining the key requirements for magnetic-electric field coupling (Figure 4).[87] Firstly, the molecule must lack an overall centre of inversion to allow transitions between spin states of opposite chirality. Secondly, the exchange bridges must possess a permanent dipole, although the molecule is not required to. Finally, the molecule must possess weak antisymmetric exchange (also referred to as Dzyaloshinskii-Moriya interactions) between spin centres to mediate spin-electric coupling. See 0 for further discussions and new results on spin frustration.

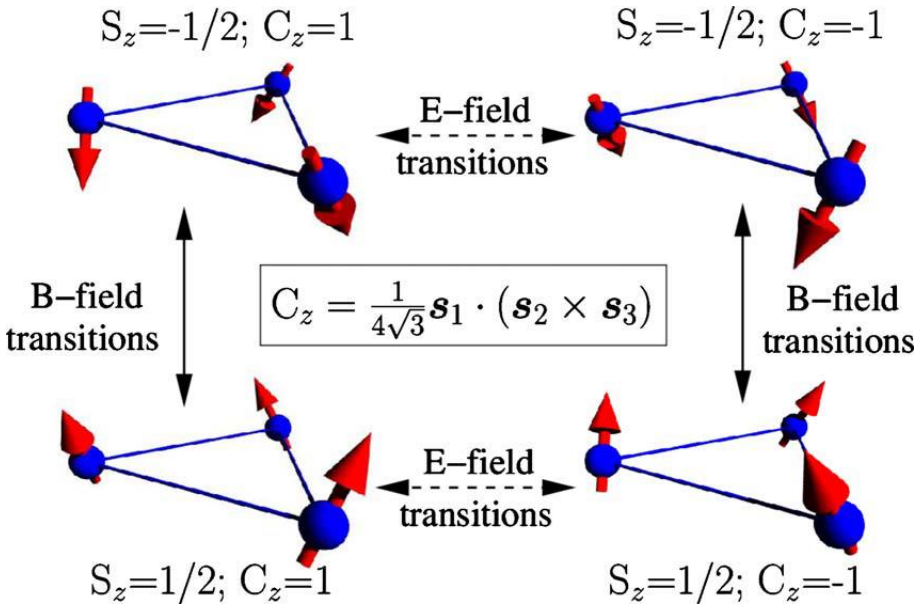

Figure 4: Diagram of magnetic field induced (*B*-field) transitions between spin states of opposite spin (S_Z) and electric field induced (*E*-field) transitions between spin states of opposite chirality (C_Z). Reproduced with permission of the American Physical Society.[87]

2.2.5 Molecular Wheels

First reported by Taft and Lippard in the United States,[88, 89] molecular wheels are cyclic arrays of metals supported by bridging organic ligands. They are essentially more complex versions of the triangles discussed above, with the potential complexity of the physical properties increasing with the size. The {Fe_{10}} molecular ferric wheel (Figure 5a) [$Fe_{10}(OMe)_{20}(O_2CCH_2Cl)_{10}$] reported by Taft *et al.* is a planar decametallic arrangement of Fe^{III} atoms bridged internally by μ_2 methoxides and externally by η_2 monochloroacetate ligands with each Fe^{III} site showing a distorted octahedral geometry. The Fe^{III} spins are antiferromagnetically coupled, with J = - 4.3 cm^{-1}.

A similar complex, the octametallic wheel [$Cr_8F_8(O_2C^tBu)_{16}$] {Cr_8} (Figure 5b), was first synthesised by Timco and co-workers in the former USSR (Moldova) in 1985, but due to patent restrictions could not be published in an English speaking journal until 1990.[90] {Cr_8} is synthesised in a one-pot template-mediated reaction using a metal fluoride, a large excess of a carboxylic acid and an amine as the template. It is a ring of Cr^{III} metals held together by μ_2 bridging fluorides on the inside of the metal ring and η_2 bridging carboxylates on the outside (in this case pivalic acid). Similar to {Fe_{10}}, it is planar with all the metal sites in a distorted octahedral coordination environment. The

eight Cr^{III} sites are antiferromagnetically coupled (J = -5.89 cm^{-1}), leading to an S = 0 ground state.[91]

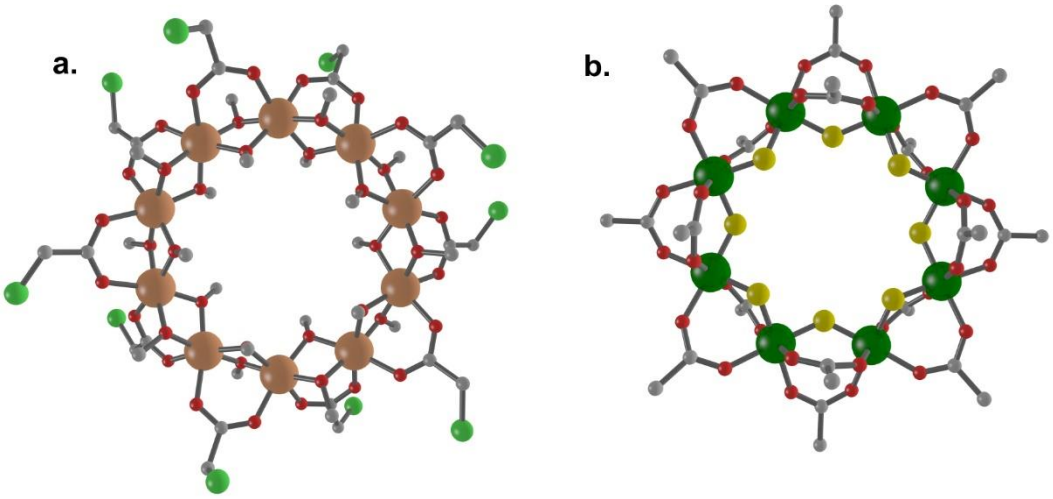

Figure 5: a. X-ray crystal structure of {Fe_{10}}. Fe (brown), Cl (pale green), O (red), C (grey). Protons omitted for clarity. b. X-ray crystal structure of {Cr_8}. Cr (green), F (yellow), O (red), C (grey). Protons, tert-butyl methyl groups and solvent omitted for clarity.

Since the discovery of {Cr_8} and {Fe_{10}}, hundreds of wheels have been published with the number of composite metals ranging from 6 to 32. The wheels can be either homometallic or heterometallic with metal constituents including Ag, Al, Bi, Co, Cr, Cu, Fe, Ga, Gd, In, Mn, Mo, Nd, Pb, Pd, Sm, Ti, V and Zn.[92] More complex structures have also been reported that do not have equivalent metal sites but still show a wheel-like structure, including the "magic number" rings of {Mn_{84}} and {Pd_{54}} as well as the spectacular {Mo_{154}}, {Mo_{172}} and {Mo_{248}} rings from Müller and co-workers.[93, 94] For a comprehensive review of the literature on molecular wheels up to 2011 see the thesis of T. Faust (2011).[92]

Since 2011, there has continued to be a wealth of reported structures. A series of hexametallic wheels have been published with Mn^{II} [95, 96] as well as a chiral hexametallic Fe^{III} wheel[97] and a dodecametallic Mn^{II} wheel (as opposed to the {Mn_{12}} cluster) with three distinct Mn coordination environments showing ferromagnetic coupling (J = + 11.11, + 6.71, + 1.90 cm^{-1}) between the metals.[98] More unusual structures have been reported recently, including a carboxylate free octametallic Fe^{III} wheel with an unusually large antiferromagnetic coupling between the Fe^{III} sites of J_1 = - 26.4 cm^{-1} and J_2 = - 170 cm^{-1} (Figure 6a) but an S = 0 ground state.[99] Also reported by Mazzanti

and co-workers was a highly distinctive mixed metal Mn/Uranyl complex containing a wheel of six Mn^{II} sites held together by cation-interaction bridged uranyl-salen dimers, which can be considered as six $\{MnU_2\}$ triangles linked together by oxygen bridges (Figure 6b).[100] Magnetic characterisation suggested a strong antiferromagnetic interaction between the U^V and Mn^{II} centres with a weaker antiferromagnetic interaction between the U^V pairs. At 2.5 K the complex shows step-like features in the magnetisation, indicative of quantum tunnelling of magnetisation and suggesting that this complex may be an interesting candidate for a qubit or a quantum memory device.

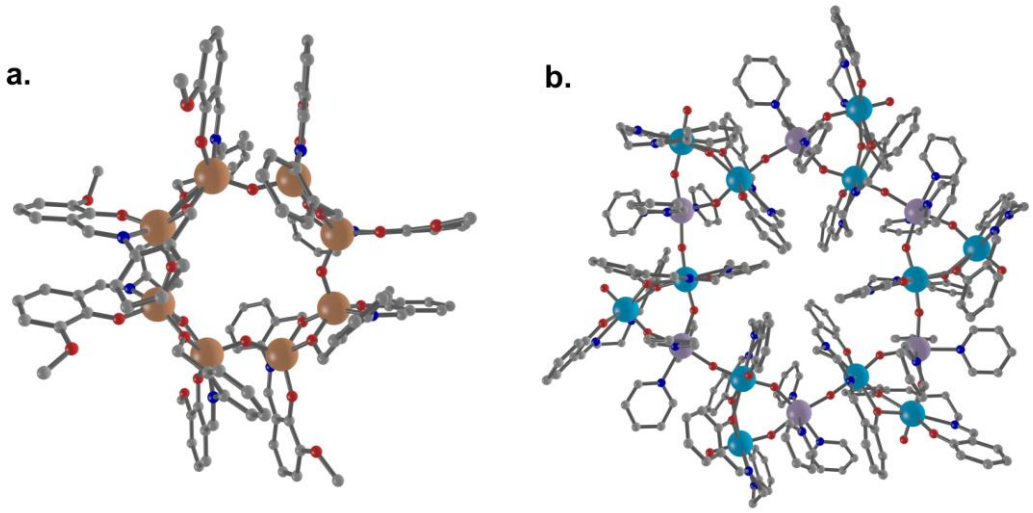

Figure 6: a. X-ray crystal structure of $\{Fe_8\}$ reported by Ahmed *et al.*[99] Fe (brown), N (blue), O (red), C (grey). Protons and disorder omitted for clarity. b. X-ray crystal structure of $\{Mn_6U_{12}\}$ reported by Mazzanti and co-workers. Mn (purple), U (pale blue), N (blue), O (red), C (grey). Protons and solvent molecules omitted for clarity.

2.2.6 Molecular Wheels as Qubits

The vast majority of reported molecular wheels are homometallic with an even number of metals and antiferromagnetic coupling, leading to an $S = 0$ ground state. The $\{Mn_6U_{12}\}$ and the $\{Mn_{12}\}$ wheels discussed above both have either different metals or differing metal coordination geometries leading to the $S > 0$ ground states. Molecular wheels have several distinct advantages over the solid-state qubit systems discussed above (see Section 2.2). In particular, there is the ability to use the full chemical toolkit to "fine tune" the underlying electronic properties of the system (the spin of the qubit), the bonding interactions between the qubits (the degree and pathway of entanglement)

and the relative arrangements of the molecules (generating ordered arrays of qubits). This allows the individual properties of a qubit to be systematically varied to gain a full understanding of the properties of the system and to meet the DiVincenzo criteria.

Introducing one equivalent of M^{II} into the synthesis of $\{Cr_8\}$ results in the formation of a new wheel where one of the Cr^{III} atoms is replaced by an M^{II} atom, with the general formula $[R_2NH_2][Cr_7MF_8(O_2CR')_{16}]$ $\{Cr_7M\}$. Unlike the neutral$\{Cr_8\}$, with solvent in the central cavity, in the $\{Cr_7M\}$ family the templating amine is protonated by the acidic reaction conditions and remains in the central cavity for charge balance, bound by hydrogen bonding. These heterometallic wheels have been synthesised with Mg, Ti, V, Mn, Fe, Co, Ni, Cu, Zn and Cd leading to a wealth of physical properties. [101-105] The $\{Cr_7Zn\}$ and $\{Cr_7Cd\}$ derivatives act as a spin chains due to the diamagnetic metal, allowing the Cr-Cr interactions to be explored.[106, 107] The $\{Cr_7Co\}$ derivative has electronic relaxation times suitable for NMR spectroscopy, introducing solution NMR spectroscopy as a tool to study the wheels (See Chapter 5 and particularly Chapter 6).

The $\{Cr_7M\}$ family of wheels has been extensively studied as potential molecular spin qubits.[71, 72, 108-111] Of particular interest as a qubit is the $\{Cr_7Ni\}$ derivative. The most widely published version uses di-*n*-propylamine ($^nPr_2NH$) as the templating amine and pivalic acid (HO_2C^tBu) as the bridging carboxylate, leading to the molecular formula $[NH_2^nPr_2][Cr_7NiF_8(O_2C^tBu)_{16}]$ (Figure 7). $\{Cr_7Ni\}$ has a well isolated $S = 1/2$ ground state with an energy gap to the $S = 3/2$ state of 13 K.[108] The T_2 time has been measured using a Hahn-Echo pulse, giving $T_2 = 0.55$ μs. [64] The phase memory time, which is a measure of the coherence time in pulsed EPR including T_2 relaxation along with molecular motion and nuclear spin interactions, has also been measured giving $T_M = 357 \pm 10$ ns for protonated $\{Cr_7Ni\}$. The main route of decoherence has been found to be via electron nuclear coupling with the ^1H nuclear spins on the ligands and the ammonium template, upon perdeuteration the T_2 time rises to 3.8 μs at 1.8 K.[84, 85] Solution NMR studies on the $\{Cr_7Co\}$ derivative have confirmed the wheel remains intact in solution,[112] introducing solution based processing as a viable route to obtain ordered arrays of $\{Cr_7Ni\}$ – necessary to meet criteria 1 and 5 proposed by DiVincenzo. The exchange interactions in $\{Cr_7Ni\}$ have been probed using both magnetic measurements and Inelastic Neutron Scattering (INS), giving $J_{Cr\text{-}Cr} = -5.87$ cm^{-1} and $J_{Cr\text{-}Ni} = -6.81$ cm^{-1} (compared to $J_{Cr\text{-}Cr} = -5.89$ cm^{-1} for $\{Cr_8\}$).[113]

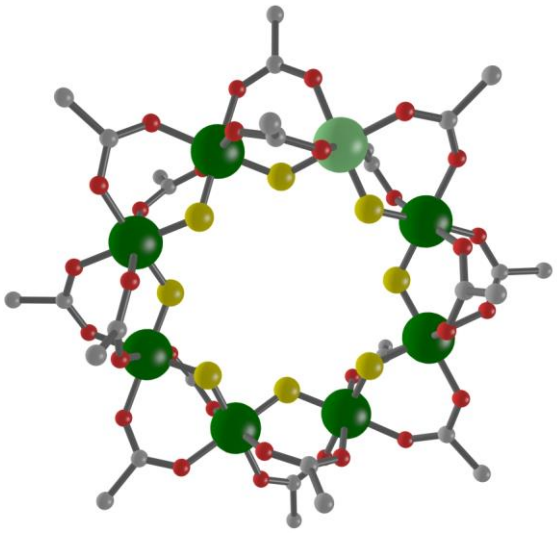

Figure 7: X-ray crystal structure of $[NH_2{}^nPr_2][Cr_7NiF_8(O_2C{}^tBu)_{16}]$ {Cr_7Ni}. Cr (green), Ni (pale green), F (yellow), O (red), C (grey). Protons, methyl carbons and template omitted for clarity.

A particularly powerful tool to study the {Cr_7Ni} wheel is EPR spectroscopy. Using Hamiltonians incorporating both the exchange interactions and the magnetic anisotropy of the individual ions it is possible to simulate the continuous wave EPR spectra for {Cr_7Ni}. This has been very successfully extended to study communication, coherence and entanglement in linked systems (see Section 2.2.8). For a full introduction to the EPR spectroscopy and physical characterisation of the {Cr_7M} family, see the reviews by Timco *et al.* (2013) [112] and McInnes *et al.* (2015).[111]

2.2.7 Linking {Cr_7Ni} wheels via Ligand Substitution

Two of the key requirements for a spin-based quantum computer are communication between the spins centres and the ability to generate an ordered array of qubits. In particular, weak communication is necessary to generate the entanglement between qubits necessary for implementation of more complex algorithms. For the {Cr_7M} family both the communication between rings and synthesising ordered arrays of rings can be controlled by linking together {Cr_7M} wheels in various arrangements. The two possible routes are introduced below, with a focus on the coordination chemistry of functionalised wheels as a route to addressable arrays of entangled qubits.[111]

The synthesis of the {Cr_7M} family is highly versatile, allowing a huge range of both pre- and post-synthetic modification of the wheels. As well as incorporating different

metals into the wheel, the bridging pivalate carboxylate ligands can be exchanged for new carboxylate ligands. Pivalic acid is a saturated hydrocarbon and, once the carboxylate has coordinated to the metals, it is chemically unreactive. Substituting one or more of the pivalate ligands with a new multi-functional carboxylate allows new chemistry to be introduced to the wheel.

All sixteen pivalate ligands can be exchanged for a new carboxylate by refluxing in a large excess of the new acid, or by attempting synthesis of the ring from scratch using the new acid and metal precursors. Full substitution has been shown to be a viable route for deposition of {Cr_7Ni} onto a surface – replacing pivalic acid with thiophene-3-carboxylic acid allowed solution phase deposition of {Cr_7Ni} onto an Au(111) surface in small clusters (Figure 8).[114, 115] Similarly, several derivatives of {Cr_7Ni} functionalised with various alkyl chains were deposited from the solution phase onto HOPG.[116] {Cr_7Ni} has also been sublimed onto a gold surface, showing either ordered hexagonal or disordered packing depending on the carboxylate used. [117]

Alternatively, a small number of the pivalate ligands can be exchanged – with substitution occurring selectively on a Cr-Ni edge due to the much higher reactivity ($\approx 10^{10}$ faster) of Ni^{II} relative to Cr^{III}.[118] Substitution of the pivalic acid for a carboxylate with additional functionality has been extensively used to turn {Cr_7Ni} into a sterically bulky ligand for the synthesis of linked arrays of wheels. The dominant product is usually a single substitution in the "axial" position, in which the new carboxylate lies either above or below the plane of the metals.

In a typical substitution reaction, the {Cr_7Ni} wheel is refluxed in the presence of the new carboxylate for a given period of time – the exact conditions depend on the new ligand – resulting in substitution of one or more of the pivalate ligands with the new ligand. Column chromatography can be used to separate the products from the starting material, yielding mono-, di- and sometimes higher substituted products. The discussion below is focused on mono-substituted {Cr_7Ni} as this is the focus of work in Chapter 5, Chapter 6 and Chapter 7. Considerable work has been reported on a derivative of {Cr_7Ni} known as the purple ring, in which five of the bridging fluorides are replaced by N-ethyl-$_D$-glucamine leaving an open coordination site on the nickel. Readers are directed to references for further details.[119-122]

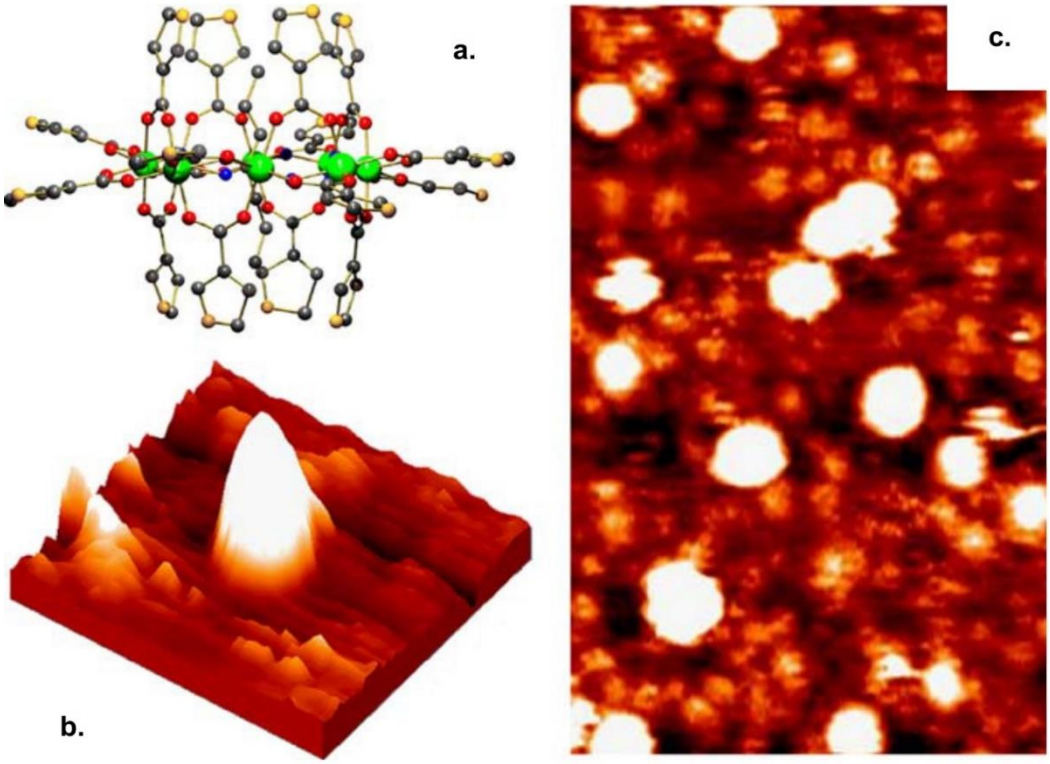

Figure 8: a. X-ray crystal structure of $[NH_2{}^nPr_2][Cr_7NiF_8(O_2CC_4H_3S)_{16}]$. Cr (green), S (yellow), F (blue), O (red), C (grey). Protons and template omitted for clarity. b. 3D view of a single cluster. c. STM image (50 x 25 nm^2) of the $\{Cr_7Ni\}$ wheels on the Au(111) surface. Modified with permission from the American Physical Society.[123]

$\{Cr_7Ni\}$ has been substituted with an oxygen donor (isophthalic acid - Scheme 1) and used to synthesise piperidinium linked dimers for reaction with tetrametallic $\{Zn_4\}$ and $\{Cu_4\}$ linkers.[124] Extensive research has been performed on $\{Cr_7Ni\}$ substituted with nitrogen donors - such as isonicotinic acid (Scheme 1) – and its coordination to a wide range of metal complexes. Using paramagnetic $Cu(NO_3)_2(H_2O)$ a central linker between two functionalised $\{Cr_7Ni\}$ wheels resulted in a three qubit system with clear evidence of strong interactions, observable by EPR spectroscopy. Moving to the diamagnetic dimer $Cu_2(O_2C{}^tBu)_4$ as the linking unit switched off communication between the wheels (Figure 9).[109, 125, 126]

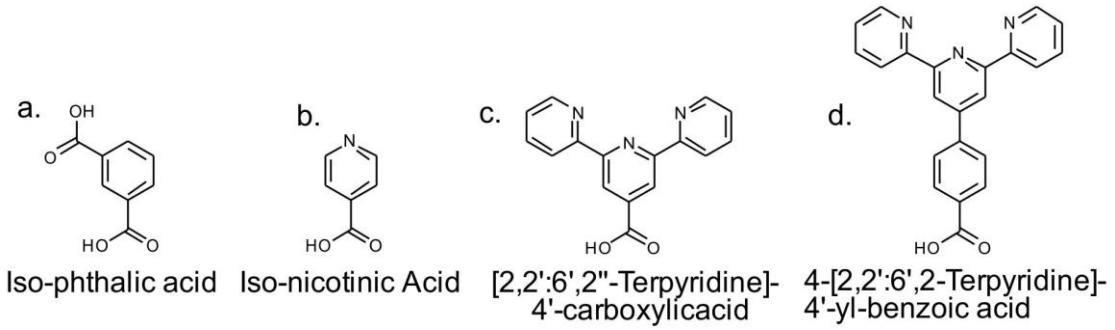

Scheme 1: Structures of chemicals used to introduce donor functionality to $\{Cr_7Ni\}$.

Other linkers explored include an $\{Fe^{III}_2Co^{II}\}$ triangle linking together three $\{Cr_7Ni\}$, a $\{Mn_4\}$ cluster linking four $\{Cr_7Ni\}$ wheels, and a $\{Ni_{12}\}$ wheel linker resulting in a "ring of rings".[127] A family of $\{Cr_7Ni\}$ wheels linked by various nickel salts was structurally characterised and modelled to extract various physical parameters, showing that the choice of the linking metal can be used to tune the interactions within the linked qubit system.[128] Further reactions with a wide range of metal salts and the resulting structures were reported in a recent paper by Whitehead *et al.* (2015).[129]

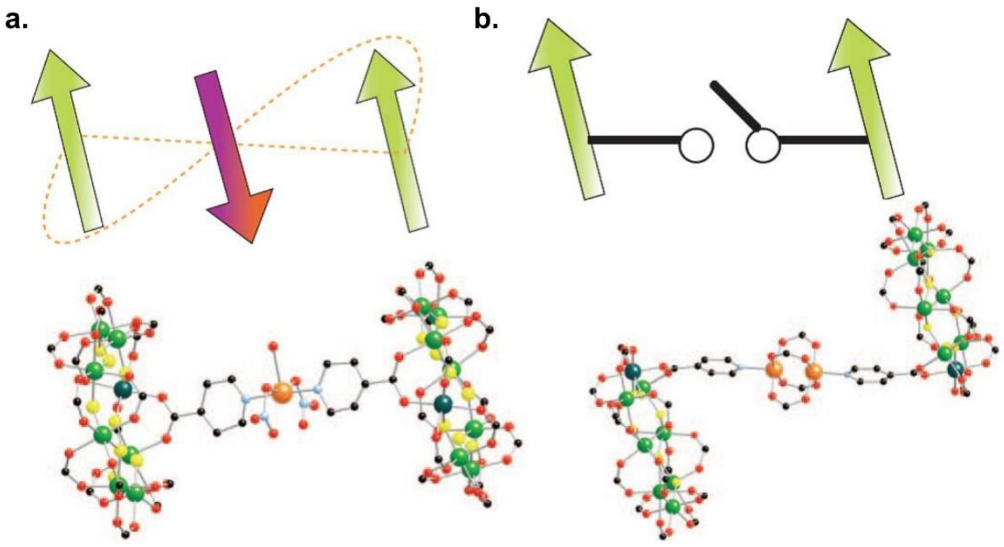

Figure 9: a. Two $\{Cr_7Ni\}$ wheels linked through a single Cu^{II} centre with communication throughout system (shown schematically on top). b. Two $\{Cr_7Ni\}$ wheels linked through a diamagnetic Cu^{II} dimer with no coupling (shown schematically on top). Cr (green), Ni (dark green), Cu (orange) F (yellow), O (red), C (black). Methyl groups, protons and templating ammonium cation omitted for clarity. Reprinted with permission from Nature Publishing Group.[109]

Finally, isonicotinic acid, [2,2':6',2"-Terpyridine]-4'-carboxylic acid and 4-[2,2':6',2-Terpyridine]-4'-yl-benzoic acid (Scheme 1) substituted $\{Cr_7Ni\}$ wheels were linked

together using various Co^{II} salts and an electrochemically active $\{Ru_2Co\}$ triangle (Figure 10). These qubit systems were then computationally modelled as the basis for discussing the practical implementation of gate operations on molecular wheel based qubits.[130] The two gates considered were the CNOT gate, in which the spin of a target qubit is flipped by a magnetic field only if the spin of a control cubit is in the $|1\rangle$ state, and the $\sqrt{\text{iSWAP}}$ gate, in which the two qubit state $|01\rangle$ is transformed into the superposition $|01\rangle + i|10\rangle = \sqrt{2}$ by a local electric field.

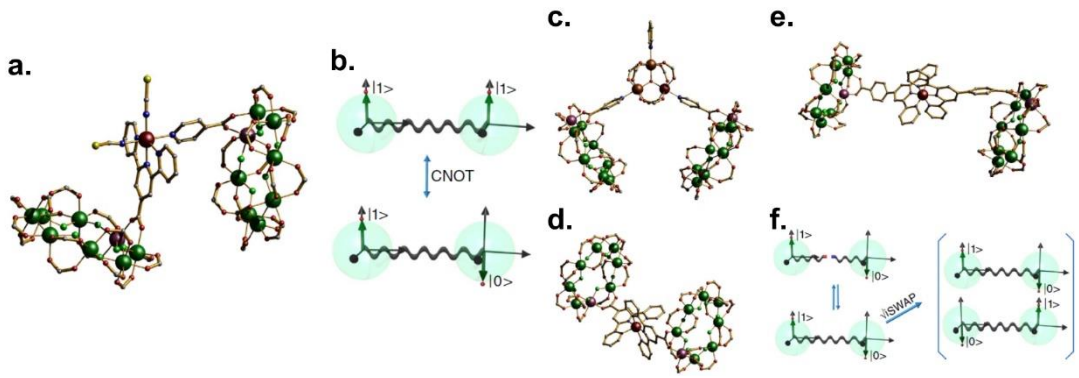

Figure 10: a. X-ray crystal structure of substituted $\{Cr_7Ni\}$ wheels linked together by $Co(SCN)_2$. b. Schematic representation of the CNOT gate. c. X-ray crystal structure of iso-nicotinic substituted $\{Cr_7Ni\}$ wheels linked together by a $\{Ru_2Co\}$ triangle. d. X-ray crystal structure of substituted $\{Cr_7Ni\}$ wheels linked together by $Co(ClO_4)$. e. X-ray crystal structure of substituted $\{Cr_7Ni\}$ wheels linked together by $Co(ClO_4)$. f. Schematic representation of an $\sqrt{\text{iSWAP}}$ gate. Cr(green), Co (dark red), Ni (purple), Ru (brown), N (cyan), O (red), S (yellow), C (grey), F (pale green). Tert-butyl groups, protons, templating ammonium cation and perchlorate anions omitted for clarity. Reproduced under the Creative Commons Licence.[131]

2.2.8 Functionalising $\{Cr_7Ni\}$ wheels via Threads

A second route to modify the rings is to change the templating amine used in the reaction. Using di-*iso*-propylamine as the template results in the formation of the $\{Cr_9\}$ family (see 0 for details), as well as $\{Cr_8Cu_2\}$, $\{Cr_{10}Cu_2\}$ and $\{Cr_{11}Cu_2\}$.[132-134] If imidazoles are used as the template $\{Cr_9Ni\}$, $\{Cr_8Ni_2\}$, $\{Cr_8Cd\}$ and $\{Cr_8Ni\}$, as well as derivatives of the $\{Cr_7Ni\}$ family can all be obtained depending on the alkyl chain present.[135, 136]

Using a functionalised amine as the template allows the $\{Cr_7Ni\}$ wheels to be incorporated into pseudo-rotaxane architectures. In these complexes the template

becomes the thread with the wheel non-covalently bound to the thread, but positioned on the ammonium site for charge balance. If the thread contains two amine sites separated by a linker of a suitable length, [3]-rotaxanes can be formed.[125] The wheels have been incorporated into hybrid inorganic-organic molecular shuttles via functional threads.[137, 138] Introducing terminal coordinating groups onto the threads allows rotaxanes to be linked together into poly-[3]-rotaxanes[139] or, using a thiol stopper they can be deposited as a monolayer onto an Au(111) surface.[140]

A *g*-engineering approach to generating {Cr_7Ni} based qubits was explored using a pyridyl terminated rotaxane containing {Cr_7Ni} and $Cu(hfac)_2$ (Figure 11). The communication between the two spin centres was studied by EPR spectroscopy, showing an NMR like splitting pattern due to a small antiferromagnetic interaction (J = -0.032 cm^{-1}) between the Cu^{II} and the {Cr_7Ni}. The interaction was modelled as isotropic, suggesting it is through bond and not through space – although the pathway remains unclear.[65] Extending this study to AB_2 and A_2B_2 spin systems again suggested weak antiferromagnetic coupling between the spins, with no significant effect on the T_M of the wheel (0.6 ms). This rotaxane based approach has been extended to create larger spin systems linked together by Cu^{II} or by {Fe_2Co} triangles leading to the synthesis of [7]-rotaxanes. Pulsed EPR (DEER) measurements suggested weak anisotropic dipolar interactions between the wheels.[131]

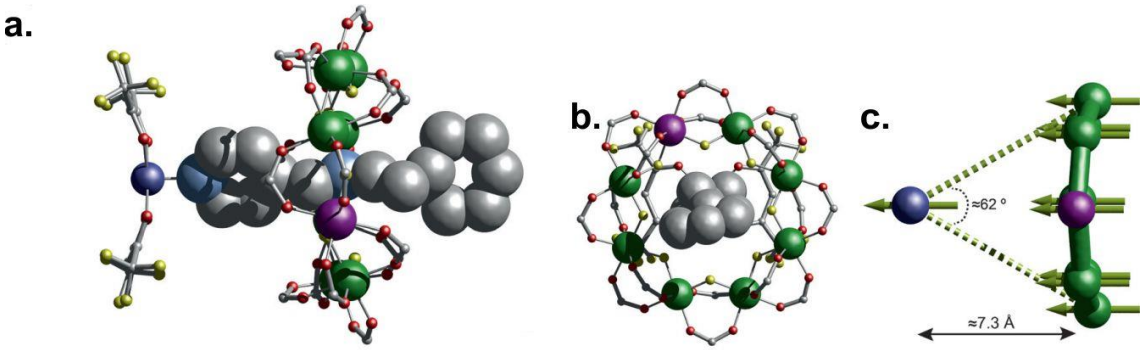

Figure 11: X-ray crystal structure of {Cr_7Ni} with a [$PyCH_2NH_2C_2H_5Ph$] thread linked to $Cu(hfac)_2$ view a. side on and b. perpendicular to the {Cr_7Ni} metal plane. C. Representation of the g_z-components of the Cu^{II} and {Cr_7Ni} spin vectors. Cr (green), Ni (purple), Cu (dark blue), F (yellow), O (red), C (grey). Tert-butyl groups, protons and disorder omitted for clarity. Adapted with permission from John Wiley and Sons.[65]

Chapter 3 Methodology

3.1 Methods Used

A range of characterisation techniques feature in the research discussed below. Outlined below is the general characterisation process used in all four papers and introductions to the key techniques, with a focus on their applications in this work. In all cases, readers are directed to the cited literature for more detailed introductions.

3.1.1 Orbitrap Mass Spectrometry

Chemical and structural characterisation was performed primarily by mass spectrometry, elemental analysis and X-ray crystallography. The author has been fortunate to have access to an "Orbitrap" Fourier transform mass spectrometer, allowing high resolution mass spectrometry of many of the novel compounds reported below with molecular weights > 500 Da (the typical resolution limit for a time of flight accurate mass spectrometer).

An Orbitrap is a modified quadrupole ion trap that uses static electric fields to induce orbital motion around a central electrode with simultaneous oscillations along the electrode (Figure 12). The ions are generated using an electrospray source and transferred into the Orbitrap, where ions with equivalent mass/charge ratios will oscillate along the electrode at the same frequency. A signal is then detected using the current generated by the motion of the ions along the electrode, giving a "transient" in the time domain. This "transient" signal is then converted to the mass/charge domain by Fourier transform techniques, giving the familiar mass spectrum via Fourier Transform Mass Spectrometry (FTMS). The dramatic increase in the resolution at high masses is due to the ability to tightly control the strength of the electric field causing the oscillations along the Orbitrap electrode – along with the ability to trap ions independent of their mass/charge ratio. For full details of the underlying physics and components in an Orbitrap mass spectrometer, readers are directed to reviews by Hu *et al*. (2005)[141] and Perry *et al.* (2008).[142]

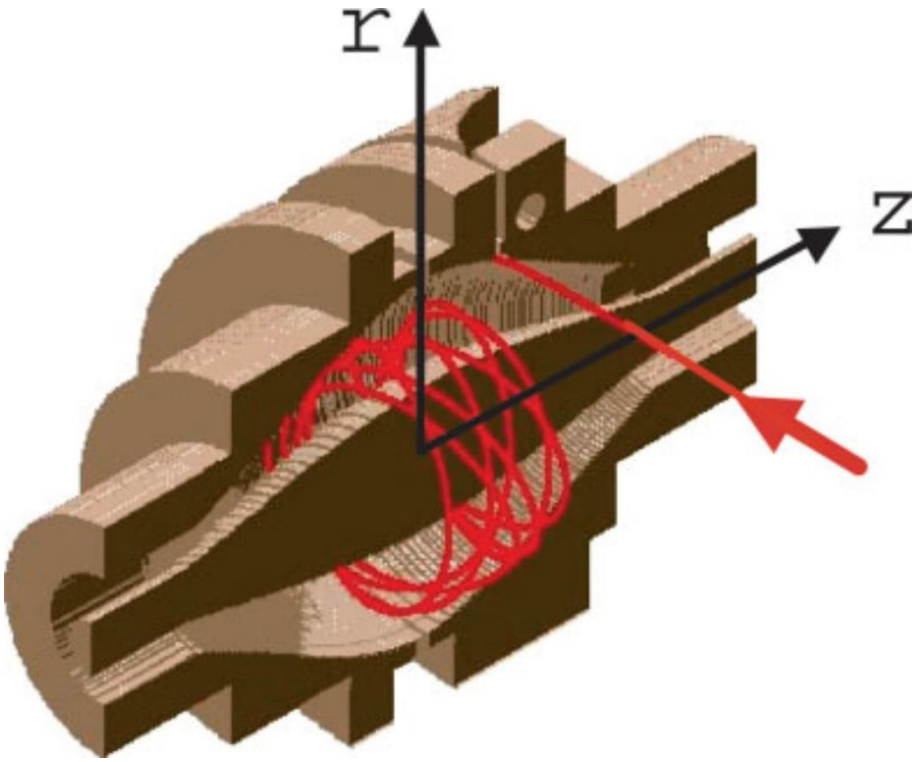

Figure 12: Cutaway diagram of an Orbitrap mass analyser. Ion pathway indicated by the red arrow. Injection occurs with velocity perpendicular to the axial direction (z-axis) of the Orbitrap, followed by rotation both around and along the inner electrode. Reproduced with permission from John Wiley and Sons.[141]

3.1.2 Elemental Analysis

Particularly when a mass spectrum could not be obtained, or when multiple peaks were present, elemental analysis was essential to confirm the identity of new compounds. Carbon, hydrogen, nitrogen and sulfur analyses were performed using combustion analysis, *i.e.* burning the sample in oxygen and measuring the release of CO_2, H_2O, SO_2 and NO. Metal analysis was performed using inductively coupled plasma atomic emission spectroscopy (ICP-AES), in which a plasma produced by an electric current – the inductively coupled plasma – is used to produce excited ions. Each ion produces a characteristic emission spectra, with the magnitude of signal related to the amount of element present, allowing quantitative analysis of metal composition.[143]

3.1.3 X-ray Crystallography

The final step in the structural characterisation of many of the complexes reported below was obtaining an X-ray crystal structure. An X-ray crystallography experiment involves the measurement of the diffraction pattern obtained by shining a monochromatic beam of X-rays through an ordered crystalline sample in which the

individual molecules are arranged in a regular array of repeat units (unit cells). Diffraction only occurs at specific angles *i.e.* when the waves diffracted by the electron density at each site are in phase and the Bragg equation (Eq. 3) is satisfied. In general, every part of a structure will contribute to the observed reflections and therefore a full diffraction pattern is needed to successfully determine a structure.

$$n\lambda = 2d \sin\theta \qquad \text{Eq. 3}$$

The obtained diffraction pattern can be converted by a reverse Fourier Transform into a map of electron density, however during this process information on the relative phases of the diffracted X-ray waves is lost. To overcome this problem and develop a model for the structure (solve the structure), the Direct Methods route was used in which the electron density is assumed to be positive everywhere and the relative intensities of reflections used to calculate the phases. In combination with the calculated structure factors for each reflection, obtained from the atomic form factors (*F*) of the elements in the structure, this allows an electron density map to be obtained and a model of the structure to be developed.

This was performed using the SHELX[144, 145] suite of programs in the Olex2 interface.[146] Data sets were refined against structure factors squared (F_o^2) – to ensure weak reflections were included in the solution – with the quality of the solution measured using the residual R^1 (Eq. 4) and the weighted residual wR^2 (Eq. 5). The R^1 value gives the residual deviation between the observed and calculated structure factors based on F_o values, whilst the wR^2 value, based on F_0^2, takes into account the statistical importance of a reflection (Eq. 6). In both cases, lower values suggest a better fit to the data. In Eq. 4 and Eq. 5, F_o is the observed structure factor and F_c is the calculated structure factor. In Eq. 6, σ is the statistical error obtained from the diffractometer for each reflection.

$$R^1 = \frac{\sum_{hkl}(|F_o| - |F_c|)}{\sum_{hkl}|F_o|} \qquad \text{Eq. 4}$$

$$wR^2 = \frac{\sum_{hkl} w(|F_o^2| - |F_c^2|)^2}{\sum_{hkl} w(|F_o^2|)^2} \qquad \text{Eq. 5}$$

$$w = 1/\sigma^2 \qquad \text{Eq. 6}$$

Datasets in this thesis were obtained using three diffractometers – an Agilent Supernova with a Mo source (λ = 0.71 Å), a Bruker X8 Prospector with a Cu source (λ = 1.54 Å)

and for particular small or poorly diffracting crystals, the high intensity I19 beamline at the Diamond Light Source using synchrotron X-ray radiation (λ = 0.6889 Å).[147]

It should be noted that, for the {Cr_7M} family, refinement of the position of the heterometal is challenging and the metals are often assigned as 7/8 occupancy for Cr and 1/8 occupancy for M. Once a ligand substitution has been performed, the metal position can be localised to one of two sites as ligand substitutions occur on the Cr...M edge, and occupancy can be assigned as 50:50 across those two sites. Representations of the localised heterometal position in figures contained within this thesis are for illustrative purposes only.

For further details on both the underlying theory of X-ray diffraction and the practical aspects of structure refinements, readers are directed to the excellent books by Massa (2004)[148] and Müller (2006).[149]

3.1.4 Physical Characterisation

Characterisation of the physical properties of the novel compounds reported below has been performed using a wide range of methods, and the properties modelled using various freely available computational toolkits. Introductions to the techniques specific to each paper are given in the relevant chapter introduction, notably inelastic neutron scattering (0) and nuclear magnetic resonance of paramagnetic systems (Chapter 6). For an introduction to the theory of ^{31}P NMR spectroscopy, readers are directed to the encyclopaedia of magnetic resonance article by K. Karaghiosoff (2007)[150] or the book by O. Kühl (2008).[151]

3.1.5 SQUID Magnetometry

A superconducting quantum interference device (SQUID) magnetometer is used to obtain precise measurements of minute magnetic fields. In a typical SQUID experiment, a sample is magnetised by an applied uniform magnetic field. The sample is then oscillated perpendicular to the field within a superconducting detection coil, inducing a current. By converting the current to a voltage, the magnetic susceptibility of the sample can be calculated. For a system containing multiple spins, a plot of χT against T (where χ is the measured susceptibility) can be used to determine the interaction between the spins and the overall ground state. The χT value for ferromagnetically coupled spins will increase with decreasing temperature, saturating to a maximum as the spins orient in the same direction. For antiferromagnetically coupled spins, the χT value will decrease with increasing temperature as the spins orient in opposite directions. The

ground state at low temperatures – when only the lowest energy level will be populated – can also be determined using Eq. 7.

$$\chi T = \frac{g^2}{8} S_T(S_T + 1) \qquad \text{Eq. 7}$$

3.1.6 Computational Modelling

Density Functional Theory (DFT) is a powerful technique used to model a wide range of properties of chemical systems. A discussion of the fundamental theory of DFT is beyond the scope of this review, readers are directed to the review by Geerlings *et al*. (2003)[152] or the book by Koch and Holthausen (2001) for full details.[153] However, computational packages based on DFT calculations can be employed by chemists to model physical properties of a system without a full understanding of the theoretical underpinnings.

The SambVca toolkit is used to model the steric hindrance of a ligand by measuring the percentage buried volume ($\%V_{bur}$) of the phosphine site. The $\%V_{bur}$ concept was originally developed as a replacement for the Tolman cone angle in the characterisation of N-heterocyclic carbine ligands (NHCs). To calculate the $\%V_{bur}$ value, a metal is assumed to be a set distance (*d*) from the donor site and the space occupied by the ligand is calculated as a percentage of a sphere of radius (*r*) 2.8 Å using DFT calculations (Figure 13). Providing a consistent set of *d* and *r* values are used, comparisons can be made between ligands.[154, 155]

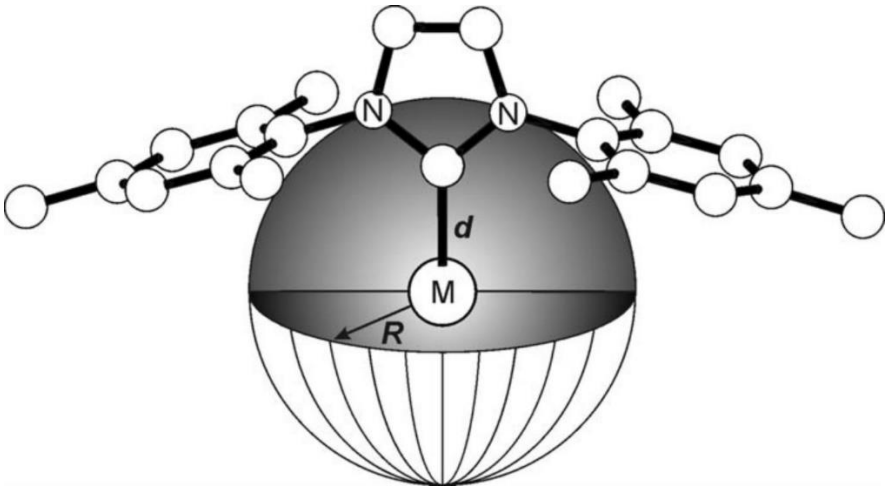

Figure 13: Graphical representation of the sphere used for calculation of $\%V_{bur}$ values with *d* and *r* shown. Reproduced with permission from John Wiley and Sons.[154]

The Finding ANisotropy TENsors (FANTEN) toolkit, developed at the magnetic resonance centre at Florence University (CERM), uses experimentally measured pseudocontact shifts (pcs) values from an NMR spectroscopy experiment on a paramagnetic molecule as restraints to calculate the anisotropy tensor for a paramagnetic metal ion (see Chapter 6 for an introduction to NMR spectroscopy of paramagnetic systems).[156] In the method employed here, the positions of the metals and protons are fixed using the crystallographic coordinates. The anisotropy tensor is then obtained by fitting calculated pcs values against the experimentally observed pcs values to give the best fit, yielding the tensor components and a quality of fit factor (Q – see Chapter 6 for definition).

Chapter 4 Paper 1

"[CrF(O_2C^tBu)$_2$]$_9$: Synthesis and Characterization of a Regular Homometallic Ring with an Odd Number of Metal Centres and Electrons"

Robert J. Woolfson, Grigore A. Timco, Alessandro Chiesa, Inigo J. Vitorica-Yrezabal, Floriana Tuna, Tatiana Guidi, Eva Pavarini, Paolo Santini, Stefano Caretta and Richard E.P. Winpenny

Angew. Chem. Int. Ed., 2016, **55**, 8856-8859

Molecules showing spin frustration are of interest both for their potential use as molecular qubits and the insights they provide into the underlying physics of spins (see Section 2.2.4). Whilst molecular triangles are the prototypical systems for the study of spin frustration, larger molecular systems with an odd number of unpaired electrons should also show spin frustration. As introduced briefly above (Section 2.2.8), using di-*iso*-propylamine as the template in the synthesis of a molecular wheel results in the formation of the {Cr_9} family. In 2012, Baker *et al*. reported the synthesis and characterisation of two members of this family, the synthesis of the samples studied in this work was part of this author's Master's degree. Both [$NH_2{}^iPr_2$][$Cr_9F_{10}(O_2C^tBu)_{18}$] and [$NH_2{}^iPr_2$][$Cr_9F_{11}(O_2C^tBu)_{17}$], {$Cr_9F_{10}$} and{$Cr_9F_{11}$}, are nonametallic rings with a single Cr...Cr edge different from the others - an edge defect. In {Cr_9F_{10}} (Figure 14a) there is one additional terminal fluoride and a η^1 pivalate group. In {Cr_9F_{11}} (Figure 14b) there are two additional terminal fluorides and one less η^2 pivalate group.

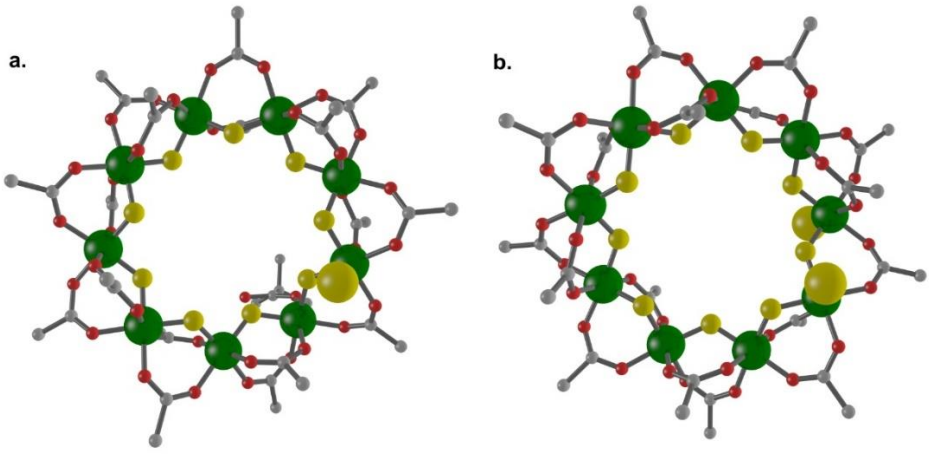

Figure 14: a. X-ray crystal structure of {Cr_9F_{10}} with terminal fluoride emphasised. b. X-ray crystal structure of {Cr_9F_{11}} with terminal fluorides emphasised. Cr (green), F (yellow), O (red), C (grey). Tert-butyl methyl groups, protons and templating ammonium cation omitted for clarity.

Inelastic neutron scattering (INS) is a powerful technique to study the underlying energy level structure of molecular systems. Neutrons have no charge but possess a small magnetic dipole moment, allowing them to penetrate deeply into samples and interact with any electrons present. The energy of cold neutrons (0.1 – 10 meV / 0.8 – 8 cm^{-1}) is of the same order of magnitude as the transitions between low lying energy levels in a molecular system, making them ideal probes for studying electron transitions. However, neutrons have a low cross section of interaction with most materials. This imposes the requirement for large quantities of a sample (> 1 g for a powder INS experiment) and long experiment times. Furthermore, proton nuclei produce strong incoherent scattering – ≈ 40 times larger than deuterium – making the use of perdeuterated samples preferable to reduce the experimental background.

In a typical time of flight experiment (the type employed in Paper 1), a sample is irradiated with a monochromatic beam of neutrons and the momentum or energy transfer between the neutrons and the sample is measured using the scattering angle 2θ and the time taken to travel a known distance. Neutrons lose (or gain) momentum (energy) in proportion to the process causing the scattering, meaning the momentum (energy) transfer between the neutron and the sample can be related back to the scattering angle and the initial and final wavevectors (k_i and k_f) (Eq. 8 and Eq. 9). The momentum (energy) transfer can then be related back to the underlying spin transitions in the molecular system.

$$\vec{Q} = \vec{k}_\mathrm{i} - \vec{k}_\mathrm{f} \qquad \text{Eq. 8}$$

$$\Delta E = \hbar\omega = E_\mathrm{i} - E_\mathrm{f} = \frac{\hbar^2}{2m_n}\,(\vec{k}_i^{\,2} - \vec{k}_f^{\,2}) \qquad \text{Eq. 9}$$

The selection rules for an INS experiment are $\Delta S = 0, \pm 1$, $\Delta M_S = 0, \pm 1$ allowing a large range of transitions to be probed, including transitions forbidden in an EPR experiment ($\Delta M_S = \pm 1$). Measurements are generally performed at cryogenic temperatures, ensuring isolation of the ground state. For detailed introductions to the use of INS to study molecular systems, see the thesis of Michael Baker (2010)[157] or Chapter 4 of Molecular Cluster Magnets (2012) by Tatiana Guidi.[158]

INS was used to characterise {Cr_9F_{10}} and {Cr_9F_{11}}, revealing that the differing edge defects had significant effects on the underlying energy structure in both wheels. Despite both molecules having an odd number of metal sites and unpaired electrons,

neither met the strict Kahn definition of frustration (see section 2.2.4).[85] In $\{Cr_9F_{10}\}$ the edge defect acts as a break in the spin system (J = -0.0074), leading to spin chain like behaviour and a classical S = 3/2 ground state. In $\{Cr_9F_{11}\}$ the edge defect does not break the cyclic nature of the spin system but does break the degeneracy of the ground state, resulting in a non-degenerate S = 1/2 ground state. Winpenny and co-workers proposed a new definition of spin frustration using three classes of frustrated system. A Type III system has an odd number of electrons but a classical ground state – $\{Cr_9F_{10}\}$, a Type II system has an odd number of electrons and a non-degenerate S = 1/2 state – $\{Cr_9F_{11}\}$ whilst a Type I system would have a degenerate S = 1/2 ground state, meeting the strict definition of spin frustration proposed by Kahn.

The paper below reports the synthesis and characterisation of a new nonametallic wheel – $[CrF(O_2C^tBu)]_9$ $\{Cr_9F_9\}$. INS, performed using the LET spectrometer at ISIS, was used to characterise the electronic structure of $\{Cr_9F_9\}$ and explore the extent of spin frustration within this novel odd-metal odd-electron spin system. The frustration is classified using the definitions proposed by Baker *et al*., and the theoretical potential for electric field switching of the spin states is examined as a route to meeting Criteria 5 of the DiVincenzo criteria.

Molecular Magnetism

International Edition: DOI: 10.1002/anie.201601734
German Edition: DOI: 10.1002/ange.201601734

$[CrF(O_2C^tBu)_2]_9$: Synthesis and Characterization of a Regular Homometallic Ring with an Odd Number of Metal Centers and Electrons

*Robert J. Woolfson, Grigore A. Timco, Alessandro Chiesa, Inigo J. Vitorica-Yrezabal, Floriana Tuna, Tatiana Guidi, Eva Pavarini, Paolo Santini, Stefano Carretta, and Richard E. P. Winpenny**

Abstract: *The first regular homometallic ring containing an odd number of metal centers is reported. The ring was synthesized by means of amine-templated self-assembly. Extensive physical characterization studies, including magnetic measurements, powder inelastic neutron scattering (INS), and DFT calculations, show that the molecule has a near perfect match to the expected behavior for a frustrated system with the lowest energy pair of $S = 1/2$ spin states separated by only 0.1 meV (0.8 cm^{-1}).*

The literature on polymetallic compounds with cyclic metal cores has certain unusual gaps. Since the publication in 1990 of both $\{Fe_{10}\}$[1] by Lippard and Taft and $\{Cr_8\}$[2] by Timco and co-workers, a wide range of sizes have been reported for homometallic rings, including $\{Fe_{18}\}/\{Ga_{18}\}$[3] rings (currently the largest reported regular wheels, that is, where every edge and every vertex is chemically equivalent) to the more complex $\{Mn_{32}\}$ double decker structure.[4] "Magic number" rings of $\{Mn_{84}\}$[5] and $\{Pd_{84}\}$[6] have also been reported. The largest cyclic metal structures remain the extraordinary molybdate wheels from Müller and co-workers.[7] However, rings with odd numbers of metal centers (termed herein odd-numbered rings), particularly those larger than triangles, are conspicuous by their near absence.

There are a few reported heterometallic nine-metal rings, including $\{Cr_7V_2\}$ and a $\{Cr_8M\}$ family.[8] However, regular homometallic rings containing odd numbers of metal centers are restricted to metal triangles, a small number of pentagons,[9,10] and a single heptametallic $\{V_7\}$ ring made by Oshio and co-workers with the vanadium sites bridged by a cyclodextrin ligand.[11]

Large regular odd-numbered rings would show interesting physics associated with spin frustration,[12,13] which occurs when the classical magnetic energy cannot be simultaneously minimized for all individual two-spin interaction terms. Theoretical studies to classify the degree of frustration in such systems have been recently reported.[14] In 2002 the structures of two toroidal thiolate-bridged nickel structures, $\{Ni_9\}$ and $\{Ni_{11}\}$, were published by Dahl and co-workers, both of which showed considerable geometric irregularity; however, no characterization beyond crystallography was reported.[15] In 2004, Mezei et al. reported a nonametallic copper ring $\{Cu_9\}$ that was not isolated but co-crystallized with a range of other copper rings.[16]

We previously reported two nonametallic rings $\{Cr_9F_{10}\}$ and $\{Cr_9F_{11}\}$ (see below), each of which contained one edge with a defect breaking the regularity of the ring.[17] Herein, we report the synthesis of the first regular nine-metal homometallic ring, $[CrF(O_2C^tBu)_2]_9$ **1**, along with characterization of the ring by magnetometry and inelastic neutron scattering (INS) to explore the extent of spin frustration.

The synthesis of **1** is based on a procedure we previously developed for synthesizing hexametallic and heptametallic chromium horseshoes[18]—addition of a templating amine to a reaction that would conventionally give $[CrF(O_2C^tBu)_2]_8$ **2** (see Figure S1 in the Supporting Information). Using diisopropylamine as the template along with the addition of trifluoromethanesulfonic acid leads to a mixture of octa- and nonametallic rings which can be purified by column chromatography, resulting in the separation of **1** and **2**, along with the previously published[17] $[NH_2^iPr_2][Cr_9F_{10}(O_2C^tBu)_{18}]$ (**3**; $\{Cr_9F_{10}\}$) and $[NH_2^iPr_2][Cr_9F_{11}(O_2C^tBu)_{17}]$ (**4**; $\{Cr_9F_{11}\}$; see Figure S6). The templating ammonium cation is not present in **1** but addition of diisopropylamine is essential for the compound to form.

[*] R. J. Woolfson, Dr. G. A. Timco, Dr. I. J. Vitorica-Yrezabal, Dr. F. Tuna, Prof. R. E. P. Winpenny
School of Chemistry and Photon Science Institute
University of Manchester
Oxford Road, Manchester, M20 4NZ (UK)
E-mail: richard.winpenny@manchester.ac.uk
Dr. A. Chiesa, Prof. P. Santini, Prof. S. Carretta
Dipartimento di Fisica e Scienze della Terra, Università di Parma
Parco Area della Scienze 7/A, I-43124 Parma (Italy)
Dr. T. Guidi
ISIS Facility, Rutherford Appleton Laboratory
Didcot, OX11 0QX (UK)
Prof. E. Pavarini
Institute for Advanced Simulation, Forschungzentrum Jülich
52425 Jülich (Germany)
and
JARA High Performance Computing, RWTH Aachen University
52062 Aachen (Germany)

Supporting information (containing full details of synthesis, measurements, and theoretical modelling) and the ORCID identification number(s) for the author(s) of this article can be found under http://dx.doi.org/10.1002/anie.201601734.

© 2016 The Authors. Published by Wiley-VCH Verlag GmbH & Co. KGaA. This is an open access article under the terms of the Creative Commons Attribution License, which permits use, distribution and reproduction in any medium, provided the original work is properly cited.

Crystals of **1** can be grown from a range of solvents (toluene, acetone, *n*-propanol) resulting in two distinct types of crystals. Crystals with hexagonal space group $P6_3/m$ show significant disorder in the pivalate carbons and only the Cr, F, and O positions can be refined with confidence. However, crystals with the orthorhombic space group *Pcba* can be grown from *n*-propanol and the full crystal structure determined (Figure 1). A list of average Cr—Cr and Cr—F bond lengths as well as average bridging Cr-F-Cr angles for **1**–**4** is given in Table 1.

Structurally, **1** is more closely related to the regular octagon **2** rather than nine-metal rings **3** and **4** that each have a unique edge breaking the regularity of the metal polygon. The chromium atoms in **1** do not lie in a plane but rather take a bowl-shaped conformation. Each chromium site has a slightly distorted octahedral coordination environment. The Cr—Cr distances and Cr-F-Cr angles are very regular, as in **2** (see Table 1). Unlike **3** and **4**, **1** is neutral and therefore solvent, rather than the templating amine, occupies the central cavity.

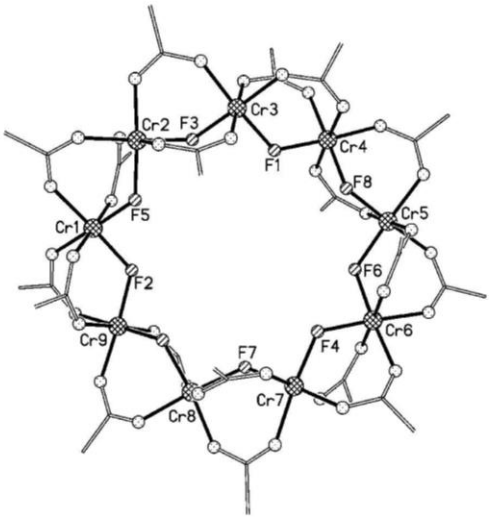

Figure 1. Crystal structure of **1**, crystals grown from *n*-propanol. Cr (cross-hatched circles), F (striped circles), O (dotted circles), C (lines). Methyl groups of pivalates and solvent molecules are omitted for clarity.

Table 1: Selected average bond lengths [Å] and angles [°] for compounds **1**–**4**.

Compound	Cr—Cr bond[a]	Cr—F bond[a]	Cr-F-Cr angle[a]
1	3.376 ± 0.016 (0.052)	1.918 ± 0.013 (0.044)	123.300 ± 0.748 (2.100)
2	3.383 ± 0.018 (0.051)	1.916 ± 0.006 (0.023)	124.000 ± 0.735 (0.051)
3	3.390 ± 0.049 (0.158)	1.929 ± 0.012 (0.041)	123.067 ± 3.304 (11.000)
4	3.391 ± 0.047 (0.164)	1.927 ± 0.016 (0.061)	123.278 ± 2.952 (9.700)

[a] The largest difference in value for each parameter is given in parentheses.

Given the regular structure of **1**, we have studied samples of **1** recrystallized from toluene to assess the degree to which it shows spin frustration. According to the strict definition given by Kahn,[19] frustration would manifest itself as the presence of two degenerate $S = 1/2$ ground multiplets. Magnetic measurements, specifically variable-temperature susceptibility ($\chi_m(T)$; Figure S7) and variable-field magnetization ($M(H)$; Figure S8), show the expected behavior for an antiferromagnetic exchange between the Cr^{III} centers in **1**, and can be fitted to a Hamiltonian containing a single antiferromagnetic exchange parameter $J = 1.35(3)$ meV (1 meV = 8.066 cm^{-1}). These thermodynamic measurements confirm the presence of an $S = 1/2$ ground state and support the presence of spin frustration, but they are comparatively insensitive compared with spectroscopic techniques. The size of the exchange coupling is somewhat smaller than that found in **2** which is 1.46 meV.[20]

Inelastic neutron scattering (INS) probes the spin dynamics of the system and can directly detect any splitting of the pair of potentially degenerate ground-state doublets. INS data were collected using the low energy transfer (LET) spectrometer on a powder sample of **1** recrystallized from toluene (Figure 2, top), using 7.48 meV incident neutron energy (E_i) measured at 1.5, 7, and 15 K. The dominant peak at low temperature corresponds to the transition between the ground $S = 1/2$ states and the lowest energy $S = 3/2$ multiplet, labelled transition I. At higher resolution ($E_i = 2.5$ meV), a splitting of this peak of about 0.1 meV is detected (Figure 3). Higher-energy peaks are detected at all temperatures, corresponding to transitions from the $S = 1/2$ ground state to higher-energy excited states with $S = 3/2$ (transitions II and V in Figure 2, bottom) or $S = 1/2$ (transitions III and IV, respectively). At 15 K, hot transitions can be detected due to additional excitations from the lowest energy $S = 3/2$ state (transitions VI and VII). The seemingly temperature-independent broad peak at 3 meV is due to an overlap of two peaks corresponding to one cold (III) and one hot transition (VIII). All these results are well reproduced by a Hamiltonian with C_9 symmetry, thus demonstrating that the spin dynamics of **1** matches that expected of a perfectly frustrated antiferromagnetic ring (a spectrum calculated with a C_9 Hamiltonian is reported in Figure S9).

To investigate the degree of frustration in **1** quantitatively, we performed high-resolution ($E_i = 1.24$ meV and 22 μeV full-width half-maximum, FWHM, at elastic line) INS measurements which revealed a small (0.1 meV) splitting between the two $S = 1/2$ ground states (Figure 3, inset), indicating a slight lifting of the degeneracy in **1** and thus a small removal of frustration from that of a perfectly frustrated ring.

All the INS data can be well reproduced using the minimal Hamiltonian in Equation [1], where for simplicity we model the splitting of the lowest-energy doublets by breaking the C_9 symmetry of the enneagon on one edge with the introduction of a second exchange constant, J'.

$$H = \sum_{i=1}^{8} J\boldsymbol{s}_i \cdot \boldsymbol{s}_{i+1} + J'\boldsymbol{s}_9 \cdot \boldsymbol{s}_1 + d\sum_i s_{z_i}^2 + \sum_{i<>j=1}^{9} \boldsymbol{s}_i \cdot D_{ij} \cdot \boldsymbol{s}_j \qquad (1)$$

 © 2016 The Authors. Published by Wiley-VCH Verlag GmbH & Co. KGaA, Weinheim

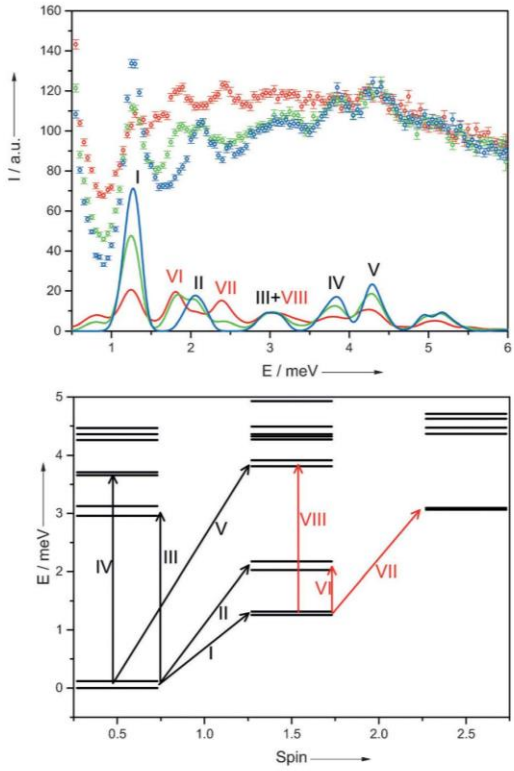

Figure 2. Top: Powder INS data for **1** recorded on an LET spectrometer using 7.48 meV incident neutron energy. Experimental (open circles) and simulated (solid lines) spectra shown for 1.5 K (blue), 7 K (green), and 15 K (red) with peaks labelled corresponding to transitions in the diagram below. Bottom: Isotropic exchange diagram for **1** derived using calculated $J = 1.32$ meV (10.6 cm^{-1}) and $J'/J = 1.2$.

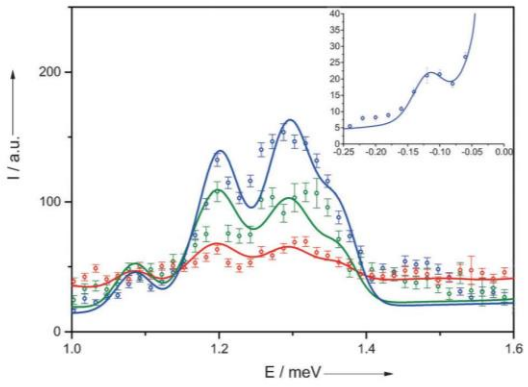

Figure 3. INS spectra recorded using $E_i = 2.5$ meV incident energy neutrons. Experimental (open circles) and simulated (solid lines) spectra at 1.5 K (blue), 7 K (green), and 15 K (red) are shown. A background has been added to the simulated curves. Inset: Experimental and simulated data for the $E_i = 1.24$ meV (10.0 cm^{-1}) spectrum showing an intra-multiplet $S = 1/2$ transition.

In this Hamiltonian, $\boldsymbol{s}_i$ are spin operators for site i and d is the axial single-ion zero-field-splitting parameter. The last term describes intramolecular magnetic dipole–dipole interactions, with couplings D_{ij} calculated in the point-dipole approximation (no additional free parameters). Fitting the INS data resulted in parameters of $J = 1.32$ meV (10.6 cm^{-1}), $J' = 1.2 \cdot J = 1.58$ meV and $d = -0.022$ meV. It is worth noting that the average value of the exchange constants is the same found from magnetometry. This model reproduces the observed splitting of the peak corresponding to transition I ($S = 1/2 \rightarrow S = 3/2$; Figure 3), which is due to the combined action of the zero-field splitting and of the slight lifting of the ideal ring symmetry. Figure 2 (bottom) shows the energy-level diagram for **1** calculated with the isotropic part of Equation [1]. The measured dependence of the neutron intensity on the momentum transfer Q for the main peak I (see Figure S10) is in good agreement with calculations, confirming that the structure of the states involved in the transition is well reproduced by our model.

To validate our findings, we have performed density functional theory (DFT) calculations employing the NWChem software,[21] using the broken symmetry approach to compute the isotropic exchange couplings (see the Supporting Information for details). Calculations have been done on the Jülich supercomputer Jureca. An average J value of 1.40 meV is found from these calcuations, which is in very good agreement with that obtained by fitting magnetometry and INS data (1.35 meV). The distribution of the calculated couplings is much more uniform than those of the previously reported Cr9 wheels,[17] with a small standard deviation of 0.17 meV.

The internal spin structure of the ground state of **1** has been investigated through analysis of the scalar spin chirality $\hat{C}$ [Eq. (2)], which is a measure of the planarity of the spin configuration.

$$\hat{C} = \sum_{i=1}^{9} \boldsymbol{s}_i \cdot \boldsymbol{s}_{i+1} \times \boldsymbol{s}_{i+2} \qquad (2)$$

The results show that the quantum ground state of **1** is an equal superposition of chirality eigenstates with opposite eigenvalues (see Figures S11 and S12). Thus, in contrast to the classical spin configurations (in which all of the spins lie in the same plane), Cr_9 fluctuates between nonplanar states with opposite chirality keeping $<C> = 0$, consistent with the behavior expected for an ideally frustrated antiferromagnetic ring.

Compound **1** is the first compound reported containing a regular homometallic ring containing nine metal centers. The INS data for the compound reveal nearly frustrated spin dynamics, with a slight lifting of the degeneracy of the lowest-energy states resulting in a splitting of the two $S = 1/2$ multiplets of only 0.1 meV. Compared to systems such as triangles where highly rigid ligand systems are required to ensure spin frustration,[22] obtaining a near perfect frustrated ground state from such a sterically undemanding set of starting materials is remarkable. Given the strong evidence for spin frustration in **1**, further studies of the spin properties, such as spin density or correlation dynamics, will provide

 © 2016 The Authors. Published by Wiley-VCH Verlag GmbH & Co. KGaA, Weinheim

fascinating information on the physics of such large frustrated spin systems.

Acknowledgements

We acknowledge financial support from the EPSRC (grant reference EP/L018470/1), for funding an X-ray diffractometer (EP/K039547/1) and for the Centre for Doctoral Training NoWNANO and from the Italian MIUR (FIRB Project No. RBFR12RPD1).

Keywords: inelastic neutron scattering · magnetic properties · molecular magnetism · spin frustration · supramolecular chemistry

How to cite: *Angew. Chem. Int. Ed.* **2016**, *55*, 8856–8859
Angew. Chem. **2016**, *128*, 9002–9005

[1] K. L. Taft, S. J. Lippard, *J. Am. Chem. Soc.* **1990**, *112*, 9629.
[2] N. V. Gerbeleu, Y. T. Struchkov, G. A. Timko, A. S. Batsanov, K. M. Indrichan, G. A. Popovich, *Dokl. Akad. Nauk SSSR* **1990**, *313*, 1459.
[3] P. King, T. C. Stamatatos, K. A. Abboud, G. Christou, *Angew. Chem. Int. Ed.* **2006**, *45*, 7379; *Angew. Chem.* **2006**, *118*, 7539.
[4] M. Manoli, R. Inglis, M. J. Manos, V. Nastopoulos, W. Wernsdorfer, E. K. Brechin, A. J. Tasiopoulos, *Angew. Chem. Int. Ed.* **2011**, *50*, 4441; *Angew. Chem.* **2011**, *123*, 4533.
[5] A. J. Tasiopoulos, A. Vinslava, W. Wernsdorfer, K. A. Abboud, G. Christou, *Angew. Chem. Int. Ed.* **2004**, *43*, 2117; *Angew. Chem.* **2004**, *116*, 2169.
[6] F. Xu, H. N. Miras, R. A. Scullion, D.-L. Long, J. Thiel, L. Cronin, *Proc. Natl. Acad. Sci. USA* **2012**, *109*, 11609.
[7] A. Müller, E. Krickemeyer, J. Meyer, H. Bögge, F. Peters, W. Plass, E. Diemann, S. Dillinger, F. Nonnebruch, M. Randerath, C. Menke, *Angew. Chem. Int. Ed. Engl.* **1995**, *34*, 2122; *Angew. Chem.* **1995**, *107*, 2293.
[8] a) O. Cador, D. Gatteschi, R. Sessoli, F. K. Larsen, J. Overgaard, A.-L. L. Barra, S. J. Teat, G. A. Timco, R. E. P. Winpenny, *Angew. Chem. Int. Ed.* **2004**, *43*, 5196; *Angew. Chem.* **2004**, *116*, 5308; b) G. A. Timco, A. S. Batsanov, F. K. Larsen, C. A. Muryn, J. Overgaard, S. J. Teat, R. E. P. Winpenny, *Chem. Commun.* **2005**, 3649; c) A. B. Boeer, D. Collison, C. A. Muryn, G. A. Timco, F. Tuna, R. E. P. Winpenny, *Chem. Eur. J.* **2009**, *15*, 13150; d) M. L. Baker, T. Lancaster, A. Chiesa, G. Amoretti, P. J. Baker, C. Barker, S. J. Blundell, S. Carretta, D. Collison, H. U. Güdel, T. Guidi, E. J. L. McInnes, J. S. Möller, H. Mutka, J. Ollivier, F. L. Pratt, P. Santini, F. Tuna, P. L. W. Tregenna-Piggott, I. J. Vitorica-Yrezabal, G. A. Timco, R. E. P. Winpenny, *Chem. Eur. J.* **2016**, *22*, 1779.
[9] V. L. Pecoraro, A. J. Stemmler, B. R. Gibney, J. J. Bodwin, H. Wang, J. W. Kampf, A. Barwinski, *Prog. Inorg. Chem.* **1997**, *45*, 83.
[10] a) B. Hasenknopf, J.-M. Lehn, B. O. Kneisel, G. Baum, D. Fenske, *Angew. Chem. Int. Ed. Engl.* **1996**, *35*, 1838; *Angew. Chem.* **1996**, *108*, 1987; b) C. S. Campos-Fernádez, R. Clérac, J. M. Koomen, D. H. Russell, K. R. Dunbar, *J. Am. Chem. Soc.* **2001**, *123*, 773.
[11] N. Hoshino, M. Nakano, H. Nojiri, W. Wernsdorfer, H. Oshio, *J. Am. Chem. Soc.* **2009**, *131*, 15100.
[12] a) J. Schnack, *Dalton Trans.* **2010**, *39*, 4677; b) K. Barwinkel, P. Hage, H.-J. Schmidt, J. Schnack, *Phys. Rev. B* **2003**, *68*, 054422; c) K. Barwinkel, H.-J. Schmidt, J. Schnack, *J. Magn. Magn. Mater.* **2000**, *220*, 227.
[13] M. Trif, F. Troiani, D. Stepanenko, D. Loss, *Phys. Rev. B* **2010**, *82*, 045429.
[14] a) M. Antkowiak, P. Kozłowski, G. Kamieniarz, G. A. Timco, F. Tuna, R. E. P. Winpenny, *Phys. Rev. B* **2013**, *87*, 184430; b) P. Kozłowski, *Phys. Rev. B* **2015**, *91*, 174432; c) G. Kamieniarz, W. Florek, M. Antkowiak, *Phys. Rev. B* **2015**, *92*, 140411.
[15] S. A. Ivanov, M. A. Kozee, A. W. Merrill, S. Agarwal, L. F. Dahl, *J. Chem. Soc. Dalton Trans.* **2002**, 4105.
[16] G. Mezei, P. Baran, R. G. Raptis, *Angew. Chem. Int. Ed.* **2004**, *43*, 574; *Angew. Chem.* **2004**, *116*, 584.
[17] M. L. Baker, G. A. Timco, S. Piligkos, J. S. Mathieson, H. Mutka, F. Tuna, P. Kozłowski, M. Antkowiak, T. Guidi, T. Gupta, H. Rath, R. J. Woolfson, G. Kamieniarz, R. G. Pritchard, H. Weihe, L. Cronin, G. Rajaraman, D. Collison, E. J. L. McInnes, R. E. P. Winpenny, *Proc. Natl. Acad. Sci. USA* **2012**, *109*, 19113.
[18] F. K. Larsen, J. Overgaard, S. Parsons, E. Rentschler, A. A. Smith, G. A. Timco, R. E. P. Winpenny, *Angew. Chem. Int. Ed.* **2003**, *42*, 5978; *Angew. Chem.* **2003**, *115*, 6160.
[19] O. Kahn, *Chem. Phys. Lett.* **1997**, *265*, 109.
[20] M. L. Baker, T. Guidi, S. Carretta, H. Mutka, G. Timco, E. J. L. McInnes, G. Amoretti, R. E. P. Winpenny, P. Santini, *Nat. Phys.* **2012**, *8*, 906.
[21] M. Valiev, E. J. Bylaska, N. Govind, K. Kowalski, T. P. Straatsma, H. J. J. van Dam, D. Wang, J. Nieplocha, E. Apra, T. L. Windus, W. A. de Jong, *Comput. Phys. Commun.* **2010**, *181*, 1477.
[22] E. T. Spielberg, A. Gilb, D. Plaul, D. Geibig, D. Hornig, D. Schuch, A. Buchholz, A. Ardavan, W. Plass, *Inorg. Chem.* **2015**, *54*, 3432.

Received: February 18, 2016
Revised: March 30, 2016
Published online: June 13, 2016

 © 2016 The Authors. Published by Wiley-VCH Verlag GmbH & Co. KGaA, Weinheim

Angewandte Chemie
Eine Zeitschrift der Gesellschaft Deutscher Chemiker

Supporting Information

$[CrF(O_2C^tBu)_2]_9$: Synthesis and Characterization of a Regular Homometallic Ring with an Odd Number of Metal Centers and Electrons

*Robert J. Woolfson, Grigore A. Timco, Alessandro Chiesa, Inigo J. Vitorica-Yrezabal, Floriana Tuna, Tatiana Guidi, Eva Pavarini, Paolo Santini, Stefano Carretta, and Richard E. P. Winpenny**

anie_201601734_sm_miscellaneous_information.pdf

SUPPLEMENTARY INFORMATION

1. Experimental Section

All reagents and solvents were purchased from commercial sources and used as received. Reactions were performed in Erlenmeyer Teflon flasks. Column chromatography was performed using 45-60 μm Silica as a gel with wet loading in toluene.

Pivalic acid (40 g, 396 mmol), chromium (III) trifluoride hexahydrate (5.0 g, 27.61 mmol) di-*iso*propylamine (0.58 g, 0.81 mL, 5.73 mmol) and trifluoromethanesulfonic acid (0.42 g, 0.25 ml, 3.68 mmol) were stirred together at 150 °C for 24 h. The flask was allowed to cool for 15 m, MeCN (100 mL) added and the solution stirred for 2 h resulting in a solid green precipitate. This was collected by filtration, washed with MeCN and then extracted with acetone (500 mL) while stirring overnight. The resulting solution was filtered and then evaporated to dryness by rotary evaporation. The green powder contained a mix of **1, 2, 3** and **4** that was separated by column chromatography. With toluene as the eluent, **2** eluted first followed more slowly by **1**. Increasing the polarity to 40:1 toluene:ethyl acetate resulted in elution of **3** and 10:1 toluene:ethyl acetate eluted **4**. See reference 17 in main text for physical characterisation of **3** and **4**. CCDC entries 164814, 893834 and 893835 contain the supplementary crystal data for **2**, **3** and **4**.

Evaporation of the fraction containing **1** gave a green powder with a yield of 0.21 g (2.7 %). Positive ion electrospray mass spectrometry (FTMS+) using THF as carrier solvent gave m/z values of 2460 (M + H); 2477 (M + H + H_2O); 2492 (M + H + MeOH); 2513 (M + Na + MeOH); 2520 (M + H + iso-propanol); 2533 (M + H + THF); 2556 (M + pivalate) (Figure S1). Water, methanol, iso-propanol and sodium are common ions observed in our mass spectrometer and THF was the carrier solvent. Elemental analysis (calculated): Cr 18.73 (19.03), C 43.76 (43.96), H 6.60 (6.64) N 0 (0). ATIR (cm^{-1}): 2966 (C-H stretch); 1552; 1484; 1427; 1363; 1229; 768; 613 (Figures S2 and S3).

Single crystals of **1** suitable for X-ray diffraction were grown from either – (1) slow evaporation of a saturated *n*-propanol solution for orthorhombic crystals, (2) slow evaporation of acetone for monoclinic crystals or (3) slow evaporation of toluene for hexagonal crystals.

INS data were collected using the LET[1] time-of-flight spectrometer at ISIS, Rutherford Appleton Laboratory, United Kingdom, on a 0.4 g of polycrystalline non-deuterated sample crystallised from toluene and powdered. The sample was wrapped in aluminium foil and then loaded into a standard orange cryostat for measurements. Measurements were performed at 1.5, 7 and 15 K with 7.48, 2.5 and 1.24 meV incident neutron energies using the repetition rate multiplication mode.

Magnetic characterisation of polycrystalline **1** was performed in the temperature range 1.8 – 300 K using a Quantum Design MPMS XL SQUID magnetometer equipped with a 7 T magnet. Diamagnetic correction for the sample was calculated using Pascal's constants and measured for the sample holder.

1.1. Mass Spectrometry

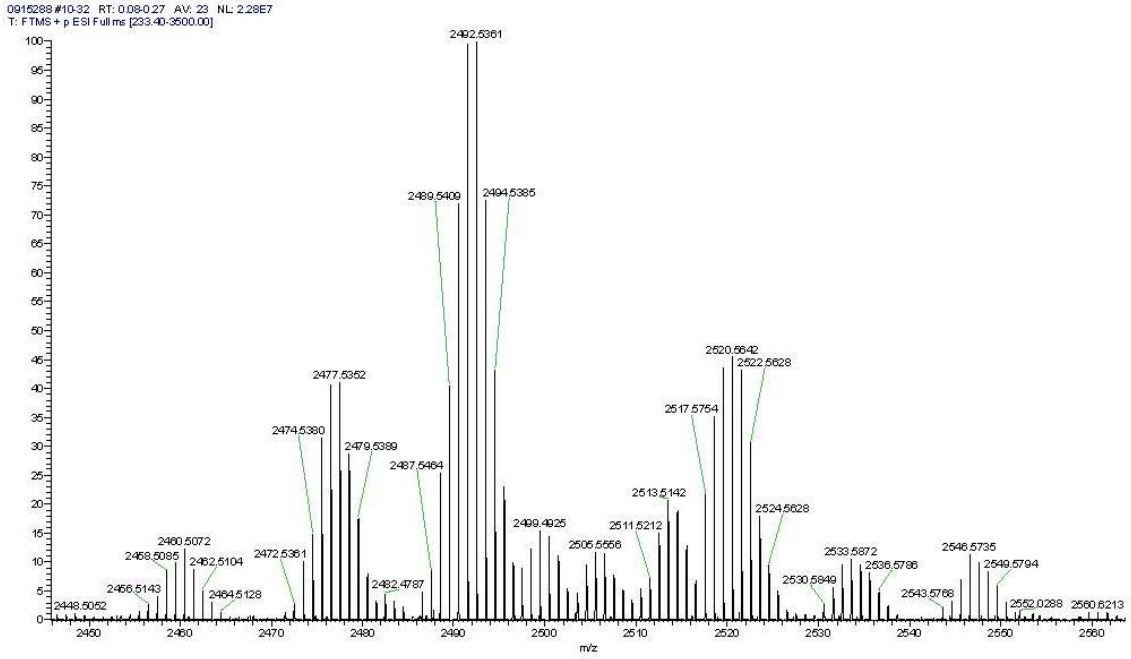

Figure S1: FTMS+ spectrum for **1**

1.2. Infra-red Spectra

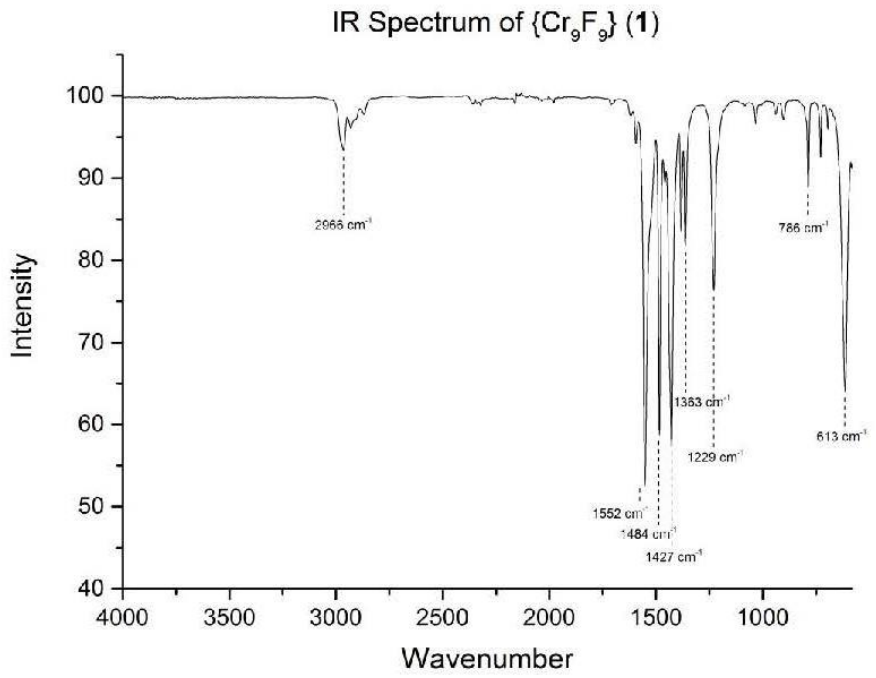

Figure S2: Infra-red spectrum of **2**

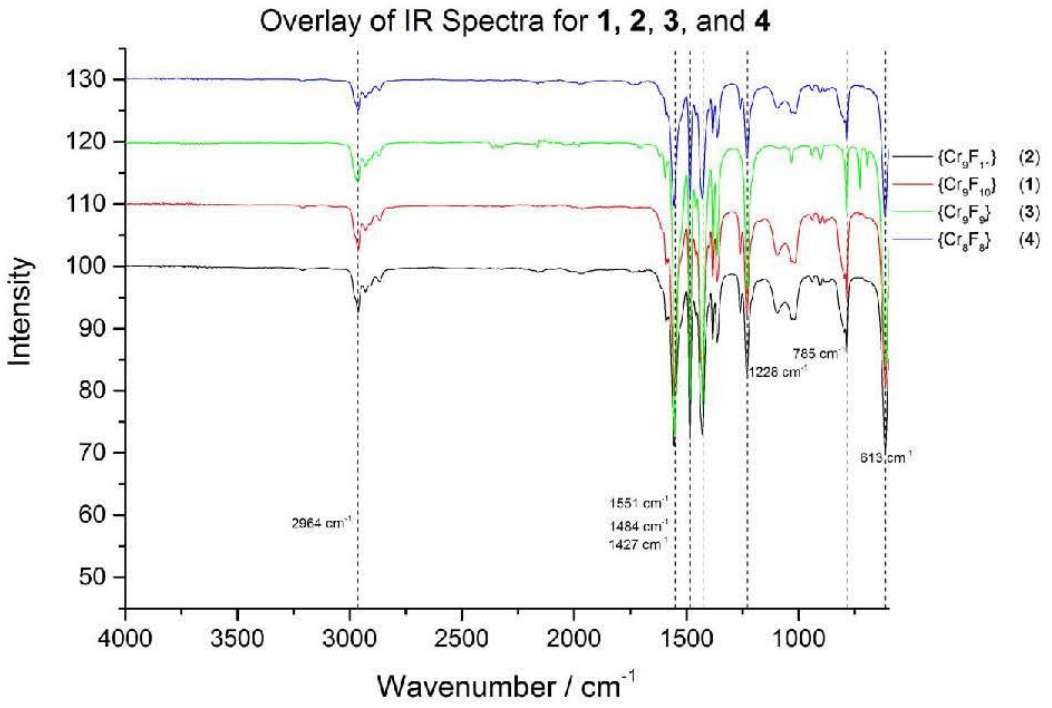

Figure S3: Overlay of the infra-red spectra for **1**, **2**, **3** and **4** showing no significant differences in the observed spectra of the four compounds.

2. Crystallography

Data Collection. X-ray data for compound **1/n-propanol** was collected at a temperature of 150 K using a using Mo-K_α radiation on a microfocus Agilent Supernova diffractometer, equipped with an Oxford Cryosystems Cobra nitrogen flow gas system. Data were measured using CrysAlisPro suite of programs. X-ray data for compound **1/acetone** was collected at a temperature of 100 K using Cu-K_α radiation on a microfocus Bruker X8 prospector diffractometer, equipped with an Oxford Cryosystems Cobra nitrogen flow gas system. Data were measured using Apex2 suite of programs. X-ray data for compound **1/toluene** was collected at beamline I19 in Diamond Light Source at a temperature of 100 K using synchrotron radiation (λ = 0.6889),[2] equipped with an Oxford Cryosystems Cobra nitrogen flow gas system. Data were measured using CrystalClear-SM Expert 2.0 r5 suite of programs.

Crystal structure determinations and refinements. X-ray data were processed and reduced using CrysAlisPro suite of programs. Absorption correction was performed using empirical methods based upon symmetry-equivalent reflections combined with measurements at different azimuthal angles.[3] The crystal structure was solved and refined against all F^2 values using the SHELX and Olex2 suite of programs.[4] Atoms corresponding to compound **1/n-propanol** and **1/acetone** were refined anisotropically. Acetone solvent molecules and some of the pivalates in compound **1/acetone** were refined isotropically in order to keep the data/parameter ration as high as possible. Hydrogen atoms were placed in calculated positions refined using idealized geometries (riding model) and assigned fixed isotropic displacement parameters. Pivalates ligands were highly disorder. The C-C distances of the pivalate ligands were restrained to be the same using DFIX and SADI commands. The atomic displacement parameters (adp) of the ligands have been restrained using RIGU and SIMU commands.

Compound **1/acetone** presents a large amount scattered electron density, the SQUEEZE protocol inside PLATON suites was used to account the electron density.[5] The results of the SQUEEZE protocol indicated that the remaining electron density correspond to two disordered molecules of acetone.

A large number of A and B alerts were found in compound **1/acetone** due to poor resolution (1.1 Å) data. Poor resolution data affects the shapes of the electron density maps obtained, and consequently to the accuracy of the model produced.

CCDC entry 1421216 contains the supplementary crystal data for **1/n-propanol** and entry 1470536 contains the crystal data for **1/acetone**.

Single crystal X-ray diffraction data for **1/toluene** was collected in both "in-house" diffractometers and with synchrotron radiation. Crystals only diffracted until 1.4 Å of resolution at I19 beamline in Diamond Light Source. As we can see in the Figure S4, smeared diffraction spots formed the diffraction pattern obtained. Decrease of the scan width or data collection at different temperatures did not improve the quality of the diffraction patterns. Due to the extremely complex disorder of the Cr9 rings in the crystal packing, the structure remains unsolved and it is impossible to discuss any structural characteristics of the Cr9 rings. However as the ring can be recrystallised intact from two other solvents we are confident they are intact in crystals grown from toluene.

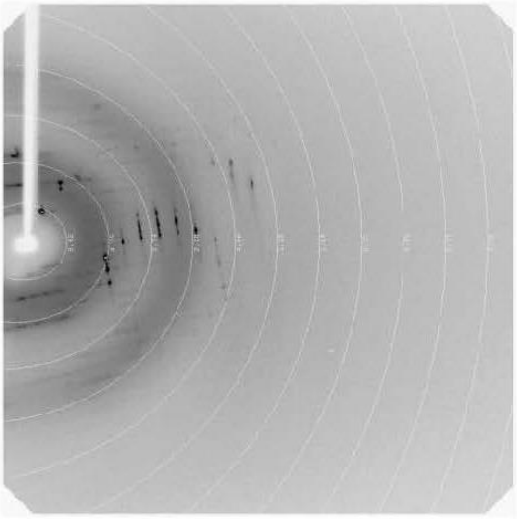

Figure S4. Diffraction pattern of **1/toluene** obtained at beamline I19 in Diamond Light Source.

Nevertheless, the crystal packing of both **1/acetone** and **1/toluene** present some similarities. As we can see in Figure S5, the crystal packing of **1/toluene** in the (001) plane S5a) and (010) plane S5c) are similar to the crystal packing of **1/acetone** in the (001) plane S5b) and (101) plane S5d). We can also appreciate how the molecules of compound **1/acetone** are tilted with respect to the (001) and (101) planes in the crystal structure. The angles formed by the molecules with respect to these planes are a consequence of the internal symmetry dictated by the space group. **1/toluene** molecules shown in the pictures are perfectly parallel to the (001) and (010) planes. The ellipsoids generated in **1/toluene** are extraordinary large, suggesting that the molecules of **1** are randomly disordered above and below the (001) and (010) planes. Therefore, it can be speculated that the diffused diffraction spots obtained in the diffraction pattern are consequence of the severe disordered found in **1/toluene.**

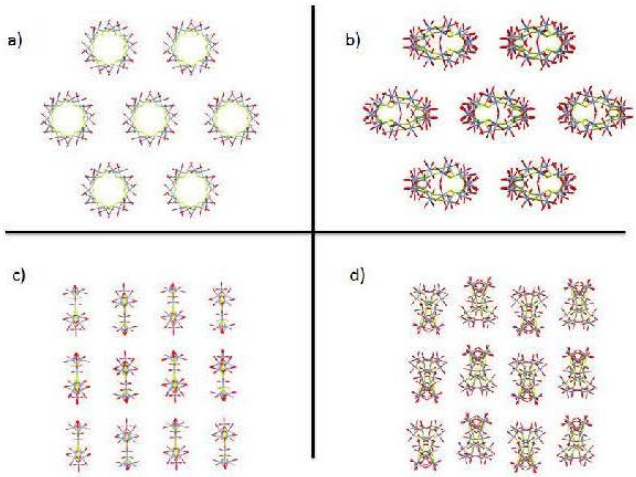

Figure S5. Crystal packing view of a) **1/toluene** plane (001); b) **1/acetone** plane (001); c) **1/toluene** plane (010); and d) **1/acetone** plane (101)

Table S1. Crystallographic information for **1/n-propanol, 1/acetone** and **1/toluene**

	1/n-propanol	**1/acetone**	**1/toluene**
Crystal colour	green	green	green
Crystal size (mm)	0.35 × 0.2 × 0.07	0.3 × 0.15 × 0.08	0.15 × 0.15 × 0.15
Crystal system	Orthorombic	Monoclinic	Hexagonal
Space group, *Z*	Pbca, 8	$P2_1/n$, *4*	$P6_3/m$, *6*
a (Å)	30.5495(5)	19.2354(8)	19.4172(6)
b (Å)	25.4613(7)	24.077(2)	19.4172(6)
c (Å)	34.4733(9)	32.214(2)	26.310(3)
β (°)	90	90.937(4)	90
V (Å^3)	26814(1)	14918(2)	7937(1)
Density (Mg.m^{-3})	1.248	1.198	
Wavelength (Å)	0.71073	1.54718	0.6889
Temperature (K)	150	100	100
μ(Mo-Kα) (mm^{-1})	0.778	5.836	
2Θ range (°)	6.302 to 52.768	6.458 to 79.94	
Reflns collected	118555	26536	70044
Independent reflns (R_{int})	27371 (0.098)	9002 (0.1163)	5520 (0.2138)
L.S. parameters, *p*	1727	1120	
No. of restraints, *r*	1688	2604	
$R1$ $(F)^a$ $I > 2.0\sigma(I)$	0.0949	0.1390	
$wR2(F^2)$,[a] all data	0.3048	0.3900	
$S(F^2)$,[a] all data	1.056	1.428	

[a] $R1(F) = \Sigma(|F_o| - |F_c|)/\Sigma|F_o|$; [b] $wR^2(F^2) = [\Sigma w(F_o^2 - F_c^2)^2/\Sigma wF_o^4]^{1/2}$; [c] $S(F^2) = [\Sigma w(F_o^2 - F_c^2)^2/(n + r - p)]^{1/2}$

2.1. **Structures of compounds 2,3 and 4**

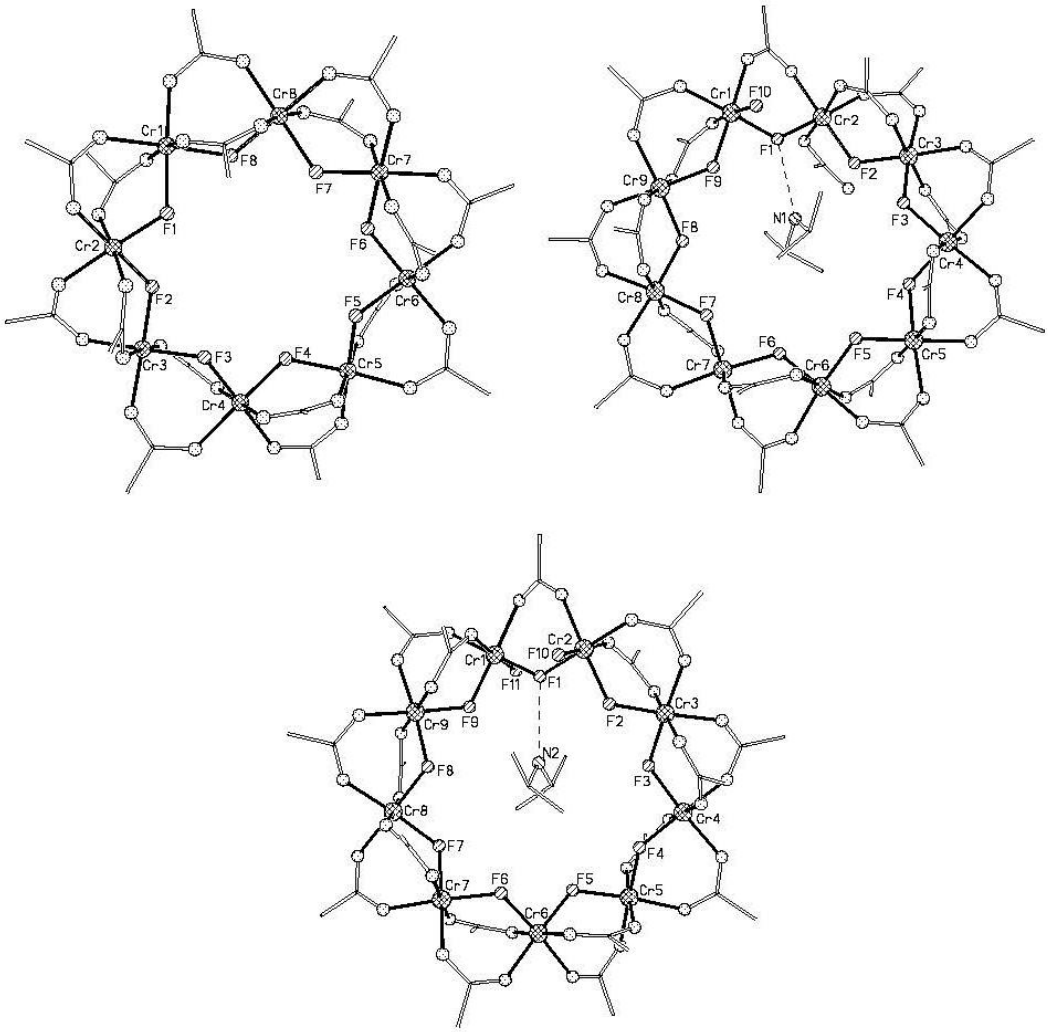

Figure S6: The structures of compounds **2** (top left), **3** (top right) and **4** (bottom). The inequivalent edge in **3** and **4** is at the top of each molecule and contains F1. Cr (cross-hatched circles), F (striped), O (dotted circles), C (lines). Methyl groups of pivalates and solvent molecules omitted for clarity.

3. Magnetisation

Magnetic data were simulated using the isotropic Hamiltonian below with the parameters given in the main text (J = 1.32 meV, J' = 1.58 meV).

$$H = \sum_{i=1}^{8} J\, s_i \cdot s_{i+1} + J'\, s_9 \cdot s_1$$

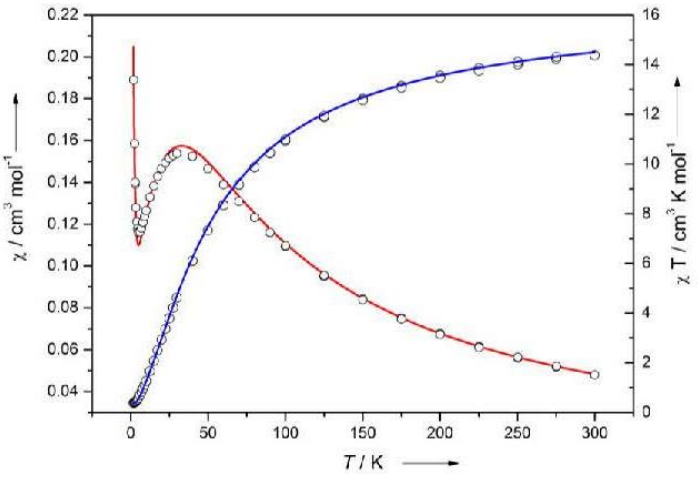

Figure S7: Magnetic susceptibility (χ) versus temperature (T) and χT versus T for compound 1 with data (open circles) and calculation (solid lines).

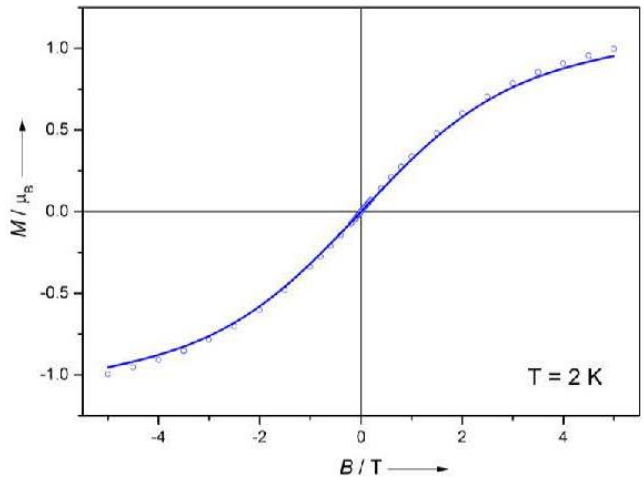

Figure S8: Magnetization (M) versus field (B) for compound **1** with simulation (solid line).

4. INELASTIC NEUTRON SCATTERING

Figure S9 below reports the comparison between the fit of the E_i =2.5 meV data with an ideally frustrated model (uniform J couplings, left panel) and the one reported in Eq. 1 of the main text (J'/J=1.2, right). Although the detailed splitting of the peak is better reproduced by using spin Hamiltonian (1), the main features are captured by the frustrated model Hamiltonian. In addition, higher-energy peaks are well reproduced by both models. This shows that the spin dynamics of the system is essentially the same of a frustrated ring.

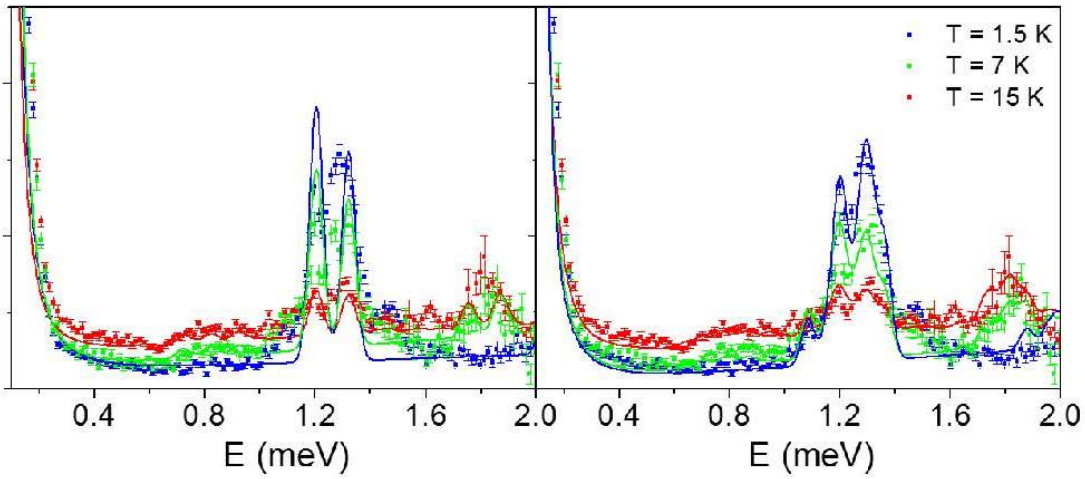

Figure S9: Left: Fitting with an ideally frustrated model (J = 1.35 meV, 10.9 cm^{-1}). Right: fitting with the model reported in the main text (Eq. 1), with J' = 1.2 J, J = 1.32 meV (10.6 cm^{-1}). Measurements performed with 2.5 meV energy of incident neutrons and 58 μeV energy resolution (full width at half maximum at the elastic peak).

In the fit reported in the main text we have assumed easy-axis zero field splitting anisotropy. Indeed, the structural similarity of **1** with other Cr-based rings provides a well-defined starting point. The here-determined value of d (-0.022 meV) is in line with those reported for Cr_8 (-0.029 meV)[6] or Cr_8Zn rings (-0.028 meV).[7] However, a good fit can also be obtained with a positive (even if larger) value of d (0.048 meV).

In the fitting procedure a Gaussian line shape is associated with each allowed transition, with the full width at half maximum fixed by the value at the elastic peak (apart from the high-resolution E_i = 1.24 meV data, where a larger width is used).

Below we report the dependence of the scattered neutron intensity on the momentum transfer Q for the peak at 1.3 meV (Figure S7), together with the simulation using the model discussed in the main text.

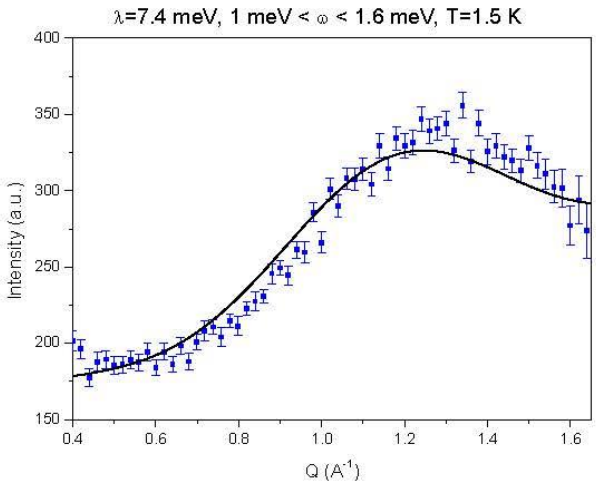

Figure S10: Dependence of the scattered neutron intensity on the momentum transfer Q for the main peak (transition I, S=1/2->S=3/2). There is a good agreement between experimental data (points) and the simulated curve (continuous line), showing that the spatial structure of the states involved in the transition is well reproduced by the model. The curve was calculated using the spin Hamiltonian reported in the text (Eq. 1), with parameters *J*, *J'* and *d* previously obtained from the fit of the energy dependence of the scattered neutron intensity. A contribution quadratic in Q was added to account for the phonon scattering.[8]

5. Classical spin configuration

The classical spin configuration was calculated by treating the spins as classical vectors of length $\sqrt{s(s+1)} = \sqrt{15}/2$ and minimizing the classical (isotropic) energy of the system:

$$E = \sum_{i=1}^{8} J\, \boldsymbol{s}_i \cdot \boldsymbol{s}_{i+1} + J'\, \boldsymbol{s}_9 \cdot \boldsymbol{s}_1$$

Since the interaction is isotropic, there are infinitely many spin configurations minimizing *E* (which depends only on the relative angles between them). The figure reported below was obtained by fixing the position of one of the spins (red arrow). We show two different views of the same spin configuration minimizing *E*. From S11-left, it is clear that all the spins lie on parallel planes, even if the odd number of anti-ferromagnetically coupled spins make the configuration non-collinear (S11-right).

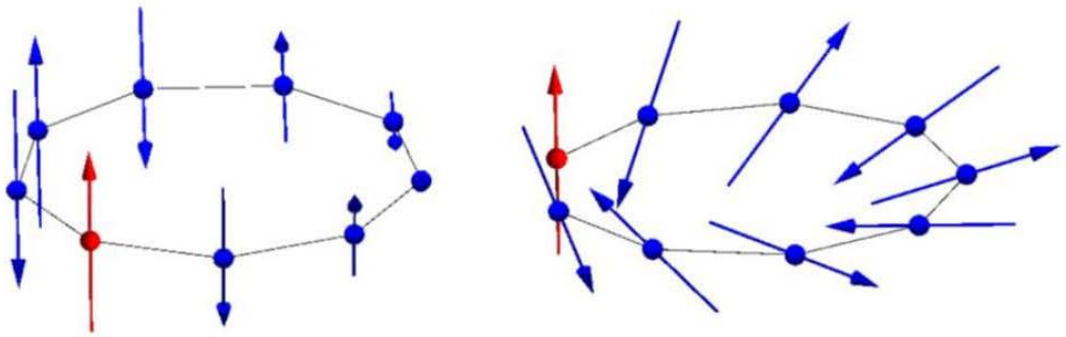

Figure S11. Two views of one of the configurations minimizing the classical energy of the isotropic part of the Hamiltonian, equation (1). The arrows represent Cr spins, with length $\sqrt{s(s+1)} = \sqrt{15}/2$. All the spins belong to the same plane (left), but they are not collinear (right).

5.1. **Spin Chirality**

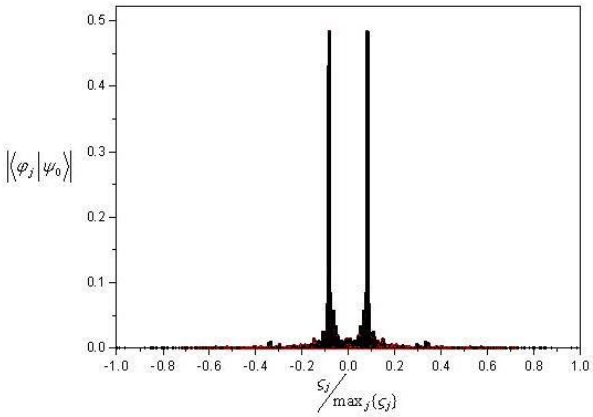

Figure S12. Decomposition of the spin Hamiltonian ground state $|\psi_0\rangle$ onto the eigenstates $|\phi_j\rangle$ of the scalar chirality operator $\hat{C} = \sum_{i=1}^{9} \boldsymbol{s}_i \cdot \boldsymbol{s}_{i+1} \times \boldsymbol{s}_{i+2}$ (i.e., $\hat{C}|\phi_j\rangle = \varsigma_j|\phi_j\rangle$). The quantum ground state is an equal superposition of states with opposite chirality eigenvalues.

6. DFT Calculations

The Density Functional Theory (DFT) calculations reported in this paper were based on the X-ray structure simplified by replacing pivalates with acetates in order to reduce the computational effort, as commonly done for this kind of calculations (see Tomecka *et al.*).[9] We employed NWChem quantum chemistry package[10] and exploit the B3LYP hybrid functional[11] to account for exchange-correlation effects, as typically done in DFT calculations on magnetic molecules.[12] Calculations were performed on the Jülich supercomputer Jureca.

The isotropic exchange couplings were computed by comparing total energy calculations with different spin configurations (according to the broken symmetry approach).[13] Ahlrichs valence triple-ζ (VTZ) basis set for the transition metal ions, and Ahlrichs valence double-ζ (VDZ) basis set for the rest of the elements have been used.[14]

To extract all the nearest-neighbor exchange couplings between Cr ions (s=3/2), we performed total energy calculations on 11 spin configurations: (i) a ferromagnetic arrangement with the maximum projection of the total spin along z (M=27/2); (ii) a staggered state with alternating up and down spins (M=3/2); (iii) nine configurations with eight spins up and one spin down (M=21/2). Energy differences between pairs of these configurations allowed us to extract all the exchange couplings.

SUPPLEMENTARY REFERENCES

1. R.I. Bewley, J.W. Taylor, S.M. Bennington, Nuclear Instruments and Methods in Physics, **2011**, ***637*** 128-134.
2. H. Nowell, S. A. Barnett, K. E. Christensen, S. J. Teat, D. R. Allan, *J. Synchrotron Radiat.* **2012**, *19*, 435-441.
3. (a) L. Krause, R. Herbst-Irmer, G. M. Sheldrick, D. Stalke, *J. Appl. Cryst.* **2015**, *48*, 3-10; (b) R. H. Blessing, *Acta Crystallogr.* **1995**, *A51*, 33-38.
4. (a) G. M. Sheldrick. *Acta Crystallogr.*, **2015,** *C71*, 3-8; (b) O. V. Dolomanov, L. J. Bourhis, R. J. Gildea, J. A. K. Howard, H. Puschmann, *J. Appl. Cryst.* **2009,** *42*, 339–341.
5. PLATON, A Multipurpose Crystallographic Tool (Utrecht University, Utrecht, The Netherlands, 2008).
6. S. Carretta, J. van Slageren, T. Guidi, E. Liviotti, C. Mondelli, D. Rovai, A. Cornia, A. L. Dearden, F. Carsughi, M. Affronte, C. D. Frost, R. E. P. Winpenny, D. Gatteschi, G. Amoretti, and R. Caciuffo, *Phys. Rev. B* **2003**, *67*, 094405.
7. A. Bianchi, S. Carretta, P. Santini, G. Amoretti, T. Guidi, Y. Qiu, J. R. D. Copley, G. Timco, C. Muryn, and R. E. P. Winpenny, *Phys. Rev. B* **2009**, *79*, 144422.
8. S. W. Lovesey, *Theory of Neutron Scattering from Condensed Matter*, Volume 1 (Oxford University Press, New York 1984)
9. D. M. Tomecka, V. Bellini, F. Troiani, F. Manghi, G. Kamieniarz, and M. Affronte, *Phys. Rev. B* **2008**, *77*, 224401.
10. M. Valiev, E.J. Bylaska, N. Govind, K. Kowalski, T.P. Straatsma, H.J.J. van Dam, D. Wang, J. Nieplocha, E. Apra, T.L. Windus, W.A. de Jong, *Comput. Phys. Commun.* **2010**, *181*, 1477.
11. A.D. Becke, *J. Chem. Phys.* **1993**, *98*, 5648.
12. E. Ruiz, S. Alvarez, J. Cano, V. Polo, *J. Chem. Phys.* **2005**, *123*, 164110.
13. L. Noodleman, *J. Chem. Phys.*, **1981**, *74*, 5737.
14. Schafer, A.; Horn, H.; Ahlrichs, R. *J. Chem. Phys.* **1992**, *97*, 2571.

Chapter 5 Paper 2

"The Synthesis, Characterisation and Coordination Chemistry of a Highly Sterically Hindered Phosphine Ligand"

Robert. J. Woolfson, Grigore. A. Timco, David Collison and Richard E.P. Winpenny

Manuscript submitted to Dalton Transactions

One route to linking molecular qubits together in ordered arrays is via substitution of the bridging ligands to introduce new functionality on the periphery of qubits. For example, functionalisation of $\{Mn_{12}\}$ with carboxylates other than acetate has been extensively explored. This can be used to modify the solubility by introducing more polar groups,[159] to introduce radicals to the outside of the cluster[160] or – through careful control of pK_a values – to selectively replace carboxylates on specific sites of the cluster. Sessoli and co-workers reported an $\{Mn_{12}\}$ derivative in which a bi-carboxylic acid was substituted onto the axial positions of $\{Mn_{12}\}$, leaving an acetylsulfanyl group open for potential coordination to a gold surface.[161]

Winpenny and co-workers have reported a range of functionalised derivatives of $\{Cr_7Ni\}$ with oxygen and nitrogen donors (See Section 2.2.8). With all these ligand exchange products, the $\{Cr_7Ni\}$ wheel has been converted to a Lewis base with a hard donor site. Binding of these wheels to a range of d-block metals has been performed and the effect of different metal salts on the binding geometry around the metal explored. For a more detailed introduction to ligand exchange on $\{Cr_7Ni\}$ and previous results, see Section 2.2.7.

Using $Ni(hfac)_2$ as the metal linker with a 4-pyridine carboxylic acid substituted wheel gave a bis-$\{Cr_7Ni\}$ structure with the wheels in a *trans*- orientation across the metal (Figure 15a). Moving to a 4-pyridazine carboxylic acid substituted wheel gave a similar bis-$\{Cr_7Ni\}$ structure, but with the wheels in a *cis*- orientation across the metal (Figure 15b). However, no reason for the change in coordination isomerism could be found.[129]

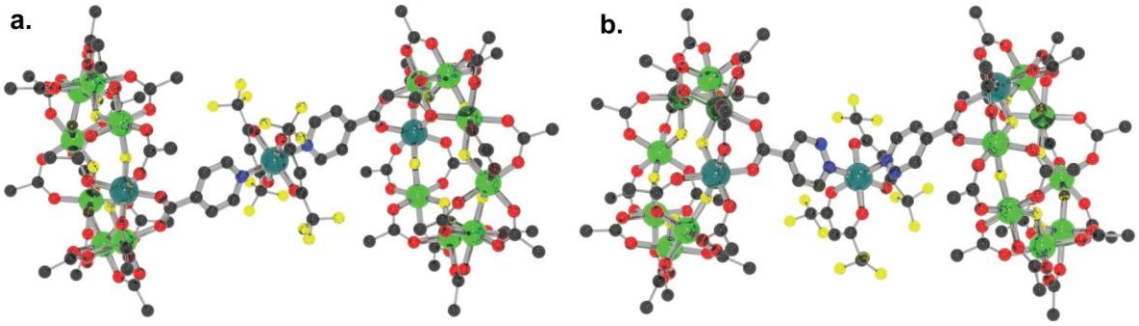

Figure 15: a. X-ray crystal structure of $Ni(hfac)_2$ linked structure ($[NH_2{}^nPr_2][Cr_7NiF_8(O_2C{}^tBu)_{15}(O_2CC_5H_5N)])_2$ $Ni(hfac)_2$ with wheels in *trans*- geometry around metal. b. X-ray crystal structure of $Ni(hfac)_2$ linked structure ($[NH_2{}^nPr_2][Cr_7NiF_8(O_2C{}^tBu)_{15}(O_2CC_4H_4N_2)]$) with wheels in *cis*- geometry around metal. Cr (green), Ni (turquoise), F (yellow), O (red), C (black), N (blue). Tert butyl methyl groups, protons and ammonium cation omitted for clarity.

In the following paper, $\{Cr_7Ni\}$ and $\{Cr_7Co\}$ were successfully functionalised with a phosphine donor – leading to $\{Cr_7Ni\}$ acting as a sterically bulky soft Lewis base ligand. The coordination chemistry of this novel mono-substituted triphenylphosphine derivative to gold was explored, with characterisation of the novel structures by X-ray crystallography. A combination of ^{31}P NMR spectroscopy and DFT modelling was used to study the effect of the $\{Cr_7M\}$ moiety on the underlying electronic and steric properties of the new ligand.

Dalton Transactions

PAPER

The Synthesis, Characterisation and Coordination Chemistry of a Highly Sterically Hindered Phosphine Ligand

Received 00th January 20xx,
Accepted 00th January 20xx

DOI: 10.1039/x0xx00000x

www.rsc.org/dalton

Robert J. Woolfson,[a] Grigore A. Timco,[a] David Collison[a] and Richard E. P. Winpenny[a]*

Two heterometallic wheels have been substituted with a phosphine donor, yielding a highly sterically hindered phosphine ligand $[NH_2{}^nPr_2][Cr_7M(O_2C^tBu)_{15}(O_2CPh_3P)]$ (M = Ni, Co). The effect of the heterometallic wheel on the steric and electronic properties of the phosphine ligand have been explored, showing a remarkably large cone angle for a mono-substituted aryl phosphine of 170.1 °. Furthermore, a sizeable reduction in the strength of coordination to gold chloride is suggested by a -13.76 ppm change in the ^{31}P NMR signal upon metal binding. Exploiting the coordination chemistry of this bulky phosphine ligand with gold chloride resulted in synthesis of a three coordinate gold compound along with a novel trimeric structure.

Introduction

Supramolecular systems show promise in a wide range of applications, due to the potential for chemical control of the constituent building blocks. A recently published supramolecular knot shows catalytic properties in Lewis acid driven reactions, and supramolecular coordination cages have been shown to trap chemical warfare agents.[1, 2] Other applications include drug delivery agents for targeted medicines,[3, 4] components in self-healing polymers and other functional materials,[5, 6] and as potential components in molecular spintronic devices.[7-9] The underlying principle of spintronics is to use the response of a material to an applied magnetic field to modulate the electronic current running through that material; this introduces the "spin" degree of freedom and is already used in solid-state devices.[10, 11] Using molecules as the spin carriers creates the idea of "molecular spintronics,[12-15] with the use of molecular systems allowing the properties of a system to be systematically varied under chemical control, helping to develop useful molecular spintronic devices.[16-18]

The heterometallic family of wheels $\{Cr_7M\}$, and particularly $[NH_2{}^nPr_2][Cr_7NiF_8(O_2C^tBu)_{16}]$ ($\mathbf{1^{Ni}}$) $\{Cr_7Ni\}$ has been proposed as a potential quantum bit – or 'qubit' – for quantum computing due to its overall $S = 1/2$ ground state and the long coherence times of the spin states.[19-21] These same properties, combined with the ability to "fine tune" the molecular and electronic structure by variation of the reaction components, make the $\{Cr_7M\}$ family suitable for exploring the underlying physical effects involved in molecular spintronics.

There are multiple routes to functionalization of $\{Cr_7Ni\}$ wheels. We have previously shown that changing the template to more complex amines leads to the potential for rotaxane formation and can be used to build cages,[22] coordination polymers and other linked systems.[23, 24] A second route to using $\mathbf{1^{Ni}}$ as a building block in coordination chemistry is substituting one of the bridging pivalate ligands for a different carboxylate with donor functionality. These functionalised wheels can be regarded as sterically demanding ligands for use in developing larger supramolecular systems to explore more complex physical phenomena.[25, 26] Here, we

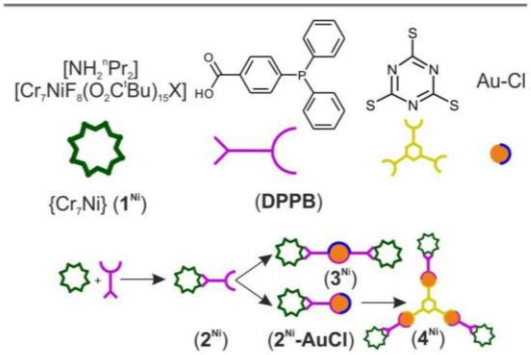

Scheme 1: Schematic representation of the functionalisation of $\mathbf{1^{Ni}}$ with DPPB to form $\mathbf{2^{Ni}}$, followed by reactions with gold chloride to form $\mathbf{2^{Ni}}$-**AuCl**, $\mathbf{3^{Ni}}$ and $\mathbf{4^{Ni}}$

[a] *School of Chemistry, The University of Manchester, Oxford Road, Manchester, M13 9PL, UK*

† Footnotes relating to the title and/or authors should appear here. Electronic Supplementary Information (ESI) available: [details of any supplementary information available should be included here]. See DOI: 10.1039/x0xx00000x

This journal is © The Royal Society of Chemistry 20xx

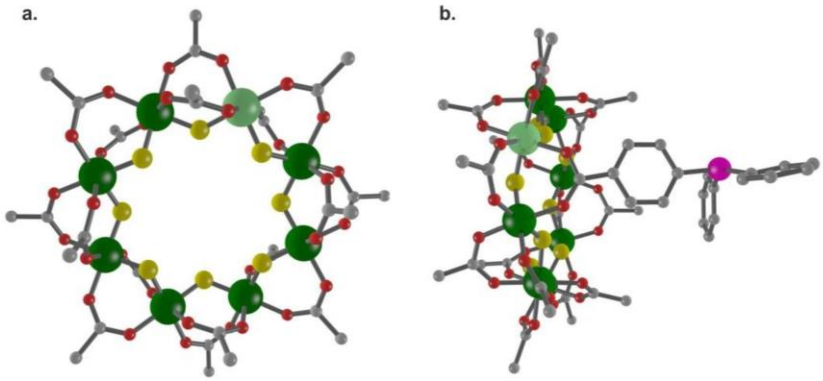

Figure 1: a. X-ray crystal structure of $\mathbf{1^{Ni}}$ viewed perpendicular to the plane of the ring. b.Mono-substituted ring $\mathbf{2^{Ni}}$-$\mathbf{AuCl_{(1)}}$ viewed close to the plane of the $\{Cr_7Ni\}$ ring. Colours – Cr (green), Ni (pale green), Au (gold), P (purple) F (yellow), O (red), C (grey), Cl (bright green). Disorder, tert-butyl methyl groups, protons and ammonium cation omitted for clarity.

introduce a phosphine ligand to $\mathbf{1^{Ni}}$ and make a series of gold coordination complexes using this new bulky phosphine (Scheme 1); the resulting supramolecular complexes have been characterised using X-ray crystallography and ^{31}P NMR.

Supramolecular Structures

The Building Block

In this work, we have introduced a phosphine functionality to $\{Cr_7Ni\}$ by reacting $\mathbf{1^{Ni}}$ with 4-diphenylphosphino-benzoic acid (HO_2C-C_6H_4-PPh_2) (DPPB), which is a commercially available bifunctional phosphine where one of the substituent phenyl rings is functionalised with a carboxylic acid in the *para*-position (Scheme 1).

Refluxing DPPB together with $\mathbf{1^{Ni}}$ for 18 h produces the target building block, however a nitrogen atmosphere and dry solvent are required to prevent formation of the phosphine oxide. The crude mixture was separated by column chromatography, using 5% diethyl ether in hexane as the eluent resulted in isolation of pure mono-substituted $[NH_2{}^nPr_2][Cr_7NiF_8(O_2C{}^tBu)_{15}(O_2C$-$C_6H_4$-$PPh_2)]$ $\mathbf{2^{Ni}}$.

Compound $\mathbf{2^{Ni}}$ crystallised from CH_2Cl_2/MeCN as thin green plates in an orthorhombic space group. The $\{Cr_7Ni\}$ wheel is a ring of eight metals in a roughly planar arrangement. The metal ions are bridged by fluoride ions on the inside of the wheel and carboxylate groups on the outside of the wheel, initially pivalate ligands. Eight of the pivalate ligands are in the plane of the metal ring and eight are approximately perpendicular to the plane. As expected, one of the bridging pivalate ligands in $\mathbf{2^{Ni}}$ perpendicular to the plane of the metal sites (an "axial" site) was substituted by DPPB with the carboxylate bound to a Cr..Ni edge rather than a Cr…Cr edge due to the much higher reactivity of the Ni (Figure 1).[27]

The metal core of the wheel is unchanged by the ligand substitution, with an average Cr-Cr bond length of 3.389(17) Å compared in $\mathbf{2^{Ni}}$ to 3.390(17) Å in $\mathbf{1^{Ni}}$.[26] The PPh_3 moiety is disordered over two possible conformations with the shortest intermolecular separation between the phosphorus atoms 3.733(9) Å. X-ray crystallography, combined with mass spectroscopy and elemental analysis, confirmed the presence of pure phosphine rather than phosphine oxide.

Stirring $\mathbf{2^{Ni}}$ with $AuCl(SMe_2)$ resulted in formation of $[NH_2{}^nPr_2][Cr_7NiF_8(O_2C{}^tBu)_{15}(O_2C$-$C_6H_4$-$PPh_2)AuCl)]$ ($\mathbf{2^{Ni}}$-$\mathbf{AuCl}$), with the phosphine from $\mathbf{2^{Ni}}$ coordinated to the gold chloride by displacement of dimethylsulfide. $\mathbf{2^{Ni}}$-$\mathbf{AuCl}$ crystallised from CH_2Cl_2/MeCN as small green blocks in a monoclinic space group. The gold chloride was crystallographically disordered over two sites, with 89.67 % occupancy in a near linear conformation with a P-Au-Cl bond angle of 176.31(2)° ($\mathbf{2^{Ni}}$-$\mathbf{AuCl_{(1)}}$) (Figure 1b) and 10.33 % occupancy in a bent conformation with a P-Au-Cl bond angle of 156.19(1)° ($\mathbf{2^{Ni}}$-$\mathbf{AuCl_{(2)}}$) (Figure S14)

Salt Metathesis

A classic route to forming supramolecular structures with gold is to exchange the chloride for a non-coordinating anion such as $[PF_6]^-$ or $[BF_4]^-$ followed by addition of new ligands to coordinate to the vacant sites on gold.[28-32] Reacting $\mathbf{2^{Ni}}$-$\mathbf{AuCl}$ with a stoichiometric amount of AgX (X = BF_4, PF_6) followed by filtration resulted in formation of the corresponding salts $[NH_2{}^nPr_2][Cr_7NiF_8(O_2C{}^tBu)_{15}(O_2C$-$C_6H_4$-$PPh_2)Au][BF_4]$ $\mathbf{3^{Ni}}$-$\mathbf{BF_4}$ and $[NH_2{}^nPr_2][Cr_7NiF_8(O_2C{}^tBu)_{15}(O_2C$-$C_6H_4$-$PPh_2)Au][PF_6]$ $\mathbf{3^{Ni}}$-$\mathbf{PF_6}$. No crystals suitable for X-ray

 This journal is © The Royal Society of Chemistry 20xx

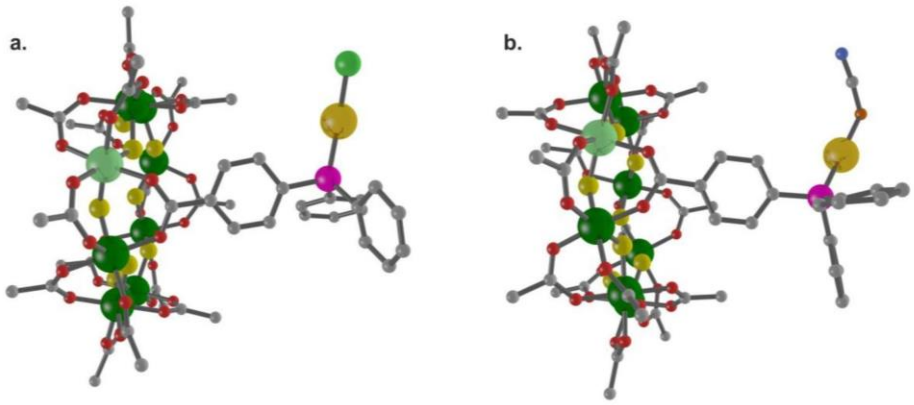

Figure 2: a. X-ray crystal structure of 2^{Ni}-**AuCl**$_{(1)}$ viewed close to the plane of the ring b. X-ray crystal structure of 2^{Ni}-**AuSCN** viewed close to the plane of the ring. Cr (green), Ni (pale green), Au (gold), P (purple) F (yellow), O (red), C (grey), Cl (bright green), S (orange), N (blue). Disorder, tert-butyl methyl groups, protons and ammonium cation omitted for clarity.

crystallography could be obtained for either compound but elemental analysis confirmed complete exchange of the chloride. Attempts to synthesise the bis-phosphine gold chloride complexes by coordination of further equivalents of 2^{NI} to 2^{Ni}-**AuBF$_4$** and 2^{Ni}-**AuPF$_6$**, along with attempts to form gold nanoclusters by reduction of 2^{Ni}-**AuCl** with $NaBH_4$, were unsuccessful.[31]

An alternative to non-coordinating anions is a coordinating pseudo-halide such as thiocyanate where the sulfur atom will bind to the gold, leaving the cyano group free for further reactions. Reacting 2^{Ni}-**AuCl** with a stoichiometric amount of KSCN resulted in quantitative formation of the desired product, $[NH_2{}^nPr_2][Cr_7NiF_8(O_2C{}^tBu)_{15}(O_2C\text{-}C_6H_4\text{-}PPh_2)AuSCN]$ (2^{Ni}-**AuSCN**). 2^{Ni}-**AuSCN** crystallised from CH_2Cl_2/MeCN as thin green plates in a monoclinic space group (Figure 2). Unlike the gold chloride in 2^{Ni}-**AuCl**, the gold thiocyanate is not disordered, with one molecule of CH_2Cl_2 present in the asymmetric unit, coordinated by hydrogen bonding to the nitrogen atom of the thiocyanate.

Gold Bridged {Cr_7Ni} Systems

Whilst attempts to link 2^{Ni} via salt metathesis reactions of 2^{Ni}-**AuCl** followed by reaction with further equivalents of 2^{Ni} were unsuccessful, the reaction of 2^{Ni} with $[AuCl(SMe_2)]$ in the ratio 2.5:1 resulted in formation of the gold bridged compound $([NH_2{}^nPr_2][Cr_7NiF_8(O_2C{}^tBu)_{15}(O_2C\text{-}C_6H_4\text{-}PPh_2])_2AuCl$ 3^{Ni} (Figure 3a). 3^{Ni} crystallised from CH_2Cl_2/MeCN as thin plates with a monoclinic space group. The gold atom shows an unusual three-coordinate geometry, it is bound to two molecules of 2^{Ni} and a chloride. The two {Cr_7Ni} wheels are *trans*- across the P-Au-P bond but show an eclipsed geometry (Figure S15), most likely due to packing effects (see below).

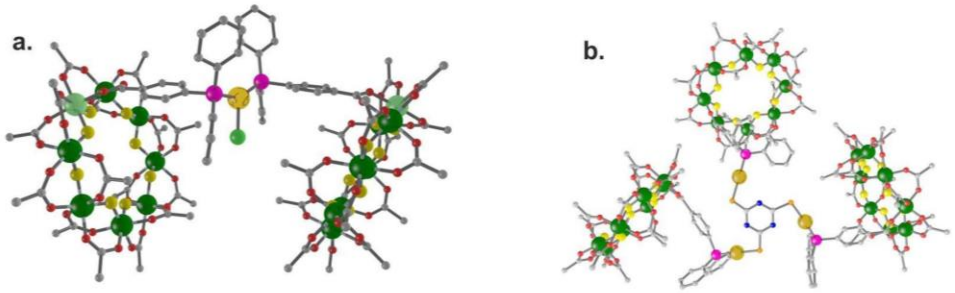

Figure 3: a. X-ray crystal structure of 3^{Ni}. b. X-ray crystal structure of 4^{Ni} viewed parallel to the plane of the central $C_3S_3N_3$ heterocycle. Cr (green), Ni (pale green), Au (gold), P (purple), F (yellow), O (red), C (grey), N (blue), S (orange). Disorder, tert-butyl methyl groups, protons and ammonium cation omitted for clarity.

This journal is © The Royal Society of Chemistry 20xx

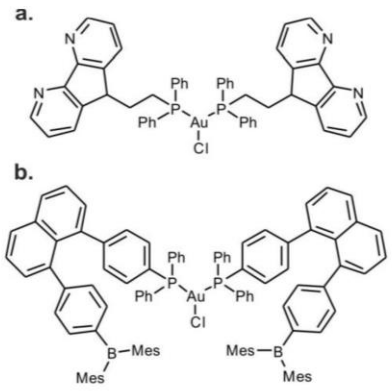

Scheme 2: Structures of bis-phosphine gold chloride compounds with mono-substituted phosphine ligands 9-(2-(diphenylphosphino)ethyl)-4,5-diazafluorene (a.) and [4-[8-[4-[bis(2,4,6-trimethylphenyl)boryl]phenyl]-1-naphthalenyl]phenyl]diphenylphosphine (b.)

Gold Bridged Trimer

Having previously exploited the affinity of sulfur for gold to synthesise **2^{Ni}-AuSCN**, it was decided to explore the potential of trithiocyanuric acid as a bridging ligand (Scheme 1). Trithiocyanuric acid contains three thiol sites around a central C_3N_3-ring, This was converted to the sodium salt and then reacted with three equivalents of **2^{Ni}**, resulting in the formation of $[\{[NH_2{}^nPr_2][Cr_7NiF_8(O_2C{}^tBu)_{15}(O_2C\text{-}C_6H_4PPh_2Au)\}_3(S_3C_3N_3)]$ **4^{Ni}** (Figure 3b).

4^{Ni} crystallised as very small green blocks in a triclinic space group. The three {Cr_7Ni} rings in **4^{Ni}** are not equivalent, with each showing slightly different bond lengths and angles (see below for full discussion). Cyclic voltammetry was used to explore the electrochemistry of **4^{Ni}**, particularly whether a radical could be introduced on the central linker. However, under the conditions used no redox processes could be observed (Figure S18).

Structural and Electronic Characterisation

Structural Comparisons

Reported below are the relevant structural parameters for Ph_3PAuCl,[33] $CO_2H\text{-}C_6H_4\text{-}PPh_2AuCl$[34] and **$2^{Ni}$-AuCl$_{(1)}$** (Table 1). The gold-phosphine bond lengths are virtually unchanged across the three structures. Any changes in the observed P-Au bond lengths on moving from Ph_3P to DPPB (+0.001(5) Å) and DPPB to **2^{Ni}** (+0.008(16) Å) as the ligand are within the margin of the errors in the X-ray crystallography. This suggests that if either the carboxylate in DPPB or the {Cr_7Ni} in **2^{Ni}** are inducing changes in the underlying electronic properties of the ligand, these changes are not visible in the Au-P bond lengths.

3^{Ni} is an unusual example of a three coordinate gold chloride structure with a bulky monodentate phosphine ligand. There are extensive reports of bis-phosphine gold chloride complexes but many have a dissociated chloride ion in the solid-state structure. The majority of structures reported with the chloride bound are formed using bidentate phosphine ligands with only a few examples of this class of structure reported with monodentate phosphines.[35]

The simplest complex is $[(Ph_3P)_2AuCl]$, which has a P-Au-P angle approaching that for an ideal trigonal complex.[41] A more direct comparison can be gained by looking at similar mono substituted aryl phosphine ligands, such as ethyl-4,5-diazafluorene[39] or dimesityl

Table 1: Comparison of bond lengths and bonding angles for a range of gold-phosphorus compounds

Formula		Bond Length (Å)		Bond Angle (°)		%V_{bur}
		P-Au	Au-X	P-Au-P	P-Au-X	
Ph_3PAuCl[33]		2.231(4)	2.290(4)	-	179.24(15)	29.9
$O_2C\text{-}C_6H_4\text{-}PPh_2AuCl$[34]		2.232(4)	2.278(4)	-	177.50(1)	30.2
$[NH_2{}^nPr_2][Cr_7NiF_8(O_2C{}^tBu)_{15}(O_2C\text{-}C_6H_4\text{-}PPh_2)AuCl]$	**2^{Ni}-AuCl$_{(1)}$**	2.238(4)	2.271(5)	-	176.30(2)	35.3
	2^{Ni}-AuCl$_{(2)}$	2.235(4)	2.271(5)	-	156.40(18)	
$Ph_3PAuSCN$[36]		2.254(1)	2.331(2)	-	177.88(6)	
$[NH_2{}^nPr_2][Cr_7NiF_8(O_2C{}^tBu)_{15}(O_2C\text{-}C_6H_4\text{-}PPh_2)AuSCN]$	**2^{Ni}-AuSCN**	2.225(6)	2.265(5)	-	179.30(2)	-
$(Ph_3PAu)_3N_3S_3C_3$[37]		2.262(4)	2.304(4)	-	177.70(2)	-
		2.258(5)	2.303(5)	-	177.50(2)	-
		2.251(5)	2.304(5)	-	175.50(2)	-
$([NH_2{}^nPr_2][Cr_7NiF_8(O_2C{}^tBu)_{15}(O_2C\text{-}C_6H_4\text{-}PPh_2)Au])_3C_3N_3S_3$*	**4^{Ni}-Ring 1**	2.240(2)	2.331(19)	-	176.2(9)	-
	4^{Ni}-Ring 2	2.217(17)	2.298(17)	-	177.6(8)	-
	4^{Ni}-Ring 3	2.208(2)	2.280(2)	-	177.0(8)	-
$(Ph_3P)_2AuCl$[38]		2.322(3)	2.523(6)	133.02(17)	113.49(9)	-
$(C_{11}N_2H_7\text{-}C_2H_4\text{-}PPh_2)_2AuCl$[39]		2.302(14)	2.665(15)	147.23(5)	111.04(6)	29.8†
$(Mes_2B(C_6H_4\text{-}C_{10}H_6\text{-}C_6H_4\text{-}Ph_2P))_2AuCl$[40]		2.319(18)	2.788(3)	158.31(9)	100.84(5)	34.4†
$([NH_2{}^nPr_2][Cr_7NiF_8(O_2C{}^tBu)_{15}(O_2C\text{-}C_6H_4\text{-}PPh_2)])_2AuCl$	**3^{Ni}**	2.311(4)	2.498(7)	146.30(2)	106.85(11)	-‡

*All three {Cr_7Ni} wheels show significant disorder in **4^{Ni}** and the ESD values reflect uncertainty in the precise bond length and angle values due to this disorder
† %V_{bur} calculated based on coordination of one ligand. ‡ **3^{Ni}** is larger than the modelling capacity of SambVca.

This journal is © The Royal Society of Chemistry 20xx

boron naphthalene[40] derivatives of diphenylphosphine (Scheme 2). In these two complexes the trigonal geometry is significantly distorted towards a more linear geometry (+14.21(22) ° and +25.19(26) ° respectively) due to a mixture of steric and crystal packing effects. Both ligands contain aromatic moieties with the X-ray crystal structures showing strong evidence for T-shaped pi-stacking driving the solid state structure and therefore the observed changes in P-Au-P bond angle.[40]

3^{Ni} shows a similar deviation from the idealised trigonal geometry around the gold centre (+13.18(19) °). Given the lack of structural elements, particularly the absence of aromatic units with the potential for pi-stacking, in **3^{Ni}** the packing geometry and solid state structure are due to the steric requirements of the {Cr_7Ni} moiety combined with the need for long range ordering in a single crystal. These two forces in **3^{Ni}** can be assumed to drive deviations from the near-trigonal geometry of $(Ph_3P)_2AuCl$. The shortening of the Au-Cl bond by 0.025(15) Å relative to $(Ph_3P)_2AuCl$ is consistent with a slight reduction in the electron density at gold due to reduced electron donation from the phosphine ligand.[42]

Upon changing the counter-ion from chloride (**2^{Ni}-AuCl**) to thiocyanate (**2^{Ni}-AuSCN**) the P-Au bond length remains virtually unchanged at 2.225(5) Å. Compared to the previously reported $Ph_3PAuSCN$[36] the P-Au bond length is 0.029(19) Å shorter and the Au-S bond is 0.066(19) Å longer, suggesting a slight increase in the strength of the P-Au bond in **2^{Ni}-AuSCN**. However, these changes are only marginally larger than the error in the crystallography therefore no firm conclusions can be drawn.

Gold trimer complexes linked by trithiocyanuric acid have previously been reported with both PPh_3 and less sterically demanding phosphine ligands on the gold.[37, 43, 44] For the PPh_3 structures, the P-Au and Au-S bond lengths, along with the P-Au-S bond angles are comparable to those observed for the $Ph_3PAuSCN$ structure discussed above.

As with the thiocyanate compounds above, the {Cr_7Ni} moiety in **4^{Ni}** results in significant changes in the observed bond lengths compared to the previously reported structure, with a general trend of shorter P-Au and longer Au-S bond lengths suggesting a slight strengthening of the gold-phosphorus bond. The three **2^{Ni}** moieties are not equivalent, with each showing different bond lengths and angles. Two of the {Cr_7Ni} rings lie almost perpendicular to the plane of the central heterocycle with torsion angles of 75.38 ° and 87.52 °, whilst the third one lies closer to co-parallel with a torsion angle of 35.52 ° (Figure S16). The differing orientations can be explained by looking at the intermolecular packing, where the different orientation of the third ring allows molecules to lie side-on in the structure (Figure S17).

Table 2: ^{31}P NMR Data for phosphine ligands before and after coordination to gold

	^{31}P NMR δ (ppm)		^{31}P NMR δ (ppm)
Ph_3P	-5.40	**Ph_3PAuCl**	+33.06
HO_2CPh_3P	-4.76	**HO_2C-C_6H_4-Ph_2PAuCl**	+33.18
2^{CO}	-3.42	**2^{Co}-AuCl**	+19.42
$(C_6F_5)_3P$	-76.00	**$(C_6F_5)_3P$-AuCl**	+57.08

Quantification of the Steric Effect

The historical method for the characterisation of phosphine ligands is the Tolman cone angle.[45] Statistical analysis of reported X-ray structures has shown that, for the same ligand, a range of cone angles can be calculated depending on the metal complex to which it is bound.[46] The Tolman cone angle also causes challenges when used to analyse bulky ligands such as Buchwald's phosphines.[47]

An alternative metric of the steric bulk of a phosphine is the percentage buried volume (%V_{bur}), a measure of the space occupied by a ligand in the first coordination sphere of the metal centre. First proposed by Hiller *et al.* as a measure of the steric hindrance of N-heterocyclic carbenes,[48] it has since been extended to a range of ligands including phosphines and can be calculated via DFT using the freely available online software package SambVca.[49, 50]

Simulated values were calculated using the crystal structures reported above, but the metal centre was set at 2.28 Å from the phosphorus site to allow comparison with previously published results. The calculated %V_{bur} for PPh_3 showed a good fit to that previously reported (29.9 % vs 29.6 %), with a similar value calculated for DPPB (30.2 %) suggesting the carboxylate moiety has minimal effect on the steric properties of the ligands.[47] Upon addition of the **2^{Ni}** moiety to DPPB the calculated %V_{bur} rises significantly to 35.3 %, a rise in steric bulk making **2^{Ni}** sterically similar to $P(C_6F_5)_3$ (%V_{bur} = 37.3 %) and bulkier than the comparable mono naphthalene substituted phosphine discussed above (%V_{bur} = 34.3). As there is an approximately linear correlation between Tolman cone angle and %V_{bur},[47] the value for the cone angle of **2^{Ni}** can be estimated as 171 ° - a significant increase from PPh_3 (145 °) and suggesting that the addition of a {Cr_7Ni} moiety on one phenyl ring results in a large rise in the steric bulk of the phosphine ligand and larger than observed for the naphthalene compound (165 °).

^{31}P NMR

To characterise the underlying electronic properties of the phosphine functionalised with {Cr_7Ni}, a ^{31}P NMR spectroscopy study was carried out using the cobalt analogues of **2^{NI}** and **2^{Ni}-AuCl**. Synthesised from $[NH_2{}^nPr_2][Cr_7Co(O_2C{}^tBu)_{16}]$ **1^{Co}** via analogous conditions, **2^{Co}** and **2^{Co}-AuCl** were synthesised in comparable yields to the nickel analogues. Structurally, **1^{Co}** is identical to **1^{Ni}** in all cases we have studied.[26] NMR spectra of **1^{Ni}** are uninformative due to slow relaxation of the Ni(II) on the

This journal is © The Royal Society of Chemistry 20xx

NMR timescale. However, due to the fast relaxation times of the Co(II) in $\mathbf{1^{Co}}$, we have shown that it is possible to collect and interpret NMR spectra of compounds containing $\mathbf{1^{Co}}$.[51]

The proton decoupled ^{31}P NMR spectra of $\mathbf{2^{Co}}$ and $\mathbf{2^{Co}}$**-AuCl** were collected and the chemical shifts compared to those of Ph_3P, HO_2C-C_6H_4-PPh_2, Ph_3PAuCl and HO_2C-C_6H_4-PPh_2AuCl (Table 2) (Figure S11-S13). To rule out any paramagnetic effects on the ^{31}P NMR from the $\mathbf{1^{Co}}$ moiety, NMR spectra for $\mathbf{2^{Co}}$ were recorded at 298 K and 238 K. No strong temperature dependence was observed, suggesting the phosphorus NMR spectroscopy can be treated as diamagnetic in this system (Figure S10).[52]

Upon coordination to gold chloride, the ^{31}P chemical shifts for PPh_3 and DPPB change by 38.5 and 37.9 ppm respectively, (Table 2) due to a strong deshielding effect on the phosphorus nuclei caused by electron donation from the phosphine to the gold. In $\mathbf{2^{Co}}$ the ^{31}P NMR signal is observed 1.34 ppm downfield relative to the free DPPB, possibly due to a small electron withdrawing effect from {Cr_7Co}. Upon coordination to AuCl, giving $\mathbf{2^{Co}}$**-AuCl**, a downfield shift of 23.00 ppm is observed. The is a much smaller change in the chemical shift than for DPPB which suggests that the {Cr_7Co} moiety in $\mathbf{2^{Co}}$ has reduced the electron donating ability (and therefore the observed deshielding) of the phosphorus donor in $\mathbf{2^{Co}}$. For comparison, the ^{31}P chemical shift value for $(C_6F_5)_3P$ changes by 133.1 ppm, suggesting extremely strong binding despite the steric bulk of the perfluoro-phenyl rings.[53, 54]

The value of ^{31}P NMR chemical shifts has been shown to be dependent on the bond angles at phosphorus, the electronegativity of the substituents and the extent of the π-bonding in the system.[55] As discussed above, the P-Au and Au-Cl bond lengths do not vary in a statistically meaningful way. The extent of π-donation can be estimated from the changes in the P-C bond lengths, with a shorter average phosphorus carbon bond length suggesting greater π-bonding. [40, 42] The average P-C bond length in Ph_3PAuCl is 1.811(5) Å whilst in $\mathbf{2^{Ni}}$**-AuCl** it is 1.841(5) Å, suggesting a reduction in the π-bonding between Au and P for $\mathbf{2^{Ni}}$, which is consistent with the NMR shift behaviour.

Conclusions

A heterometallic {Cr_7Ni} ring has been functionalised to make a highly sterically demanding mono-substituted phosphine ligand. The electronic and steric properties of the new ligand have been characterised. A DFT approach has been used to calculate the steric bulk, and ^{31}P NMR spectroscopy to examine the electronic properties; together they show that the new "ligand" is as bulky as $P(C_6F_5)_3$ but with a significant weakening of the donor properties. This new bulky phosphine ligand has been successfully bound to gold chloride and then reacted further to form a three coordinate gold bis-phosphine as well as a unique trimer structure around trithiouric acid, showing its versatile nature. We have previously shown that a {Cr_7Ni} wheel functionalised with sulphur will bind to an Au(111) surface, causing changes in the underlying magnetism.[56] The interaction of this weakly binding phosphine with gold surfaces and the effect on the magnetic properties are being explored.

Experimental

All reagents were purchased from commercial sources and used as received. Column chromatography was performed using a Grace Reverelis® Autocolumn with Reverelis® Flash Cartridges. NMR spectroscopy was performed using a Bruker AVIII HD 500 spectrometer with a CryoProbe™ Prodigy BBO probe at room temperature (unless otherwise specified). Mass spectrometry was performed with a Thermo Fisher Scientific "Exactive Plus EMR orbitrap" in electrospray mode, spectral simulations were performed using the ChemCalc toolkit.[57] See SI for full spectra and simulations. Electrochemistry measurements were performed using a PGSTAT302N potentiostat (Metrohm Autolab B. V.). See SI for experimental details. Elemental analysis for carbon, nitrogen, phosphorus and hydrogen analysis was performed using a Flash 200 elemental analyser. Metal elemental analysis was performed by Thermo iCap 6300 Inductively Coupled Plasma Optical Emission Spectroscopy (ICP-OES). Single crystal X-ray structures were collected either on a Bruker Apex II Prospector with a Cu source at 100 K ($\mathbf{2^{Ni}}$, $\mathbf{2^{Ni}}$**-AuCl**, $\mathbf{2^{Ni}}$**-AuSCN**, $\mathbf{3^{Ni}}$) or on beamline i19 at the Diamond Light Source ($\mathbf{4^{Ni}}$).[58] Data sets were reduced with CrysAlisPro then solved and refined by full matrix least squares techniques on F^2 using the Shelxl[59] suite in Olex2.[60] Hydrogen atoms were included in the refinement process as per the riding model. CCDC entries 1499587-1499591 contain the supplementary crystal data for $\mathbf{2^{Ni}}$**, $\mathbf{2^{Ni}}$-AuCl, $\mathbf{2^{Ni}}$-AuSCN, $\mathbf{3^{Ni}}$ and $\mathbf{4^{Ni}}$. Errors in ESD values have been reported to a 3σ level of confidence.

Synthetic Procedures

$\mathbf{1^{Ni}}$ was synthesised as previously reported.[21]

$\mathbf{1^{Co}}$ was synthesised as previously reported.[26]

Ph_3P-AuCl was synthesised using the method published by Price *et al.*,[61] Ph_3P (0.08 g, 0.305 mmol) was added to a solution of $AuCl(SMe_2)$ in CH_2Cl_2 (5 mL) and stirred for 3 h. The solution was filtered over celite, dried by rotary evaporation and washed with hexane (2 x 10 mL) yielding the product (0.1198 g, 79.7 %) as a white powder. ESMS+: 517.022 (M + Na). Elemental anal. (calc): C, 43.98 (43.79); H, 3.11 (2.86); Cl, 7.20 (7.18); P, 6.01 (6.27). See SI for NMR spectra.

HO_2C-C_6H_4-PPh_2-AuCl was synthesised using the method published by Galassi *et al.*,[62] DPPB (0.1 g, 0.326 mmol) was added to a solution of $AuCl(SMe_2)$ (0.096 g, 0.326 mmol) in CH_2Cl_2 (5 mL) and stirred at r.t. for 3 h.

This journal is © The Royal Society of Chemistry 20xx

The solution was filtered over celite, dried by rotary evaporation, washed with hexane (2 x 10 mL) and diethyl ether (2 x 10 mL) yielding the product (0.1361 g, 77.6 %) as a white powder. ESMS-: 537.009 (M - H). Elemental Anal. (calc.): C, 42.16 (42.44); H, 2.48 (2.62); P, 5.76 (5.56); Cl, 6.45 (6.59). See SI for NMR spectra.

2^{Ni} was synthesised by refluxing $[NH_2{}^nPr_2][Cr_7NiF_8(O_2C{}^tBu)_{16}]$ (**1^{Ni}**) (1.0 g, 0.43 mmol) with 4-diphenylposphino-benzoic acid (0.4 g, 1.29 mmol) in dry xylenes (15 mL) at 160 °C for 18 h under a nitrogen atmosphere. After cooling, the mixture was dried by rotary evaporation, dissolved in hexane, filtered and purified by column chromatography. Using a 40 g silica cartridge and 98% hexane: 2% diethyl ether as the eluent, a mixture of unreacted **1^{Ni}** and **2^{Ni}** eluted followed closely by 0.054 g (5.02 %) of pure **2^{Ni}** ESMS+: 2498.618 (M + H); 2521.611 (M + Na). Elemental Anal. (calc.): C, 48.04 (48.06); H, 6.79 (6.65); N, 0.54 (0.56); P, 1.44 (1.25); Cr, 13.88 (14.56); Ni, 2.17 (2.34). Crystals suitable for X-ray diffraction were grown from slow evaporation of a CH_2Cl_2/MeCN solution.

2^{Co} was synthesised and purified by an analogous procedure to **2^{Ni}** yielding 0.197 g (18 %) as a green powder. ESMS+: 2499 (M + H); 2522.600 (M + Na). Elemental Anal. (calc.): C, 48.69 (48.06); H, 6.46 (6.85); N, 0.54 (0.56); P, 1.39 (1.25); Cr, 14.21 (14.56); Co, 2.19 (2.36).

2^{Ni}-AuCl was synthesised by reacting **2^{Ni}** (0.1 g, 0.04 mmol) with $AuCl(SMe_2)$ (12.9 mg, 0.044 mmol) in dry CH_2Cl_2 (10 mL). The reaction was filtered over celite and the solvent removed by rotary evaporation yielding a green powder (0.108 g, 0.0395 mmol, 99 % yield). Crystals suitable for X-ray diffraction were grown from slow evaporation of a CH_2Cl_2/MeCN solution. ESMS+: 2732.560 (M + H). Elemental Anal. (calc.): C, 44.15 (43.72); H 6.28 (6.12); N, 0.51 (0.52); Cl, 1.62 (1.30); P, 1.04 (1.14); Cr, 12.90 (13.38); Ni, 2.12 (2.16); Au, 7.41 (7.26). Crystals suitable for X-ray diffraction were grown from slow evaporation of a CH_2Cl_2/MeCN solution.

2^{Co}-AuCl was synthesised by an analogous procedure to **3^{Ni}-Cl** yielding the product quantitatively. ESMS+ : 2732.563 (M + H). Elemental Anal. (calc.): C, 44.26 (43.97); H, 6.14 (6.09); N, 0.53 (0.51); Cl, 1.08 (1.30); P, 1.01 (1.13); Cr, 13.66 (13.22); Co, 2.09 (2.16); Au, 7.39 (7.21).

2^{Ni}-AuBF$_4$ was synthesised by adding $AgBF_4$ (20 mg, 0.101 mmol) to a solution of **5-Cl** (0.275 g, 0.101 mmol) in CH_2Cl_2 (10 mL) and stirring for 30 m. The resulting suspension was filtered over celite and dried by rotary evaporation yielding the product in a quantitative yield as a green powder. Elemental anal. (calc): C, 43.81 (43.16); H, 6.00 (5.98); N, 0.46 (0.50); Cl, 0 (0); Cr, 13.01 (13.08); Ni, 2.01 (2.11); B, 0.36 (0.39); P 0.96 (1.13).

2^{Ni}-AuPF$_6$ was synthesised by an analogous procedure to **2^{Ni}-AuBF$_4$** using $AgPF_6$ (26 mg, 0.101 mmol), yielding the product in a quantitative yield as a green powder. Elemental anal. (calc): C, 42.60 (42.28); H, 5.86 (5.85); N, 0.43 (0.49); Cl, 0 (0); Cr, 12.21 (12.81); Ni, 2.05 (2.07); P, 1.63 (2.18).

2^{Ni}-AuSCN was synthesised by adding KSCN (10.7 mg, 0.110 mmol) to a suspension of **2^{Ni}-AuCl** (0.3 g, 0.110 mmol) in acetone and stirring for 1 h, filtered over celite and dried by rotary evaporation. Crystals suitable for X-ray crystallography were grown from slow evaporation of a CH_2Cl_2/MeCN solution. ESMS+: 2776.531 (M + H). Elemental anal. (calc): C, 43.82 (44.05); H, 5.86 (6.04); N, 0.89 (1.02); Cl, 0 (0); Cr, 13.66 (13.22); Ni, 2.14 (2.13); Au, 7.42 (7.15); S, 1.10 (1.16); P, 1.16 (1.12).

3^{Ni}: was synthesised by dissolving **2^{Ni}** (0.1 g, 0.04 mmol) in CH_2Cl_2 and adding $AuCl(SMe_2)$ (4.7 mg, 0.016 mmol). The resulting solution was stirred for 1 h and filtered over celite. Crystals suitable for single crystal X-ray diffraction were grown from slow evaporation of a CH_2Cl_2/MeCN solution. ESMS+: 5193.260 (M – Cl). Elemental Anal. (calc.): C; 47.92 (46.93); H, 6.79 (6.73); N, 0.56 (0.54); P, 0.93 (1.18); Cr, 13.49 (13.98); Ni, 2.23 (2.24); Au, 3.03 (3.77).

4^{Ni} was synthesised in two step procedure. Trithiocyanuric acid (0.5 g, 2.82 mmol) was dissolved in methanol (25 mL) and sodium methoxide (0.457 g 8.46 mmol) added. The solution was stirred for 1 h, filtered and dried by rotary evaporation yielding the tri-sodium salt. **2^{Ni}-AuCl** (0.2 g, 0.07 mmol) was dissolved in CH_2Cl_2 (10 mL) and trisodium-trithiocyanuric acid (6 mg, 0.024 mmol) in CH_2Cl_2 (2 ml) was added. The solution was stirred at r.t. for 4 h and dried by rotary evaporation yielding the product quantitatively. ESMS+: 8262.439 (M + H), 8285.492 (M + Na) Elemental anal. (calc): C, 44.53 (44.05); H, 6.44 (6.05); N, 1.03 (1.02); Cl, 0 (0); Cr, 13.70 (13.22); Ni, 2.18 (2.13); Au, 7.64 (7.15); S, 1.22 (1.16); P, 1.09 (1.12).

Acknowledgements

This work was supported by North-West Nanoscience Doctoral Training Centre, EPSRC grant EP/G03737X/1. RJW acknowledges a studentship from Doctoral Training Centre NoWNANO. Dr Chris Muryn and Dr Inigo Vitorica-Yzerabal are thanked for their considerable help with crystallography. Dr Ralph Adams is thanked for help with the NMR spectroscopy. Stephen Worrall is thanked for performing the electrochemistry measurements. All data supporting this study are provided as supplementary information accompanying this paper.

Notes and references

1. V. Marcos, A. J. Stephens, J. Jaramillo-Garcia, A. L. Nussbaumer, S. L. Woltering, A. Valero, F. J. Lemonnier, I. J. Vitorica-Yrezabal and D. A. Leigh, *Science*, 2016, **352**, 1555-1559.

2. C. G. P. Taylor, J. R. Piper and M. D. Ward, *Chem. Commun.*, 2016, **52**, 6225-6228.

This journal is © The Royal Society of Chemistry 20xx

3. Z. Liu, X. Sun, N. Nakayama-Ratchford and H. Dai, *ACS Nano*, 2007, **1**, 50-56.
4. P. Cordier, F. Tournilhac, C. Soulié-Ziakovic and L. Leibler, *Nature*, 2008, **451**, 977-980.
5. A. R. Hirst, B. Escuder, J. F. Miravet and D. K. Smith, *Angew. Chem. Int. Ed.*, 2008, **47**, 8002-8018.
6. M.-C. Dul, E. Pardo, R. Lescouëzec, Y. Journaux, J. Ferrando-Soria, R. Ruiz-García, J. Cano, M. Julve, F. Lloret, D. Cangussu, C. L. M. Pereira, H. O. Stumpf, J. Pasán and C. Ruiz-Pérez, *Coordin. Chem. Rev.*, 2010, **254**, 2281-2296.
7. M. Urdampilleta, S. Klyatskaya, J. P. Cleuziou, M. Ruben and W. Wernsdorfer, *Nat. Mater.*, 2011, **10**, 502-506.
8. M. Ruben, E. Breuning, J. M. Lehn, V. Ksenofontov, F. Renz, P. Gütlich and G. B. M. Vaughan, *Chem-Eur. J.*, 2003, **9**, 4422-4429.
9. M. Gonidec, R. Biagi, V. Corradini, F. Moro, V. D. Renzi, U. D. Pennino, D. Summa, L. Muccioli, C. Zannoni, D. B. Amabilino and J. Veciana, *J. Am. Chem. Soc.*, 2011, **133**, 6603-6612.
10. Y. Ohno, D. K. Young, B. Beschoten, F. Matsukura, H. Ohno and D. D. Awschalom, *Nature*, 1999, **402**, 790-792.
11. I. Žutić, J. Fabian and S. D. Sarma, *Rev. Mod. Phys.*, 2004, **76**, 323.
12. L. Bogani, in *Molecular Nanomagnets and Related Phenomena*, ed. S. Gao, Springer Berlin Heidelberg, Berlin, Heidelberg, 2015, pp. 331-381.
13. M. Ganzhorn, S. Klyatskaya, M. Ruben and W. Wernsdorfer, *ACS Nano*, 2013, **7**, 6225-6236.
14. S. Thiele, F. Balestro, R. Ballou, S. Klyatskaya, M. Ruben and W. Wernsdorfer, *Science*, 2014, **344**, 1135-1138.
15. R. Vincent, S. Klyatskaya, M. Ruben, W. Wernsdorfer and F. Balestro, *Nature*, 2012, **488**, 357-360.
16. L. F. Jones, M. E. Cochrane, B. D. Koivisto, D. A. Leigh, S. P. Perlepes, W. Wernsdorfer and E. K. Brechin, *Inorg. Chim. Acta*, 2008, **361**, 3420-3426.
17. A. Candini, D. Klar, S. Marocchi, V. Corradini, R. Biagi, D. V. De Renzi, U. del Pennino, F. Troiani, V. Bellini, S. Klyatskaya, M. Ruben, K. Kummer, N. B. Brookes, H. Huang, A. Soncini, H. Wende and M. Affronte, *Sci. Rep.*, 2016, **6**, 21740.
18. C. R. Ganivet, B. Ballesteros, G. de la Torre, J. M. Clemente-Juan, E. Coronado and T. Torres, *Chem-Eur. J.*, 2013, **19**, 1457-1465.
19. C. J. Wedge, G. A. Timco, E. T. Spielberg, R. E. George, F. Tuna, S. Rigby, E. J. L. McInnes, R. E. P. Winpenny, S. J. Blundell and A. Ardavan, *Phys. Rev. Lett.*, 2012, **108**, 107204.
20. A. Fernandez, J. Ferrando-Soria, E. M. Pineda, F. Tuna, I. J. Vitorica-Yrezabal, C. Knappke, J. Ujma, C. A. Muryn, G. A. Timco, P. E. Barran, A. Ardavan and R. E. P. Winpenny, *Nat. Commun.*, 2016, **7**, 10240.
21. G. A. Timco, S. Carretta, F. Troiani, F. Tuna, R. J. Pritchard, C. A. Muryn, E. J. L. McInnes, A. Ghirri, A. Candini, P. Santini, G. Amoretti, M. Affronte and R. E. P. Winpenny, *Nat. Nanotechnol.*, 2009, **4**, 173-178.
22. G. F. S. Whitehead, B. Cross, L. Carthy, V. A. Milway, H. Rath, A. Fernandez, S. L. Heath, C. A. Muryn, R. G. Pritchard, S. J. Teat, G. A. Timco and R. E. P. Winpenny, *Chem. Commun.*, 2013, **49**, 7195-7197.
23. A. Fernandez, E. M. Pineda, C. A. Muryn, S. Sproules, F. Moro, G. A. Timco, E. J. McInnes and R. E. P. Winpenny, *Angew. Chem. Int. Ed.*, 2015, **54**, 10858-10861.
24. E. J. McInnes, G. A. Timco, G. F. Whitehead and R. E. P. Winpenny, *Angew. Chem. Int. Ed.*, 2015, **54**, 2-28.
25. G. F. S. Whitehead, F. Moro, G. A. Timco, W. Wernsdorfer, S. J. Teat and R. E. P. Winpenny, *Angew. Chem. Int. Ed.*, 2013, **52**, 9932-9935.
26. F. K. Larsen, E. J. L. McInnes, H. Mkami, J. Overgaard, S. Piligkos, G. Rajaraman, E. Rentschler, A. A. Smith, G. M. Smith, V. Boote, M. Jennings, G. A. Timco and R. E. P. Winpenny, *Angew. Chem. Int. Ed.*, 2003, **42**, 101-105.
27. S. F. Lincoln, *Helv. Chim. Acta*, 2005, **88**, 523-545.
28. C. E. Briant, B. R. C. Theobald, J. W. White, L. K. Bell, D. M. P. Mingos and A. J. Welch, *J. Chem. Soc., Chem. Commun.*, 1981, 201-202.
29. R. C. B. Copley and D. M. P. Mingos, *J. Chem. Soc. Dalton*, 1996, 479-489.
30. K. P. Hall, B. R. C. Theoblad, D. I. Gilmour, D. M. P. Mingos and A. J. Welch, *J. Chem. Soc., Chem. Commun.*, 1982, 528-530.
31. D. M. P. Mingos, *Gold Bull.*, 1984, **17**, 5-12.
32. D. M. P. Mingos, *Dalton T.*, 2015, **44**, 6680-6695.
33. A. O. Borissova, A. A. Korlyukov, M. Y. Antipin and K. A. Lyssenko, *J. Phys. Chem. A*, 2008, **112**, 11519-11522.
34. F. Mohr, M. C. Jennings and R. J. Puddephatt, *Angew. Chem. Int. Ed.*, 2004, **43**, 969-971.
35. H. Schmidbaur, T. Pollok, R. Herr, F. E. Wagner, R. Bau, J. Riede and G. Müller, *Organometallics*, 1986, **5**, 566-574.
36. D. Schneider, S. Nogai, A. Schier and H. Schmidbaur, *Inorg. Chim. Acta*, 2003, **352**, 179-187.
37. W. J. Hunks, M. C. Jennings and R. J. Puddephatt, *Inorg. Chem.*, 1999, **38**, 5930-5931.
38. M. Hoshino, H. Uekusa, S. Ishii, T. Otsuka, Y. Kaizu, O. Yoshiki and K. Toriumi, *Inorg. Chem.*, 2010, **49**, 7257-7265.
39. R. Tan, F. S. N. Chiu, A. Hadzovic and D. Song, *Organometallics*, 2012, **31**, 2184-2192.
40. Y. Li, Y. Kang, J.-S. Lu, I. Wyman, S.-B. Ko and S. Wang, *Organometallics*, 2014, **33**, 964-973.
41. R. J. Gillespie and R. S. Nyholm, *Q. Rev. Chem. Soc.*, 1957, **11**, 339-380.
42. O. Kühl, *Phosphorus-31 NMR spectroscopy: A Concise Introduction for the Synthetic Organic and Organometallic chemist*, Springer, Berlin Heidelberg, 2008.
43. B.-C. Tzeng, C.-M. Che and S.-M. Peng, *Chem. Commun.*, 1997, 1771-1772.
44. K. Nunokawa, T. Sunahara, S. Onaka, K. Okazaki, H. Imai, K. Inoue and T. Ozeki, *Chem. Lett.*, 2004, **33**, 1300-1301.
45. C. A. Tolman, *Chem. Rev.*, 1977, **77**, 313-348.

 This journal is © The Royal Society of Chemistry 20xx

46.T. E. Müller and D. M. P. Mingos, *Transit. Metal Chem.*, 1995, **20**, 533-539.
47.H. Clavier and S. P. Nolan, *Chem. Commun.*, 2010, **46**, 841-861.
48.A. C. Hillier, W. J. Sommer, B. S. Yong, J. L. Petersen, L. Cavallo and S. P. Nolan, *Organometallics*, 2003, **22**, 4322-4326.
49.A. Poater, B. Cosenza, A. Correa, S. Giudice, F. Ragone, V. Scarano and L. Cavallo, *Eur. J. Inorg. Chem.*, 2009, **2009**, 1759-1766.
50.L. Falivene, R. Credendino, A. Poater, A. Petta, L. Serra, R. Oliva, V. Scarano and L. Cavallo, *Organometallics*, 2016, **35**, 2286-2293.
51.C. E. Sañudo, T. B. Faust, C. A. Muryn, R. G. Pritchard, G. A. Timco and R. E. P. Winpenny, *Inorg. Chem.*, 2009, **48**, 9811-9818.
52.J. D. Satterlee, *Concepts in Magnetic Resonance*, 1990, **2**, 69-79.
53.J. Tong, S. Liu, S. Zhang and S. Z. Li, *Spectrochim. Acta A.*, 2007, **67**, 837-846.
54.C. Nieto-Oberhuber, S. López and A. M. Echavarren, *J. Am. Chem. Soc.*, 2005, **127**, 6178-6179.
55.K. Karaghiosoff, in *eMagRes*, John Wiley & Sons, Ltd, 2007.
56.V. Corradini, F. Moro, R. Biagi, D. V. Renzi, U. del Pennino, V. Bellini, S. Carretta, P. Santini, V. A. Milway, G. Timco, R. E. P. Winpenny and M. Affronte, *Phys. Rev. B*, 2009, **79**.
57.L. Patiny and A. Borel, *J. Chem. Inf. Model.*, 2013, **53**, 1223-1228.
58.H. Nowell, S. A. Barnett, K. E. Christensen, S. J. Teat and D. R. Allan, *J. Synchrotron Rad.*, 2012, **19**, 435-441.
59.G. M. Sheldrick, *Acta Crystallogr. A*, 2007, **64**, 112-122.
60.O. V. Dolomanov, L. J. Bourhis, R. J. Gildea, J. A. K. Howard and H. Puschmann, *J. Appl. Crystallogr.*, 2009, **42**, 339-341.
61.G. A. Price, A. K. Brisdon, K. R. Flower, R. G. Pritchard and P. Quayle, *Tetrahedron Lett.*, 2014, **55**, 151-154.
62.R. Galassi, C. Oumarou, A. Burini, A. Dolmella, D. Micozzi, S. Vincenzetti and S. Pucciarelli, *Dalton T.*, 2014, **44**, 3043-3056.

This journal is © The Royal Society of Chemistry 20xx

The Synthesis, Characterisation and Coordination Chemistry of a Highly Sterically Hindered Phosphine Ligand

Supporting Information

Robert J. Woolfson, Grigore A. Timco, David Collison and Richard E.P. Winpenny*

School of Chemistry, The University of Manchester, Oxford Road, Manchester, M13 9PL

Contents

Contents 1
1. Experimental Section 2
1.1. Mass Spectrometry 2
2.1.1 $[NH_2{}^nPr_2][Cr_7NiF_8(O_2C^tBu)_{15}\{O_2C(C_6H_5)P(C_6H_5)_2\}]$ **2^{Ni}** 2
2.1.2 $[NH_2{}^nPr_2][Cr_7NiF_8(O_2C^tBu)_{15}\{O_2C(C_6H_5)P(C_6H_5)_2\}AuCl]$ **2^{Ni}-AuCl** 3
2.1.3 $[NH_2{}^nPr_2][Cr_7NiF_8(O_2C^tBu)_{15}\{O_2C(C_6H_5)P(C_6H_5)_2\}AuPF_6]$ **2^{Ni}-$AuPF_6$** 3
2.1.4 $[NH_2{}^nPr_2][Cr_7NiF_8(O_2C^tBu)_{15}\{O_2C(C_6H_5)P(C_6H_5)_2\}AuBF_4]$ **2^{Ni}-$AuBF_4$** 3
2.1.5 $[NH_2{}^nPr_2][Cr_7NiF_8(O_2C^tBu)_{15}\{O_2C(C_6H_5)P(C_6H_5)_2\}AuSCN]$ **2^{Ni}-AuSCN** 4
2.1.6 $\{[NH_2{}^nPr_2][Cr_7NiF_8(O_2C^tBu)_{15}\{O_2C(C_7H_7)P(C_6H_5)_2\}]\}AuCl$ **3^{Ni}** 5
2.1.7 $\{[NH_2{}^nPr_2][Cr_7NiF_8(O_2C^tBu)_{15}\{O_2C(C_7H_7)P(C_6H_5)_2\}]Au\}_3(C_3S_3N_3)$ **4^{Ni}** 6
2.1.8 $[NH_2{}^nPr_2][Cr_7CoF_8(O_2C^tBu)_{15}\{O_2C(C_6H_5)P(C_6H_5)_2\}]$ **2^{Co}** 7
2.1.9 $[NH_2{}^nPr_2][Cr_7CoF_8(O_2C^tBu)_{15}\{O_2C(C_6H_5)P(C_6H_5)_2\}]AuCl$ **2^{Co}-AuCl** 8
2.1.10 Ph_3P-AuCl 9
2.1.11 $(O_2C\text{-}C_6H_4)P(C_6H_5)_2AuCl$ 10
1.2. NMR Spectroscopy 11
2. Crystallographic Information 13
2.1. Crystallography tables 13
2.2. Disordered binding conformations in **2^{Ni}-AuCl** 14
2.3. Torsion angle for **3^{Ni}** 15
2.4. Crystal Structure of **4^{Ni}** 16
3. Electrochemistry of trimer **4^{Ni}** 18
References 19

1. Experimental Section

1.1. Mass Spectrometry

Due to the size and complexity of the molecules discussed below, the mass spectra often show a large number of peaks corresponding to a range of adducts and degradation products. For simplicity, only the major peaks of interest have been assigned and simulated below. Where an intense peak corresponds to an impurity or an unknown adduct this is discussed.

2.1.1 $[NH_2{}^iPr_2][Cr_7NiF_8(O_2C^tBu)_{15}(O_2C(C_6H_5)P(C_6H_5)_2)]$ 2^{Ni}

Shown below (Figure S1) is the FTMS+ spectrum for 2^{Ni}. The peak centred on 2498.619 corresponds to the M+H peak whilst the peak centred on 2521.611 corresponds to the M+Na peak. Both peaks show a good fit to the simulations.

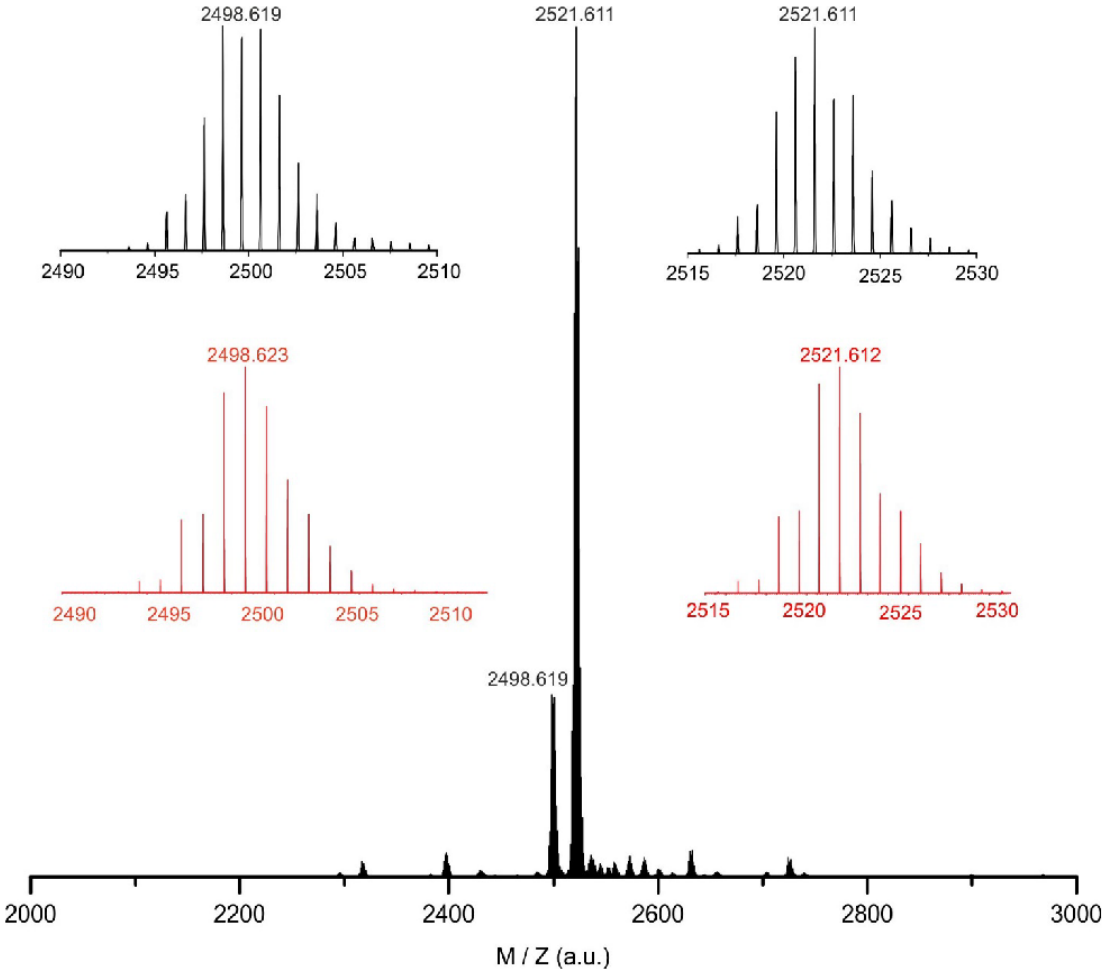

Figure S1: Mass Spectrum for 2^{Ni}. Experimental spectrum (black). Inset (left) – Enlargement of M+H peak with simulation (red). Inset (right) – Enlargement of M+Na Peak with simulation.

2.1.2 $[NH_2{}^nPr_2][Cr_7NiF_8(O_2C{}^tBu)_{15}(O_2C(C_6H_5)P(C_6H_5)_2)AuCl]$ 2^{Ni}-AuCl

Shown below (Figure S2) is the FTMS+ for **2^{Ni}-AuCl**. The peak centred at 2732.560 is the M+H peak and shows a good fit to the simulation.

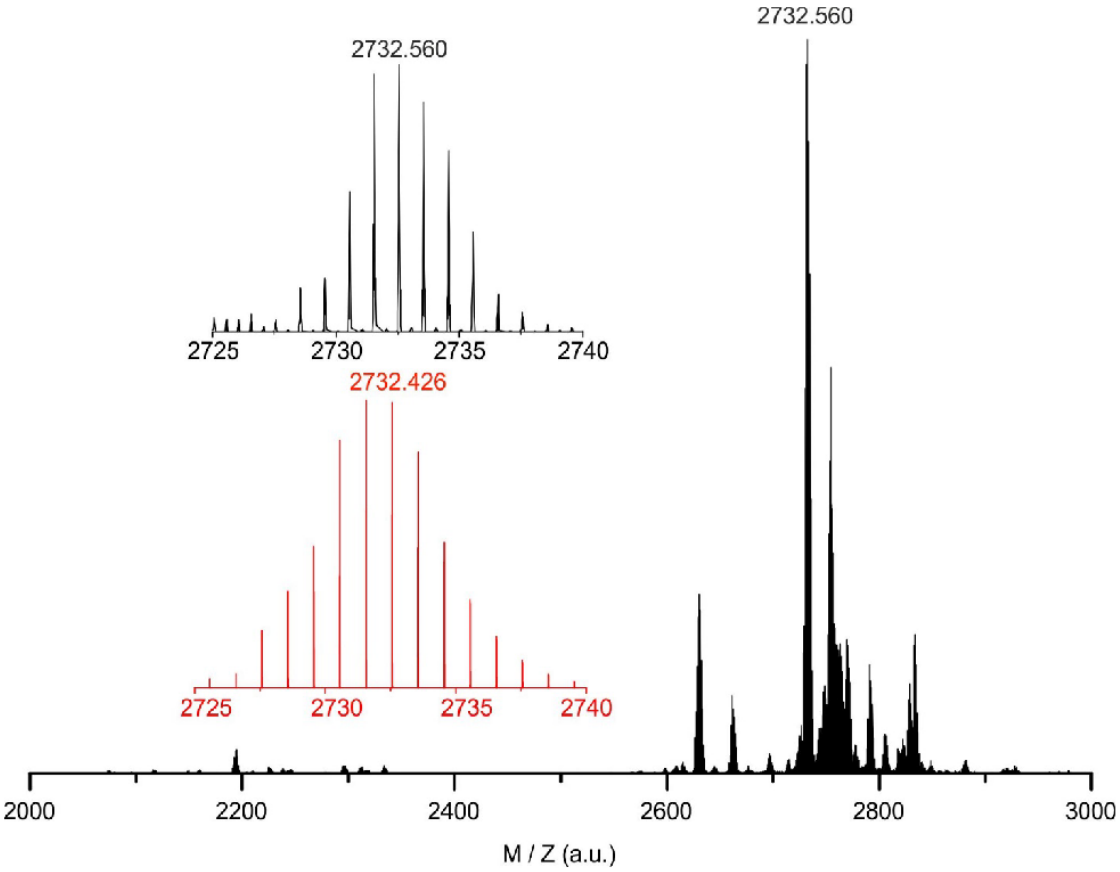

Figure S2: Mass Spectrum for **2^{Ni}-AuCl**. Experimental spectrum (black). Inset - Enlargement of M+H peak with simulation (red).

2.1.3 $[NH_2{}^nPr_2][Cr_7NiF_8(O_2C{}^tBu)_{15}(O_2C(C_6H_5)P(C_6H_5)_2)AuPF_6]$ 2^{Ni}-$AuPF_6$

No satisfactory mass spectra could be obtained for this compound

2.1.4 $[NH_2{}^nPr_2][Cr_7NiF_8(O_2C{}^tBu)_{15}(O_2C(C_6H_5)P(C_6H_5)_2)AuBF_4]$ 2^{Ni}-$AuBF_4$

No satisfactory mass spectra could be obtained for this compound

2.1.5 $[NH_2{}^nPr_2][Cr_7NiF_8(O_2C{}^tBu)_{15}(O_2C(C_6H_5)P(C_6H_5)_2)AuSCN]$ 2^{Ni}-AuSCN

Shown below (Figure S3) is the FTMS+ spectrum for **2^{Ni}-AuSCN**. The peak centred at 2776.531 is the M+H peak and shows a good fit to the simulation.

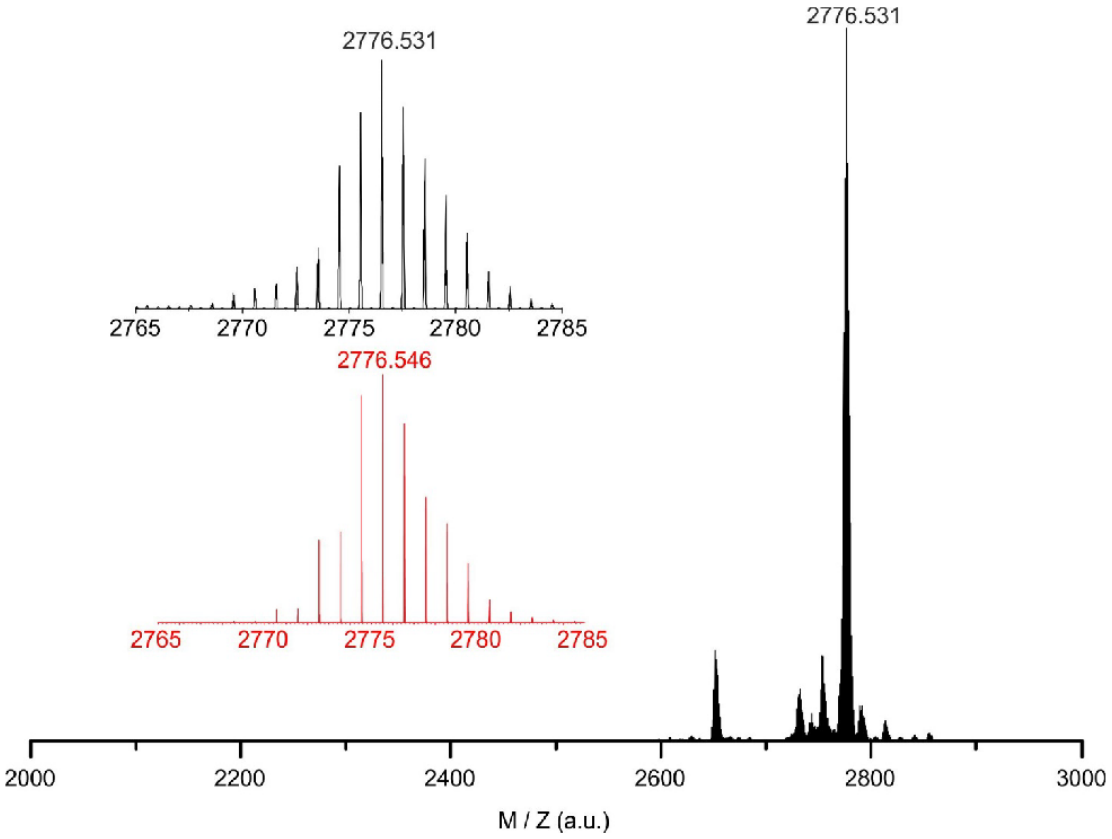

Figure S3: Mass Spectrum for **2^{Ni}-AuSCN**. Experimental spectrum (black) and simulated spectrum (red). Inset - Enlargement of M+H peak with simulation.

2.1.6 $\{[NH_2{}^nPr_2][Cr_7NiF_8(O_2C^tBu)_{15}(O_2C(C_7H_7)P(C_6H_5)_2)]\}AuCl$ $\mathbf{3^{Ni}}$

Shown below (Figure S4) is the FTMS+ spectrum for gold bridged compound $\mathbf{3^{Ni}}$. The peak centred at 5193.260 can be assigned to the molecular ion with loss of the chloride (M – Cl) and fits the simulation well. The peak centred at 2529.632 cannot be assigned to any expected by-product but does not seem to be an impurity as the elemental analysis matches that expected from the pure compound.

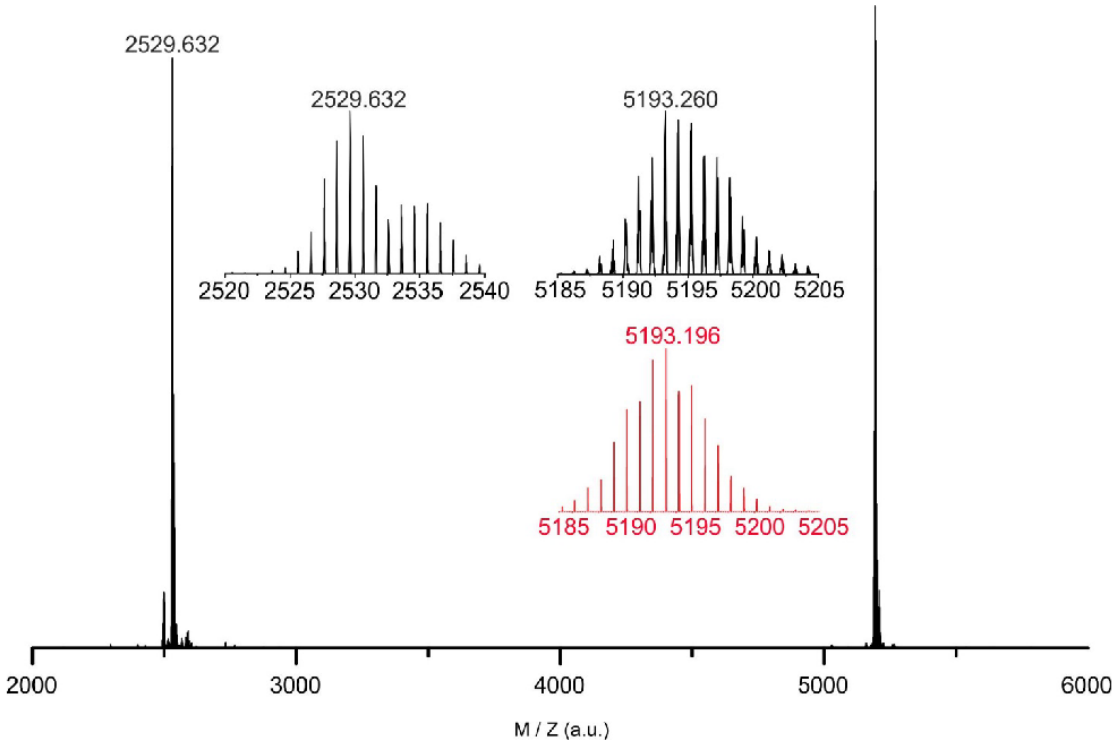

Figure S4: Mass spectrum for compound $\mathbf{3^{Ni}}$. Experimental spectrum (black) and simulated spectrum (red). Inset (left) – Expansion of unknown peak. Inset (right) – Expansion and simulation of M – Cl peak.

2.1.7 $\{[NH_2{}^nPr_2][Cr_7NiF_8(O_2C^tBu)_{15}(O_2C(C_7H_7)P(C_6H_5)_2)]Au\}_3(C_3S_3N_3)$ 4^{Ni}

Shown below (Figure S5) is the FTMS+ spectrum for 4^{Ni}. The mass spectrum was collected with a Thermo Fisher Scientific "Exactive Plus EMR Orbitrap" mass spectrometer. The mass resolution (~140000) was optimised to achieve the resolution of the peaks at the region of interest. A Thermo Fisher "UltiMate 3000" liquid chromatograph was used for sample delivery (the chromatography column was taken out). ~1 µl of the sample was injected into the HPLC grade methanol mobile phase with 0.1 ml/min flow rate. The molecules were ionised in the electrospray ion source operated in positive modes (~3.5 kV was applied to the capillary). The produced ions were accumulated for ~1 s and detected using an electrostatic trap. The electrospray probe and a mass spectrometer transfer capillary both were heated up to 150 C to aid in ionisation. The spectrometer is equipped with a nitrogen collision dissociation cell, however to reduce fragmentation no acceleration voltage was applied during experiment.

The peaks centred at 8262 and 8285 correspond to the M + H and M + Na peak, both show a good fit to the simulations. The peak centred at 4153 corresponds to the doubly charged adduct of M + H peak. The peak centred at 2776 corresponds to the triply charged adduct of the M + H peak. The peak centred at 5589 corresponds to loss of one moiety of $\{Cr_7Ni\}$, whilst the peak centred at 2844 corresponds to the loss of two of the $\{Cr_7Ni\}$ moieties, suggesting the sample does not remain entirely intact in solution. The peak at 5193 cannot be assigned.

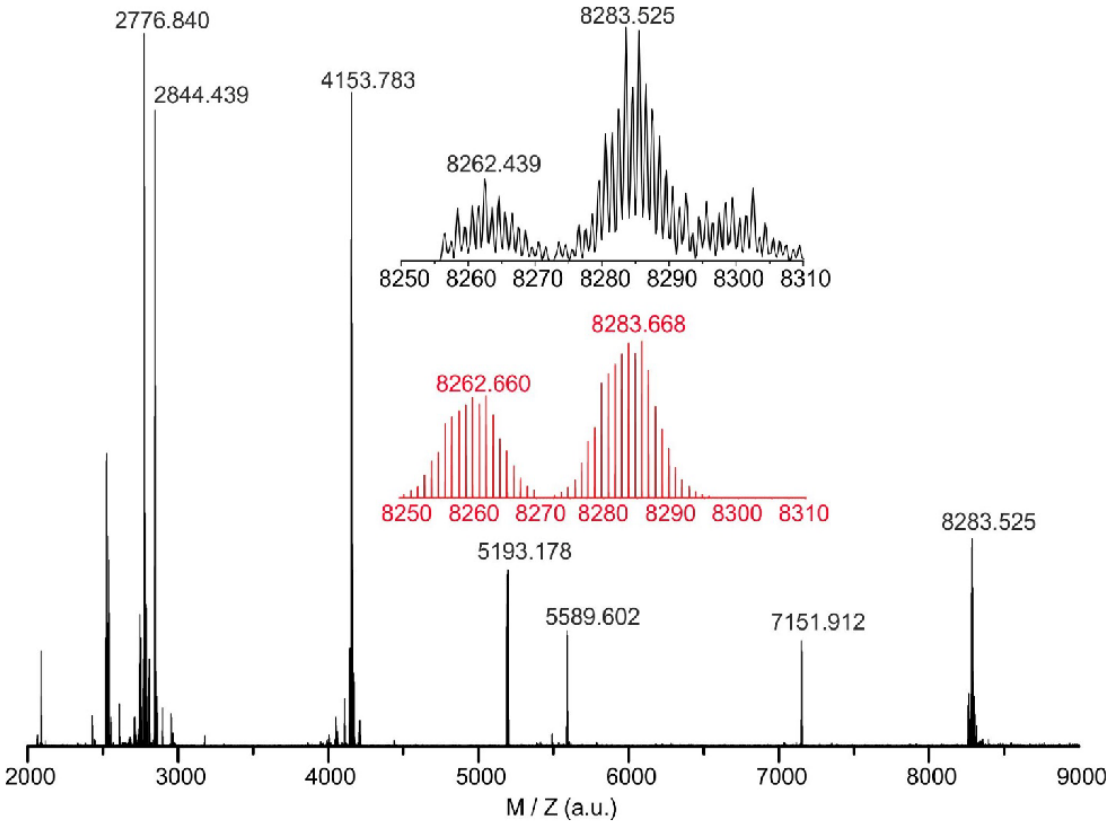

Figure S5: Mass spectrum for compound 4^{Ni}. Experimental spectrum (black) and simulated spectrum (red). Inset – Expansion and simulation of M + H peak (8262) and M + Na peak (8283) with simulations shown below.

2.1.8 $[NH_2{}^nPr_2][Cr_7CoF_8(O_2C^tBu)_{15}(O_2C(C_6H_5)P(C_6H_5)_2)]$ 2^{Co}

Shown below (Figure S6) is the FTMS+ spectrum for **2^{Co}**. The peak centred at 2499 corresponds to the M + H peak and the peak centred at 2522 corresponds to the M + Na peak, both show a good fit to the simulations.

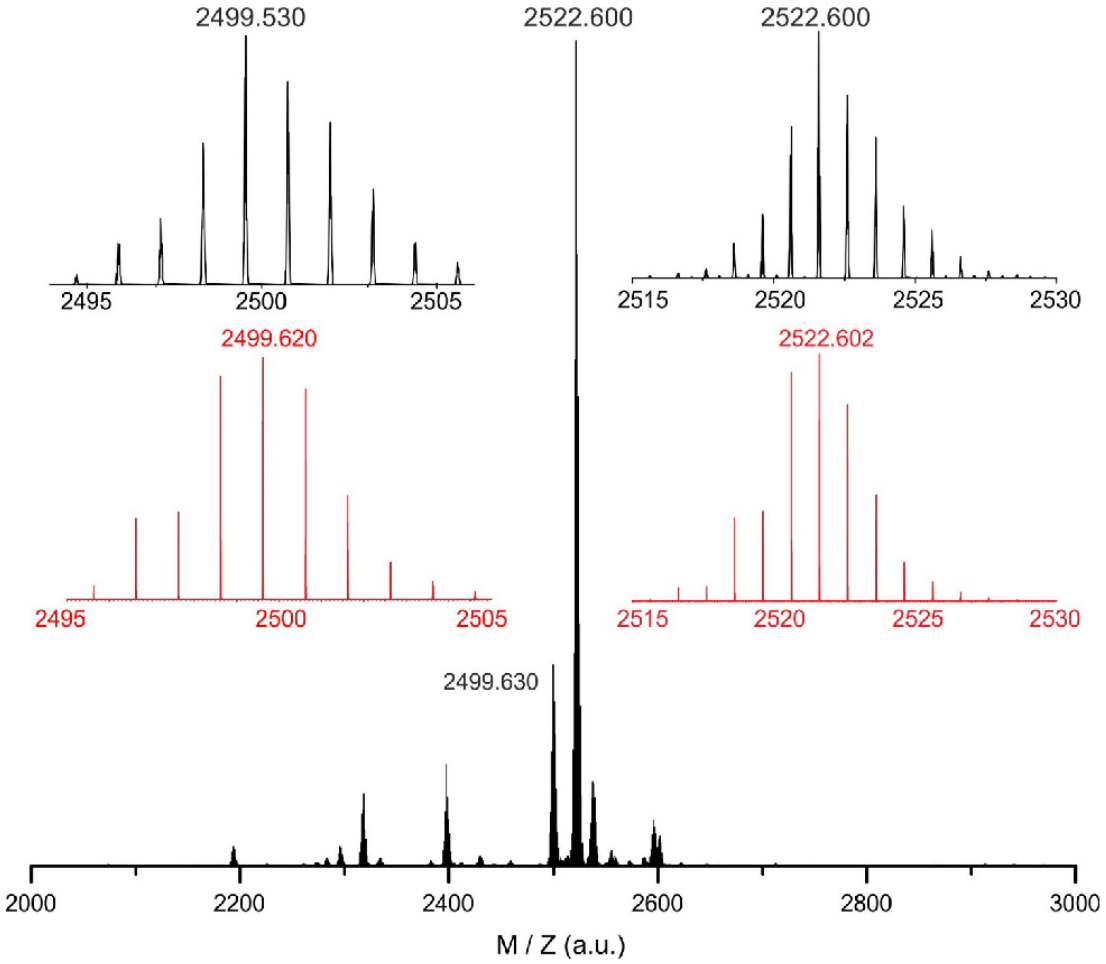

Figure S6: Mass spectrum of compound **2^{Co}**. Experimental spectrum (black) and simulated spectrum (red). Inset (left) – Expansion and simulation of M + H. Inset (right) – Expansion and simulation of M + Na peak.

2.1.9 $[NH_2{}^nPr_2][Cr_7CoF_8(O_2C{}^tBu)_{15}(O_2C(C_6H_5)P(C_6H_5)_2)]AuCl$ 2^{Co}-AuCl

Shown below (Figure S7) is the FTMS+ spectrum for **2^{Co}-AuCl.** The peak centred at 2730 corresponds to the M + H peak and shows a good fit to the simulation.

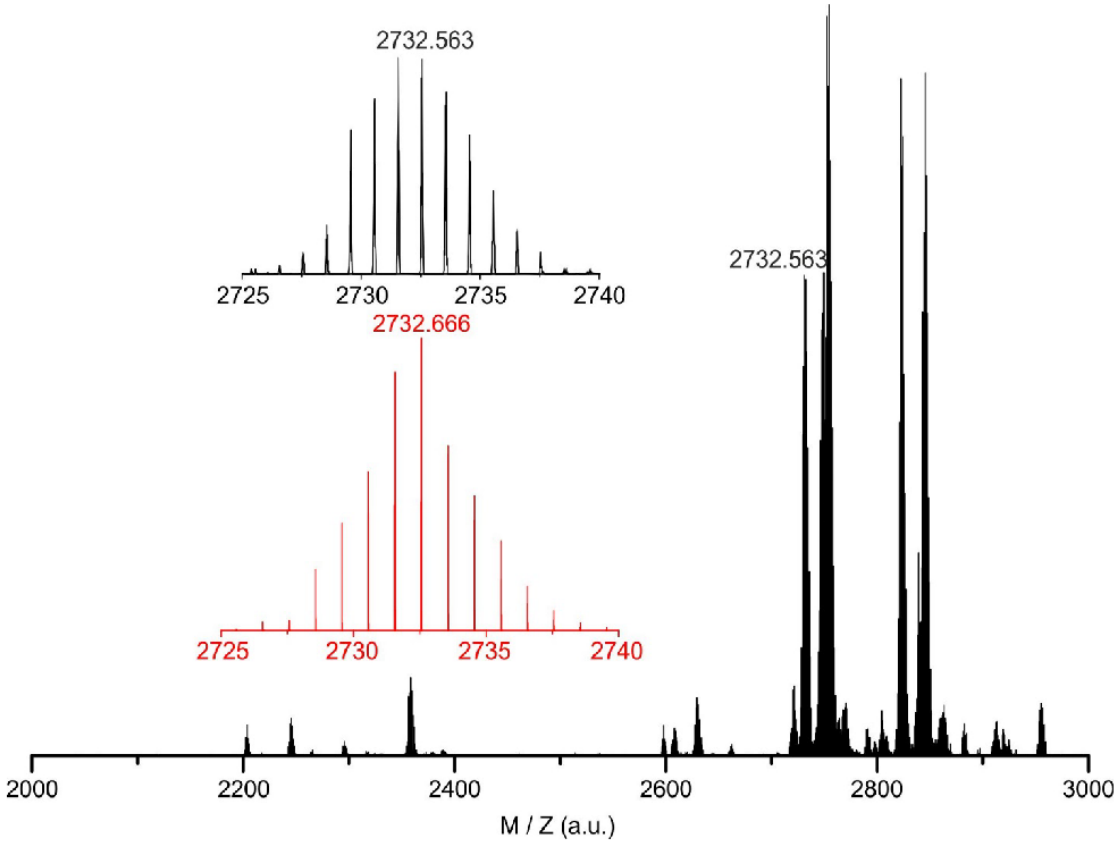

Figure S7: Mass spectrum of compound **2^{Co}-AuCl**. Experimental spectrum (black) and simulated spectrum (red). Inset – Expansion and simulation of M + H.

2.1.10 Ph_3P-AuCl

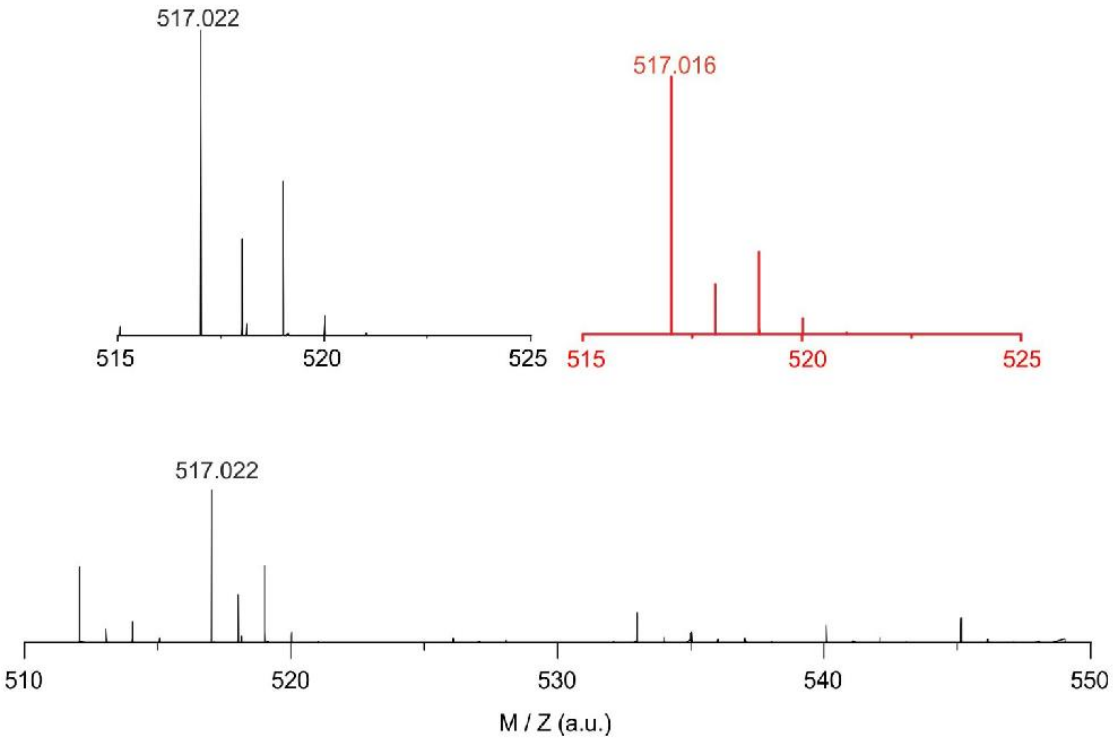

Figure S8: Mass Spectrum of compound Ph_3P-AuCl. Experimental spectrum (black) and simulated spectrum (red). Inset – expansion and simulation of the M + Na peak.

2.1.11 $(O_2C\text{-}C_6H_4)P(C_6H_5)_2AuCl$

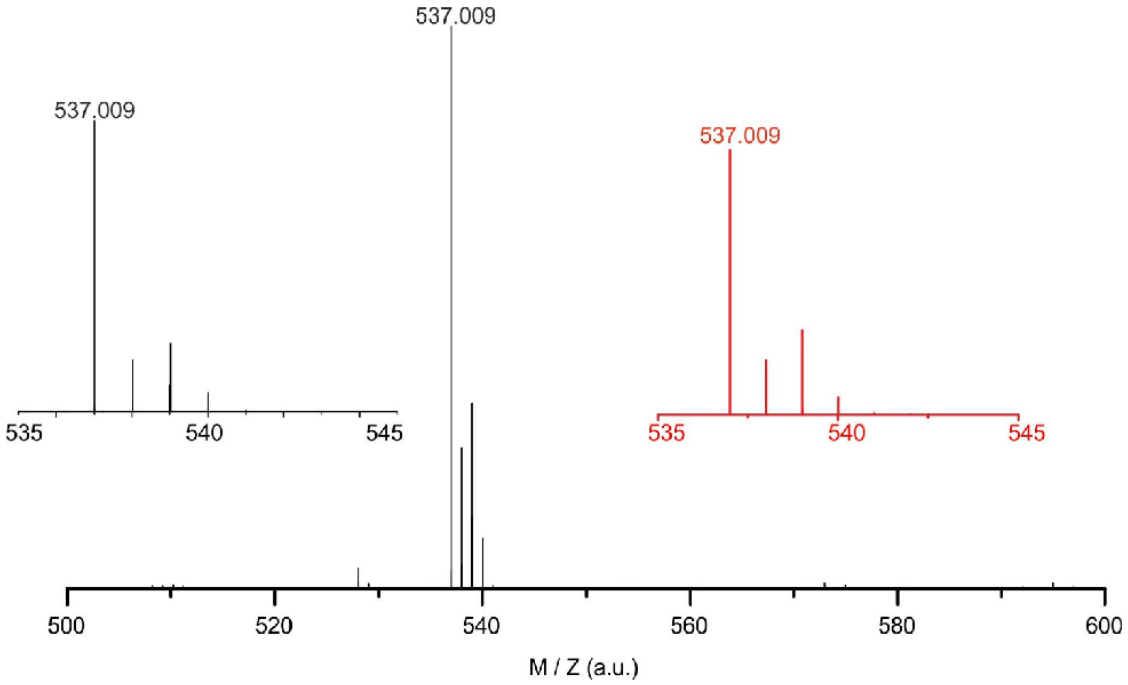

Figure S9: ESMS- spectrum for compound $HO_2C\text{-}C_6H_4\text{-}PPh_2\text{-}AuCl$. Experimental (black) and simulated (red). Inset – experimental and simulated spectra for the M – H adduct.

1.2. NMR Spectroscopy

All NMR spectra were recorded on a 500 MHz Bruker Advance II+ at room temperature (unless otherwise specified). Datasets were processed with Topsin 3.2. A window function was applied using the peak with in Hz at the FWHM followed by Fourier transform, phasing and polynomial baseline correction.

1.2.1. Variable Temperature ^{31}P NMR Spectra for 2^{Co}

Shown below (Figure S10) are ^{31}P NMR spectra for **2^{Co}** recorded at 238 K and 298 K. Across a 60 K temperature range a negligible change in chemical shift was observed, confirming that the ^{31}P NMR can be treated as diamagnetic.

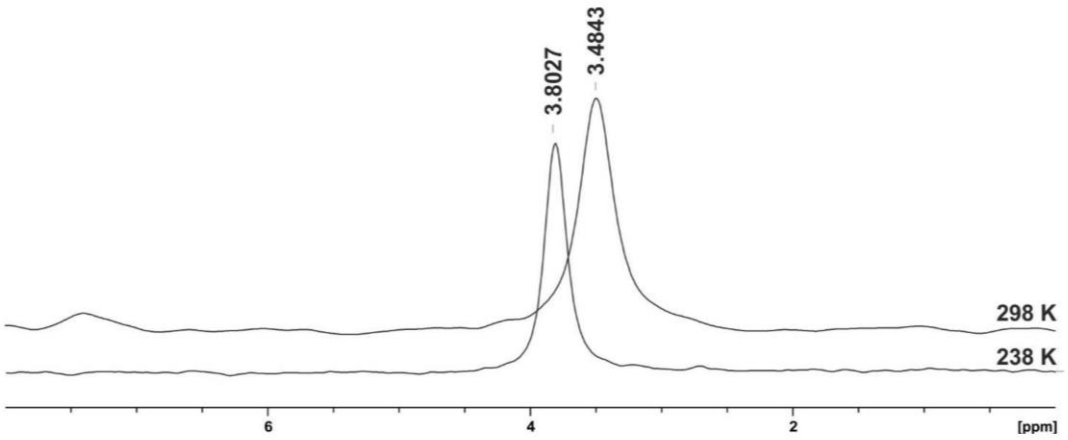

Figure S10: ^{31}P NMR spectra of **2^{Co}** recorded at 298 K (top) and 238 K (bottom) in $CDCl_3$.

1.2.2. ^{31}P NMR Spectra for phosphine-gold coordinated compounds

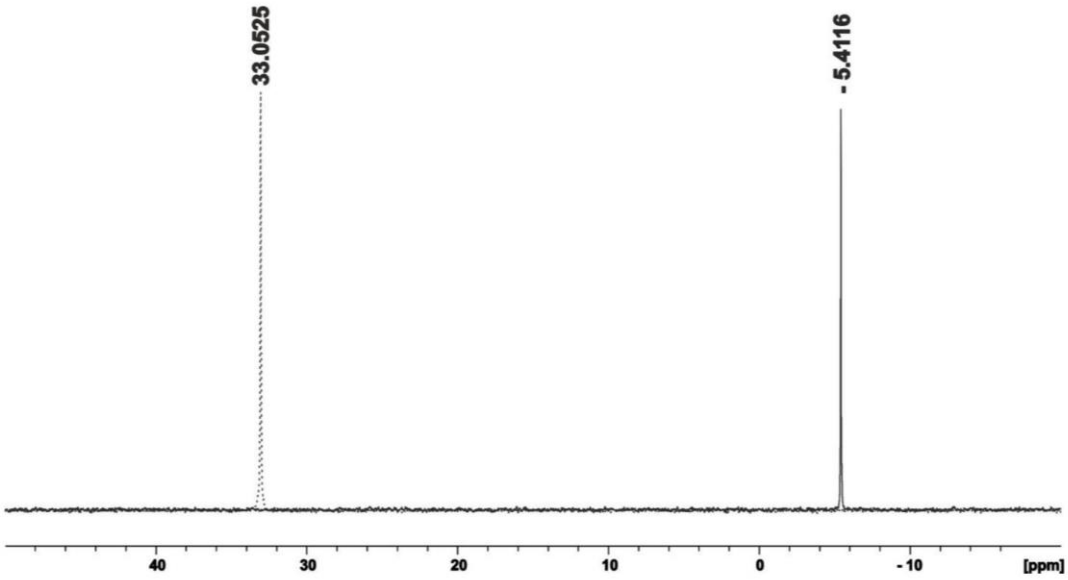

Figure S11: ^{31}P NMR spectra of Ph_3P (solid line) and Ph_3P-AuCl (dashed line) at 298 K in $CDCl_3$

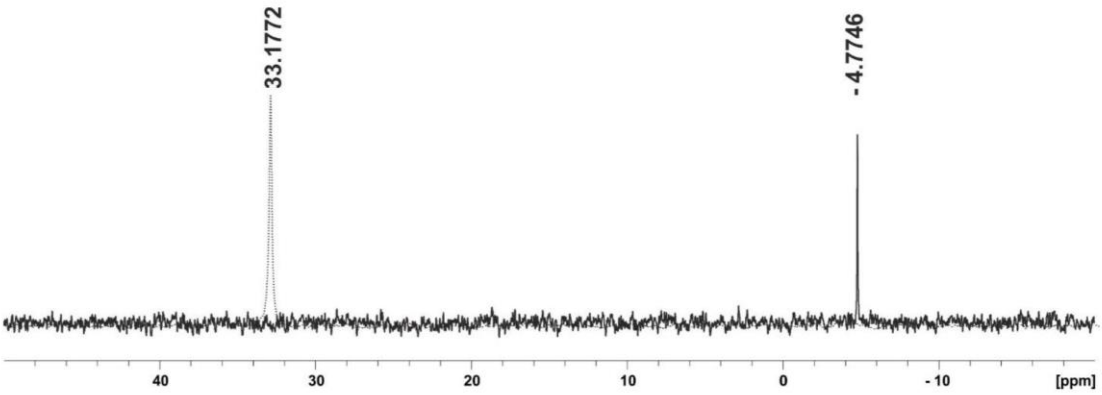

Figure S12: ^{31}P NMR spectra of DPPB (solid line) and HO_2C-C_6H_4-PPh_2-AuCl (dashed line) at 298 K in $CDCl_3$

Shown below are the ^{31}P NMR spectra for **2^{Co}** and **2^{Co}-AuCl**. The peak for 15, centred at 19.1 ppm, is considerably broadened due to quadrupolar effects from the Au atom.

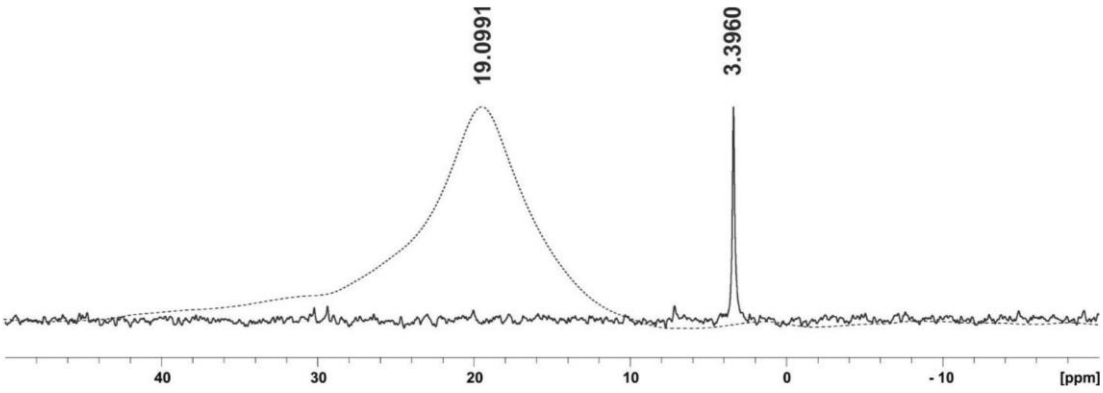

Figure S13: ^{31}P NMR spectra of **2^{Co}** (solid line) and **3^{Co}-Cl** (dashed line) recorded at 298 K in $CDCl_3$

2. Crystallographic Information

X-ray data were collected on a Agilent Supernova (Mo), a Bruker Prospector (Cu) or the I19 beamline at the Diamond Light Source (synchrotron).[1] Datasets were processed and reduced using the CrysAlisPro suite of programs. Absorption correction was performed using empirical methods based upon symmetry equivalent reflections combined with measurements at different azimuthal angles.[2, 3] All crystal structures were solved and refined against all F^2 values using the SHELX suite of programs in Olex2.[4-6] Non-hydrogen atoms were refined anisotropically where possible, whereas hydrogen atoms were placed in calculated positions using idealised geometry (riding model) and assigned fixed isotropic displacement parameters. In all of the structures determined, pivalate ligands were disordered with carbon atoms modelled using SADI and SAME distance restrain commands. The templating ammonium cation was modelled using DFIX and SADI commands. The aryl rings of the triphenylphosphine were modelled using AFIX and FLAT. The atomic displacement parameters of the pivalate ligands, the central ammonium cation and the solvent were restrained using RIGU, DELU and where necessary SIMU. The SQUEEZE algorithm was applied to all structures to account for disordered solvent in the intermolecular voids.

2.1. Crystallography tables

Table S1: Structural metrics for X-ray crystal structures

Compound	2^{Ni}	2^{Ni}-AuCl	2^{Ni}-AuSCN	3^{Ni}	4^{Ni}
Empirical formula	$C_{100}H_{165}Cr_7F_8NNiO_{32}P$	$C_{100}H_{165}AuClCr_7F_8NNiO_{32}P$	$C_{102}H_{167}AuCl_2Cr_7F_8N_2NiO_{32}PS$	$C_{200}H_{330}AuClCr_{14}F_{16}N_2Ni_2O_{64}P_2$	$C_{303}H_{494}Au_3Cr_{24}F_{24}N_6O_{96}P_3S_3$
M_w	2499.00	2731.42	2838.97	5230.42	8241.00
Crystal System	monoclinic	monoclinic	monoclinic	monoclinic	Triclinic
Space Group	C2/c	$P2_1/c$	I2/a	C2/c	P-1
a Å	47.177(3)	25.2554(5)	50.211(3)	47.273(10)	16.831(3)
b Å	16.5209(9)	16.5156(4)	16.5239(11)	16.388(3)	29.996(6)
c Å	33.9089(15)	32.7311(7)	33.774(3)	33.769(7)	45.326(9)
α °	90	90	90	90	76.93(3)
β °	92.231(5)	90.9080(19)	96.432(6)	93.46(3)	88.56(3)
γ °	90	90	90	90	86.70(3)
V Å^3	26409(3)	13650.7(5)	27845(3)	26113(9)	22251
Z	8	4	8	4	2
ρ_{calc} g cm^{-3}	1.257	1.329	1.354	1.330	1.230
λ Å	0.71	1.54	1.54	1.54	0.6889
T K	150.0	100.0	100.0	100.0	100.0
Goof on F^2	1.035	1.031	0.895	0.985	1.089
R^2 [I>=2σ (I)]	0.1195	0.1123	0.1237	0.1309	0.1414
wR^2 [all data]	0.3802	0.3563	0.3662	0.3945	0.3867

2.2. Disordered binding conformations in 2^{Ni}-AuCl

Shown below (Figure S14) are the two distinct binding conformations for gold in compound **2^{Ni}-AuCl**. **2^{Ni}-AuCl$_{(1)}$** is the major conformation, with a crystallographic occupancy of 89.67 %. It is near linear with a P-Au-Cl bond angle of 176.30 (2) °. **2^{Ni}-AuCl$_{(2)}$** is a minor conformation, with a crystallographic occupancy of 10.33 %. It is distinctly bent with a P-Au-Cl angle of 156.40 (18) °.

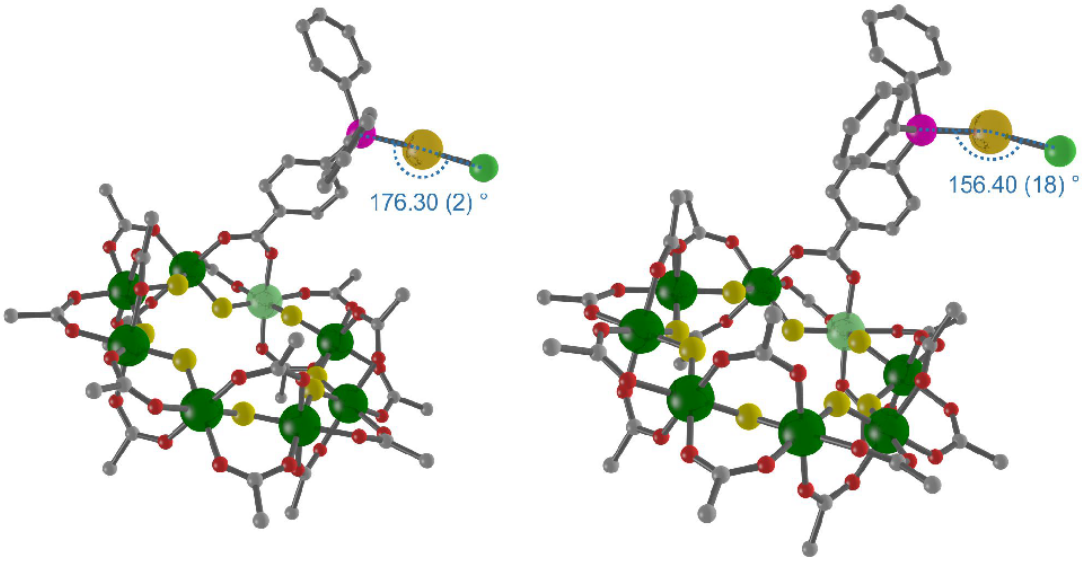

Figure S14: Single crystal X-ray structure of **2^{Ni}-AuCl** showing the two different P-Au-Cl conformations, **2^{Ni}-AuCl$_{(1)}$** (left) and **2^{Ni}-AuCl$_{(2)}$** (right). Colours – Cr (green), Ni (pale green), Au (gold), F (yellow), O (red), P (purple), C (grey), Cl (grass green). Protons, methyl groups and ammonium cation omitted for clarity.

2.3. Torsion angle for 3^{Ni}

Shown below (Figure S15) is a schematic representation of the planes of the rings of metals in the two {Cr_7Ni} wheels with the torsion angle between the two marked.

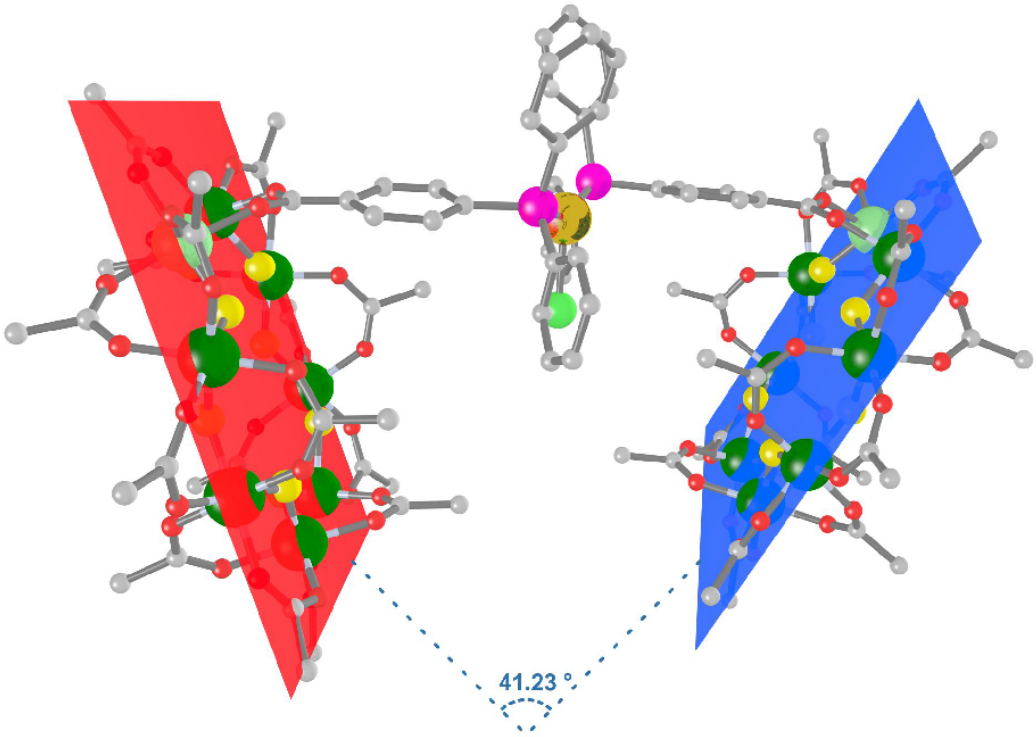

Figure S15: Diagram showing planes of {Cr_7Ni} rings in $\mathbf{3^{Ni}}$ with the torsion angle marked. Colours as above.

2.4. Crystal Structure of 4^{Ni}

Shown below (Figure S16) is the crystal structure of $\mathbf{4}^{Ni}$ with the relative orientations of the {Cr_7Ni} ring planes shown. Two of the rings (green and blue planes) are aligned perpendicular to the central heterocycle whilst one of the rings (red) is aligned parallel.

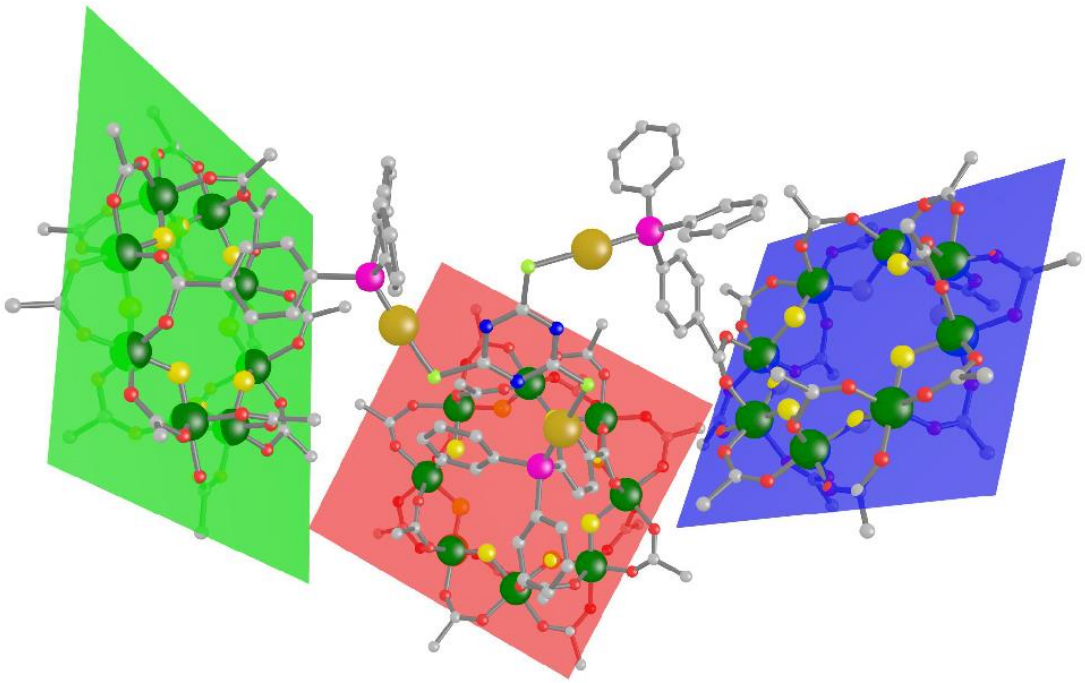

Figure S16: Diagram showing relative orientations of the three {Cr_7Ni} rings in $\mathbf{4}^{Ni}$. Colours as above, S (grass green). Protons, methyl groups and ammonium cation omitted for clarity.

Shown below (Figure S17) is the packing of $\mathbf{4}^{Ni}$ in the unit cell. One {Cr_7Ni} ring on each structure has a different orientation to the other two (see above) allowing the structure to pack as a dimer in the unit cell.

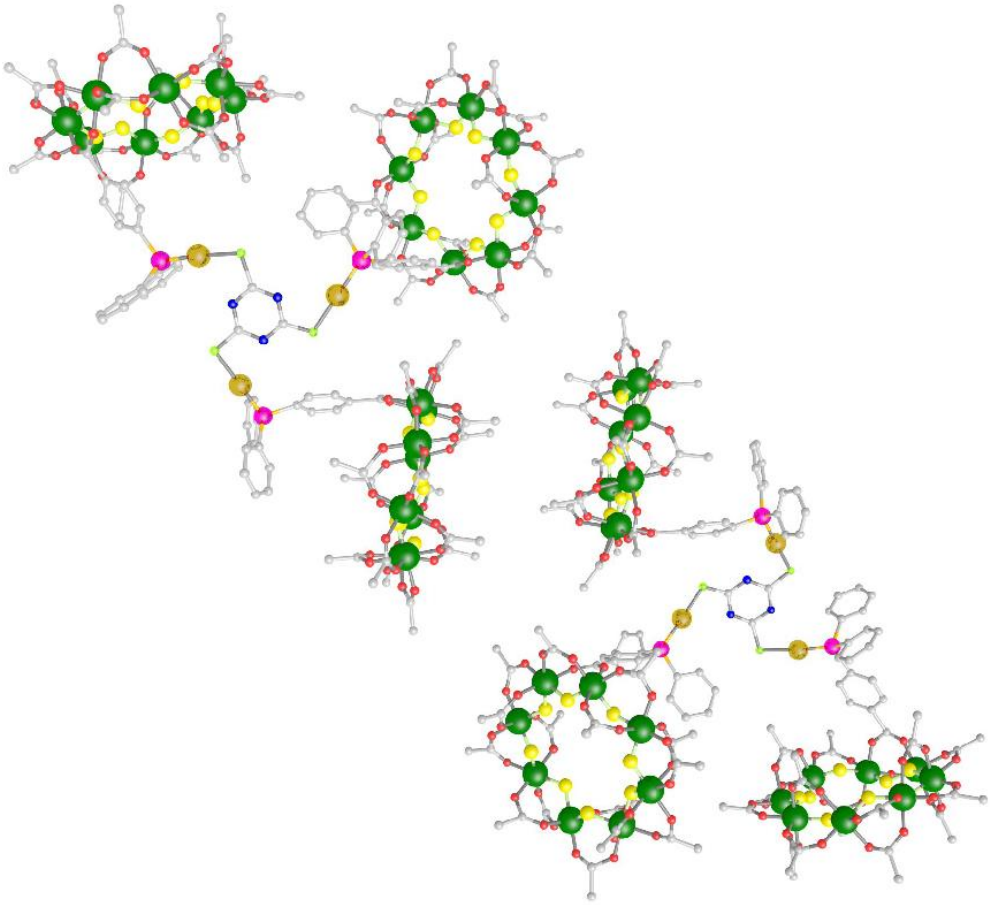

Figure S17: Unit cell packing of $\mathbf{4}^{Ni}$. Colours as above, S (grass green). Protons, methyl groups and ammonium cation omitted for clarity.

3. Electrochemistry of trimer 4^{Ni}

Shown below (Figure S18) are the cyclic voltammograms for $\mathbf{4^{Ni}}$. The data was recorded in CH_2Cl_2 (10 mL) with an $Ag/AgClO_4$ reference electrode, a glassy carbon working electrode and a platinum counter electrode. The electrolyte was 0.1 M $[^tBu_4N][PF_6]$ in CH_2Cl_2. The scan rate was 50 mVs^{-1}, the step size was 0.61 mV and the potential window was 2 V to -1 V. The blank spectrum (Figure S18 - black) was recorded, followed by addition of 0.5 mmol of $\mathbf{4^{Ni}}$. The solution was degassed with N_2 for 5 minutes before the spectrum was recorded (Figure S18 – blue). After recording the sample spectrum, a 0.5 mM ferrocene solution was added and a spectrum recorded (Figure S18 - red).

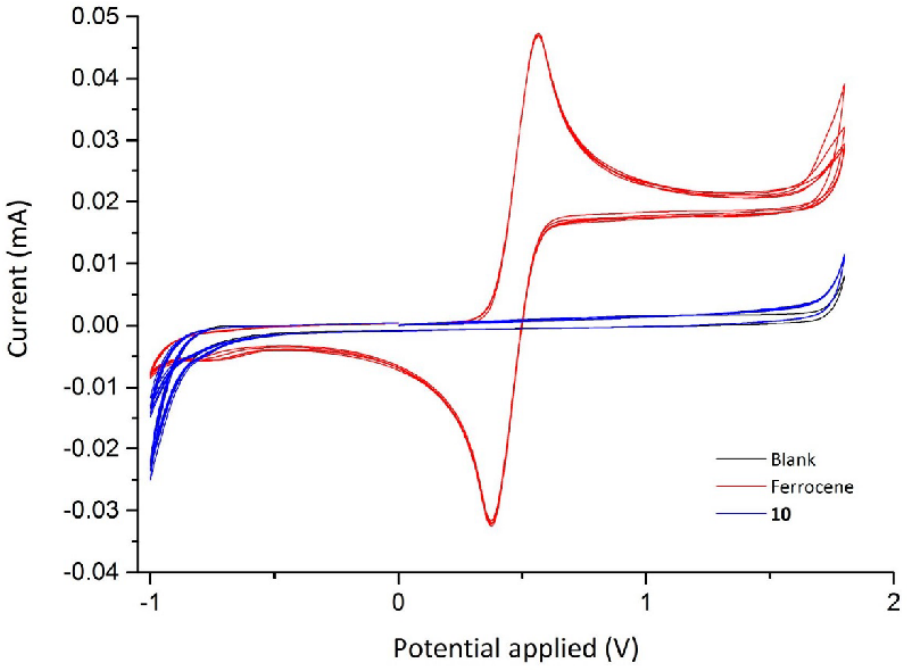

Figure S18: Overlay of cyclic voltamograms for $\mathbf{4^{Ni}}$. Blank (black), sample (blue) ferrocene (red)

References

1. H. Nowell, S. A. Barnett, K. E. Christensen, S. J. Teat and D. R. Allan, *J. Synchrotron Rad.*, 2012, **19**, 435-441.
2. R. H. Blessing, *Acta Crystallogr. A*, 1995, **51**, 33-38.
3. L. Krause, R. Herbst-Irmer, G. M. Sheldrick and D. Stalke, *J. Appl. Crystallogr.*, 2015, **48**, 3-10.
4. O. V. Dolomanov, L. J. Bourhis, R. J. Gildea, J. A. K. Howard and H. Puschmann, *J. Appl. Crystallogr.*, 2009, **42**, 339-341.
5. G. M. Sheldrick, *Acta Crystallogr. A*, 2007, **64**, 112-122.
6. G. M. Sheldrick, *Acta Crystallogr. C*, 2015, **71**, 3-8.

Chapter 6 Paper 3

"Application of Paramagnetic NMR Spectroscopy to the Characterisation of Magnetic Anisotropy in Supramolecular Systems"

Robert J. Woolfson, Ralph W. Adams, Grigore A. Timco, David Collison and Richard E.P. Winpenny

Manuscript in Preparation

Whilst previous work has shown that ligand substitution has no effect on the physical structure of the central core of metals (see Chapter 5 or Whitehead *et al*. (2016)[129]), the effect of ligand substitution on the electronic structure of the wheels has not been studied in detail. This understanding is required to help meet Criteria 1 of the DiVincenzo criteria. Previous work within the molecular magnetism group at The University of Manchester by Angelika Boeer[162] and James Walsh[163] has focussed on the molecular anisotropy in linked metal dimers, with a Co^{II} dimer showing a change in the exchange interaction from ferro- to antiferromagnetic upon changing the terminal ligands from pivalic acid to pyridine (Figure 16) – suggesting that the local crystal field has a significant impact on intramolecular interactions between spins.[164]

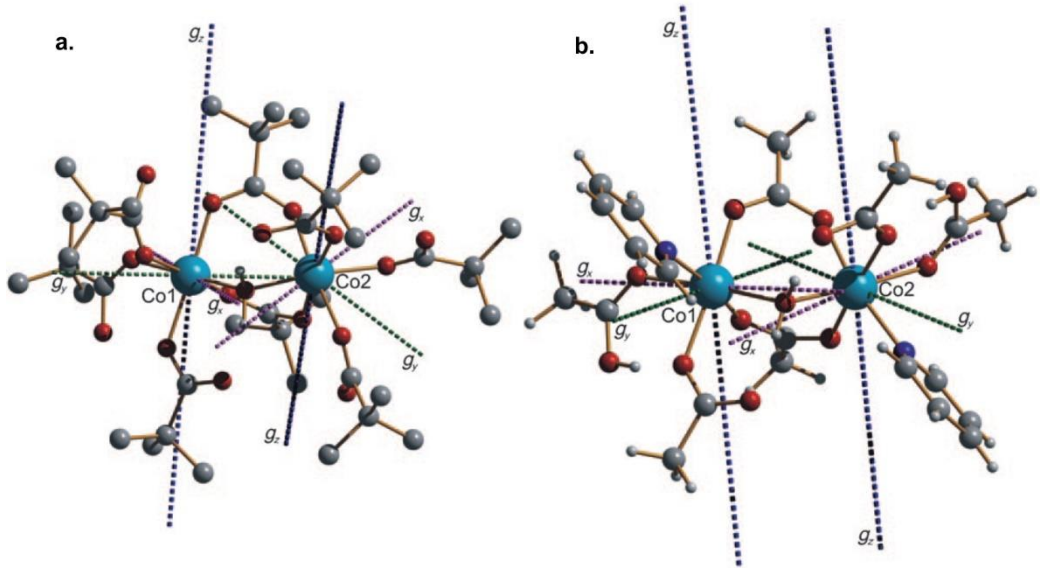

Figure 16: Diagram showing principle axes of the *g*-tensors for two Co^{II} dimers. The magnitude of the vectors is proportional to the magnitude of *g*. a. X-ray crystal structure of $[Co_2(H_2O)(O_2C^tBu)_4(HO_2C^tBu)_4]$ b. X-ray crystal structure of $[Co_2(H_2O)(O_2C^tBu)_4(HO_2C^tBu)_2(py)_2]$. Co (blue), O (red), N (dark blue), C (grey). Protons omitted for clarity. Reproduced with permission from John Wiley and Sons.[164]

A detailed study on the effect of different carboxylates on a {Mn_4} cluster was published by Kampert *et al*. (2009).[165] In this work, a rigid central core was synthesised with a series of bridging and terminal carboxylates and the intramolecular interactions studied using magnetometry and DFT calculations (Figure 17). It was found that electron withdrawing carboxylates (O_2CCF_3 vs O_2CCH_3) significantly altered the exchange couplings between the Mn ions by weakening the antiferromagnetic exchange and introducing a small ferromagnetic exchange between two of the ions.

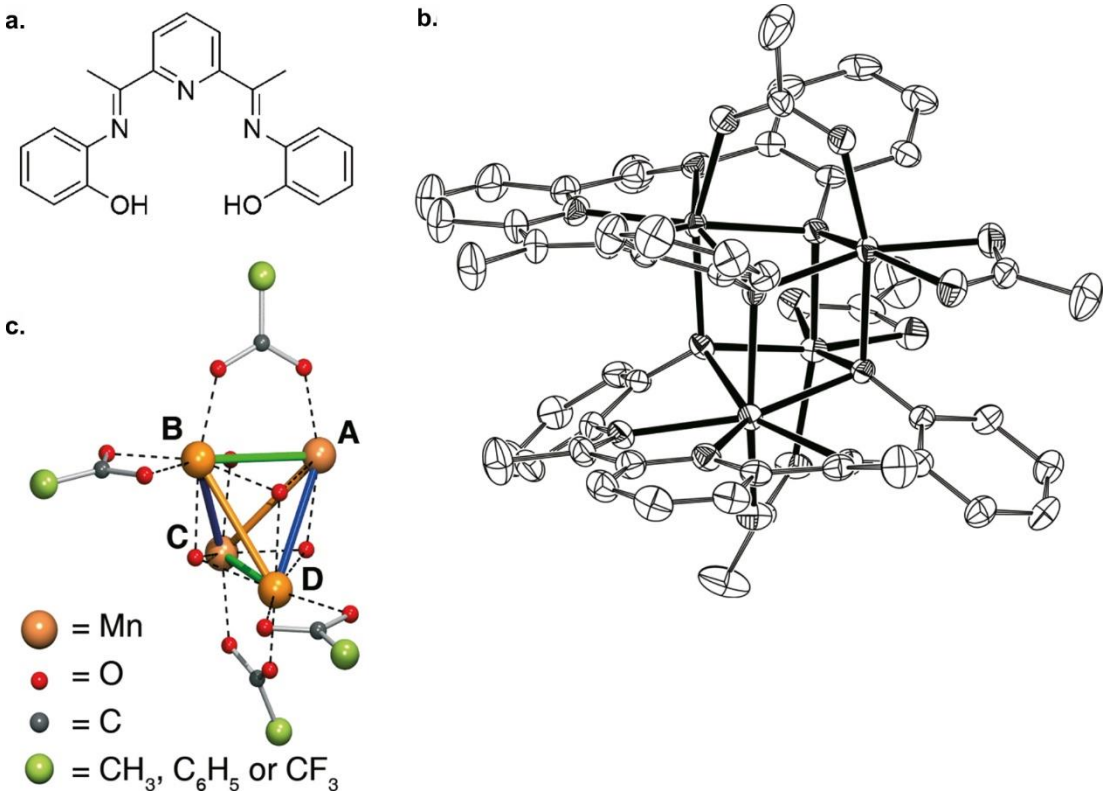

Figure 17: a. Structure of the bridging ligand in the equatorial plane of the {Mn_4} clusters. b. X-ray crystal structure of {Mn_4} with thermal ellipsoids set at 50 % probability. Solvent and protons omitted for clarity. c. Schematic representation of the distorted cubane-like core consisting of four manganese ions, four oxygens, two bridging carboxylates and two chelating carboxylates.

This effect has also been observed for {Mn_{12}}. In 2010, Boukhvalov *et al.* reported a computational study on various {Mn_{12}} derivatives suggesting a potential relationship between the accumulated electronegativity of a ligand and the exchange parameters within {Mn_{12}}.[166] Using a simple linear combination of electronegativities – the accumulated electronegativity – they found that increasing electronegativity reduced the antiferromagnetic interactions between spins and, in some cases, resulted in a switch from antiferro- to ferromagnetic interactions.[167]

As discussed briefly in Chapter 2 and Chapter 5, using Co^{II} as the hetero-metal in {Cr_7M} allows NMR spectroscopy to be used for structural characterisation. The fast relaxation of an octahedral Co^{II} nuclear spin (on the NMR timescale) allows NMR spectra to be collected, even when incorporated with the relatively slow relaxing Cr^{III} ions. Co^{II} is a $3d^7$ ion with a ^4F free ion ground term. In an octahedral crystal field, this term splits into a $^4T_{1g}$ (S = 3/2) ground state with $^4T_{2g}$ and $^4A_{2g}$ excited states. The ground state is then split by first order spin-orbit interactions (SOI) into a doublet (J = 1/2), a quartet (J = 3/2) and a sextet (J = 5/2) [Figure 18].[163, 168]

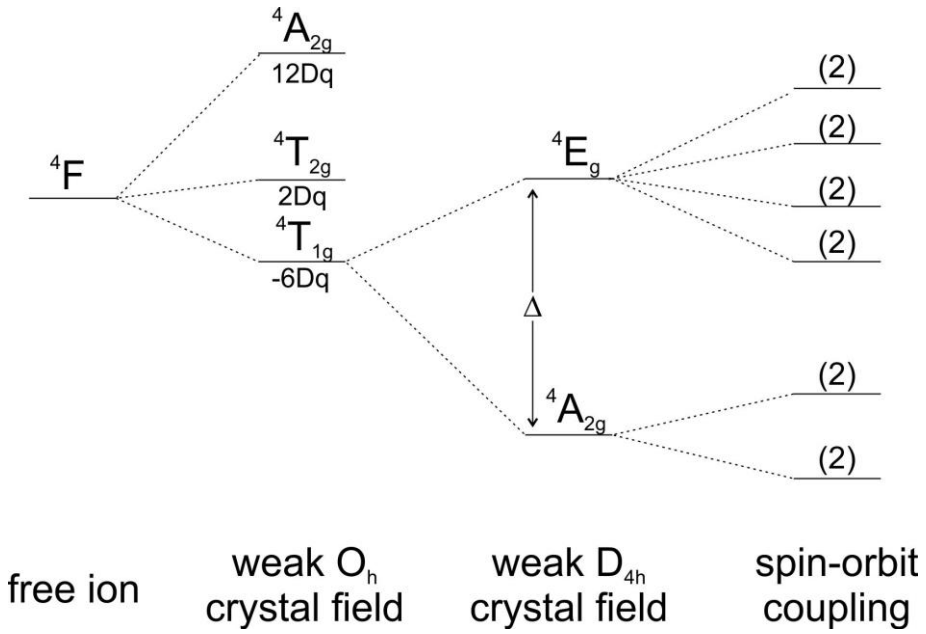

Figure 18: Energy level diagram qualitatively showing the splitting of the Co^{II} ^4F free ion term under various crystal fields. [169]

However, pure octahedral coordination environments are rarely observed. An axial distortion, reducing the symmetry to D_{4h}, further splits the $^4T_{1g}$ state into $^4A_{2g}$ and ^4E_g states. These are then split by SOI into a total of six Kramers doublets with the ground state an effective S = 1/2 (Figure 18). The presence of multiple low-lying excited states leads to very efficient relaxation of the electron spins and sharply resolved NMR spectra. However, it also makes precise modelling of the magnetic properties of Co^{II} highly challenging.[162, 163]

In this paper, the variable temperature ^1H NMR spectra of {Cr_7Co} and the triphenylphosphine substituted derivative introduced in Chapter 5 are modelled to study the effects of a change in the local crystal field on the orientation of the Co^{II} anisotropy tensor. A brief introduction to the relevant theory is given in the paper below. For a full

introduction to the theory underpinning the NMR spectroscopy of paramagnetic systems and the use of metal ions as structural restraits, see the books by Bertini *et al.* (2001) and Banci and Piccioli (2007) and reviews by Bertini *et al.* (2005) and Arnesano *et al* (2005).[170-173]

The paper made extensive use of the FANTEN toolkit, designed primarily for protein structure elucidation using pseudocontact (or dipolar) shifts.[156] In this case, FANTEN was used to explore any potential changes in the anisotropy tensor of the Co^{II} ion in $\{Cr_7Co\}$ upon ligand substitution.

Application of Paramagnetic NMR spectroscopy to the Characterisation of Magnetic Anisotropy in Supramolecular Systems

Robert J. Woolfson, Ralph W. Adams, Grigore A. Timco, David Collison and Richard E.P. Winpenny*

School of Chemistry and Photon Science Institute, The University of Manchester, Oxford Road, Manchester, M13 9PL

The anisotropy tensor for a Co^{II} ion in two molecular wheels, $[NH_2{}^nPr_2][Cr_7CoF_8(O_2C{}^tBu)_{16}]$ and the triphenylphosphine substituted derivative $[NH_2{}^nPr_2][Cr_7CoF_8(O_2C{}^tBu)_{15}(O_2C\text{-}C_6H_4\text{-}PPh_2)]$, has been characterised using variable temperature nuclear magnetic resonance spectroscopy revealing that a small change in the local crystal field at the Co^{II} site results in an 82 ± 28 ° tilt away from the crystallographic c-axis towards the a-b plane.

Introduction

Nuclear magnetic resonance (NMR) spectroscopy of paramagnetic systems is a well-established technique in the protein characterisation toolbox. Especially in cases where a protein cannot be crystallised, substitution of a diamagnetic metal – or a paramagnetic one with a long electronic correlation time (τ_s) – by a paramagnetic metal with a suitably short τ_s can allow full structural characterisation of the area surrounding the metal site.[1] The underlying theory for systems with a single paramagnetic ion is well understood[2-5] and simulation packages of varying sophistication allow the use of paramagnetic pseudocontact shifts as structural restraints in combination with other datasets such as residual dipolar couplings.[6-8]

High spin Co^{II} has been used as a replacement for octahedral Cu^{II} in blue copper proteins, allowing determination of the copper binding sites.[9] Co^{II} has also been substituted into the tetrahedral Zn^{II} sites of zinc finger proteins,[9-12] allowing structural characterisation of the binding site,[13] study of solution state dynamics,[14] and the orientation and anisotropy of the magnetic susceptibility tensor to be established.[15]

$[NH_2{}^nPr_2][Cr_7CoF_8(O_2C{}^tBu)_{16}]$ {Cr_7Co} (**1**) (Figure 1) was first reported in 2003 by Larsen *et al.* as part of the heterometallic {Cr_7M} family of octametallic rings.[16] SQUID magnetometry measurements suggested antiferromagnetic coupling at low temperatures, leading to an $S = 0$ ground state. With increasing temperature the χT value showed no evidence of saturation, indicative of high spin Co^{II} with multiple magnetically relevant energy levels present.[17]

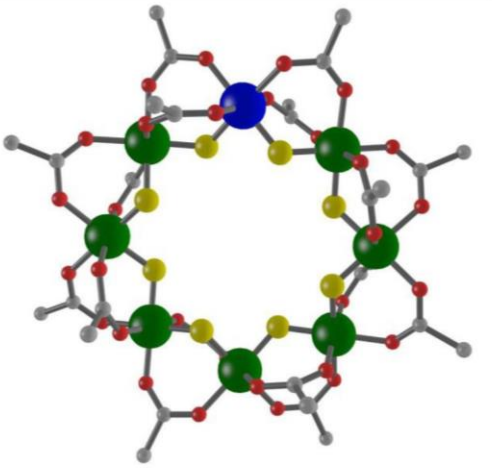

Figure 1: X-ray crystal structure of {Cr_7Co} viewed perpendicular to the plane of the metal ring. Cr (green), Co (blue), F (yellow), C (grey). Protons, tert-butyl methyl groups and ammonium cation omitted for clarity.

Unlike the analogous $[NH_2{}^nPr_2][Cr_7NiF_8(O_2C^tBu)_{16}]$ {Cr_7Ni} with ground state S = 1/2, {Cr_7Co} is suitable for study by solution state NMR spectroscopy due to the fast electronic relaxation in the octahedral Co^{II} ion (see Table 1). The {Cr_7M} family has been studied by solid state NMR spectroscopy, with the spin relaxation explored by ^{1}H spectroscopy, showing relaxation times of ≈1.5 ms for {Cr_7Ni}.[18] A combination of ^{53}Cr and ^{19}F solid state NMR spectroscopy has been used to explore the local spin density and spin dynamics in the {Cr_7M} family as well as larger rings including the {Cr_8Cd} derivative and the newly reported {Cr_9F_9} ring.[19-22] However, no solid state NMR spectroscopy has been published on the {Cr_7Co} ring.

The first solution state NMR study of {Cr_7Co} was published in 2008 by Sañudo *et al.* Focussing primarily on the protons of the templating ammonium cation (observed below -10 ppm), they also noted the pivalate (O_2C^tBu) ligand protons appeared as eight broad peaks of approximately equal intensity in the -5 to +15 ppm region.[23] The ring was assumed to have a pseudo-C_2 symmetry axis, leading to the peaks being assigned to the equivalent equatorial (in the plane of the ring of metals) and axial (out of the plane of the ring of metals) pairs of pivalate ligands (Figure 2).

The ability to perform NMR measurements on {Cr_7Co} has since been exploited to characterise the solution-phase molecular motion in organic-inorganic hybrid systems. {Cr_7Co} was grown around an organic thread with two ammonium sites and the exchange between the two sites was studied by proton NMR suggesting fast molecular rotation on the NMR time scale but slow exchange between the ammonium sites.[24, 25] The {Cr_7Co} derivative of a nanoscopic metal cage has also been used as part of a study into the solution structure of the cage by DOSY NMR spectroscopy.[26]

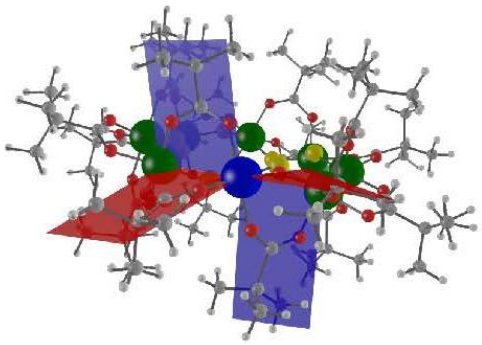

Figure 2: X-ray crystal structure of {Cr_7Co}, viewed parallel to the plane of the metal ring, with two pivalate pairs highlighted. The equatorial pair are shown by red planes and the axial pair by blue planes. Cr (green), Co (blue), F (yellow), C (grey), H (light grey). Templating ammonium cation omitted for clarity.

In this work, we have explored the variable temperature NMR spectroscopy of {Cr_7Co} to understand the magnetic anisotropy on the Co(II) site. The effect of replacing one of the bridging pivalate groups with a different carboxylate, and the concomitant break in molecular symmetry, on the NMR spectrum is also explored.

Experimental

Variable temperature ^{1}H NMR spectra were run on a Bruker AVIII HD 500 equipped with a CryoProbe™ Prodigy BBO probe. NMR spectra were modelled using the FANTEN package.[27] Anisotropy tensors were visualised using Chimera.[28] Column chromatography was performed using a Grace Reverelis® Autocolumn with Reverelis® Flash Cartridges.

{Cr_7Co} **1** and {Ga_7Zn} **2** were prepared using previously published methods.[16, 29] The crystal structures were obtained from CCDC entries 746229 and 954610 respectively.

$[NH_2{}^nPr_2][Cr_7CoF_8(O_2C{}^tBu)_{15}(O_2C\text{-}C_6H_4\text{-}PPh_2)]$ **3** was synthesised by reacting $[NH_2{}^nPr_2][Cr_7CoF_8(O_2C{}^tBu)_{16}]$ **1** (1.0 g, 0.43 mmol) with 4-diphenylposphino-benzoic acid (0.4 g, 1.29 mmol) in dry xylenes (15 mL) at 160 °C for 18 h under a nitrogen atmosphere. After cooling, the mixture was dried by rotary evaporation, dissolved in hexane, filtered and purified by column chromatography. Using a 40 g silica cartridge and 98% hexane: 2% diethyl ether as the eluent, a mixture of unreacted **1** and **2** eluted followed closely by 0.197 g (18 %) of **2** as a green powder. ESMS+: 2499 (M + H); 2522.600 (M + Na). Elemental Anal. (calc.): C, 48.69 (48.06); H, 6.46 (6.85); N, 0.54 (0.56); P, 1.39 (1.25); Cr, 14.21 (14.56); Co, 2.19 (2.36). The X-ray crystal structure of the {Cr_7Ni} analogue, used in this work as suitable crystals of **3** could not be obtained, is contained in CCDC entry 1499591.

Paramagnetic NMR

Theory

In an NMR experiment involving a paramagnetic sample, the nuclear spin experiences both the applied external field (B_0) and a second smaller magnetic moment originating from unpaired electrons. This leads to the nucleus experiencing an isotropic (paramagnetic) shift that can be broken down into three components (Eq. 1). [2, 3]

$$\delta_{obs} = \delta_{dia} + \delta_{con} + \delta_{dip} \qquad \text{(Eq. 1)}$$

The diamagnetic shift (δ_{dia}) is the chemical shift experienced in the absence of paramagnetic effects and can be obtained from a suitable diamagnetic analogue. The Fermi contact shift (δ_{con}) is due to shielding induced by unpaired electron density sited on the nuclei of interest (Eq. 2) where A is the nuclear hyperfine coupling constant (Eq. 3). The pseudocontact, or dipolar, shift (δ_{dip}) is due to long range dipolar coupling between nuclei and an unpaired electron (Eq. 4). [2, 3]

$$\delta_{con} = A\,\frac{\bar{g}\mu_B S(S+1)}{3\gamma_I \hbar k T} \qquad \text{(Eq. 2)}$$

$$A = \frac{2\mu_0}{3}\hbar\gamma_I g_e \mu_B \rho \qquad \text{(Eq. 3)}$$

$$\delta_{dip} = \frac{\mu_0}{4\pi}\frac{\mu_B^2 S(S+1)}{9kT}\left(g_{\parallel}^2 - g_{\perp}^2\right)\frac{1}{r^3}\left(3\cos^2\theta - 1\right) \qquad \text{(Eq. 4)}$$

In equation 2, A is the hyperfine contact coupling constant, $\bar{g}$ is the rotationally averaged electron g-value, μ_B is the Bohr magneton, S is the electron spin quantum number, γ_I is the nuclear gyromagnetic ratio, k is the Boltzmann constant and T is the absolute temperature. A is related to the electron density in the s-orbital of the nuclei in question – ρ in equation 3. If $g = g_e$ (the free electron g value) in equation 3, δ_{con} is isotropic, otherwise the contact shift will be anisotropic. [2, 3]

In equation 4, μ_0 is the magnetic permeability of a vacuum, $g_{\parallel}$ is the g value in the unique (z) axis (assuming axial symmetry), $g_{\perp}$ is the g value in the xy plane, r is the distance between the nucleus in question and the unpaired electron whilst θ is the angle between the electron-nucleus vector **r** and the molecular z axis. A dipolar shift will only be observed if the magnetic susceptibility of the paramagnetic ion is anisotropic. [2, 3] Both equations 2 and 4 assume $S = 1/2$ spin systems with no zero field splitting (ZFS) and well separated excited states, in which case δ_{obs} will show a $1/T$ dependence. In the case of $S > 1/2$,

Table 1: Summary of electronic parameters for Cr^{III}, Ni^{II} and Co^{II}.[3]

	Electronic configuration	Coordination Geometry	S	Ground state	Spin-Orbit Interactions	τ_s (ps)
Cr(III)	d^3	Octahedral	3/2	$^4A_{2g}$	No	≈ 400
Co(II)	d^7	Octahedral	3/2	$^4T_{1g}$	Yes	≈ 5
		Pseudo-octahedral		$^4A_{2g}$ / ^4E_g	Yes	≈ 0.5
		Tetrahedral		$^4A_{2g}$	No	≈ 100

ZFS will be present and low lying excited states will become populated, leading to both equations 2 and 4 becoming dependent on *D* (the axial ZFS parameter) and on $1/T^2$.

The presence of low lying excited states will introduce further complications as each state will have a different value for *A* and there will be a complex Boltzmann population distribution, leading to modelling of both δ_{con} and δ_{dip} becoming non-trivial.[2, 3, 30]

The Metals

Octahedral Cr^{III} is a d^3 ion with an $S = 3/2$ electron ground state corresponding to $^4A_{2g}$. It has well separated excited states and long electronic correlation relaxation times ($\tau_s \approx 400$ ps) resulting from inefficient relaxation mechanisms. Due to the excessive peak broadening associated with long relaxation times, the use of Cr^{III} in paramagnetic NMR spectroscopy is normally restricted to binding studies observing spectral changes with increasing concentration of Cr^{III} ions.[31, 32]

Much of the literature on paramagnetic NMR of Co^{II} is based on tetrahedral coordination environments.[33-36] Tetrahedral Co^{II} has an orbitally non-degenerate $^4A_{2g}$ ground state with well separated excited states ($\tau_s \approx 100$ ps) leading to a slight broadening of NMR signals and large dipolar shifts. Octahedral Co^{II} has a $^4T_{1g}$ ground state split by first order spin orbit coupling and Zeeman splitting, leading to very short relaxation times ($\tau_S \approx 5$ ps) and relatively sharp NMR signals. If the coordination geometry is slightly distorted to pseudo-octahedral (D_{4h} symmetry), the ground state becomes $^4A_{2g}$ with a low-lying ^4E_g state and up to six Kramers doublets can be expected at low energy (up to ca. 1000 cm^{-1}), resulting in very efficient relaxation ($\tau_s \approx 0.5$ ps).

The Diamagnetic Reference

To obtain a value for δ_{dia}, the NMR spectrum of the diamagnetic wheel $[NH_2Me_2][Ga_7ZnF_8(O_2C^tBu)_{16}]$ (**2**) {Ga_7Zn} was

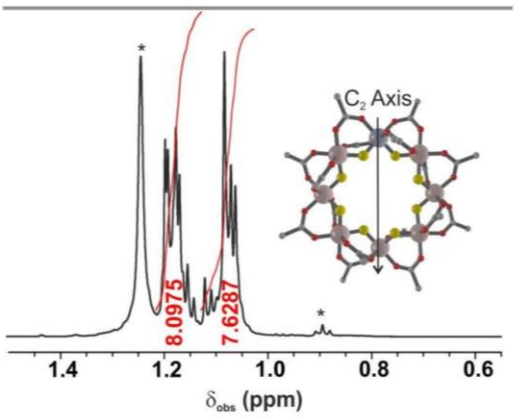

Figure 3: NMR spectrum of {Ga7Zn} collected at 298 K in $CDCl_3$ with integrals referenced to 9 protons = 1 pivalate group. * = grease impurity. Inset – X-ray crystal structure of {Ga7Zn} with molecular C2 axis labelled. Ga (pink), Zn (blue), O (red), F (yellow), C (grey). Pivalate methyl groups and templating ammonium cation omitted for clarity.

collected at 298 K (Figure 3). The pivalate ligands in {Ga_7Zn} are of two distinct types, axial and equatorial relative to the plane of the metal ring (see Figure 1). The two are chemically inequivalent as they are not symmetry related, leading to differing δ values.

Two major peaks were observed (the peak at 1.26 ppm is a grease impurity that could not be removed from the sample) centred at 1.17 ppm and 1.07 ppm, corresponding to the axial and equatorial pivalate ligands – although no assignment is made here. The observed fine structure is due to the differing electronegativity between Zn and Ga – χ_{Zn} = 1.65 and χ_{Ga} = 1.81 on the Pauling electronegativity scale[37, 38] – resulting in subtly different electronic environments for protons closer to the zinc site. The overall peak width is 0.14 ppm (70 Hz) and δ_{dia} was taken to be 1.12 ppm.

Variable Temperature NMR

{Cr_7Co}

The variable temperature ^{1}H NMR spectra for {Cr_7Co} were collected in $CDCl_3$ (sharp signal at 7.27 ppm) from 243 K to 318K (Figure 4a). The NMR spectra show a strong temperature dependence, with overlapping peaks at low temperatures resolving into eight distinct peaks at room temperature. The temperature dependence of each peak can be followed, allowing the derivation of a Curie plot of δ_{obs} (Figure 4b). None of the signals display true Curie behaviour, i.e. 1/T plot with linear slope and a 0 intercept at x = 0. Instead, a range of Curie and Anti-Curie behaviour is seen, as well as non-linear 1/T dependences, indicative of multiple accessible energy levels.[30]

Significant deviations from the expected magnetic behaviour have been reported for cobalt complexes.[39] In organometallic compounds, a mixture of Curie and anti-Curie behaviour has been reported in a dimetallic Co^{II} mesityl complex[40] and in both the monomer and dimer of a Co^{II} salen complex[41] but in neither case was the underlying cause explored. Banci *et al*. (1998) successfully modelled deviations from Curie behaviour in a Ferricytochrome C active site using a single excited state with temperature dependant occupancy.[30]

Inelastic Neutron Scattering (INS) studies

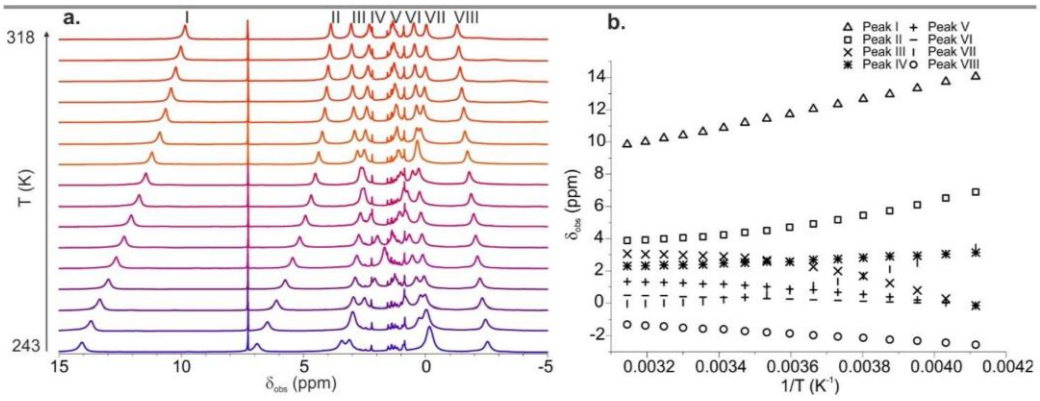

Figure 4: a. Variable temperature 1H NMR spectra for {Cr7Co} recorded from 243 K to 318 K in $CDCl_3$ (δ = 7.27 ppm). b. Plot of observed chemical shift against 1/T. Peaks labelled as on VT NMR spectra.

on the electronic structure of {Cr_7Co} have suggested a significant number of low lying excited states within 50 cm^{-1} of the ground state,[17] all of which would be expected to be populated at room temperature ($kT \approx 200\ cm^{-1}$) - contributing to the electron density and observed isotropic shifts. Given the complex nature of the electronic structure of {Cr_7Co}, with clear evidence for a range of accessible magnetic excited states from INS and SQUID magnetometry, the strong observed deviations from Curie behaviour are not surprising.

The T_1 values for {Cr_7Co} and {Ga_7Zn} were measured using an inversion recovery pulse sequence, giving values of 5.30 – 6.64 ms and 1.12 s respectively (Table S1). The drop of three orders of magnitude in the value of T_1 on going to the strongly paramagnetic {Cr_7Co} was as expected given there are several highly efficient pathways for relaxation in {Cr_7Co} due to the complex electronic structure.

{Cr_7Co-PPh_3}

To explore the effect on the NMR spectrum of breaking the apparent molecular C_2 symmetry axis of {Cr_7Co}, one of the bridging pivalate ligands was replaced with the triphenylphosphine derivative 4-diphenylphosphino-benzoic acid, yielding the axially monosubstituted product $[NH_2{}^nPr_2][Cr_7CoF_8(O_2C{}^tBu)_{15}(O_2CC_6H_4P(C_6H_5)_2]$ {Cr_7Co-PPh_3} (**3**). Previous work has shown that there are no changes in the structure of the ring or the coordination geometry around the metal site upon ligand substitution.[42] It is known that ligand substitution on {Cr_7Co} occurs on a Cr-Co edge due to the greater reactivity of Co^{II} vs. Cr^{III}, meaning the site of the cobalt can be localised to one of two sites via the position of the new ligand.

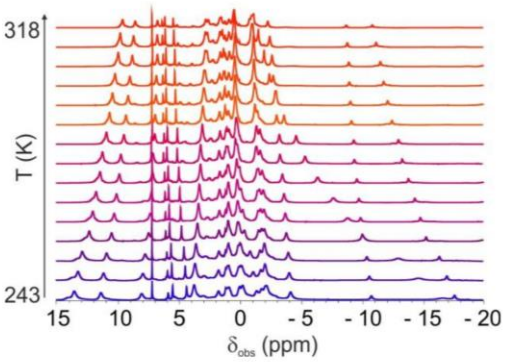

Figure 5: Variable temperature NMR spectra for 3 recorded at 500 MHz from 243 K to 318 K in $CDCl_3$

The loss of symmetry results in an increase in the number of signals in the ^1H NMR spectrum (**Figure 5**). At all temperatures there is significant overlap between neighbouring peaks, making integration and assignment of the pivalate ligand signals challenging.

Three new peaks appear in the 4.5 – 6 ppm region, corresponding to protons from the PPh_3 moiety. This assignment was confirmed by room temperature COSY measurements, showing cross correlations matching those expected from the C_6H_5 rings (See Figure S1). These peaks show inter-proton J coupling at lower temperatures that disappears at higher temperatures, suggesting hindered rotation of the phenyl rings below 293 K.

The T_1 values for all peaks in {Cr_7Co-PPh_3} were measured with the three peaks assigned to the phenyl protons showing lifetimes of 53.84, 23.62 and 12.53 ms respectively. These values, whilst still short, are significantly longer than those measured for the peaks assigned to the pivalate protons and confirm these protons are further away from the paramagnetic metals. All three signals show a 1/T temperature dependence (Figure S2) with

Curie-like behaviour, suggesting they are relatively well separated from the Co^{II} site. The signals corresponding to the C_6H_4 phenyl protons could not be identified – they are likely to be strongly shifted by dipolar effects and are most likely masked by pivalate signals.

Modelling

To model the paramagnetic NMR spectra of {Cr_7Co}, δ_{con} was initially assumed to be constant and the dipolar shifts modelled using the FANTEN package written by Rinaldelli *et al*. to obtain $\Delta\chi$ values and Euler angles.[27] The Euler angles are reported in the rzyz convention, meaning the angles are reported as rotations around the initial z axis (α), the new y' axis (β) and the new z'' axis (γ) respectively. All three angles are reported, but the α and γ angles define rotations of the tensor along the z-axis (*i.e.* the tensor is rotating around itself) whilst the β rotation defines the tilt of the anisotropy tensor away from the crystallography z-axis and is the angle of interest here.

The cobalt position was fixed at one of the metal sites and the NMR signals assigned on the basis of their chemical shift, assuming protons on axial ligands experienced a downfield shift, i.e. a +ve change in δ_{obs} (**Table 2** – Model 1). To account for rotational averaging of the nine pivalate protons, the calculated chemical shifts were averaged for each pivalate ligand (δ_{calc}) and errors calculated against δ_{calc} (Tables S2 – S5). To account for the diamagnetic shift, δ_{dia} was subtracted from the δ_{obs} giving a value for the dipolar shift.

Model 1 gave a reasonable fit to the experimental data with a Q value (Quality factor, see Eq. S1, where 0 corresponds to an ideal fit) of 0.828. The calculated anisotropy

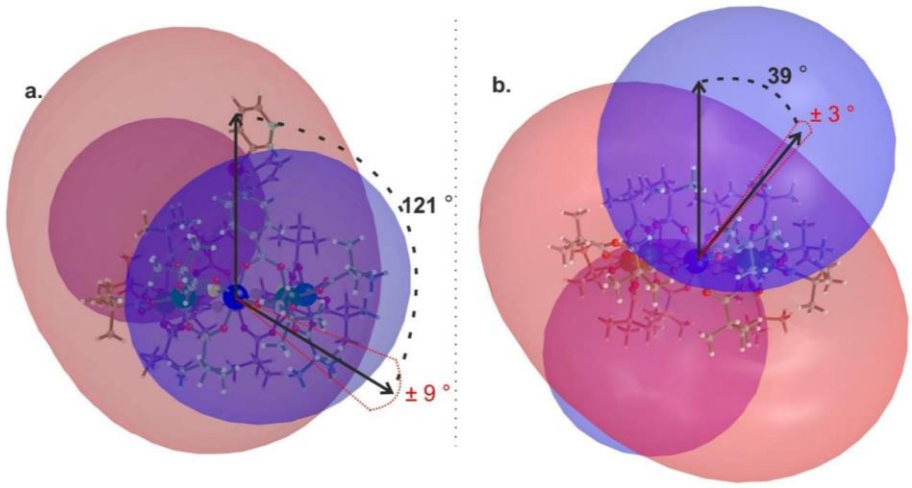

Figure 6: a. Anisotropy tensor from Model 2 calculated for {Cr_7Co-PPh_3}, showing rotation of 121 ° relative to crystallographic c-axis. b. Anisotropy tensor from Model 4 calculated for {Cr_7Co}, showing rotation of 39 ° relative to crystallographic c-axis. Isosurface calculated for 1.0 ppm shift, upfield shift (red), downfield shift (blue). Cr (green), Co (blue), O (red), C (grey), H (white). Templating ammonium cation and disorder omitted for clarity.

Table 2: Calculated values for model magnetic anisotropy tensors of {Cr_7Co} and {Cr_7Co-PPh_3}

	Compound	χ_{ax} ($x10^{-32}$ m^3)	χ_{rh} ($x10^{-32}$ m^3)	A (°)	β (°)	γ (°)	Q
Model 1	{Cr_7Co}	2.304 ± 0.151	-0.438 ± 0.168	26.89 ± 3.54	38.88 ± 2.35	119.34 ± 41.06	0.818
Model 2	{Cr_7Co-PPh_3}	8.522 ± 3.126	-1.712 ± 1.214	84.60 ± 38.54	121.57 ± 9.08	85.19 ± 121.50	0.007
Model 3*	{Cr_7Co}	8.522	-1.712	26.89	38.88	119.34	0.338

* Due to a limitation in FANTEN, Montecarlo error statistics for model 3 could not be obtained.

tensor was strongly axial, with $\Delta\chi_{ax}$ = 2.26 $x10^{-32}$ m^3 and $\Delta\chi_{rh}$ = -0.397 $x10^{-32}$ m^3 (see Eq. S2 & S3). The calculated tensor suggests a 39° rotation of the anisotropy tensor z-axis away from the crystallographic z-axis i.e. the c-axis running through the centre of the wheel. {Cr_7Co-PPh_3} was modelled using the parameters from Model 1, however a poor fit was obtained (Q = 1.006).

Due to the number of bonds between the Co^{II} site and the C_6H_5 phenyl protons in {Cr_7Co-PPh_3}, it can be assumed there is no contact shift contribution and δ_{obs} is a combination of δ_{dia} and δ_{dip}. Modelling the phenyl proton signals with FANTEN gave a new magnetic anisotropy tensor (**Table 2** – Model 2) with $\Delta\chi_{ax}$ = 8.522 $x10^{-32}$ m^3, $\Delta\chi_{rh}$ = -1.712 $x10^{-32}$ m^3 and an angle of 123 ° between the crystallographic z-axis and the anisotropy z-axis.

The calculated tensor can be visualised using an isosurface – defined as the distance from the metal site at which a proton will experience a given chemical shift (Figure 6a). These susceptibility values are similar to those reported for a 5-coordinate Co^{II} system and the calculated Q factor is 0.007, suggesting a good fit to the data.[34] The Q-factor for Model 2 is substantially lower than the others as the experimental data includes only δ_{dip} due to the distance between the protons and the Cr^{III}/Co^{II} sites.

Separating Contact and Dipolar Effects

It has been shown that changing the terminal ligands on a water bridged Co^{II} dimer, *i.e.* a change in the local crystal field, results in reorientation of the Co^{II} principal magnetic axes (the g matrix) and a change from anti-ferromagnetic to ferromagnetic coupling.[43] It is clearly feasible for a small change in the local crystal field to cause significant changes in the magnetic properties of an octahedral Co^{II} complex.

Here, we suggest that replacing one of the bridging pivalate ligands in {Cr_7Co} results in a change in orientation but not magnitude of the anisotropy tensor. With this in mind, we have modelled the NMR spectrum of {Cr_7Co} with the orientation from Model 1 and the magnitude from Model 2 (**Table 2** – Model 3)

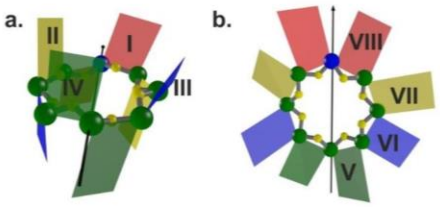

Figure 7: Pictorial representation of the pivalate assignments in {Cr_7Co} with pseudo-C_2 axis shown in black through Co^{II} and Cr^{III}. a. Axial pivalate pairs I (red), II (yellow), III (blue) and IV (green). b. Equatorial pivalate pairs V (green), VI (blue), VII (yellow) and VIII (red).

(Figure 5b). This gave a significantly improved Q factor (*c.f.* Model 1) of 0.338 with major differences between predicted and observed chemical shifts only found for pivalate protons on ligands adjacent to the cobalt site (see Figure 7 for pictorial representation of pivalate assignments).

A change in temperature would be expected to change the distribution of electrons among the various energy states leading to changes in the anisotropy tensor observed for {Cr7Co}. Fitting the variable temperature data recorded for {Cr_7Co} using the parameters from Model 3 confirms this, with a linear trend of decreasing fit (as measured by the Q-factor) with decreasing temperature (Figure S3).

An attempt was made to fit the variable temperature data recorded for **3**, however no clear correlation could be observed. As can be seen from Figure 5, the peaks corresponding to the phenyl protons show fine structure indicative of hindered rotation at low temperatures. This would likely have an effect on the observed δ value as the paramagnetic contributions would depend on the precise position of the protons relative to the cobalt.

Calculating the contact shift using the values of δ_{dip} in Model 3 and δ_{dia} from {Ga_7Zn} suggests that close to the cobalt sites the contact and dipolar effects are opposite in sign. Protons residing on edges away from the Co^{II} site show a much smaller contact shift, in the range -1.5 - +6.7 ppm but there is no clear pattern of positive and negative contributions.

The literature on solution state ^1H NMR of Cr^{III} systems is sparse due to the relaxation properties giving large peak broadening effects (see above). However, studies of octahedral Cr^{III} in oxo-bridged Cr^{III} triangles have shown a wide range of δ_{con} values, with spectra observable despite the properties of a Cr^{III} single ion.[44, 45] The observation of these spectra is ascribed to the antiferromagnetic coupling between Cr^{III} sites reducing the magnetic moment of the triangle. A more likely explanation is that the coupling of the Cr^{III} ions results in a more complex energy level structure – providing efficient relaxation pathways not accessible in the single ion system and lowering τ_s. The observation of a range of δ_{con} values for chromium triangles suggests that Model 3, whilst not capturing the subtleties of the electron density throughout {Cr_7Co}, is predicting δ_{dip} values of a reasonable order of magnitude.

Conclusions

The magnetic anisotropy tensors for both the heterometallic wheel {Cr_7Co} and the mono-substituted derivative {Cr_7Co-PPh_3) have been determined using paramagnetic NMR spectroscopy. In {Cr_7Co}, the axes of the magnetic anisotropy tensor are not aligned with the crystallographic axes, but instead tilted by around 39 ° towards the plane of the metal ring. Substituting one of the bridging pivalate ligands for a triphenylphosphine derivative results in a further 83 ° tilt of the anisotropy tensor towards the ring of metals, suggesting that even small changes in the local crystal field not localisable by crystallography can result in significant changes in the magnetic anisotropy of a molecular wheel. Small changes in ligand field have previously been observed to have significant effects on the exchange interactions and magnetic properties in Co^{II} and Ni^{II} compounds [17, 46-48]

These results build on the previously reported solid and solution state NMR spectroscopy of the {Cr_7M} family and point to a potential route towards exploring the effect

of ligand exchange on the local magnetic environments of paramagnetic systems such as {Cr_7Co}. Performing polarised neutron diffraction measurements would be a significant test of these results as this technique has previously been used to determine the anisotropy axis on Co^{II} single ions and dimers.[49]

Acknowledgements

RJW acknowledges a studentship from the North-West Nanoscience Doctoral Training Centre, EPSRC grant EP/G03737X/1. The EPSRC is thanked for funding an NMR core capability, EPSRC grant EP/K039547/1. All data supporting this study are provided as supplementary information accompanying this paper.

Notes and references

1. I. Bertini, C. Luchinat and G. Parigi, *Concept Magnetic Res.*, 2002, **14**, 259-286.
2. G. N. La Mar, W. D. Horricks and R. H. Holm, *NMR of Paramagnetic Molecules*, Academic Press, London, 1973.
3. I. Bertini, C. Luchinat and G. Parigi, *Solution NMR of Paramagnetic Molecules: Application to Metalobiomolecules and Models*, Elsevier, Amsterdam, 2001.
4. I. Bertini, C. Luchinat, G. Parigi and R. Pierattelli, *ChemBioChem*, 2005, **6**, 1536-1549.
5. F. Arnesano, L. Banci and M. Piccioli, *Q. Rev. Biophys.*, 2005, **38**, 167-219.
6. L. Banci, I. Bertini, K. L. Bren, M. A. Cremonini, H. B. Gray, C. Luchinat and P. Turano, *J. Biol. Inorg. Chem.*, 1996, **1**, 117-126.
7. C. Schmitz, M. J. Stanton-Cook, X. C. Su, G. Otting and T. Huber, *J. Biomol. NMR*, 2008, **41**, 179-189.
8. J. D. Swarbrick, P. Ung, M. L. Dennis, M. D. Lee, S. Chhabra and B. Graham, *Chem-Eur. J.*, 2016, **22**, 1228-1232.
9. L. Banci and M. Piccioli, in *eMagRes*, John Wiley & Sons, 2007.
10. J. S. Thompson, T. Sorrell, T. J. Marks and J. A. Ibers, *J. Am. Chem. Soc.*, 1979, **101**, 4193-4200.
11. M. Piccioli, C. Luchinat, T. J. Mizoguchi, B. E. Ramirez, H. B. Gray and J. H. Richards, *Inorg. Chem.*, 1995, **34**, 737-742.
12. T. Okamura, S. Takamizawa, N. Ueyama and A. Nakamura, *Inorg. Chem.*, 1998, **37**, 18-28.
13. B. Krizek, B. T. Amann, V. J. Kilfoil, D. L. Merkle and J. M. Berg, *J. Am. Chem. Soc.*, 1991, **113**, 4518-4523.
14. S. F. Michael, V. J. Kilfoil, M. H. Schmidt, B. T. Amann and J. M. Berg, *P. Natl. Acad. Sci. USA*, 1992, **89**, 4796-4800.
15. L. V. Harper, B. T. Amann, V. Vinson and J. M. Berg, *J. Am. Chem. Soc.*, 1993, **115**, 2577-2580.
16. F. K. Larsen, E. J. L. McInnes, H. Mkami, J. Overgaard, S. Piligkos, G. Rajaraman, E. Rentschler, A. A. Smith, G. M. Smith, V. Boote, M. Jennings, G. A. Timco and R. E. P. Winpenny, *Angew. Chem. Int. Ed.*, 2003, **42**, 101-105.
17. A. B. Boeer, Ph.D, The University of Manchester, 2009.
18. H. Amiri, A. Lascialfari, Y. Furukawa, F. Borsa, G. A. Timco and R. E. P. Winpenny, *Phys. Rev. B*, 2010, **82**.
19. L. Bordonali, E. Garlatti, C. M. Casadei, Y. Furukawa, A. Lascialfari, S. Carretta, F. Troiani, G. Timco, R. E. P. Winpenny and F. Borsa, *The Journal of Chemical Physics*, 2014, **140**, 144306.
20. E. Micotti, Y. Furukawa, K. Kumagai, S. Carretta, A. Lascialfari, F. Borsa, G. A. Timco and R. E. P. Winpenny, *Phys. Rev. Lett.*, 2006, **97**.
21. F. Adelnia, A. Chiesa, S. Bordignon, S. Carretta, A. Ghirri, A. Candini, C. Cervetti, M. Evangelisti, M. Affronte, I. Sheikin, R. Winpenny, G. Timco, F. Borsa and A. Lascialfari, *The Journal of chemical physics*, 2015, **143**, 244321.
22. E. Garlatti, S. Bordignon, S. Carretta, G. Allodi, G. Amoretti, D. R. Renzi, A. Lascialfari, Y. Furukawa, G. A. Timco, R. Woolfson, R. E. P. Winpenny and P. Santini, *Phys. Rev. B*, 2016, **93**.
23. C. E. Sañudo, T. B. Faust, C. A. Muryn, R. G. Pritchard, G. A. Timco and R. E. P. Winpenny, *Inorg. Chem.*, 2009, **48**, 9811-9818.
24. C. F. Lee, D. A. Leigh, R. G. Pritchard, D. Schultz, S. J. Teat, G. A. Timco and R. E. P. Winpenny, *Nature*, 2009, **458**, 314-318.
25. B. Ballesteros, T. B. Faust, C.-F. F. Lee, D. A. Leigh, C. A. Muryn, R. G. Pritchard, D. Schultz, S. J. Teat, G. A. Timco and R. E. P. Winpenny, *J. Am. Chem. Soc.*, 2010, **132**, 15435-15444.

26. J. Ferrando-Soria, A. Fernandez, E. Moreno-Pineda, S. A. Varey, R. W. Adams, I. J. Vitorica-Yrezabal, F. Tuna, G. A. Timco, C. A. Muryn and R. E. P. Winpenny, *J. Am. Chem. Soc.*, 2015, **137**, 7644-7647.
27. M. Rinaldelli, A. Carlon, E. Ravera, G. Parigi and C. Luchinat, *J. Biomol. NMR*, 2015, **61**, 21-34.
28. E. F. Pettersen, T. D. Goddard, C. C. Huang, G. S. Couch, D. M. Greenblatt, E. C. Meng and T. E. Ferrin, *J. Comput. Chem.*, 2004, **25**, 1605-1612.
29. F. Moro, D. Kaminski, F. Tuna, G. F. S. Whitehead, G. A. Timco, D. Collison, R. E. P. Winpenny, A. Ardavan and E. J. L. McInnes, *Chem. Commun.*, 2013, **50**, 91-93.
30. L. Banci, I. Bertini, C. Luchinat, R. Pierattelli, N. V. Shokhirev and F. A. Walker, *J. Am. Chem. Soc.*, 1998, **120**, 8472-8479.
31. J. R. Bocarsly and J. K. Barton, *Inorg. Chem.*, 1989, **28**, 4189-4190.
32. J. R. Bocarsly and J. K. Barton, *Inorg. Chem.*, 1992, **31**, 2827-2834.
33. L. Banci, L. B. Dugad, G. N. Mar, K. A. Keating, C. Luchinat and R. Pierattelli, *Biophys. J.*, 1992, **63**, 530-543.
34. A. Donaire, J. Salgado and J.-M. Moratal, *Biochemistry*, 1998, **37**, 8659-8673.
35. A. Donaire, B. Jiménez, J.-M. Moratal, J. F. Hall and S. S. Hasnain, *Biochemistry*, 2001, **40**, 837-846.
36. V. V. Novikov, A. A. Pavlov, A. S. Belov, A. V. Vologzhanina, A. Savitsky and Y. Z. Voloshin, *J. Phys. Chem. Lett.*, 2014, **5**, 3799-3803.
37. A. J. Downs, *Chemistry of Aluminium, Gallium, Indium and Thallium*, Springer, Netherlands, 1993.
38. Z. Rappoport and I. Marekm, *The Chemistry of Organozinc Compounds: R-Zn*, John Wiley & Sons, London, 2007.
39. K. E. Barefield, D. H. Busch and S. M. Nelson, *Q. Rev. Chem. Soc.*, 1968, **22**, 457-498.
40. K. H. Theopold, J. Silvestre, E. K. Byrne and D. S. Richeson, *Organometallics*, 1989, **8**, 2001-2009.
41. Y. Ohashi and M. Nakamura, *Chem. Lett.*, 1993, 1389-1392.
42. G. F. S. Whitehead, J. Ferrando-Soria, L. Carthy, R. G. Pritchard, S. J. Teat, G. A. Timco and R. E. P. Winpenny, *Dalton Trans.*, 2016, **45**, 1638-1647.
43. A. B. Boeer, A. L. Barra, L. F. Chibotaru, D. Collison, E. J. L. McInnes, R. A. Mole, G. G. Simeoni, G. A. Timco, L. Ungur, T. Unruh and R. E. P. Winpenny, *Angew. Chem. Int. Ed.*, 2011, **50**, 4007-4011.
44. M. M. Glass, K. Belmore and J. B. Vincent, *Polyhedron*, 1993, **12**, 133-140.
45. K. F. Kingry, A. C. Royer and J. B. Vincent, *J. Inorg. Biochem.*, 1998, **72**, 79-88.
46. M. A. Halcrow, J.-S. Sun, J. C. Huffman and G. Christou, *Inorg. Chem.*, 1995, **34**, 4167-4177.
47. J. P. S. Walsh, S. Sproules, N. F. Chilton, A.-L. Barra, G. A. Timco, D. Collison, E. J. L. McInnes and R. E. P. Winpenny, *Inorg. Chem.*, 2014, **53**, 8464-8472.
48. M. R. Saber and K. R. Dunbar, *Chem. Commun.*, 2014, **50**, 12266-12269.
49. K. Ridier, B. Gillon, A. Gukasov, G. Chaboussant, A. Cousson, D. Luneau, A. Borta, J.-F. Jacquot, R. Checa, Y. Chiba, H. Sakiyama and M. Mikuriya, *Chem-Eur. J.*, 2016, **22**, 724-735.

Application of Paramagnetic NMR to the Characterisation of Magnetic Anisotropy in Supramolecular Systems

SUPPORTING INFORMATION

Robert J. Woolfson, Ralph W. Adams, Grigore A. Timco, David Collison and Richard E.P. Winpenny*

School of Chemistry, The University of Manchester, Oxford Road, M13 9PL

Contents

1. NMR Spectra and analysis for {Cr_7Co-PPh_3} 2
   1.1 COSY spectrum measured for {Cr_7Co-PPh_3} 2
   1.2 Temperature dependence of (C_6H_5) aryl protons in {Cr_7Co-PPh_3} 3
   1.3 Measured T_1 values 4
2. Q-Factors 5
   2.1. Q-Factors calculated for Variable Temperature NMR Spectra of {Cr_7Co} 5
3. Definition of $\Delta\chi_{ax}$ and $\Delta\chi_{eq}$ 5
4. Tables of values for models of dipolar shifts in {Cr_7Co} and {Cr_7Co-PPh_3} 6

1. NMR Spectra and analysis for {Cr_7Co-PPh_3}

1.1 COSY spectrum measured for {Cr_7Co-PPh_3}

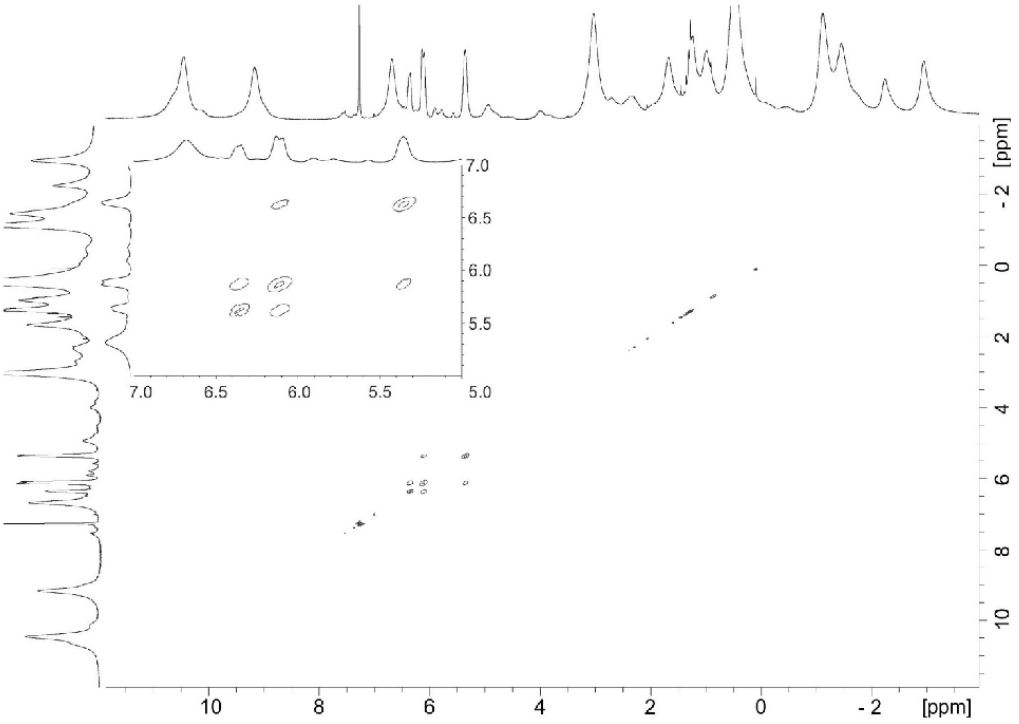

Figure S1: COSY NMR spectrum recorded for {Cr_7Co-PPh_3} showing correlations between phenyl protons. Inset – Expansion of phenyl region.

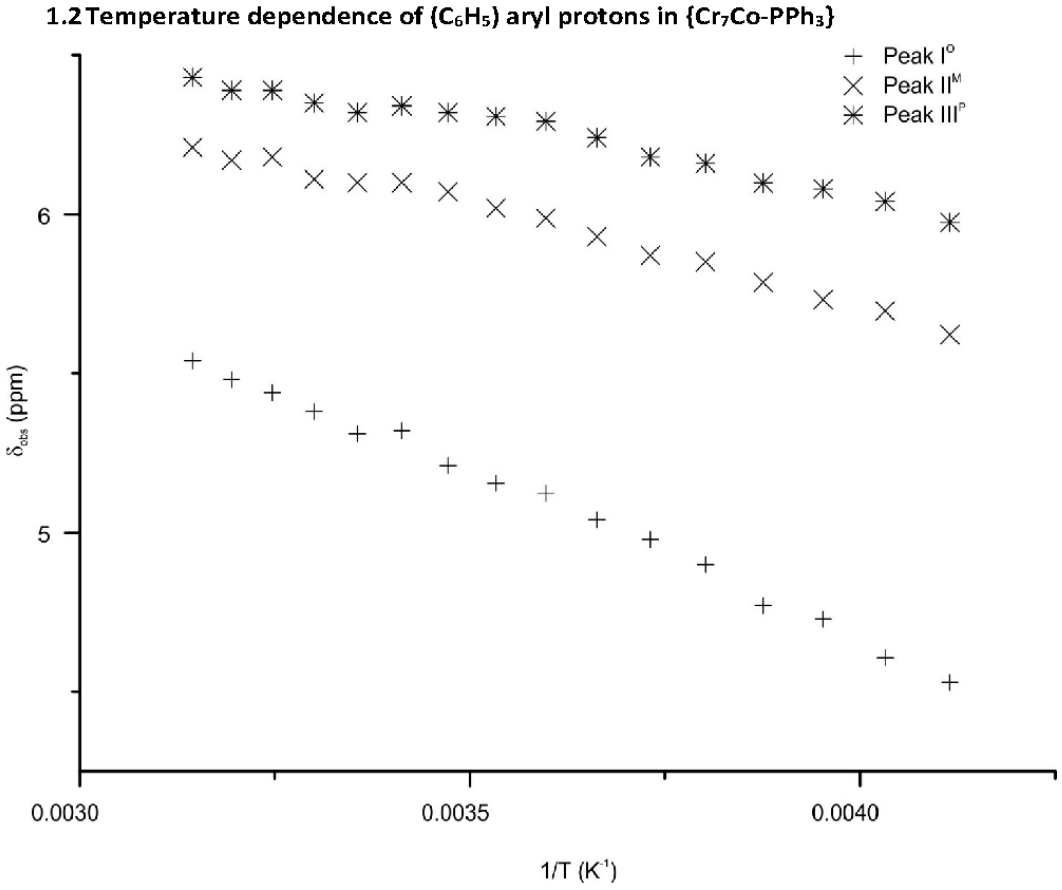

Figure S2: 1/T Dependence of phenyl signals in C_6H_5 rings on {Cr_7Co-PPh_3} showing a near linear temperature dependence

1.3 Measured T_1 values

Table S1: T_1 values for **1**, 2 and 3 measured using inversion recovery pulse sequence

	Chemical shift (δ_{obs}) / ppm	T_1 / ms
{Ga_7Zn}	+1.19	1121±1.854
	+1.095	1134±4.346
{Cr_7Co}	+10.662	6.110±0.005
	+4.137	6.636±0.002
	+2.971	6.115±0.004
	+2.427	5.295±0.009
	+1.245	5.581±0.009
	+0.398	5.704±0.009
	+0.097	5.919±0.017
	-1.535	6.071±0.028
{Cr7Co-PPh_3}	+10.508	6.401±0.009
	+9.220	7.202±0.016
	+6.972	8.161±0.043
	+6.375	57.842±0.021
	+6.136	23.617±0.051
	+5.367	12.533±0.044
	+4.957	4.692±0.063
	+4.110	4.950±0.034
	+3.055	5.519±0.010
	+2.385	5.484±0.015
	+1.716	5.858±0.005
	+1.275	6.135±0.006
	+1.007	5.065±0.020
	+0.482	5.432±0.033
	-1.102	5.212±0.012
	-1.367	5.532±0.013
	-2.885	4.060±0.033
	-3.239	5.427±0.008
	-8.858	5.120±0.079

2. Q-Factors

Shown below (Equation S1) is the equation for calculating Q-factors for a given set of data. It taken directly from refs …

$$Q = \sqrt{\frac{\left(\sum_i \delta_i^{obs} - \sum_i \delta_i^{calc}\right)^2}{\left(\sum_i \delta_i^{obs}\right)^2}} \qquad \text{(Eq. S1)}$$

2.1. Q-Factors calculated for Variable Temperature NMR Spectra of {Cr_7Co}

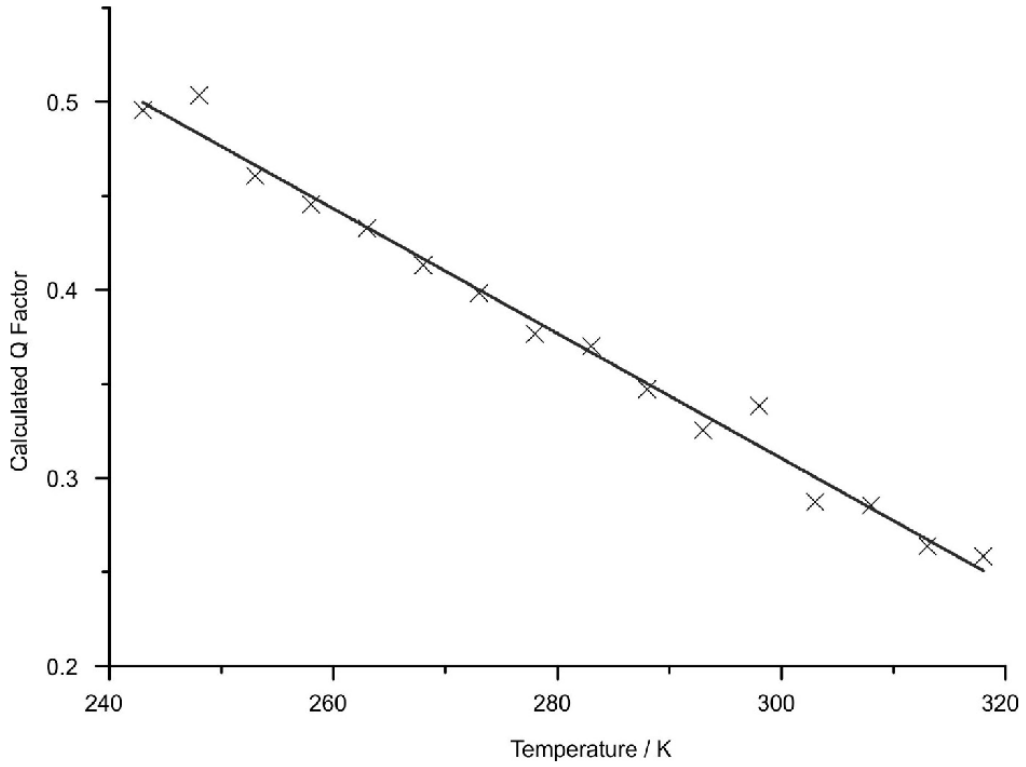

Figure S3: Plot of Q-factor against temperature for {Cr_7Co} calculated using Model 3.

3. Definition of $\Delta\chi_{ax}$ and $\Delta\chi_{eq}$

$$\Delta\chi_{ax} = \frac{3}{2}\chi_{zz} \qquad \text{(Eq. S2)}$$

$$\Delta\chi_{rh} = \chi_{xx} - \chi_{yy} \qquad \text{(Eq. S3)}$$

4. Tables of values for models of dipolar shifts in {Cr_7Co} and {Cr_7Co-PPh_3}

Table S2 : Chemical shift values obtained from modelling {Cr_7Co} using Model **1**

Piv		Peak	δ_{calc} (ppm)	δ_{obs} (ppm)	% Error
2	ax	I	7.588	9.482	-24.953
3	eq	VIII	-3.537	-2.708	23.448
4	eq	VII	-0.812	-1.060	-30.470
5	ax	II	-0.801	2.968	470.691
6	ax	III	0.337	1.800	-434.653
7	eq	VI	-0.410	-0.716	-74.540
8	eq	V	-0.195	0.064	132.746
9	ax	IV	-0.281	1.252	546.081
10	ax	IV	-0.182	1.252	787.912
11	eq	V	-0.206	0.064	131.068
12	eq	VI	-0.446	-0.716	-60.698
13	ax	III	0.217	1.800	-730.343
14	ax	II	-0.674	2.968	540.284
15	eq	VII	-0.689	-1.060	-53.871
16	eq	VIII	-3.420	-2.708	20.816
17	ax	I	7.331	9.482	-29.333

Table S3: Chemical shift values obtained via modelling {Cr_7Co-PPh_3} phenyl shifts using Model **1**

^1H		Peak	δ_{obs} (ppm)	δ_{dia} (ppm)	δ_{dip} (ppm)	δ_{calc} (ppm)	% Error
H88	Ortho	I	5.2659	6.9955	-1.730	0.235	-21.408085
H87	Meta	II	6.0276	7.234	-1.206	0.009	-668.73333
H86	Para	III	6.2705	7.1825	-0.912	-0.099	64.338384
H85	Meta	II	6.0276	7.234	-1.206	-0.149	41.453691
H84	Ortho	I	5.2659	6.9955	-1.730	-0.209	26.195694
H94A	Ortho	I	5.2659	6.9955	-1.730	0.156	-32.755769
H93A	Meta	II	6.0276	7.234	-1.206	0.208	-27.978846
H92A	Para	III	6.2705	7.1825	-0.912	0.095	-65.005263
H91A	Meta	II	6.0276	7.234	-1.206	-0.166	37.310843
H90A	Ortho	I	5.2659	6.9955	-1.730	-0.433	13.161432

Table S4: Chemical shift values obtained from modelling {Cr_7Co-PPh_3} using model 2

^1H		Peak	δ_{obs} (ppm)	δ_{dia} (ppm)	δ_{dip} (ppm)	δ_{calc} (ppm)	% Error
H88	Ortho	I	5.2659	6.9955	-1.730	-1.915	3.749817
H87	Meta	II	6.0276	7.234	-1.206	-0.967	7.233299
H86	Para	III	6.2705	7.1825	-0.912	-1.012	7.196146
H85	Meta	II	6.0276	7.234	-1.206	-1.207	5.993869
H84	Ortho	I	5.2659	6.9955	-1.730	-1.706	4.086694
H94A	Ortho	I	5.2659	6.9955	-1.730	-1.579	4.334959
H93A	Meta	II	6.0276	7.234	-1.206	-1.087	6.54517
H92A	Para	III	6.2705	7.1825	-0.912	-1.086	6.773941
H91A	Meta	II	6.0276	7.234	-1.206	-1.15	6.241391
H90A	Ortho	I	5.2659	6.9955	-1.730	-1.762	3.988593

Table S5: Chemical shift values obtained from modelling {Cr_7Co} using Model 3

Piv		Peak	δ_{calc} (ppm)	δ_{obs} (ppm)	% Error	δ_{obs} (ppm)	δ_{dia} (ppm)	δ_{con} (ppm)
2	ax	I	28.343	9.482	-18.861	9.482	1.12	-18.861
3	eq	VIII	-14.754	-2.708	12.046	-2.708	1.12	12.046
4	eq	VII	-1.186	-1.060	0.126	-1.060	1.12	0.126
5	ax	II	-0.366	2.968	3.334	2.968	1.12	3.334
6	ax	III	0.763	1.800	1.037	1.800	1.12	1.037
7	eq	VI	-1.498	-0.716	0.782	-0.716	1.12	0.782
8	eq	V	-1.266	0.064	1.330	0.064	1.12	1.330
9	ax	IV	-1.830	1.252	3.082	1.252	1.12	3.082
10	ax	IV	-1.505	1.252	2.757	1.252	1.12	2.757
11	eq	V	-1.319	0.064	1.383	0.064	1.12	1.383
12	eq	VI	-1.597	-0.716	0.881	-0.716	1.12	1.661
13	ax	III	0.061	1.800	1.739	1.800	1.12	1.739
14	ax	II	-1.193	2.968	4.161	2.968	1.12	4.161
15	eq	VII	-0.775	-1.060	-0.285	-1.060	1.12	-0.285
16	eq	VIII	-14.263	-2.708	11.555	-2.708	1.12	11.555
17	ax	I	27.519	9.482	-18.037	9.482	1.12	-18.037

Chapter 7 Paper 4

"Heterometallic Wheels Linked by Lanthanide tris- β-diketonates as ABA Qubit Systems"

Robert J. Woolfson, Andreas K. Kostopoulos, Grigore A. Timco, Alistair J. Fielding and Richard E.P. Winpenny

Manuscript in preparation

As introduced in Section 2.2.2, the *g*-engineering approach is one route being explored to develop a working quantum computer. Lloyd, in his original 1993 proposal, suggested using a three spin system with each spin having a different *g*-matrix – termed an ABC system.[62] In the absence of any communication between spins, each spin can be individually switched between the $|0\rangle$ and $|1\rangle$ states using a pulse of a particular frequency. If the spins interact, their wavefunctions will mix with the precise change in wavefunction depending on the state of each spin. The resonance frequency of the pulse required to manipulate a given spin will then depend on both the state of that spin and the states of the spin centres coupled to it.

Two systems utilising the concept of *g*-engineering have been developed by Takui and co-workers. An organic triple helicate structure was reported in which Mn^{II} or Zn^{II} ions have three different coordination positions within the helix, resulting in non-equivalent *g*-matrices with different orientations – a prototype ABC spin system (Figure 19).[63] The diamagnetic Zn^{II} derivative was used to prevent intermolecular interactions in magnetic dilution studies. Single crystal Q-band EPR spectroscopy, combined with SQUID magnetometry measurements, provided evidence of three different environments for the Mn^{II} ions with weak interactions between the spin centres. A second system was also reported in which an organic bi-radical complex showed two different *g*-matrices, again due to differing orientations of the spins – an AB spin system. Using a sample diluted in a diamagnetic analogue, the system was shown to have the potential to act as a CNOT gate with a coherence time of 200 ns.[64]

Aromí and co-workers reported a heterometallic lanthanide complex series {LnLn'} using various combinations of Ln = Ce, Er and Y. Both ions in the {CeEr} complex are $I = 0$, reducing decoherence, and were found to have the degenerate ground states required for a qubit (Figure 20a). SQUID magnetometry and EPR measurements suggested a weak antiferromagnetic interaction between the two spin centres, leading to an AB spin system. The four energy levels of the system were found to be unequally

spaced, theoretically allowing specific transitions to be addressed individually using magnetic pulses of different energy (Figure 20b). This system was again proposed as a prototype for a CNOT gate, with a measured coherence time of ≈ 400 ns.

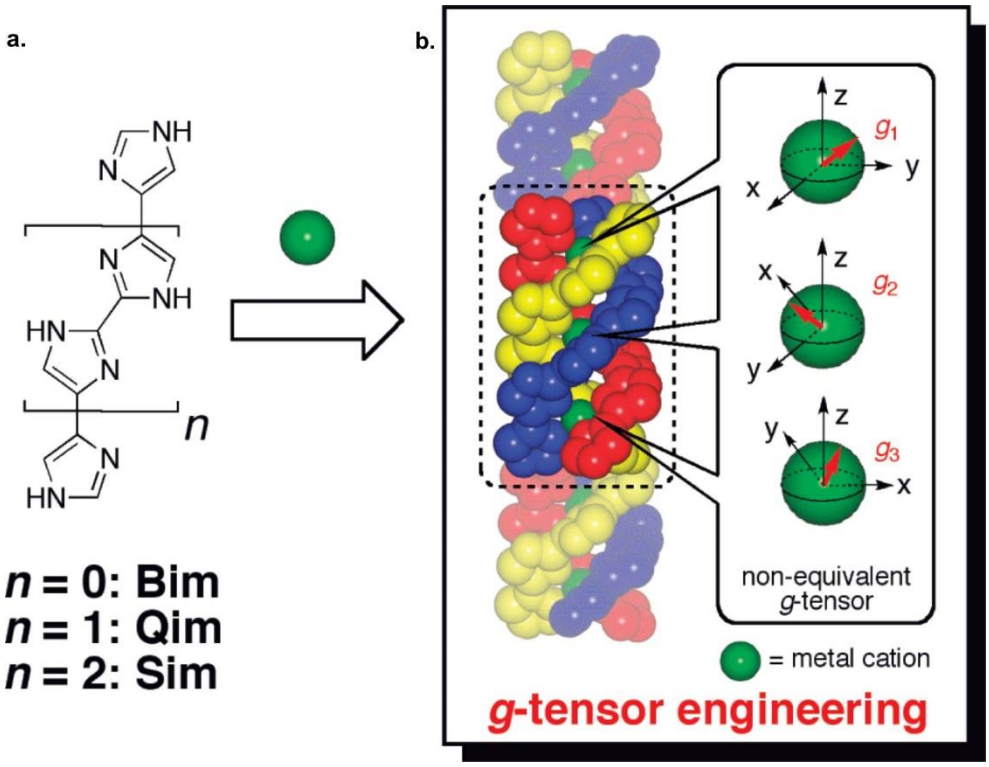

Figure 19: a. Chemical structure of the monomer for the triple helicate (Sim) structure. b. Space fill model of the triple helicate with strands shown in red, blue and yellow, Mn green. Non-equivalent g-tensors for each Mn^{II} ion shown schematically. Adapted with permission from the American Chemical Society.[63]

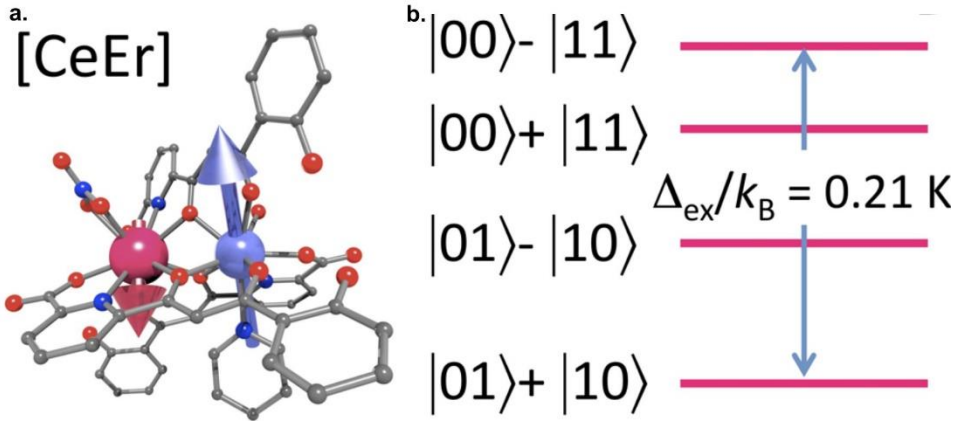

Figure 20: a. X-ray crystal structure of [CeEr] dimer with spin direction and magnitude. b. Scheme of ground state energy level separation. Reproduced under the ACS AuthorsChoice license.[70]

As discussed in Section 2.2.8, Winpenny and co-workers have been exploring supramolecular systems utilising functionalised {Cr_7Ni} wheels and various linkers with different *g*-values as potential qubits.[65, 130, 131] In all cases, the {Cr_7Ni} has been functionalised with a nitrogen donor, either on the thread to make rotaxane based arrangements or directly on the wheel, and then bound to either a single Cu^{II} ion, a Cu^{II} dimer or an {Fe_2Co} triangle to make larger arrays. In the paper below, a different approach was taken. A {Cr_7Ni} wheel was functionalised with a triphenylphosphine oxide moiety and bound to Gd^{III} and Eu^{III} to explore *g*-engineering with {Cr_7Ni} and lanthanide based linkers.

Heterometallic Wheels Linked by Lanthanide tris-β-diketonates as ABA Qubit Systems

Robert J. Woolfson, Andreas K. Kostopoulos, Grigore A. Timco, Alistair J. Fielding and Richard E. P. Winpenny*

School of Chemistry, The University of Manchester, Oxford Road, Manchester, M13 9PL

A novel mixed electron spin system consisting of two heterometallic {Cr_7Ni} wheels linked together by $Ln(C_5F_6H_2O_2)_3$ (Ln = Gd, Eu) has been synthesised and characterised. The lanthanide was found to have a distorted triangular dodecahedral coordination geometry. Continuous wave EPR spectroscopy of the Gd^{III} linked ABA system was used to study the interactions between the spin centres, suggesting no measurable interaction. Luminescence spectroscopy of the Eu^{III} linked AB^*A system suggested that a potential EPR active excited state is accessible via optical excitation with a lifetime of ≈ 1 μs, long enough for use as a gate in a quantum computer.

Introduction

The development of a working, scalable quantum computer is a significant research challenge.[1-4] Molecular systems with unpaired electrons are promising candidates for the quantum bits – qubits – in a quantum computer. Synthesising molecular systems containing electron spins with different *g*-matrices and weak entanglement – the "*g*-engineering" approach suggested by Lloyd for ABC spin systems[5] – introduces the potential for selective control of individual spins, allowing gate operations to be performed.

This route has been explored by Takui and co-workers using Mn^{II} ions with three different *g*-matrices in an organic triple-helicate host as an ABC spin system.[6] Takui has also reported an organic-bi-radical system in which the two radicals have different orientations of their *g*-matrices, with this AB spin system used as a proof of concept for an entangled electron spin based CNOT gate.[7] The "*g*-engineering" approach has also been explored by Aromí and co-workers using mixed-lanthanide systems,[8] and Winpenny

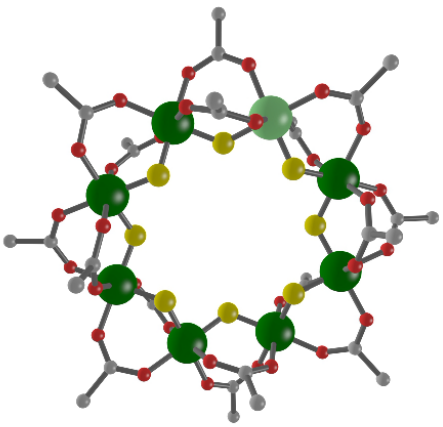

Figure 1: X-ray crystal structure of {Cr_7Ni} viewed perpendicular to the plane of the metal ring. Cr (green), Ni (pale green), F (yellow), O (red), C (grey). Tert-butyl methyl groups, protons and templating ammonium cation omitted for clarity.

and co-workers have suggested using heterometallic triangles and d-block metals as linkers to produce arrays of the heterometallic molecular ring $[NH_2{}^nPr_2][Cr_7NiF_8(O_2C^tBu)_{16}]$ {Cr_7Ni} **1** (Figure 1).[9, 10]

{Cr_7Ni} is an octametallic ring of metals held together by μ_2 bridging fluoride ions and 2,1,1-bridging carboxylate ligands with an ammonium cation in the central cavity for charge balance – also acting as a template for ring formation.[11] The bridging carboxylates, initially pivalate ligands, can be substituted for carboxylates with additional functionality – transforming the wheel into a bulky Lewis base for coordination to metal ions. {Cr_7Ni} has a well isolated $S = 1/2$ ground state, a distinctive *g*-value of 1.78, and a phase memory time sufficient for use as qubits.[12] Previous work has explored coordination between {Cr_7Ni} rings and d-block ions including Cu^{II}, Ag^{I}, Ni^{II}, Mn^{II}, Re^{II} and Co^{II}, with detailed studies of {Cr_7Ni}-M interactions performed on rings with a modified template linked to Cu^{II} ions in various A_nB_m arrangements.[9, 13-16]

In this work, we have functionalised the heterometallic wheel {Cr_7Ni} with 4-diphenylphosphinyl-benzoic acid, coordinated these functionalised rings to lanthanide tris-β-diketonates and explored potential communication between spin systems with different *g*-values in ABA systems.[17, 18] Firstly, using continuous wave EPR spectroscopy we have studied the interactions between a potential electron spin qubit system containing one Gd^{III} ion and two {Cr_7Ni} rings. Secondly, through luminescence spectroscopy we have begun to explore the possibility of developing a qubit where communication between spin centres is mediated by a third, photo-switchable, spin centre with a different g-value using a Eu^{III} ion linking two {Cr_7Ni} rings - an AB^*A spin system where B^* represents an excited spin state.

Structural Characterisation

Refluxing **1** with 4-diphenylphosphinyl-benzoic acid in 1-butanol for 48 h followed by column chromatography resulted in isolation of $[NH_2{}^nPr_2][Cr_7NiF_8(O_2C^tBu)_{15}(O_2C\text{-}C_6H_4\text{-}P(O)Ph_2)]$ **2** in good yield (Figure 2). **2** crystallised as small green blocks in a monoclinic space group. One of the pivalate ligands out of the plane of the metal ring, i.e. an "axial" site, has been replaced by the phosphine-oxide moiety with substitution taking place on the Cr...Ni edge due to the greater lability of the Ni^{II} site compared to that of Cr^{III}.[19] As in previous work, the structure of the metal core was not affected by the ligand substitution,

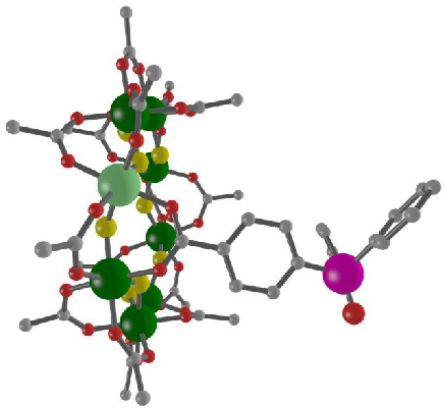

Figure 2: X-ray crystal structure of **2** viewed almost parallel to the plane of the metal ring. Cr (green), Ni (pale green), F (yellow), P (purple), O (red), C (grey). Tert-butyl methyl groups, protons and templating ammonium cation omitted for clarity.

with average M...M distances of 3.390(15) in **2** vs. 3.390(17) Å in **1**.

Reacting two equivalents of **2** with $Ln(hfac)_3(H_2O)_2$ (Ln = Gd, Eu) (hfac = $CF_3C(O)CHC(O)CF_3^-$) resulted in formation of $([NH_2^nPr_2][Cr_7NiF_8(O_2C^tBu)_{15}(O_2C\text{-}C_6H_4\text{-}POPh_2)])_2 \cdot Ln(hfac)_3$ $\mathbf{3}^{Ln}$. $\mathbf{3}^{Gd}$ crystallised as small green plates in a monoclinic space group (Figure 3). A high quality dataset could not be obtained for $\mathbf{3}^{Eu}$, but indexing of a single crystal gave an identical unit cell to that of $\mathbf{3}^{Gd}$. Previously published X-ray crystal structures of $Ln(C_5H_2F_6O_2)_3(OPPh_3)_2$ (Ln = Tb, Er, Eu, Y) show that the family is isostructural.[20-22] The two $\{Cr_7Ni\}$ rings in $\mathbf{3}^{Gd}$ are *trans*- across the Gd^{III} linker but show an eclipsed geometry, similar to previously reported structures.[16]

The rings are not coplanar, but tilted inwards towards the central linker with a dihedral angle between the planes of metals of 82.95 ° and inter-ring distances ranging from 13.415(2) Å to 25.399(2) Å – determined using the shortest and longest inter-metal distances. The distance between the metals in the two $\{Cr_7Ni\}$ rings and the Gd^{III} ion is 11.398(24) Å, with the distance to the centroid of the $\{Cr_7Ni\}$ ring 10.550 Å. The two rings are oriented identically around the Gd^{III} ion, with differences in the separation between the $\{Cr_7Ni\}$ and the Gd^{III} ion statistically insignificant.

The coordination geometry around the Gd site in $\mathbf{3}^{Gd}$ was modelled using the SHAPE tool built by S. Alvarez *et al.*, suggesting a distorted triangular dodecahedral geometry (D_{2d}) around the gadolinium.[23] By comparison the previously published $Eu(C_5H_2F_6O_2)_3(OPPh_3)_2$ structure showed a square antiprismatic (D_{4d}) symmetry,[20] suggesting the $\{Cr_7Ni\}$ moiety results in a distortion of the coordination geometry with a concomitant lowering of the symmetry.

A significant difference is observed in the P-O-Gd bond angles in $\mathbf{3}^{Gd}$ compared to previously reported structures (Table 1). Bis-triphenylphosphine oxide lanthanide structures have typical bond angles of 148-156 ° with slight variations between the two ligands, whereas in $\mathbf{3}^{Gd}$ the observed angles are 167.9(4) ° and 170.6(4) °. The move to a more linear geometry can be explained by the increase in the steric bulk of the ligand and has previously been observed for a $\{Cr_7Ni\}$ functionalised triphenylphosphine ligand complexed with gold.[24] The observed solid state structure is therefore a compromise between the steric demands of the $\{Cr_7Ni\}$ moiety

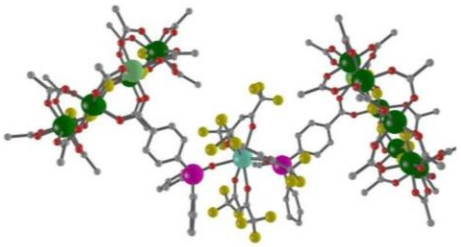

Figure 3: X-ray crystal structure of $\mathbf{3}^{Gd}$. Cr (green), Ni (pale green), F (yellow), P (purple), O (red), C (grey), Gd (pale blue). Tert-butyl methyl groups, protons and ammonium cations omitted for clarity.

Table 1: Collected P-O-Ln bond angles

	Metal	Angle 1 °	Angle 2 °
$Eu(hfac)_3(Ph_3PO)_2$	Eu[20]	148.8(1)	153.5(1)
$\mathbf{3}^{Gd}$	Gd	167.9(4)	170.6(4)
$Tb(hfac)_3(Ph_3PO)_2$	Tb[20]	153.3(1)	153.6(1)
$Er(hfac)_3(Ph_3PO)_2$	Er[22]	155.1(2)	156.4(2)
$Yb(hfac)_3(Ph_3PO)_2$	Yb[21]	152.4(1)	153.2(1)

and optimal packing of the hfac fluorides and the phenyl rings.

EPR Spectroscopy

The EPR spectra for $\mathbf{3^{Gd}}$ were recorded at variable temperature and frequency (Figure 4 and Figures S4, S5). At all frequencies, two separate signals can be observed. The signal from {Cr_7Ni} can be seen at g = 1.78 whilst a signal from the Gd can be observed centred at g = 2.02. The lack of splitting in the {Cr_7Ni} peak at g = 1.78 suggests no measurable interaction between the {Cr_7Ni} and gadolinium spins, within the limits of the spectral linewidth. The EPR spectra were modelled as a non-interacting two component system using g_{Cr7Ni} = [1.79, 1.79, 1.76], g_{Gd} = 2.02, D_{Gd} = -0.083 cm^{-1} and E_{Gd} = -0.014 cm^{-1}. These simulations, whilst not perfectly reproducing the experimental spectra, capture the major features of the spectra and support a model of the system as non-interacting spins. However, this model only uses the *D* and *E* crystal field parameters – which map onto the B_2 crystal field operators and not any Stevens operators of higher order. As the Gd site is in (relatively low) D_{2D} symmetry, it would be expected that inclusion of further crystal field operators would be required to fully model the system.

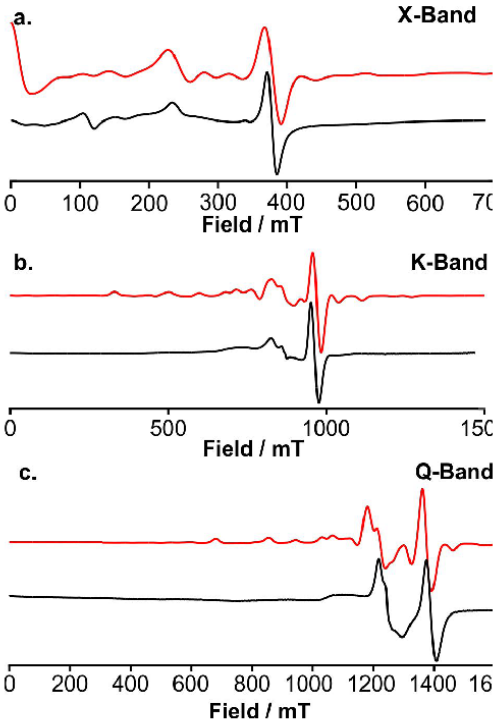

Figure 4: Experimental (black) and simulated (red) EPR spectra for $\mathbf{3^{Gd}}$ measured at X-band (9.387 GHz), K-band (24.030 GHz) and Q-band (34.111 GHz).

Luminescence Spectroscopy

EPR spectroscopy has previously been used to characterise Eu^{II} ($^8S_{7/2}$ ground state), as well as the *in-situ* reduction of Eu^{III} to Eu^{II} in doped lattices and molecular systems.[25-27] However there are no reports of EPR spectroscopy on Eu^{III} of which the authors are aware as Eu^{III} has a diamagnetic $^7F_0$ ground state separated from the first excited state – the diamagnetic $^5D_0$ state – by 17,227 cm^{-1}.[18] To explore whether $\mathbf{3^{Eu}}$ has any excited states accessible by optical excitation, solution state luminescence spectroscopy was used to characterise the electronic structure of both $Eu(hfac)_3(H_2O)_2$ and $\mathbf{3^{Eu}}$.

The emission spectrum of $Eu(hfac)_3(H_2O)_2$ was recorded with λ_{ex} = 340 nm (Figure 5 – Red). The most intense peak observed was at 612 nm, corresponding to the $^5D_0$ -> $^7F_2$ transition. The lifetime for this transition was measured,

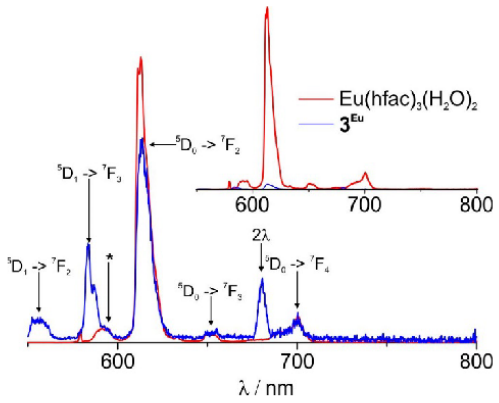

Figure 5: Normalised solution state emission spectra for $Eu(hfac)_3(H_2O)_2$ (red) and $\mathbf{3^{Eu}}$ (blue) recorded at λ_{ex} = 355 nm, 298 K, 0.2 mmol solution in dry $CHCl_3$. Spectra normalised to * = 594 nm. Inset – Absolute intensity of emission spectra.

suggesting a single decay process with a decay half-life (τ) of 268 ± 2 μs (Table 2) – comparable to the 288 μs previously reported.[28, 29] Peaks at 594, 652 and 690 nm - corresponding to the $^5D_0$ -> $^7F_1$, $^5D_0$ -> $^7F_3$ and $^5D_0$ -> $^7F_4$ transitions - were also observed confirming no paramagnetic states are accessible for $Eu(hfac)_3(H_2O)_2$. The emission spectrum of $\mathbf{3^{Eu}}$ also showed an intense peak at 612 nm (Figure 5 - blue). However, the intensity of luminescence for $\mathbf{3^{Eu}}$ was two orders of magnitude smaller than for $Eu(hfac)_3(H_2O)_2$ (Figure 5 - inset), most likely due to the introduction of additional non-radiative decay pathways by interactions with the ligand **2**.

To facilitate comparison, the spectra in Figure 4 have been normalised to the intensity at 594 nm as the intensity of the $^5D_0$ -> $^7F_1$ transition can be assumed to be constant.[18] Strictly, the integral of the $^5D_0$ -> $^7F_1$ transition peak should be used to normalise the intensities – however due to overlap between the $^5D_0$ -> $^7F_1$ and $^5D_1$ -> $^7F_3$ transitions (see below) in $\mathbf{3^{Eu}}$ this is not feasible here, hence use of the intensity at 594 nm.

The measured lifetime for the $^5D_0$ -> $^7F_2$ transition in $\mathbf{3^{Eu}}$ suggested a change to a two component decay process with $\tau_{(1)}$ = 132 ± 12 μs and $\tau_{(2)}$ = 10 ± 1 μs (Figure S8). This reduction in the measured lifetime for $\mathbf{3^{Eu}}$ again suggests that the $\{Cr_7Ni\}$ moiety provides an efficient non-radiative decay mechanism. Comparison of the excitation spectra with the UV-vis spectra for $Eu(hfac)_3(H_2O)_2$ and $\mathbf{3^{Eu}}$ (Figures S6 and S7) confirmed ligand sensitised emission due to a strong overlap between the two spectra.[30]

Similar to the parent $Eu(hfac)_3(H_2O)_2$, peaks at 594, 652 and 690 nm corresponding to the $^5D_0$ -> $^7F_1$, $^5D_0$ -> $^7F_3$ and $^5D_0$ -> $^7F_4$ transitions were observed for $\mathbf{3^{Eu}}$. However, the emission spectrum for $\mathbf{3^{Eu}}$ showed two new peaks at 556 and 584 nm (the peak at 680 nm is the 2λ peak) with the wavelength of these peaks not matching any predicted transitions from the $^5D_0$ state.

Table 2 : Recorded lifetimes for selected electronic transitions in $\mathbf{3^{Eu}}$ and $Eu(hfac)_3(H_2O)_2$, 0.2 mmol in $CHCl_3$, 298 K

Transition		$Eu(hfac)_3(H_2O)_2$	$\mathbf{3^{Eu}}$	
λ (nm)	assignment	τ (μs)	$\tau_{(1)}$ (μs)	$\tau_{(2)}$ (μs)
612	$^5D_0$ -> $^7F_2$	268 ± 2	132 ±12	10 ± 1
556	$^5D_1$ -> $^7F_2$	-	1 ± 0.05	5 ± 0.30
584	$^5D_1$ -> $^7F_2$	-	1 ±0.04	7 ± 0.42

The lifetimes for the new peaks were measured, again suggesting a two component decay process but with a reduction of two orders of magnitude from that of the $^5D_0$ -> $^7F_2$ transition with $\tau_{(1)}$ = 5.030 ± 0.304 µs and $\tau_{(2)}$ = 0.926 ± 0.050 µs for the peak at 556 nm (Table 2 and Figure S9). The peak at 584 nm could potentially be due the $^5D_0$ -> $^7F_0$ transition, however this transition is formally forbidden and is unlikely to be observed except in extremely low symmetry coordination environments.[18] The position of these new peaks, combined with the reduction in the lifetime of the transitions, suggests that these peaks can be assigned to transitions from the $^5D_1$ state to $^7F_2$ and $^7F_3$ respectively.

Peaks due to transitions from the $^5D_1$ state have previously been reported for a tris-β-diketonate Eu(III) complex[31] and in Eu^{3+} doped inorganic lattices.[32] The tri-β-diketonate reported by Zheng *et al.* showed weak emission from the $^5D_1$ state upon excitation with a xenon lamp, but strong emission peaks when excited with a 337 nm laser. The $^5D_1$ -> $^7F_2$ transition was reported at 552-563 nm with a lifetime of around 0.6 µs, matching the values observed for **3^{Eu}** and strongly suggesting the presence of transitions from the $^5D_1$ state.

Conclusions

Previous work by Winpenny and co-workers has suggested that the phase memory time (T_m), a measure of the spin-spin relaxation time combined with other relaxation effects, is of the order of 600 ns in both free {Cr_7Ni} and in functionalised {Cr_7Ni} rings bound to transition metals.[9, 12] For **3^{Eu}** the half-life of the $^5D_2$ excited state is on the order of **1** µs, suggesting that the limiting factor in the time available to perform quantum gates is the {Cr_7Ni} moiety.

It has theoretically been shown that a two qubit CNOT gate – in which the spin state of one qubit is changed depending on the spin state of a control qubit – can be performed on a {Cr_7Ni} based qubit in as little as 30 ns.[33] Similarly, a three qubit $\sqrt{iSWAP}$ gate, in which a pure state is brought into superposition, can be performed on a {Cr_7Ni} based qubit in as little as 8 ns.

These gate times suggest that the lifetime of the Eu^{III} AB^*A spin system would be suitable for performing multiple operations required for a quantum computation. We are currently exploring whether transient EPR spectroscopy can be used to simultaneously excite **3^{Eu}** into the AB^*A state and measure any interaction between the spin centres.[34]

The Gd linked system **3^{Gd}** showed no evidence for any spin-spin interactions within the experimental linewidth, however the spectra were only simulated with first order crystal field parameters. Measurement of a diamagnetic analogue, such as a yttrium linked complex, combined with simulation using a full range of crystal field parameters should allow a full understanding of the extent of any weak communication within **3^{Gd}**.

Acknowledgements

R.J.W. was supported by a studentship from the North-West Nanoscience Doctoral Training Centre (EPSRC grant EP/G03737X/1) and the EPSRC National EPR service. Chloe Oakland and Louise Natrajan are thanked for their help with the luminescence measurements. Eric McInnes is thanked for help simulating the EPR measurements. David Collison is thanked for his

considerable support. All data supporting this study are provided as supplementary information accompanying this paper.

Experimental

See supporting information for full experimental details.

References

1. D. Deutsch, *P. Roy. Soc. A-Math. Phys.*, 1985, **400**, 97-117.
2. R. P. Feynman, *Int. J. Theor. Phys.*, 1982, **21**, 467-488.
3. S. D. Bartlett, *Nature*, 2014, **510**, 345-347.
4. F. Troiani and M. Affronte, *Chem. Soc. Rev.*, 2011, **40**, 3119-3129.
5. S. Lloyd, *Science*, 1993, **261**, 1569-1571.
6. Y. Morita, Y. Yakiyama, S. Nakazawa, T. Murata, T. Ise, D. Hashizume, D. Shiomi, K. Sato, M. Kitagawa, K. Nakasuji and T. Takui, *J. Am. Chem. Soc.*, 2010, **132**, 6944-6946.
7. S. Nakazawa, S. Nishida, T. Ise, T. Yoshino, N. Mori, R. D. Rahimi, K. Sato, Y. Morita, K. Toyota, D. Shiomi, M. Kitagawa, H. Hara, P. Carl, P. Höfer and T. Takui, *Angew. Chem. Int. Ed.*, 2012, **51**, 9860-9864.
8. D. Aguilà, L. A. Barrios, V. Velasco, O. Roubeau, A. Repollés, P. J. Alonso, J. Sesé, S. J. Teat, F. Luis and G. Aromí, *J. Am. Chem. Soc.*, 2014, **136**, 14215-14222.
9. A. Fernandez, E. Moreno-Pineda, C. A. Muryn, S. Sproules, F. Moro, G. A. Timco, E. J. McInnes and R. E. P. Winpenny, *Angew. Chem. Int. Ed.*, 2015, **54**, 10858-10861.
10. J. P. S. Walsh, S. B. Meadows, A. Ghirri, F. Moro, M. Jennings, W. F. Smith, D. M. Graham, T. Kihara, H. Nojiri, I. J. Vitorica-Yrezabal, G. A. Timco, D. Collison, E. J. L. McInnes and R. E. P. Winpenny, *Inorg. Chem.*, 2015, **54**, 12019-12026.
11. F. K. Larsen, E. J. L. McInnes, H. Mkami, J. Overgaard, S. Piligkos, G. Rajaraman, E. Rentschler, A. A. Smith, G. M. Smith, V. Boote, M. Jennings, G. A. Timco and R. E. P. Winpenny, *Angew. Chem. Int. Ed.*, 2003, **42**, 101-105.
12. C. J. Wedge, G. A. Timco, E. T. Spielberg, R. E. George, F. Tuna, S. Rigby, E. J. L. McInnes, R. E. P. Winpenny, S. J. Blundell and A. Ardavan, *Phys. Rev. Lett.*, 2012, **108**, 107204.
13. G. A. Timco, S. Carretta, F. Troiani, F. Tuna, R. J. Pritchard, C. A. Muryn, E. J. L. McInnes, A. Ghirri, A. Candini, P. Santini, G. Amoretti, M. Affronte and R. E. P. Winpenny, *Nat. Nanotechnol.*, 2009, **4**, 173-178.
14. G. F. S. Whitehead, J. Ferrando-Soria, L. G. Christie, N. F. Chilton, G. A. Timco, F. Moro and R. E. P. Winpenny, *Chem. Sci.*, 2013, **5**, 235-239.
15. G. F. S. Whitehead, F. Moro, G. A. Timco, W. Wernsdorfer, S. J. Teat and R. E. P. Winpenny, *Angew. Chem. Int. Ed.*, 2013, **52**, 9932-9935.
16. G. F. S. Whitehead, J. Ferrando-Soria, L. Carthy, R. G. Pritchard, S. J. Teat, G. A. Timco and R. E. P. Winpenny, *Dalton Trans.*, 2016, **45**, 1638-1647.
17. K. Binnemans, in *Handbook on the Physics and Chemistry of Rare Earths*, eds. Karl A. Gschneidner, J.-C. G. Bünzli and V. K. Pecharsky, Elsevier, 2005, vol. 35, pp. 107-272.
18. K. Binnemans, *Coord. Chem. Rev.*, 2015, **295**, 1-45.
19. S. F. Lincoln, *Helv. Chim. Acta*, 2005, **88**, 523-545.
20. V. A. Petrov, W. J. Marshall and V. V. Grushin, *Chem. Commun.*, 2002, 520-521.
21. S. Kishimoto, T. Nakagawa, T. Kawai and Y. Hasegawa, *Bull. Chem. Soc. Jpn.*, 2011, **84**, 148-154.
22. Q. Zhong, H. Wang, G. Qian, Z. Wang, J. Zhang, J. Qiu and M. Wang, *Inorg. Chem.*, 2006, **45**, 4537-4543.
23. S. Alvarez, P. Alemany, D. Casanova, J. Cirera, M. Llunell and D. Avnir, *Coord. Chem. Rev.*, 2005, **249**, 1693-1708.
24. R. Woolfson, G. A. Timco, D. Collison and R. E. P. Winpenny, *Dalton Trans.*, 2016, **Submitted**.
25. D. K. Patel, B. Rajeswari, V. Sudarsan, R. K. Vatsa, R. M. Kadam and S. K. Kulshreshtha, *Dalton Trans.*, 2012, **41**, 12023-12030.
26. Y. Wang, W. Guo, D. Liu, Y. Yang and W. Zheng, *Dalton Trans.*, 2016, **45**, 899-903.
27. H. Matsuoka, N. Ozawa, T. Kodama, H. Nishikawa, I. Ikemoto, K. Kikuchi, K. Furukawa, K. Sato, D. Shiomi, T. Takui and T. Kato, *J. Phys. Chem. B*, 2004, **108**, 13972-13976.

28. A. S. Chauvin, F. Gumy, I. Matsubayashi, Y. Hasegawa and J. C. G. Bünzli, *Eur. J. Inorg. Chem.*, 2006, **2006**, 473-480.
29. D. S. Velasco, A. P. de Moura, A. N. Medina, M. L. Baesso, A. F. Rubira, M. Cremona and A. C. Bento, *J. Phys. Chem. B*, 2010, **114**, 5657-5660.
30. S. Faulkner, L. S. Natrajan, W. S. Perry and D. Sykes, *Dalton Trans.*, 2009, 3890-3899.
31. Y. Zheng, Y. Zhou, J. Yu, Y. Yu, H. Zhang and W. P. Gillin, *J. Phys. D Appl. Phys.*, 2004, **37**, 531.
32. O. K. Moune, P. Porcher and P. Caro, *J. Solid State Chem.*, 1983, **50**, 41-50.
33. J. Ferrando-Soria, E. Moreno-Pineda, A. Chiesa, A. Fernandez, S. A. Magee, S. Carretta, P. Santini, I. J. Vitorica-Yrezabal, F. Tuna, G. A. Timco, E. J. McInnes and R. E. P. Winpenny, *Nat. Commun.*, 2016, **7**, 11377.
34. A. van der Est, *Photosynth. Res.*, 2009, **102**, 335-347.

Heterometallic Wheels Linked by Lanthanide tris-β-diketonates as ABA Qubit Systems

SUPPORTING INFORMATION

R.J. Woolfson,[a] A.K. Kostopoulos,[a] G.A. Timco,[a] A.J. Fielding,[a] and R.E.P. Winpenny[a,*]

School of Chemistry, The University of Manchester, Oxford Road, Manchester, M13 9PL

Contents

1. Experimental 2
   1.1. Synthetic Procedures 3
2. Mass Spectrometry 4
   2.1. O_2C-C_6H_4-$P(O)Ph_2$ 4
   2.2. $[NH_2{}^nPr_2][Cr_7NiF_8(O_2C{}^tBu)_{15}(O_2C$-$C_6H_4$-$P(O)Ph_2)]$ **2** 5
   2.3. $([NH_2{}^nPr_2][Cr_7NiF_8(O_2C{}^tBu)_{15}(O_2C$-$C_6H_4$-$P(O)Ph_2)])_2Gd(C_5F_6H_2O_2)_3$ $\mathbf{3^{Gd}}$ 6
   2.4. $([NH_2{}^nPr_2][Cr_7NiF_8(O_2C{}^tBu)_{15}(O_2C$-$C_6H_4$-$P(O)Ph_2)])_2Eu(C_5F_6H_2O_2)_3$ $\mathbf{3^{Eu}}$ 6
3. EPR Spectroscopy 7
   3.1. X-Band Spectra of $\mathbf{3^{Gd}}$ 7
   3.2. K-Band Spectra of $\mathbf{3^{Gd}}$ 8
4. UV-Vis Spectroscopy 9
   4.1. UV-Vis Spectroscopy for $\{Cr_7Ni\}$, $Eu(hfac)_3(H_2O)_2$ and $\mathbf{3^{Eu}}$ 9
5. Luminescence Spectroscopy 10
   5.1. Excitation Spectra 10
   5.2. Measured Emission Lifetimes for $^5D_0$ -> $^7F_2$ transitions 11
   5.3. Measured Emission Lifetimes for $^5D_1$ transitions in $\mathbf{3^{Eu}}$ 12
6. Crystallography 13
   6.1. Crystallography Tables 13
7. References 14

1. Experimental

All reagents were purchased from commercial sources and used as received. Eu(III) carbonate was purchased as 99.99% pure REacton from Alfa Aesar. Column chromatography was performed using a Grace Reveralis® Autocolumn with Reverelis® Flash Catridges. Mass spectrometry was performed with Mass spectrometry was performed with a Thermo Fisher Scientfic "Exactive Plus EMR orbitrap" in electrospray or atmospheric pressure chemical ionisation mode, spectral simulations were performed using the ChemCalc toolkit.[1]

Solution luminescence spectra were recorded at 0.2 mmol concentration in dry $CHCl_3$ using fused quartz cuvettes with 1 cm path length. Emission spectra were recorded on an Edinburgh Instrument FP920 Phosphorescence Lifetime Spectrometer equipped with a 450 watt steady state xenon lamp, a 5 watt microsecond pulsed xenon flashlamp, (with single 300 mm focal length excitation and emission monochromators in Czerny Turner configuration), a red sensitive photomultiplier in peltier (air cooled) housing (Hamamatsu R928P), and a liquid nitrogen cooled near-IR photomultiplier (Hamamatsu). Lifetime data were recorded following excitation with the microsecond flashlamp using time correlated single photon counting (PCS900 plug-in PC card for fast photon counting). Lifetimes were obtained by tail fit on the data obtained and quality of fit judged by minimization of reduced χ^2. UV-Vis Spectra were collected using an Agilent Cary Series UV-Vis-nIR spectrophotometer with quartz cuvettes, a 1 cm path length and 0.2 mmol solutions in CH_2Cl_2.

X-band and Q-band (~34 GHz) EPR spectra were recorded with a Bruker EMX580 spectrometer. The data were collected using 0.5 mmol solutions in CH_2Cl_2 at variable temperature using liquid helium cooling. Spectral simulations were performed using the EasySpin 4.5.5 simulation software.[2]

Metal elemental analysis was performed by Thermo iCap 6300 Inductively Coupled Plasma Optical Emission Spectroscopy (ICP-OES). Single crystal X-ray structures were collected on a Bruker Apex II Prospector at 100 K. Data sets were reduced with CrysAlisPro then solved and refined by full matrix least squares techniques on F^2 using the ShelXl[3] suite in Olex2.[4] Hydrogen atoms were included in the refinement process as per the riding model. CCDC entries 1499606-7 contain the structures for **2** and $\mathbf{3}^{Gd}$.

1.1. Synthetic Procedures

{Cr_7Ni} was synthesised as previously reported.[5]

4-diphenylphosphinyl-benzoic acid was synthesised by suspending 4-diphenylphosphino-benzoic acid (1.0 g, 3.26 mmol) in H_2O (20 mL) and adding 2M NaOH (1.8 mL). The solution was stirred until clear, filtered through cotton wool and then H_2O_2 (15 mL) added to the solution in a Teflon flask. The flask was sealed and the reaction stirred overnight. HCl (1.0 M) was added until a product precipitated. The solution was filtered, yielding the product in a quantitative yield as a cream powder. ESMS+: 323.0830 (M+H). Elemental Analysis (Calc.): C, 70.43 (70.81); H 4.52 (4.69); P, 9.22 (9.61). NMR ^{1}H (DMSO): 13.37 (1H, COOH); 8.08 (2H, dd, J = 8.13, 2.14, Ar-H); 7.76 (2H, dd, J = 11.21, 8.35, Ar-H); 7.64 (6H, m, Ar-H); 7.58 (4H, m, Ar-H). ^{31}P (DMSO): 25.16 (P=O).

$Gd(C_5F_6H_2O_2)_3(H_2O)_2$ was synthesised according to a previously reported procedure.[6]

$Eu(C_5F_6H_2O_2)_3(H_2O)_2$ was synthesised using an adaptation of a previously reported procedure.[7]

2 was synthesised by refluxing {Cr_7Ni} (2.5 g, 1.10 mmol) and 4-diphenylphosphinylbenzoic acid (1.06 g, 3.29 mmol) in 1-butanol (25 mL) at 140 °C for 48 h. The solution was dried by rotary evaporation, dissolved in CH_2Cl_2 and filtered. The filtrate was purified by column chromatography using a 40 g silica cartridge with CH_2Cl_2/EtOAC as the eluent mix. Unreacted {Cr_7Ni} was separated with 5 % EtOAc and **2** eluted with 15 % EtOAc, yielding a green powder (23.5 %) upon drying by rotary evaporation. ESMS+: 2537 (M+Na). Elemental Analysis (Calc.): C, 47.62 (47.76); H 6.89 (6.66); N, 0.54 (0.55); P, 1.03 (1.25); Cr 13.51 (14.47); Ni, 2.18 (2.33).

3^{Ln} was synthesised by dissolving $Ln(C_5H_2O_2F_6)_3(H_2O)_2$ (0.015 g, 0.02 mmol) in acetone (5 mL), adding **2** (0.1 g, 0.04 mmol) in acetone (5 mL) and heating to 80 °C for 1 h, yielding **3^{Ln}** in a quantitative yield. Crystals of **3^{Ln}** were obtained by slow evaporation of the acetone solution.

3^{Gd}: FTMS+: No satisfactory spectra could be obtained for this compound. Elemental Analysis (Calc): C, 43.94 (44.46); H, 5.88 (5.76); N, 0.51 (0.48); P, 0.96 (1.07); Cr, 11.83 (12. 53); Ni, 1.98 (2.02); Gd, 2.30 (2.71).

3^{Eu}: FTMS+: 5701 (M-[$NH_2{}^nPr_2$]+2H). Elemental Analysis (Calc): C, 44.45 (44.48); H, 5.86 (5.83); N, 0.41 (.048); P, 1.07 (1.06); Cr, 12.41 (12.54), Ni, 2.03 (2.02), Eu, 2.54 (2.62).

2. Mass Spectrometry

2.1. O_2C-C_6H_4-P(O)Ph_2

Shown below (Figure S1) is the FTMS+ spectrum for O_2C-C_6H_4-P(O)Ph_2 showing the M+H and M+Na peaks with simulations.

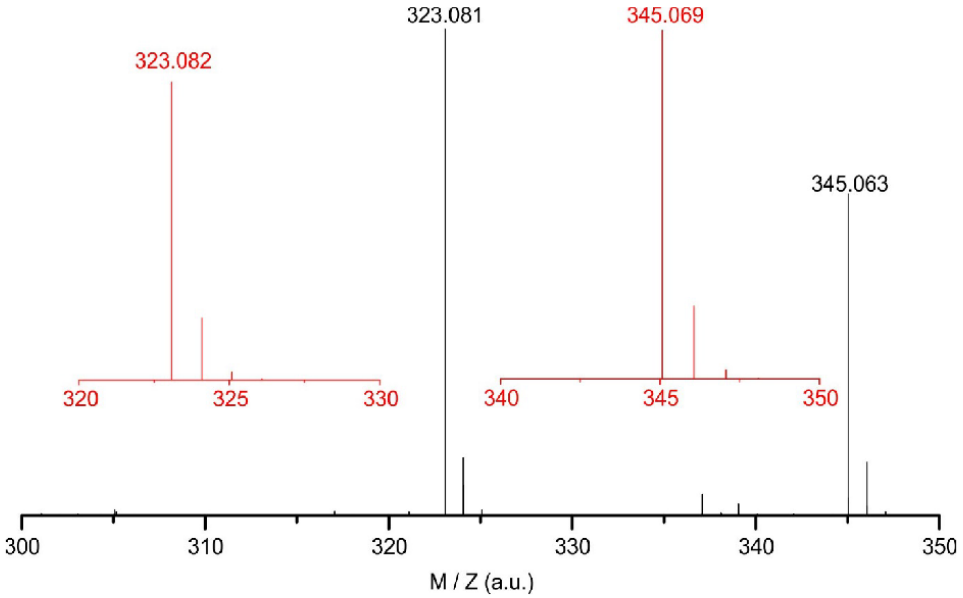

Figure S1: FTMS+ spectrum of O_2C-C_6H_4-P(O)Ph_2 (black) with simulations of M+H and M+Na peaks (red).

2.2. $[NH_2{}^nPr_2][Cr_7NiF_8(O_2C{}^tBu)_{15}(O_2C\text{-}C_6H_4\text{-}P(O)Ph_2)]$ 2

Shown below (Figure S2) is the FTMS+ spectrum for **2** showing the M+Na peak with simulation.

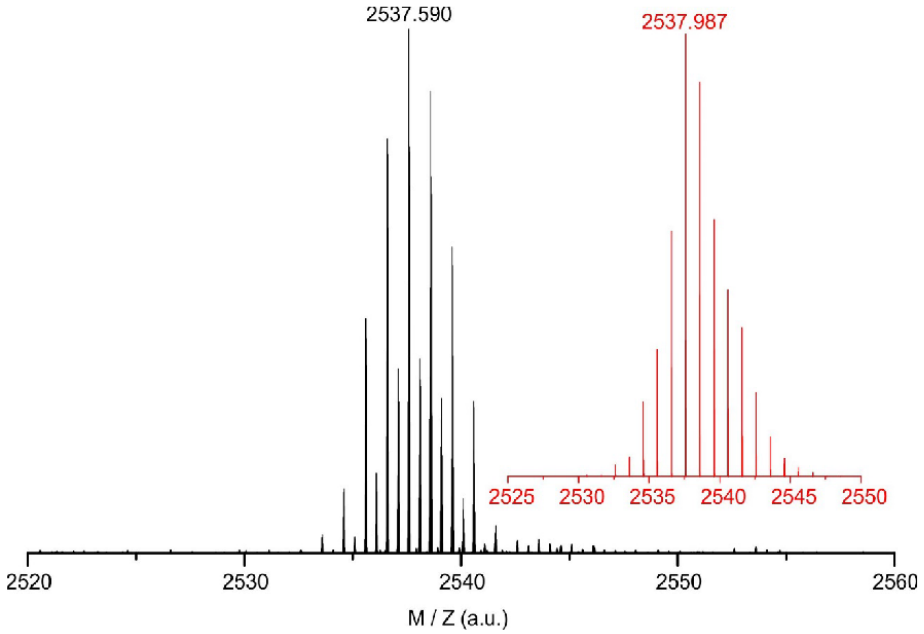

Figure S2: FTMS+ spectrum of **2** showing M + Na peak (black) with simulation (red).

2.3. $([NH_2{}^nPr_2][Cr_7NiF_8(O_2C{}^tBu)_{15}(O_2C\text{-}C_6H_4\text{-}P(O)Ph_2)])_2Gd(C_5F_6H_2O_2)_3$ 3^{Gd}

No satisfactory mass spectrum could be obtained for this compound.

2.4. $([NH_2{}^nPr_2][Cr_7NiF_8(O_2C{}^tBu)_{15}(O_2C\text{-}C_6H_4\text{-}P(O)Ph_2)])_2Eu(C_5F_6H_2O_2)_3$ 3^{Eu}

Shown below (Figure S3) is the FTMS+ spectrum for 3^{Eu} showing the M-$[NH_2{}^nPr_2]$+2H peak.

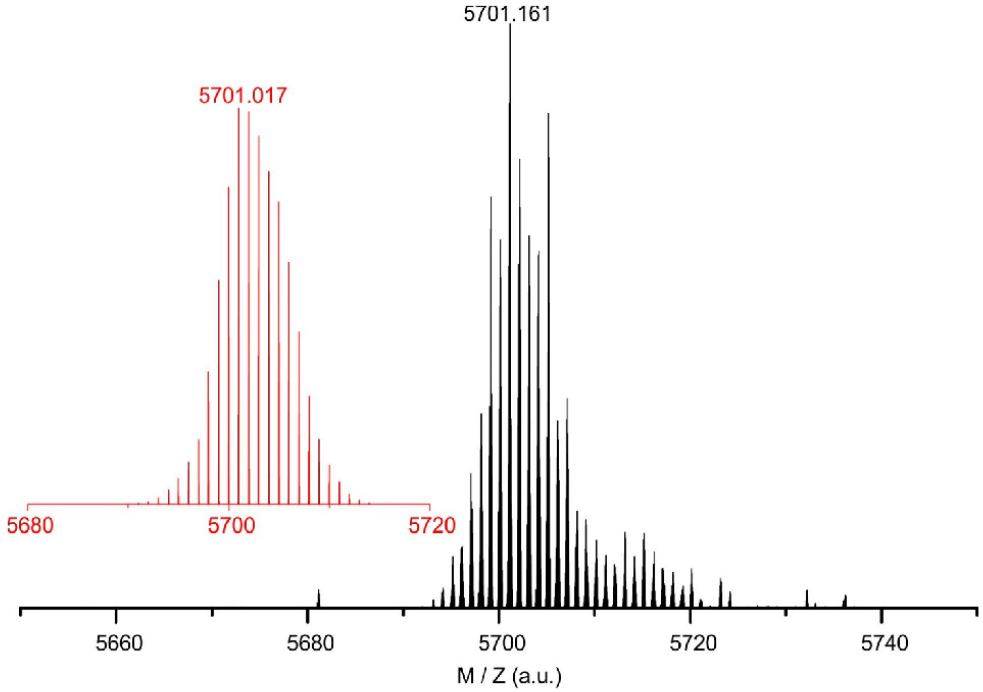

Figure S3: Mass Spectrum for 3^{Eu}. Experimental spectrum (black). Simulation of M-$[NH_2{}^nPr_2]$+2H peak (red).

3. EPR Spectroscopy

3.1. X-Band Spectra of 3^{Gd}

Shown below (Figure S4) are the variable temperature EPR spectra for $\mathbf{3^{Gd}}$ recorded from 5 K to 298 K at X-band (9.387 GHz).

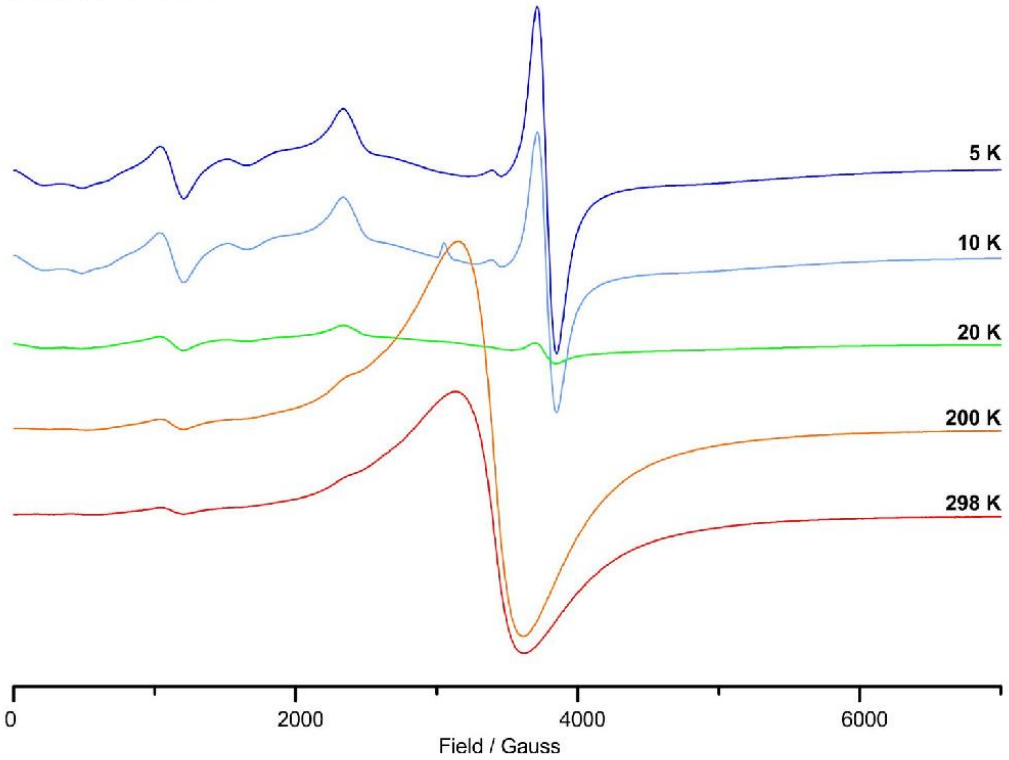

Figure S4: Variable temperature X-band EPR spectra recorded for $\mathbf{3^{Eu}}$ from 5 K to 298 K.

3.2. K-Band Spectra of 3^{Gd}

Shown below (Figure S5) are the variable temperature EPR spectra recorded for $\mathbf{3^{Gd}}$ from 5 K to 100 K at K band (24.03 GHz).

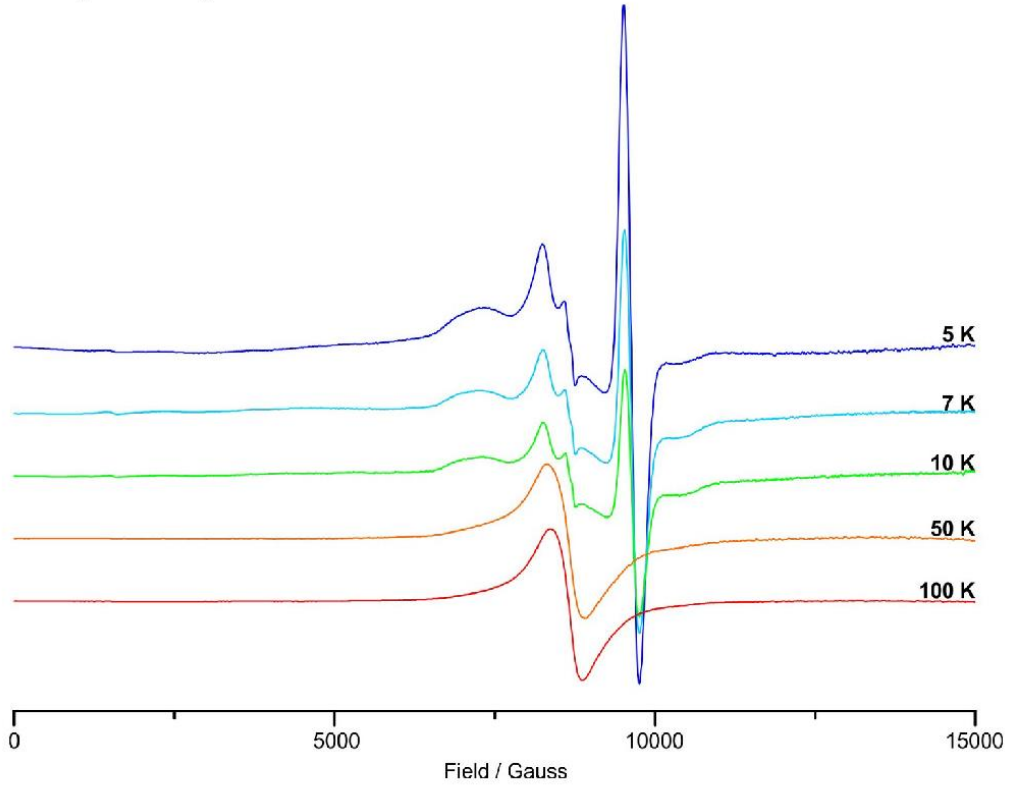

Figure S5: Variable temperature K-band EPR spectra recorded for $\mathbf{3^{Eu}}$

4. UV-Vis Spectroscopy

4.1. UV-Vis Spectroscopy for {Cr_7Ni}, $Eu(hfac)_3(H_2O)_2$ and 3^{Eu}

Shown below (Figure S6) are the UV-visible spectra recorded for **1**, $Eu(hfac)_3(H_2O)_2$ and $\mathbf{3^{Eu}}$ recorded at 0.2 mmol concentration in $CHCl_3$. The spectrum of $\mathbf{3^{Eu}}$ is predominantly an overlap of the spectra of **1** and $Eu(hfac)_3(H_2O)_2$.

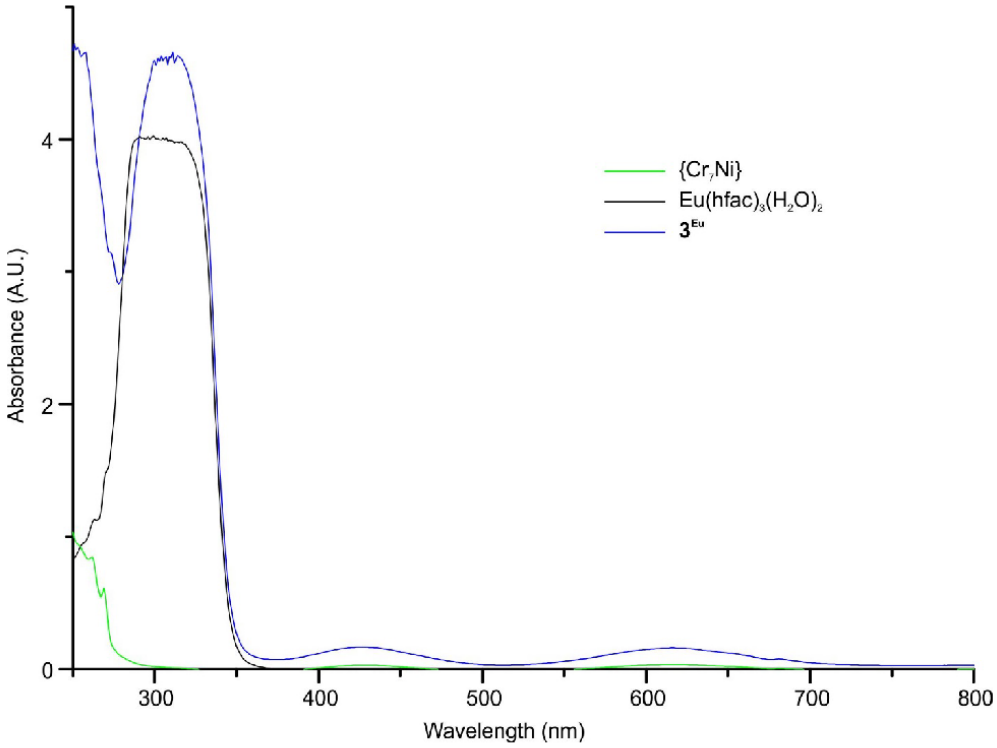

Figure S6: UV-Vis spectra for {Cr_7Ni} (green), $Eu(hfac)_3(H_2O)_2$ (black) and $\mathbf{3^{Eu}}$ (blue) recorded from 250 – 800 nm. Recorded at 298 K, 0.2 mmol solution in $CHCl_3$.

5. Luminescence Spectroscopy

5.1. Excitation Spectra

Shown below (Figure S7) are the absorption spectra for $Eu(hfac)_3(H_2O)_2$ and $\mathbf{3}^{Eu}$ recorded at 298 K using 0.2 mmol solutions in $CHCl_3$. The two spectra have very similar line-shapes, however the absorption spectrum for $\mathbf{3}^{Eu}$ is two orders of magnitude weaker. This suggests that the absorption features of $\mathbf{3}^{Eu}$ are dominated by the Eu^{III} but that either the $\{Cr_7Ni\}$ or the $[O_2C\text{-}C_6H_4\text{-}P(O)Ph_2]$ moieties are strongly absorbing photons without sensitising the Eu^{III} ion.

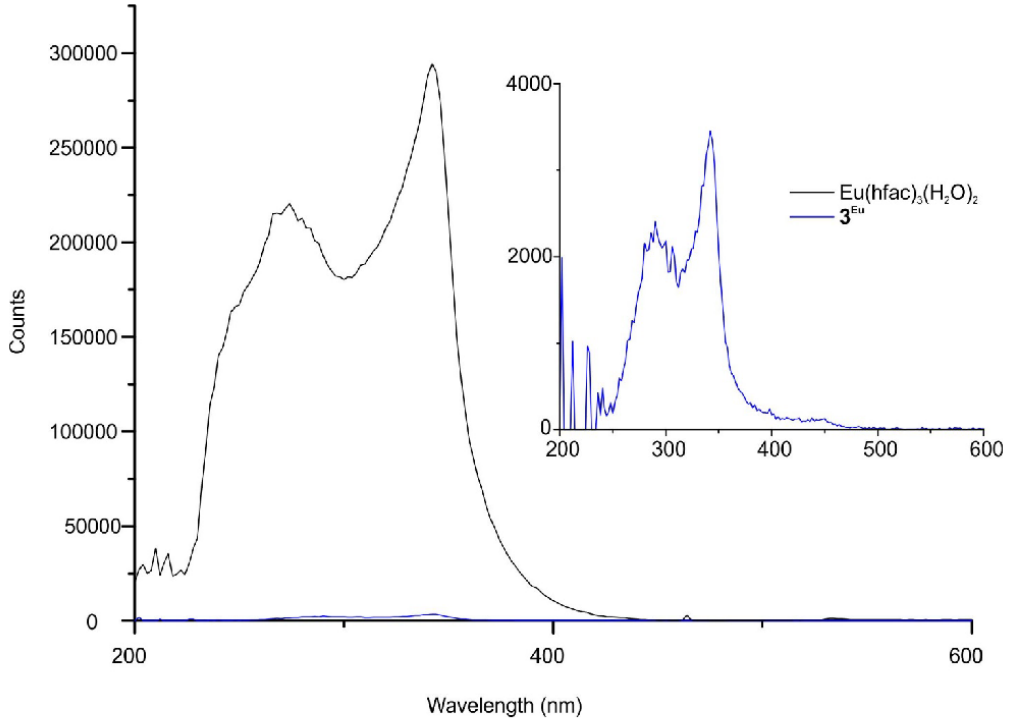

Figure S7: Excitation spectra measured for $Eu(hfac)_3(H_2O)_2$ (black) and $\mathbf{3}^{Eu}$ (blue) measured at λ_{em} = 615 nm, 0.5 nm step size, gate size = 5 nm. Recorded at 298 K, 0.2 mmol solution in $CHCl_3$.

5.2. Measured Emission Lifetimes for $^5D_0$ -> $^7F_2$ transitions

Shown below (Figure S8) are the emission lifetime decay curves for the transition from $^5D_0$ -> $^7F_2$ at 615 nm. Moving from $Eu(hfac)_3(H_2O)_2$ (black) to $\mathbf{3^{Eu}}$ results in a two order of magnitude drop in the lifetime of the emission, suggesting either the $\{Cr_7Ni\}$ or the $[O_2C\text{-}C_6H_4\text{-}P(O)Ph_2]$ moieties are providing an efficient non-radiative decay pathway in $\mathbf{3^{Eu}}$.

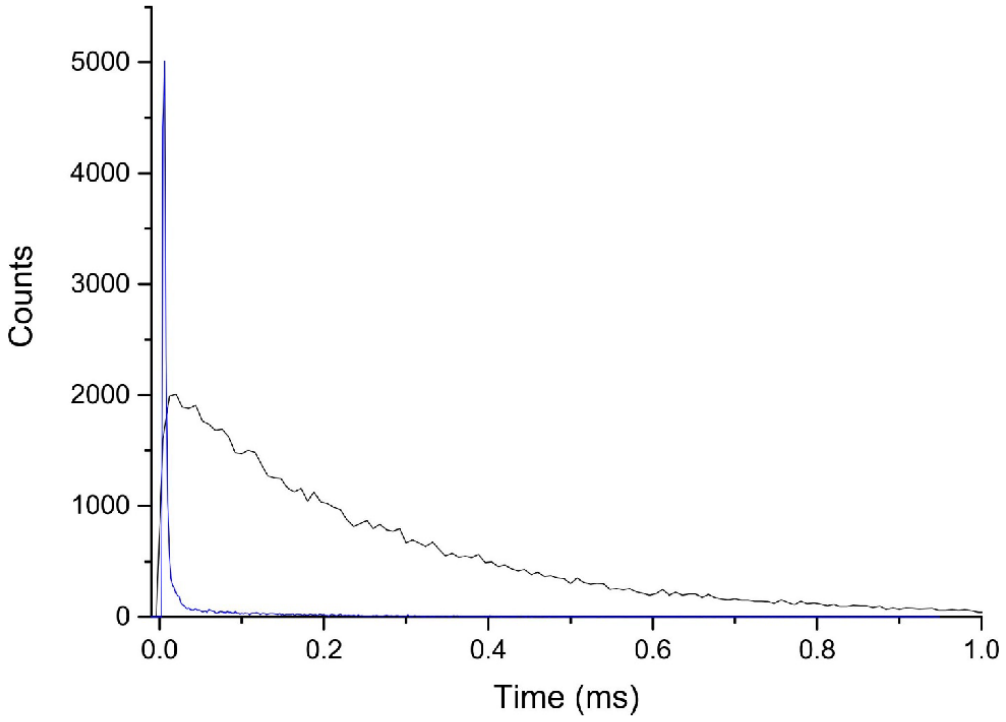

Figure S8: Measured lifetime decay curves for $^5D_0$ -> $^7F_2$ transition at 615 nm for $Eu(hfac)_3(H_2O)_2$ (black) and $\mathbf{3^{Eu}}$ (blue). Recorded at 298 K, 0.2 mmol solution in $CHCl_3$.

5.3. Measured Emission Lifetimes for $^5D_1$ transitions in 3^{Eu}

Shown below (Figure S9) are the measured emission decay curves for the transitions assigned as originating from the $^5D_1$ energy level in $\mathbf{3}^{Eu}$.

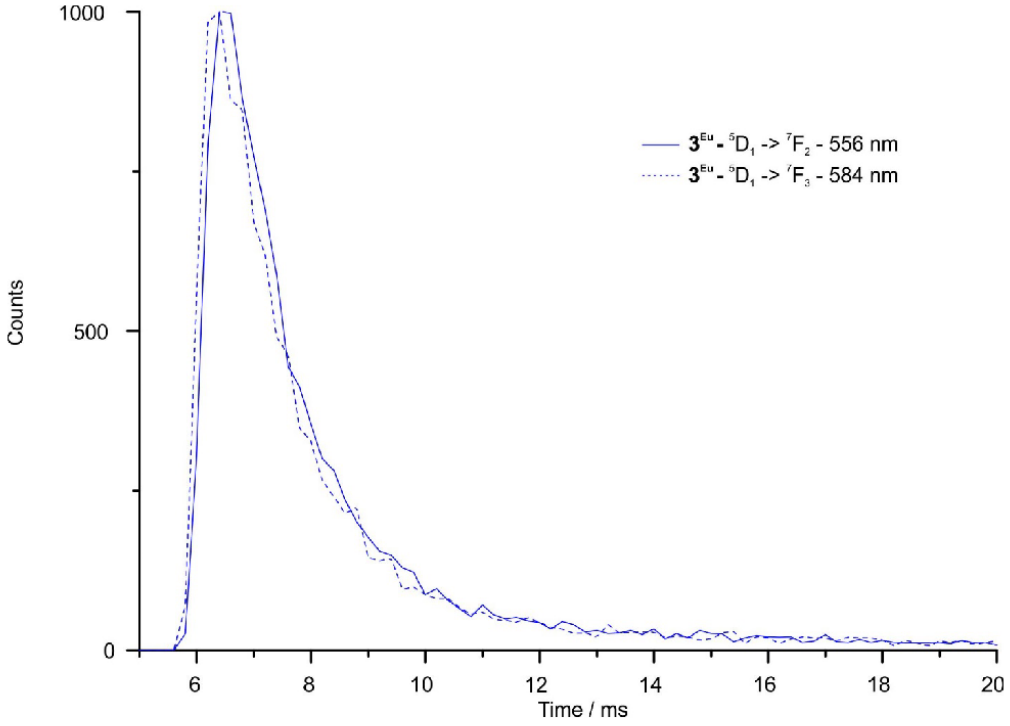

Figure S9: Measured emission lifetime decay curves for transitions from $^5D_1$ state at 556 nm (solid line) and 584 nm (dashed line) in $\mathbf{3}^{Eu}$. χ^2 = 1.514 (556 nm), 1.247 (584 nm). Recorded at 298 K, 0.2 mmol solution in $CHCl_3$.

6. Crystallography

X-ray data were processed and reduced using the CrysAlisPro suite of programs. Absorption correction was performed using empirical methods based upon symmetry equivalent reflections combined with measurements at different azimuthal angles. All crystal structures were solved and refined against all F^2 values using the SHELXTL suite of programs. Non-hydrogen atoms were refined anisotropically where possible, whereas hydrogen atoms were placed in calculated positions using idealised geometry (riding model) and assigned fixed isotropic displacement parameters. In both structures, pivalate ligands were disordered with carbon atoms modelled using SADI and SAME distance restraints. The ammonium cation was modelled using DFIX and SADI. The aryl rings of the triphenylphosphine oxide were modelled using AFIX and FLAT. The atomic displacement parameters of the pivalate ligands, the central ammonium cation and the solvent were restrained using RIGU, DELU and where necessary SIMU. The SQUEEZE algorithm was applied to account for disordered solvent in the intermolecular voids.

6.1. Crystallography Tables

Compound	2	3^{Gd}
Empirical formula	$C_{102}H_{168}Cr_7F_8N_2NiO_{33}P$	$C_{218}H_{341}Cr_{14}F_{34}GdN_2Ni_2O_{73}P_2$
M_w	2556.05	5868.52
Temperature/K	100	100
Crystal system	monoclinic	monoclinic
Space group	$P2_1/c$	P2/n
a Å	24.3056(5)	30.5900(3)
b Å	16.3862(3)	16.46591(19)
c Å	33.3495(8)	60.5325(9)
α °	90	90
B °	90.3999(19)	93.4060(12)
γ °	90	90
Volume Å^3	13282.0(5)	30435.9(6)
Z	4	4
ρ_{calc} g cm^3	1.278	1.281
λ Å	1.54	1.54
T K	100	100
Goof on F^2	1.031	1.030
R^2 [I>=2σ (I)]	0.0938	0.2831
wR^2 [all data]	0.1352	0.2984

7. References

1. L. Patiny and A. Borel, *J. Chem. Inf. Model.*, 2013, **53**, 1223-1228.
2. S. Stoll and A. Schweiger, *J. Magn. Res*, 2006, **178**, 42-55.
3. G. M. Sheldrick, *Acta. Crystall. A-Crys.*, 2007, **64**, 112-122.
4. O. V. Dolomanov, L. J. Bourhis, R. J. Gildea, J. A. K. Howard and H. Puschmann, *J. Appl. Crystallogr.*, 2009, **42**, 339-341.
5. G. A. Timco, S. Carretta, F. Troiani, F. Tuna, R. J. Pritchard, C. A. Muryn, E. J. L. McInnes, A. Ghirri, A. Candini, P. Santini, G. Amoretti, M. Affronte and R. E. P. Winpenny, *Nat. Nanotechnol.*, 2009, **4**, 173-178.
6. K. Bernot, L. Bogani, A. Caneschi, D. Gatteschi and R. Sessoli, *J. Am. Chem. Soc.*, 2006, **128**, 7947-7956.
7. I. P. Malkerova, A. S. Alikhanyan, S. V. Eliseeva, V. A. Ketsko and N. P. Kuz'mina, *Russ. J. Inorg. Chem.*, 2007, **52**, 918-921.

Chapter 8 Conclusions and Future Work

This thesis has studied the properties of spins within cyclic metal systems. The structural and physical properties of several novel systems were evaluated using a wide range of techniques, revealing a wealth of unexpected structures and physical effects.

In Chapter 4, the synthesis and characterisation of a nonametallic ring showing a near perfect match to the expected behaviour for a Type I frustrated system was discussed. This work was a continuation of a project in which this author was involved as a Masters student, see Baker *et al*. (2012).[134] Unlike {Cr_9F_{10}} and {Cr_9F_{11}}, the newly discovered {Cr_9F_9} ring shows strong evidence of spin frustration with an almost degenerate $S = 1/2$ ground state. There are continuing studies on {Cr_9F_9} involving both neutron scattering and neutron diffraction. 4-dimensional INS experiments have been performed on a single crystal of {Cr_9F_9} using beamline IN5 at the Institut Laue Langevin to study the spin dynamics, as has previously been reported for {Cr_8}.[174] Single crystal neutron diffraction experiments have also been performed on beamlines D3 and D9 to study the spin density in the ring. The experimental data requires extensive modelling which has not been completed, therefore the results are not discussed in this thesis.

Chapter 5 considered the coordination behaviour of a {Cr_7Ni} wheel functionalised with a phosphine, with the wheel acting as a soft Lewis base towards gold. Structures containing one, two and three wheels coordinated to gold in various arrangements were reported, showing the versatile binding of this new mono-substituted triphenylphosphine derivative. ^{31}P NMR spectroscopy on the {Cr_7Co} variant, combined with DFT modelling using the SambVca package, revealed a drastic change in the underlying properties of the modified phosphine compared to the parent ligand. The {Cr_7Ni} moiety introduced considerable steric bulk, with a calculated Tolman cone angle of 170.1°. Simultaneously, the ^{31}P NMR spectrum suggested a significant reduction in the strength of the coordination bonds compared to both the parent ligand and to sterically bulky phosphines such as $(C_6F_5)_3P$ – giving the {Cr_7Ni} functionalised phosphine a unique set of properties.

Chapter 6 reported a study on the effect of a ligand substitution on the anisotropy tensor of the Co^{II} ion in the {Cr_7Co} wheel. Using variable temperature NMR spectroscopy combined with the FANTEN modelling packing, the anisotropy tensor on the Co^{II} was found to tilt by ≈ 80 ± 28 ° upon substitution of the pivalate ligand for the phosphine

ligand discussed in Chapter 5. Whilst the error is significant, there is clearly a measurable change in the anisotropy caused by ligand substitution.

Chapter 7 focussed on developing mixed {Cr_7Ni} – lanthanide supramolecular arrays using {Cr_7Ni} functionalised with a phosphine oxide derivative. Disappointingly, the Gd^{III} linked structure was found to show no evidence of communication between the {Cr_7Ni} wheels and the lanthanide – although the possibility of dipolar interactions between the wheels was not excluded by the experiments performed. The Eu^{III} linked structure showed evidence for photoexcitation into a potentially paramagnetic state from the luminescence spectroscopy, but due to equipment issues the preliminary transient EPR experiments could not be performed.

All four papers in this thesis have considerable scope for continuing work. Modelling of {Cr_9F_9} suggested that this wheel has the prerequisite properties to be a candidate for testing electric field switching of magnetic fields, as introduced in Section 2.2.4. The phosphine functionalised {Cr_7Ni} wheel showed evidence for very weak metal binding, and exploring the effects of this weak binding on spin conjugation within arrays of rings – by binding to paramagnetic metals such as Cu^{II} or Ni^{II} – should yield interesting results. Furthermore, the phosphine donor would be ideal for attempting to create an ordered monolayer of the {Cr_7Ni} rings on conductive gold surfaces.

The tilting of the molecular anisotropy in {Cr_7Co} upon ligand substitution was unexpected, but is also a solitary result. A systematic study of ligand substitution on {Cr_7Co} using NMR spectroscopy, combined with X-ray crystallography to study small changes in the local crystal field, may reveal correlations between ligand properties and changes in the anisotropy tensor.

A qubit with optically switchable communication would be of considerable interest. Preliminary studies of the Eu^{III} linked complex suggest it has some of the properties required, but considerable further work is needed to characterise the accessibility of the excited state in transient EPR measurements, whether the state can be recorded using an EPR spectrometer and, most importantly, whether there is any communication between the spin centres.

As for a working quantum computer, the work here may have outlined small steps along the road to developing working spin based molecular qubits, or it may simply become footnotes in the story of molecular wheels and supramolecular chemistry. A Canadian

company – D-Wave Systems – claim to have developed a commercially available quantum computer, the D-Wave Two, based on the a 512 qubit processor. Google, NASA and Lockheed Martin, among others, have all made multi-million dollar investments in D-wave hardware. However, considerable debate rages in the scientific literature over what quantum effects the D-Wave Two exploits and if it shows any speed-up over a well-designed software package running on a (far, far cheaper) classical computer.

In 1981, when Richard Feynman introduced the idea of a quantum simulator in his keynote lecture at the California Institute of Technology, he ended his speech by saying "Nature isn't classical, dammit, and if you want to make a simulation of nature, you'd better make it quantum mechanical, and by golly it's a wonderful problem, because it doesn't look so easy." Thirty five years later, the problem is considerably better understood and prototype systems are starting to appear. However, nothing has really changed. It is still a wonderful problem, and it still doesn't look so easy.

References

1. A. Turing, *P. Lond. Math. Soc.*, 1936-37, **42**, 230-265.
2. G. E. Moore, *Electron. Lett.*, 1965, **65**, April 19th.
3. R. P. Feynman, *Int. J. Theor. Phys.*, 1982, **21**, 467-488.
4. D. Deutsch, *P. Roy. Soc. A-Math. Phys.*, 1985, **400**, 97-117.
5. A. Ardavan and G. A. D. Briggs, *P. Roy. Soc. A-Math. Phys.*, 2011, **369**, 3229-3248.
6. D. P. DiVincenzo and D. Loss, *J. Magn. Magn. Mater.*, 1999, **200**, 202-218.
7. G. A. D. Briggs, *Nanotechnology - Grey Goo or Great God?*, The Faraday Institute for Science and Religion, 2005.
8. J. S. Bell, *Speakable and Unspeakable in Quantum Mechanics*, Cambridge University Press, 2004.
9. C. H. Bennett and D. P. DiVincenzo, *Nature*, 2000, **404**, 247-255.
10. L. K. Grover, *Phys. Rev. Lett.*, 1997, **79**, 4709.
11. L. K. Grover, *Phys. Rev. Lett.*, 1997, **79**, 325.
12. P. W. Shor, Proceedings of the 35th Annual Symposium on the Foundations of Computer Science, IEEE Computer Society, Los Alamitos, CA, 1994.
13. P. W. Shor, *Phys. Rev. A*, 1995, **52**.
14. I. L. Chuang, N. Gershenfeld and M. Kubinec, *Phys. Rev. Lett.*, 1998, **80**, 3408-3411.
15. K. A. Brickman, P. C. Haljan, P. J. Lee, M. Acton, L. Deslauriers and C. Monroe, *Phys. Rev. A*, 2005, **72**, 50306.
16. T. van der Sar, Z. H. Wang, M. S. Blok, H. Bernien, T. H. Taminiau, D. M. Toyli, D. A. Lidar, D. D. Awschalom, R. Hanson and V. V. Dobrovitski, *Nature*, 2012, **484**, 82-86.
17. R. L. Rivest, A. Shamir and L. Adleman, *Commun. ACM*, 1978, **21**, 120-126.
18. G. Ausiello and R. Petreschi, *The Power of Algorithms*, Springer Berlin Heidelberg, Berlin, 2013.
19. A. Ekert and R. Jozsa, *Rev. Mod. Phys.*, 1996, **68**, 733-753.
20. L. M. K. Vandersypen, M. Steffen, G. Breyta, C. S. Yannoni, M. H. Sherwood and I. L. Chuang, *Nature*, 2001, **414**, 883-887.
21. T. Monz, D. Nigg, E. A. Martinez, M. F. Brandl, P. Schindler, R. Rines, S. X. Wang, I. L. Chuang and R. Blatt, *Science*, 2016, **351**, 1068-1070.
22. D. P. DiVincenzo, *Fortschr. Phys.*, 2000, **48**, 771-783.
23. A. Steane, *Appl. Phys. B-Lasers O.*, 1997, **64**, 623-643.
24. D. Loss and D. P. DiVincenzo, *Phys. Rev. A*, 1998, **57**, 120-126.
25. Y. Nakamura, Y. A. Pashkin and J. S. Tsai, *Nature*, 1999, **398**, 786-788.
26. C. Nayak, S. H. Simon, A. Stern, M. Freedman and S. Sarma, *Rev. Mod. Phys.*, 2008, **80**, 1083-1159.
27. J. Clarke and F. K. Wilhelm, *Nature*, 2008, **453**, 1031-1042.
28. A. Imamoglu, D. D. Awschalom, G. Burkard, D. P. DiVincenzo, D. Loss, M. Sherwin and A. Small, *Phys. Rev. Lett.*, 1999, **83**, 4204-4207.
29. Y. Makhlin, G. Schön and A. Shnirman, *Rev. Mod. Phys.*, 2001, **73**, 357-401.
30. D. Kielpinski, C. Monroe and D. J. Wineland, *Nature*, 2002, **417**, 709-711.
31. N. Tombros, C. Jozsa, M. Popinciuc, H. T. Jonkman and B. J. van Wees, *Nature*, 2007, **448**, 571-574.
32. H. J. Briegel, D. E. Browne, W. Dür, R. Raussendorf and V. M. den Nest, *Nat. Phys.*, 2009, **5**, 19-26.
33. T. D. Ladd, F. Jelezko, R. Laflamme, Y. Nakamura, C. Monroe and J. L. O'Brien, *Nature*, 2010, **464**, 45-53.
34. M. H. Devoret and R. J. Schoelkopf, *Science*, 2013, **339**, 1169-1174.

35. C. Monroe and J. Kim, *Science*, 2013, **339**, 1164-1169.
36. R. J. Warburton, *Nat. Mater.*, 2013, **12**, 483-493.
37. W. B. Gao, A. Imamoglu, H. Bernien and R. Hanson, *Nat. Photonics*, 2015, **9**, 363-373.
38. M. Veldhorst, C. H. Yang, J. C. C. Hwang, W. Huang, J. P. Dehollain, J. T. Muhonen, S. Simmons, A. Laucht, F. E. Hudson, K. M. Itoh, A. Morello and A. S. Dzurak, *Nature*, 2015, **526**, 410-414.
39. C. Wang, Y. Y. Gao, P. Reinhold, R. W. Heeres, N. Ofek, K. Chou, C. Axline, M. Reagor, J. Blumoff, K. M. Sliwa, L. Frunzio, S. M. Girvin, L. Jiang, M. Mirrahimi, M. H. Devoret and R. J. Schoelkopf, *Science*, 2016, **352**, 1087-1091.
40. Y. Wang, A. Kumar, T. Y. Wu and D. S. Weiss, *Science*, 2016, **352**, 1562-1565.
41. B. E. Kane, *Nature*, 1998, **393**, 133-137.
42. J. Wrachtrup and F. Jelezko, *J. Phys.-Condens. Mat.*, 2006, **18**.
43. T. Gaebel, M. Domhan, I. Popa, C. Wittmann, P. Neumann, F. Jelezko, J. R. Rabeau, N. Stavrias, A. D. Greentree, S. Prawer, J. Meijer, J. Twamley, P. R. Hemmer and J. Wrachtrup, *Nat. Phys.*, 2006, **2**, 408-413.
44. F. A. Zwanenburg, A. S. Dzurak, A. Morello, M. Y. Simmons, L. C. L. Hollenberg, G. Klimeck, S. Rogge, S. N. Coppersmith and M. A. Eriksson, *Rev. Mod. Phys.*, 2013, **85**, 961.
45. K. Saeedi, S. Simmons, J. Z. Salvail, P. Dluhy, H. Riemann, N. V. Abrosimov, P. Becker, J. H. Pohl, J. J. L. Morton and M. L. W. Thewalt, *Science*, 2013, **342**, 830-833.
46. M. Steger, K. Saeedi, M. L. W. Thewalt, J. J. L. Morton, H. Riemann, N. V. Abrosimov, P. Becker and H. J. Pohl, *Science*, 2012, **336**, 1280-1283.
47. S. Simmons, R. M. Brown, H. Riemann, N. V. Abrosimov, P. Becker, H.-J. J. Pohl, M. L. Thewalt, K. M. Itoh and J. J. Morton, *Nature*, 2011, **470**, 69-72.
48. J. J. L. Morton, A. M. Tyryshkin, R. M. Brown, S. Shankar, B. W. Lovett, A. Ardavan, T. Schenkel, E. E. Haller, J. W. Ager and S. A. Lyon, *Nature*, 2008, **455**, 1085-1088.
49. J. J. Pla, K. Y. Tan, J. P. Dehollain, W. H. Lim, J. J. L. Morton, F. A. Zwanenburg, D. N. Jamieson, A. S. Dzurak and A. Morello, *Nature*, 2013, **496**, 334-338.
50. A. Gruber, A. Dräbenstedt, C. Tietz, L. Fleury, J. Wrachtrup and C. von Borczyskowski, *Science*, 1997, **276**, 2012-2014.
51. E. Togan, Y. Chu, A. S. Trifonov, L. Jiang, J. Maze, L. Childress, M. V. G. Dutt, A. S. Sørensen, P. R. Hemmer, A. S. Zibrov and M. D. Lukin, *Nature*, 2010, **466**, 730-734.
52. H.-R. Wei and G. Long, *Sci. Rep.*, 2015, **5**, 12918.
53. L. Li, T. Schröder, E. H. Chen, M. Walsh, I. Bayn, J. Goldstein, O. Gaathon, M. E. Trusheim, M. Lu, J. Mower, M. Cotlet, M. L. Markham, D. J. Twitchen and D. Englund, *Nat. Commun.*, 2015, **6**, 6173.
54. A. D. Greentree, P. Olivero, M. Draganski, E. Trajkov, J. R. Rabeau, P. Reichart, B. C. Gibson, S. Rubanov, S. T. Huntington, D. N. Jamieson and S. Prawer, *J. Phys.: Condens. Matter*, 2006, **18**.
55. D. G. Cory, A. F. Fahmy and T. F. Havel, *P. Natl. Acad. Sci. U.S.A.*, 1997, **94**, 1634-1639.
56. M. N. Leuenberger and D. Loss, *Nature*, 2001, **410**, 789-793.
57. L. Thomas, F. Lionti, R. Ballou, D. Gatteschi, R. Sessoli and B. Barbara, *Nature*, 1996, **383**, 145-147.
58. J. R. Friedman, M. P. Sarachik, J. Tejada and R. Ziolo, *Phys. Rev. Lett.*, 1996, **76**, 3830-3833.
59. R. Bagai and G. Christou, *Chem. Soc. Rev.*, 2009, **38**, 1011-1026.

60. C. Sangregorio, T. Ohm, C. Paulsen, R. Sessoli and D. Gatteschi, *Phys. Rev. Lett.*, 1997, **78**, 4645-4648.
61. M. Mannini, F. Pineider, P. Sainctavit, C. Danieli, E. Otero, C. Sciancalepore, A. Talarico, M.-A. Arrio, A. Cornia, D. Gatteschi and R. Sessoli, *Nat. Mater.*, 2009, **8**, 194-197.
62. S. Lloyd, *Science*, 1993, **261**, 1569-1571.
63. Y. Morita, Y. Yakiyama, S. Nakazawa, T. Murata, T. Ise, D. Hashizume, D. Shiomi, K. Sato, M. Kitagawa, K. Nakasuji and T. Takui, *J. Am. Chem. Soc.*, 2010, **132**, 6944-6946.
64. S. Nakazawa, S. Nishida, T. Ise, T. Yoshino, N. Mori, R. D. Rahimi, K. Sato, Y. Morita, K. Toyota, D. Shiomi, M. Kitagawa, H. Hara, P. Carl, P. Höfer and T. Takui, *Angew. Chem. Int. Ed.*, 2012, **51**, 9860-9864.
65. A. Fernandez, E. Moreno-Pineda, C. A. Muryn, S. Sproules, F. Moro, G. A. Timco, E. J. McInnes and R. E. P. Winpenny, *Angew. Chem. Int. Ed.*, 2015, **54**, 10858-10861.
66. R. Vincent, S. Klyatskaya, M. Ruben, W. Wernsdorfer and F. Balestro, *Nature*, 2012, **488**, 357-360.
67. S. Thiele, F. Balestro, R. Ballou, S. Klyatskaya, M. Ruben and W. Wernsdorfer, *Science*, 2014, **344**, 1135-1138.
68. K. S. Pedersen, A.-M. Ariciu, S. McAdams, H. Weihe, J. Bendix, F. Tuna and S. Piligkos, *J. Am. Chem. Soc.*, 2016, **138**, 5801-5804.
69. K. Bader, M. Winkler and J. van Slageren, *Chem. Commun.*, 2016, **52**, 3623-3626.
70. D. Aguilà, L. A. Barrios, V. Velasco, O. Roubeau, A. Repollés, P. J. Alonso, J. Sesé, S. J. Teat, F. Luis and G. Aromí, *J. Am. Chem. Soc.*, 2014, **136**, 14215-14222.
71. M. Affronte, F. Troiani, A. Ghirri, A. Candini, M. Evangelisti, V. Corradini, S. Carretta, P. Santini, G. Amoretti, F. Tuna, G. A. Timco and R. E. P. Winpenny, *J. Phys. D: Appl. Phys.*, 2007, **40**, 2999.
72. M. Affronte, F. Troiani, A. Ghirri, S. Carretta, P. Santini, R. Schuecker, G. A. Timco and R. E. P. Winpenny, *J. Magn. Magn. Mater.*, 2007, **310**.
73. A. Ardavan, O. Rival, J. J. L. Morton, S. J. Blundell, A. M. Tyryshkin, G. A. Timco and R. E. P. Winpenny, *Phys. Rev. Lett.*, 2007, **98**, 057201.
74. S. Thiele, *Read-Out and Coherent Manipulation of an Isolated Nuclear Spin Using a Single-Molecule Magnet Spin-Transistor*, Springer, Switzerland, 2016.
75. A. Werner, *Ber. Dtsch. Chem. Ges*, 1908, **41**, 3447-3465.
76. R. F. Weinland, *Ber. Dtsch. Chem. Ges*, 1908, **41**, 3236-3245.
77. R. D. Cannon and R. P. White, *Chemical and Physical Properties of Triangular Bridged Metal Complexes*, 1988.
78. J.-P. Costes, F. Dahan and F. Nicodème, *Inorg. Chem.*, 2001, **40**, 5285-5287.
79. J. Tang, I. Hewitt, N. T. Madhu, G. Chastanet, W. Wernsdorfer, C. E. Anson, C. Benelli, R. Sessoli and A. K. Powell, *Angew. Chem. Int. Ed.*, 2006, **45**, 1729-1733.
80. A. Ohto, Y. Sasaki and T. Ito, *Inorg. Chem.*, 1994, **33**, 1245-1246.
81. H. Toma, *Coord. Chem. Rev.*, 2001, **219-221**, 187-234.
82. K. O. Abdulwahab, M. A. Malik, P. O'Brien, G. A. Timco, F. Tuna, C. A. Muryn, R. E. P. Winpenny, R. A. D. Pattrick, V. S. Coker and E. Arenholz, *Chem. Mater.*, 2014, **26**, 999-1013.
83. J. P. S. Walsh, S. B. Meadows, A. Ghirri, F. Moro, M. Jennings, W. F. Smith, D. M. Graham, T. Kihara, H. Nojiri, I. J. Vitorica-Yrezabal, G. A. Timco, D. Collison, E. J. L. McInnes and R. E. P. Winpenny, *Inorg. Chem.*, 2015, **54**, 12019-12026.

84. L. A. Welo, *Philos. Mag.*, 2009, **6**, 481-509.
85. O. Kahn, *Chem. Phys. Lett.*, 1997, **265**, 109-114.
86. J. Schnack, *Dalton Trans.*, 2010, **39**, 4677-4686.
87. M. Trif, F. Troiani, D. Stepanenko and D. Loss, *Phys. Rev. B*, 2010, **82**, 045429.
88. K. L. Taft and S. J. Lippard, *J. Am. Chem. Soc.*, 1990, **112**, 9629-9630.
89. K. L. Taft, C. D. Delfs, G. C. Papaefthymiou, S. Foner, D. Gatteschi and S. J. Lippard, *J. Am. Chem. Soc.*, 1994, **116**, 823-832.
90. N. V. Gerbeleu, Y. T. Struchkov, G. A. Timko, A. S. Batsanov, K. M. Indrichan and G. A. Popovich, *Doklady Akademii Nauk SSSR*, 1990, **313**, 1459-1462.
91. J. van Slageren, R. Sessoli, D. Gatteschi, A. A. Smith, M. Helliwell, R. E. Winpenny, A. Cornia, A.-L. L. Barra, A. G. Jansen, E. Rentschler and G. A. Timco, *Chem-Eur. J.*, 2002, **8**, 277-285.
92. T. B. Faust, Ph.D, The University of Manchester, 2011.
93. A. Müller, M. Koop, H. Bögge, M. Schmidtmann and C. Beugholt, *Chem. Commun.*, 1998, 1501-1502.
94. A. Müller, S. Q. N. Shah, H. Bögge and M. Schmidtmann, *Nature*, 1999, **397**, 48-50.
95. I.-R. Jeon and D. T. Harris, *Chem. Commun.*, 2015, **52**, 1006-1008.
96. L. A. Barrios, J. Salinas-Uber, O. Roubeau, S. J. Teat and G. Aromí, *Chem. Commun.*, 2015.
97. J. Fielden, M. Speldrich, C. Besson and P. Kögerler, *Inorg. Chem.*, 2012, **51**, 2734-2736.
98. S. Sanz, J. M. Frost, T. Rajeshkumar, S. J. Dalgarno, G. Rajaraman, W. Wernsdorfer, J. Schnack, P. J. Lusby and E. K. Brechin, *Chem-Eur. J.*, 2014, **20**, 3010-3013.
99. N. Ahmed, A. Upadhyay, T. Rajeshkumar, S. Vaidya, J. Schnack, G. Rajaraman and M. Shanmugam, *Dalton Trans.*, 2015, **44**, 18743-18747.
100. V. Mougel, L. Chatelain, J. Pécaut, R. Caciuffo, E. Colineau, J.-C. Griveau and M. Mazzanti, *Nature Chem.*, 2012, **4**, 1011-1017.
101. F. K. Larsen, E. J. L. McInnes, H. El Mkami, J. Overgaard, S. Piligkos, G. Rajaraman, E. Rentschler, A. A. Smith, G. M. Smith, V. Boote, M. Jennings, G. A. Timco and R. E. P. Winpenny, *Angew. Chem. Int. Ed.*, 2003, **42**, 101-105.
102. F. K. Larsen, J. Overgaard, S. Parsons, E. Rentschler, A. A. Smith, G. A. Timco and R. E. P. Winpenny, *Angew. Chem. Int. Ed.*, 2003, **42**, 5978-5981.
103. M. Affronte, A. Ghirri, S. Carretta, G. Amoretti, S. Piligkos, G. A. Timco and R. E. P. Winpenny, *Appl. Phys. Lett.*, 2004, **84**, 3468.
104. R. H. Laye, F. K. Larsen, J. Overgaard, C. A. Muryn, E. J. L. McInnes, E. Rentschler, V. Sanchez, S. J. Teat, H. U. Güdel, O. Waldmann, G. A. Timco and R. E. P. Winpenny, *Chem. Commun.*, 2005, 1125-1127.
105. M. Affronte, S. Carretta, G. A. Timco and R. E. P. Winpenny, *Chem. Commun.*, 2007, 1789-1797.
106. F. Moro, D. Kaminski, F. Tuna, G. F. S. Whitehead, G. A. Timco, D. Collison, R. E. P. Winpenny, A. Ardavan and E. J. L. McInnes, *Chem. Commun.*, 2013, **50**, 91-93.
107. S. Carretta, P. Santini, G. Amoretti, M. Affronte, A. Ghirri, I. Sheikin, S. Piligkos, G. A. Timco and R. E. P. Winpenny, *Phys. Rev. B*, 2005, **72**.
108. F. Troiani, A. Ghirri, M. Affronte, S. Carretta, P. Santini, G. Amoretti, S. Piligkos, G. A. Timco and R. E. P. Winpenny, *Phys. Rev. Lett.*, 2005, **94**, 207208.
109. G. A. Timco, S. Carretta, F. Troiani, F. Tuna, R. J. Pritchard, C. A. Muryn, E. J. L. McInnes, A. Ghirri, A. Candini, P. Santini, G. Amoretti, M. Affronte and R. E. P. Winpenny, *Nat. Nanotechnol.*, 2009, **4**, 173-178.

110. C. J. Wedge, G. A. Timco, E. T. Spielberg, R. E. George, F. Tuna, S. Rigby, E. J. L. McInnes, R. E. P. Winpenny, S. J. Blundell and A. Ardavan, *Phys. Rev. Lett.*, 2012, **108**, 107204.
111. E. J. L. McInnes, G. A. Timco, G. F. S. Whitehead and R. E. P. Winpenny, *Angew. Chem. Int. Ed.*, 2015, **54**, 2-28.
112. C. E. Sañudo, T. B. Faust, C. A. Muryn, R. G. Pritchard, G. A. Timco and R. E. P. Winpenny, *Inorg. Chem.*, 2009, **48**, 9811-9818.
113. R. Caciuffo, T. Guidi, G. Amoretti, S. Carretta, E. Liviotti, P. Santini, C. Mondelli, G. Timco, C. A. Muryn and R. E. P. Winpenny, *Phys. Rev. B*, 2005, **71**, 174407.
114. V. Corradini, F. Moro, R. Biagi, D. V. Renzi, U. del Pennino, V. Bellini, S. Carretta, P. Santini, V. A. Milway, G. A. Timco, R. E. P. Winpenny and M. Affronte, *Phys. Rev. B*, 2009, **79**.
115. V. Corradini, A. Ghirri, U. del Pennino, R. Biagi, V. A. Milway, G. A. Timco, F. Tuna, R. E. P. Winpenny and M. Affronte, *Dalton Trans.*, 2010, **39**, 4928-4936.
116. A. Ghirri, V. Corradini, C. Cervetti, A. Candini, U. del Pennino, G. Timco, R. J. Pritchard, C. A. Muryn, R. E. P. Winpenny and M. Affronte, *Adv. Funct. Mater.*, 2010, **20**, 1552-1560.
117. A. Ghirri, V. Corradini, V. Bellini, R. Biagi, U. del Pennino, V. Renzi, J. C. Cezar, C. A. Muryn, G. A. Timco, R. E. P. Winpenny and M. Affronte, *ACS Nano*, 2011, **5**, 7090-7099.
118. S. F. Lincoln, *Helv. Chim. Acta*, 2005, **88**, 523-545.
119. G. A. Timco, E. J. L. McInnes, R. G. Pritchard, F. Tuna and R. E. P. Winpenny, *Angew. Chem. Int. Ed.*, 2008, **47**, 9681-9684.
120. A. Candini, G. Lorusso, F. Troiani, A. Ghirri, S. Carretta, P. Santini, G. Amoretti, C. Muryn, F. Tuna, G. A. Timco, E. J. L. McInnes, R. E. P. Winpenny, W. Wernsdorfer and M. Affronte, *Phys. Rev. Lett.*, 2010, **104**.
121. T. B. Faust, V. Bellini, A. Candini, S. Carretta, G. Lorusso, D. R. Allan, L. Carthy, D. Collison, R. J. Docherty, J. Kenyon, J. Machin, E. J. McInnes, C. A. Muryn, H. Nowell, R. G. Pritchard, S. J. Teat, G. A. Timco, F. Tuna, G. F. S. Whitehead, W. Wernsdorfer, M. Affronte and R. E. P. Winpenny, *Chem-Eur. J.*, 2011, **17**, 14020-14030.
122. T. B. Faust, F. Tuna, G. A. Timco, M. Affronte, V. Bellini, W. Wernsdorfer and R. E. P. Winpenny, *Dalton Trans.*, 2012, **41**, 13626.
123. A. Candini, D. Klar, S. Marocchi, V. Corradini, R. Biagi, D. V. De Renzi, U. del Pennino, F. Troiani, V. Bellini, S. Klyatskaya, M. Ruben, K. Kummer, N. B. Brookes, H. Huang, A. Soncini, H. Wende and M. Affronte, *Sci. Rep.*, 2016, **6**, 21740.
124. G. F. S. Whitehead, J. Ferrando-Soria, L. G. Christie, N. F. Chilton, G. A. Timco, F. Moro and R. E. P. Winpenny, *Chem. Sci.*, 2013, **5**, 235-239.
125. M. Affronte, I. Casson, M. Evangelisti, A. Candini, S. Carretta, C. A. Muryn, S. J. Teat, G. A. Timco, W. Wernsdorfer and R. E. P. Winpenny, *Angew. Chem. Int. Ed.*, 2005, **44**, 6496-6500.
126. G. A. Timco, T. B. Faust, F. Tuna and R. E. P. Winpenny, *Chem. Soc. Rev.*, 2011, **40**, 3067-3075.
127. G. F. S. Whitehead, F. Moro, G. A. Timco, W. Wernsdorfer, S. J. Teat and R. E. P. Winpenny, *Angew. Chem. Int. Ed.*, 2013, **52**, 9932-9935.
128. A. Chiesa, G. F. S. Whitehead, S. Carretta, L. Carthy, G. A. Timco, S. J. Teat, G. Amoretti, E. Pavarini, R. E. P. Winpenny and P. Santini, *Sci. Rep.*, 2014, **4**, 7423.

129. G. F. S. Whitehead, J. Ferrando-Soria, L. Carthy, R. G. Pritchard, S. J. Teat, G. A. Timco and R. E. P. Winpenny, *Dalton Trans.*, 2016, **45**, 1638-1647.
130. J. Ferrando-Soria, E. Moreno-Pineda, A. Chiesa, A. Fernandez, S. A. Magee, S. Carretta, P. Santini, I. J. Vitorica-Yrezabal, F. Tuna, G. A. Timco, E. J. McInnes and R. E. P. Winpenny, *Nat. Commun.*, 2016, **7**, 11377.
131. A. Fernandez, J. Ferrando-Soria, E. Moreno-Pineda, F. Tuna, I. J. Vitorica-Yrezabal, C. Knappke, J. Ujma, C. A. Muryn, G. A. Timco, P. E. Barran, A. Ardavan and R. E. P. Winpenny, *Nat. Commun.*, 2016, **7**, 10240.
132. M. Shanmugam, L. P. Engelhardt, F. K. Larsen, M. Luban, E. J. L. McInnes, C. A. Muryn, J. Overgaard, E. Rentschler, G. A. Timco and R. E. P. Winpenny, *Chem-Eur. J.*, 2006, **12**, 8267-8275.
133. L. P. Engelhardt, C. A. Muryn, R. G. Pritchard, G. A. Timco, F. Tuna and R. E. P. Winpenny, *Angew. Chem. Int. Ed.*, 2008, **47**, 924-927.
134. M. L. Baker, G. A. Timco, S. Piligkos, J. S. Mathieson, H. Mutka, F. Tuna, P. Kozłowski, M. Antkowiak, T. Guidi, T. Gupta, H. Rath, R. J. Woolfson, G. Kamieniarz, R. G. Pritchard, H. Weihe, L. Cronin, G. Rajaraman, D. Collison, E. J. L. McInnes and R. E. P. Winpenny, *P. Natl. Acad. Sci. U. S. A.*, 2012, **109**, 19113-19118.
135. G. A. Timco, A. S. Batsanov, F. K. Larsen, C. A. Muryn, J. Overgaard, S. J. Teat and R. E. P. Winpenny, *Chem. Commun.*, 2005, 3649-3651.
136. A. B. Boeer, D. Collison, C. A. Muryn, G. A. Timco, F. Tuna and R. E. P. Winpenny, *Chem-Eur. J.*, 2009, **15**, 13150-13160.
137. C. F. Lee, D. A. Leigh, R. G. Pritchard, D. Schultz, S. J. Teat, G. A. Timco and R. E. P. Winpenny, *Nature*, 2009, **458**, 314-318.
138. B. Ballesteros, T. B. Faust, C.-F. F. Lee, D. A. Leigh, C. A. Muryn, R. G. Pritchard, D. Schultz, S. J. Teat, G. A. Timco and R. E. P. Winpenny, *J. Am. Chem. Soc.*, 2010, **132**, 15435-15444.
139. G. F. S. Whitehead, B. Cross, L. Carthy, V. A. Milway, H. Rath, A. Fernandez, S. L. Heath, C. A. Muryn, R. G. Pritchard, S. J. Teat, G. A. Timco and R. E. P. Winpenny, *Chem. Commun.*, 2013, **49**, 7195-7197.
140. H. Rath, G. A. Timco, V. Corradini, A. Ghirri, U. del Pennino, A. Fernandez, R. G. Pritchard, C. A. Muryn, M. Affronte and R. E. P. Winpenny, *Chem. Commun.*, 2013, **49**, 3404-3406.
141. Q. Hu, R. J. Noll, H. Li, A. Makarov, M. Hardman and G. R. Cooks, *J. Mass Spectrom.*, 2005, **40**, 430-443.
142. R. H. Perry, G. R. Cooks and R. J. Noll, *Mass Spectrom. Rev.*, 2008, **27**, 661-699.
143. R. Rezaaiyaan, G. M. Hieftje, H. Anderson, H. Kaiser and B. Meddings, *Appl. Spectrosc.*, 1982, **36**, 627-631.
144. G. M. Sheldrick, *Acta Crystallogr. A*, 2007, **64**, 112-122.
145. G. M. Sheldrick, *Acta Crystallogr. C*, 2015, **71**, 3-8.
146. O. V. Dolomanov, L. J. Bourhis, R. J. Gildea, J. A. K. Howard and H. Puschmann, *J. Appl. Crystallogr.*, 2009, **42**, 339-341.
147. H. Nowell, S. A. Barnett, K. E. Christensen, S. J. Teat and D. R. Allan, *J. Synchrotron Rad.*, 2012, **19**, 435-441.
148. W. Massa, *Crystal Structure Determination*, Springer-Verlag Berlin Heidelberg, Berlin, 2004.
149. P. Müller, *Crystal structure refinement : a crystallographers guide to SHELXL*, Oxford University Press, Oxford; New York, 2006.
150. K. Karaghiosoff, in *eMagRes*, John Wiley & Sons, Ltd, 2007.

151. O. Kühl, *Phosphorus-31 NMR spectroscopy: A Concise Introduction for the Synthetic Organic and Organometallic chemist*, Springer, Berlin Heidelberg, 2008.
152. P. Geerlings, F. d. Proft and W. Langenaeker, *Chem. Rev.*, 2003, **103**, 1793-1874.
153. W. Koch and M. C. Holthausen, *A Chemist's Guide to Density Functional Theory*, Wiley-VCH Verlag GmbH, Weinheim, 2001.
154. A. Poater, B. Cosenza, A. Correa, S. Giudice, F. Ragone, V. Scarano and L. Cavallo, *Eur. J. Inorg. Chem.*, 2009, **2009**, 1759-1766.
155. L. Falivene, R. Credendino, A. Poater, A. Petta, L. Serra, R. Oliva, V. Scarano and L. Cavallo, *Organometallics*, 2016, **35**, 2286-2293.
156. M. Rinaldelli, A. Carlon, E. Ravera, G. Parigi and C. Luchinat, *J. Biomol. NMR*, 2015, **61**, 21-34.
157. M. L. Baker, Ph.D, The University of Mancester, 2010.
158. T. Guidi, in *Molecular Cluster Magnets*, World Scientific, Singapore, 2012, pp. 181-213.
159. H. Zhao, C. P. Berlinguette, J. Bacsa, A. V. Prosvirin, J. K. Bera, S. E. Tichy, E. J. Schelter and K. R. Dunbar, *Inorg. Chem.*, 2004, **43**, 1359-1369.
160. P. Gerbier, D. Ruiz-Molina, N. Domingo, D. B. Amabilino, J. Vidal-Gancedo, J. Tejada, D. N. Hendrickson and J. Veciana, *Monatsh. Chem.*, 2003, **134**, 265-276.
161. M. Pacchioni, A. Cornia, A. C. Fabretti, L. Zobbi, D. Bonacchi, A. Caneschi, G. Chastanet, D. Gatteschi and R. Sessoli, *Chem. Commun.*, 2004, **0**, 2604-2605.
162. A. B. Boeer, Ph.D, The University of Manchester, 2009.
163. J. P. S. Walsh, Ph.D, The University of Manchester, 2014.
164. A. B. Boeer, A. L. Barra, L. F. Chibotaru, D. Collison, E. J. L. McInnes, R. A. Mole, G. G. Simeoni, G. A. Timco, L. Ungur, T. Unruh and R. E. P. Winpenny, *Angew. Chem. Int. Ed.*, 2011, **50**, 4007-4011.
165. E. Kampert, F. F. B. J. Janssen, D. W. Boukhvalov, J. C. Russcher, J. M. M. Smits, R. de Gelder, B. de Bruin, P. C. M. Christianen, U. Zeitler, M. I. Katsnelson, J. C. Maan and A. E. Rowan, *Inorg. Chem.*, 2009, **48**, 11903-11908.
166. D. W. Boukhvalov, V. V. Dobrovitski, P. Kögerler, M. Al-Saqer, M. I. Katsnelson, A. I. Lichtenstein and B. N. Harmon, *Inorg. Chem.*, 2010, **49**, 10902-10906.
167. L. A. Kushch, V. D. Sasnovskaya, A. I. Dmitriev, E. B. Yagubskii, O. V. Koplak, L. V. Zorina and D. W. Boukhvalov, *Dalton Trans.*, 2012, **41**, 13747-13754.
168. M. Murrie, *Chem. Soc. Rev.*, 2010, **39**, 1986-1995.
169. O. Kahn, *Molecular Magnetism*, Science, the University of Michigan, 1993.
170. I. Bertini, C. Luchinat and G. Parigi, *Solution NMR of Paramagnetic Molecules: Application to Metalobiomolecules and Models*, Elsevier, Amsterdam, 2001.
171. L. Banci and M. Piccioli, in *eMagRes*, John Wiley & Sons, 2007.
172. I. Bertini, C. Luchinat, G. Parigi and R. Pierattelli, *ChemBioChem*, 2005, **6**, 1536-1549.
173. F. Arnesano, L. Banci and M. Piccioli, *Q. Rev. Biophys.*, 2005, **38**, 167-219.
174. M. L. Baker, T. Guidi, S. Carretta, J. Ollivier, H. Mutka, H. U. Güdel, G. A. Timco, E. J. L. McInnes, G. Amoretti, R. E. P. Winpenny and P. Santini, *Nat. Phys.*, 2012, **8**.